UNIVERSITY OF BELGRADE

FACULTY OF PHYSICS

Veljko Janković

EXCITON DYNAMICS AT PHOTOEXCITED ORGANIC HETEROJUNCTIONS

Doctoral Dissertation

Belgrade, 2018

УНИВЕРЗИТЕТ У БЕОГРАДУ
ФИЗИЧКИ ФАКУЛТЕТ

Вељко Јанковић

ДИНАМИКА ЕКСИТОНА НА ОРГАНСКИМ ХЕТЕРОСПОЈЕВИМА ПОБУЂЕНИМ СВЕТЛОШЋУ

Докторска дисертација

Београд, 2018

Thesis advisor, Committee member:

Dr Nenad Vukmirović

Research Professor

Institute of Physics Belgrade

University of Belgrade

Committee member:

Prof. Dr Ivanka Milošević

Professor

Faculty of Physics

University of Belgrade

Committee member:

Prof. Dr Đorđe Spasojević

Associate Professor

Faculty of Physics

University of Belgrade

Exciton Dynamics at Photoexcited Organic Heterojunctions

Abstract

The last three decades have seen vigorous and interdisciplinary research activities in the field of organic photovoltaics. Research efforts in this field are driven by the promise of economically viable and environmentally friendly conversion of sunlight into electrical energy at heterojunctions between an electron-donating (donor) and an electron-accepting (acceptor) organic material. The light-to-charge conversion in organic solar cells (OSCs) requires the separation of the initially photogenerated donor exciton, whose binding energy is much larger than the thermal energy at room temperature, into free hole and electron in the donor and acceptor material, respectively. This separation is commonly thought to occur via the electron transfer from the photoexcited donor to the acceptor material that produces the so-called charge transfer (CT) exciton, in which the electron and hole are still tightly bound. Despite such large binding energies of both the donor and CT exciton, experiments on the most efficient OSCs indicate that virtually all of the photons absorbed by the cell are eventually converted into free carriers in a process that is weakly aided by both the temperature and the internal electric field in the cell. A gamut of proposals that could rationalize the aforementioned experimental findings have been put forward. However, a more detailed understanding of fundamental physical mechanisms that govern the operation of OSCs on different time scales is still lacking.

The research whose results are presented in this thesis aims to achieve the aforementioned goal by studying the relevant processes within a relatively simple, yet physically plausible, model of organic semiconductors and their heterojunctions. Our fully quantum and statistical investigations of ultrafast dynamics of photoinduced electronic excitations in such models are motivated by recent experimental results indicating that the light-to-charge conversion in the most efficient OSCs occurs on subpicosecond time scales. We find that the exciton formation in a neat organic semiconductor occurs on multiple time scales spanning the range between 50 fs and 1 ps. We conclude that an overwhelming fraction of spatially separated charges that are present on a 100-fs time scale after the photoexcitation of a donor/acceptor heterojunction are directly optically generated from the ground state, and are not obtained as a result of an ultrafast population transfer from donor states. The resonant mixing among donor states and states of spatially separated charges is at the heart of the direct accessibility of the latter group of states from the ground state. However, the light absorption still primarily occurs in the donor material, and the charge separation yields we observe at 1 ps following the excitation suggest that charges predominantly separate on much longer time scales, starting from the strongly bound donor and CT states. Our study of charge separation that takes place on long time scales indicates that the combination of moderate disorder and carrier delocalization can explain quite efficient separation of strongly bound excitons and its weak dependence on the temperature and electric field.

Keywords: organic photovoltaics, organic semiconductors, exciton, light-to-charge conversion, charge transfer, charge separation, ultrafast dynamics

Scientific field: Physics

Research area: Condensed matter physics

UDC number: 538.9

Динамика екситона на органским хетероспојевима побуђеним светлошћу

Сажетак

У току последње три деценије спроводе се интензивна и интердисциплинарна истраживања у области органских фотоволтаика. Истраживачки напори у овој области су мотивисани могућношћу економски исплативе и еколошки прихватљиве конверзије Сунчеве светлости у електричну енергију на хетероспојевима два органска материјала, од којих је један донор, а други акцептор електрона. Да би се извршила конверзија светлости у слободна наелектрисања у органским соларним ћелијама, неопходно је раздвојити иницијално генерисани донорски екситон, чија је енергија везе значајно већа од термалне енергије на собној температури, на слободне шупљину и електрон у материјалу донора, односно акцептора. Сматра се да се то раздвајање обавља путем трансфера електрона из светлошћу побуђеног материјала донора у материјал акцептора који води стварању такозваног CT екситона (екситона у којем је дошло до трансфера наелектрисања), у којем су електрон и шупљина и даље јако везани. Упркос великој вредности везивне енергије како донорског, тако и CT екситона, експерименти на најефикаснијим органским соларним ћелијама указују на то да готово сви фотони апсорбовани у ћелији бивају конвертовани у слободне носиоце, при чему је та конверзија слабо потпомогнута како температуром, тако и унутрашњим електричним пољем у ћелији. Предложени су многобројни механизми који би могли да објасне горе поменуте експерименталне резултате. Међутим, још увек недостаје подробније разумевање фундаменталних физичких механизама који су одговорни за функционисање органских соларних ћелија на различитим временским скалама.

Истраживање чији су резултати презентовани у овој тези тежи да оствари горе поменути циљ проучавајући релевантне процесе у оквирима релативно једноставних, а физички утемељених модела органских полупроводника и њихових хетероспојева. Наша у целости квантна и статистичка испитивања ултрабрзе динамике светлошћу генерисаних електронских ексцитација у таквим моделима су мотивисана недавним експерименталним резултатима који указују да се конверзија светлости у слободна наелектрисања у најефикаснијим органским соларним ћелијама обавља на временским скалама испод једне пикосекунде. Добили смо да се формирање екситона у чистом органском полупроводнику обавља на више различитих временских скала које се протежу од 50 fs до 1 ps. Закључили смо да је највећи део просторно раздвојених наелектрисања која су присутна на временским скалама реда 100 fs након побуде донор/акцептор хетероспоја директно оптички генерисан из основног стања и није последица ултрабрзог трансфера популације из донорских стања. Могућност генерисања стања просторно раздвојених наелектрисања директно из основног стања је последица њиховог резонантног мешања са донорским стањима. Ипак, апсорпција светлости се и даље примарно дешава у материјалу донора, док приноси раздвајања наелектрисања које опажамо 1 ps након побуђивања указују на то да се наелектрисања доминантно раздвајају на значајно дужим временским скалама полазећи из јако везаних донорских и CT стања. Наше испитивање раздвајања наелектрисања на дужим временским скалама показује да комбинација умерене неуређености и делокализације носилаца може да објасни веома ефикасно раздвајање јако везаних екситона и његову слабу зависност од температуре и електричног поља.

Кључне речи: органски фотоволтаици, органски полупроводници, екситон, конверзија светлости у наелектрисања, трансфер наелектрисања, раздвајање наелектрисања, ултрабрза динамика

Научна област: Физика

Област истраживања: Физика кондензоване материје

УДК број: 538.9

Acknowledgements

The research whose results are presented in this thesis has been entirely conducted in the Scientific Computing Laboratory (SCL) of the Institute of Physics Belgrade (IPB). The research project has been supervised by Dr Nenad Vukmirović, Research Professor at IPB. It was a great honor and an immense pleasure to enter the world of science under the guidance of Dr Vukmirović. After our fruitful collaboration during my master programme, Dr Vukmirović has offered me the opportunity to work with him on, at that time, extremely hot topic of free-charge generation in organic solar cells based on a heterojunction between two organic semiconductors. However, instead of performing *ab initio* calculations and obtaining quantitative insights on particular material systems, he suggested that the problem be tackled from a physicists' perspective. In the last four years, step by step, we have been building our own view of free-charge generation in organic solar cells, which has ultimately resulted in the publication of this thesis. I am deeply indebted to Dr Vukmirović for his generous help and patience during our collaboration. He has been extremely dedicated to pursuing the new research line that was launched with the start of my doctoral programme. He was always open to thorough discussions on different aspects of problems and difficulties that I encountered during my research. However, he did his best to keep my focus on the aspects that were really relevant for the topic we worked on. Dr Vukmirović has also invested a great deal of effort in finding viable ways of communicating our results to the global scientific community. Thanks to his Marie Curie Integration Grant and his active participation in the COST Action MultiscaleSolar, I had many opportunities to proudly present our findings at scientific conferences all over Europe. I appreciate very much his efforts to create a specific research climate that was supposed to mimic the one found in world's leading research institutions. I very much hope that the future will show that all these efforts have not been in vain.

I am also grateful to Dr Antun Balaž for giving me the opportunity to be part of SCL and participate in the National Project ON171017 *Modeling and Numerical Simulations of Complex Many-Particle Systems*. I would also like to acknowledge continuous support and encouragement that I have received from Dr Balaž during all these years. Despite his numerous duties, he has

always been willing to discuss with me various problems and dilemmas that I have encountered both on professional and personal level. Certain pieces of his advice, which stem from his broad life experience, have made a strong impact on me and on my attitude towards a carrier in science and life in general.

My work in SCL would not have been so pleasant if I had not been surrounded by very kind and helpful colleagues. The implementation of the equations I derived into working computational codes on high performance computing architectures would not have been possible without generous assistance of the ICT staff. In particular, I give thanks to Mr Petar Jovanović for his help in writing codes that can be run on the PARADOX Supercomputing Facility and for his invaluable advice concerning programming and information technologies in general.

During my doctoral programme, I was also involved in teaching at the Faculty of Physics as an external collaborator. I would like to thank all the people who supported my inclusion in the teaching process at the Faculty, in particular Prof. Dr Sunčica Elezović-Hadžić, Doc. Dr Duško Latas, Prof. Dr Zoran Radović, and Doc. Dr Mihajlo Vanević. I enjoyed the collaboration with Dr Vanević and Prof. Radović on teaching Quantum Statistical Physics. Their suggestions have helped me maintain balance between research and teaching activities, while thorough discussions with them have greatly impacted my view of research and science. Despite being relatively infrequent, conversations with Prof. Elezović-Hadžić have always been reassuring and full of support and understanding.

I cannot help mentioning my activities in the National Committee for High-School Physics Competitions, in which I participated as one of the authors of problems offered to the final-year students. Let me thank my coauthors, Dr Vukmirović and Ms Ana Hudomal, for very nice and fertile cooperation in preparing problems for all levels of the competition cycle. My work in the Committee was very rewarding because I had the opportunity to broaden my understanding of some basic physical phenomena, learn how science should be communicated to young generations, and make contacts with brilliant young minds that are bound to become renowned experts in the future. I had numerous opportunities to informally discuss with the President of the Committee, Doc. Dr Božidar Nikolić, who taught me many lessons that are not part of standard university curricula by sharing his rich experience in both teaching and research.

In the end, let me thank my mother Gordana for putting up with me during all these years and for providing me with unconditional love and support. Even though her expertise lies well outside research and science, she has always been at my disposal and ready to help me evaluate my own achievements and assess their position in a broader context. I firmly believe that her participation in my continuous self-evaluation has played an important role in my doctoral programme.

The research activities conducted during my doctoral studies were supported by the Ministry of Education, Science, and Technological Development of the Republic of Serbia (Project No. ON171017), the European Community FP7 Marie Curie Integration Grant ELECTROMAT, and the European Commission under H2020 project VI-SEEM, Grant No. 675121. I have also benefited from the contribution of the COST Action MP1406 (MultiscaleSolar).

Contents

Members of the Thesis Defense Committee **i**

Abstract **ii**

Abstract in Serbian **iv**

Acknowledgements **vi**

List of Figures **xiii**

List of Tables **xvii**

List of Abbreviations **xviii**

Physical Constants **xx**

List of Symbols **xxi**

1 Introduction **1**

- 1.1 Global Energy Issue 1
- 1.2 Photovoltaic Effect and Solar Cell 3
- 1.3 Organic Semiconductors 6
  - 1.3.1 Electronic Configuration of Carbon in Organic Semiconductors 7
  - 1.3.2 Different Types of Organic Semiconductors 10
  - 1.3.3 Comparison between Inorganic and Organic Semiconductors 16
- 1.4 Organic Solar Cells 18
- 1.5 Critical View of the Sequential Mechanism of OSC Operation 23

1.6 Organization of the Thesis 28

2 Standard Semiconductor Model 32

2.1 Two-Band Semiconductor Model 33

2.2 Definition of Exciton 42

2.3 Wannier and Frenkel Exciton Models 45

2.3.1 Wannier Exciton Model 46

2.3.2 Frenkel Exciton Model 50

3 Theoretical Approach to Ultrafast Exciton Dynamics 55

3.1 General Picture of the Dynamics of Photoexcited Semiconductors 56

3.2 Density Matrix Theory 57

3.3 Brief Review of Theoretical Approaches to Ultrafast Exciton Dynamics 59

3.4 Fundamentals of the DCT Scheme 62

3.5 The DCT Scheme up to the Second Order in Applied Field 68

3.5.1 Energy and Particle-Number Conservation 75

3.5.2 Closing the Phonon Branch of the Hierarchy 76

3.5.3 Another View of the Second-Order Semiconductor Dynamics 82

3.5.4 Schematic Picture of the Second-Order Semiconductor Dynamics . . . 84

Coherent and Incoherent Quantities 84

Analysis of the Semiconductor Dynamics 87

4 Ultrafast Exciton Dynamics in Photoexcited Neat Semiconductors 89

4.1 Theoretical and Experimental Background 89

4.2 Model Description 93

4.2.1 One-Dimensional Semiconductor Model 93

4.2.2 Parametrization of the Model Hamiltonian 96

4.3 Numerical Results 99

4.3.1 Organic Set of Parameters 102

4.3.2 Inorganic Set of Parameters 111

4.4 Discussion and Significance of Our Results 114

5 Origin of Ultrafast Charge Separation 116

5.1 Experimental and Theoretical Background 116

5.1.1 Overview of Recent Experimental Results 117

5.1.2 Overview of Recent Theoretical Results 121

5.2 Model Description 124

5.2.1 One-Dimensional Lattice Model of a Heterojunction 124

5.2.2 Parametrization of the Model Hamiltonian 127

5.2.3 Classification of Exciton States 131

5.3 Numerical Results 133

5.3.1 Interfacial Dynamics on Ultrafast Time Scales 134

5.3.2 Impact of Model Parameters on Ultrafast Exciton Dynamics 136

5.4 Ultrafast Spectroscopy Signatures 142

5.4.1 Basics of Ultrafast Transient Absorption Spectroscopy and Conventional Interpretation of Experimental Signals 143

5.4.2 Theoretical Treatment of Ultrafast Transient Absorption Spectroscopy . 145

5.4.3 Numerical Results: Ultrafast Differential Transmission Signals 151

5.5 Discussion and Significance of Our Results 155

6 Identification of Ultrafast Photophysical Pathways 159

6.1 Motivation 159

6.2 Model Description 162

6.2.1 Multiband Model Hamiltonian of a Heterojunction 162

6.2.2 Parameterization of the Model Hamiltonian 164

6.2.3 Role of the D/A Coupling and the Resonant Mixing Mechanism 168

6.3 Numerical Results 174

6.3.1 General Analysis of Ultrafast Interfacial Dynamics 176

6.3.2 Individuation of Ultrafast Photophysical Pathways 180

6.3.3 Influence of Model Parameters on Ultrafast Exciton Dynamics 184

6.4 Discussion and Significance of Our Results 192

7 Incoherent Charge Separation at Photoexcited Organic Bilayers 195

7.1 Solar Cells as Electric Devices 195

7.2 Experimental and Theoretical Background 198

7.2.1 Overview of Recent Experimental Results 198

7.2.2 Overview of Recent Theoretical Results 201

7.3 Model and Method 205

7.3.1 Model Hamiltonian 205

7.3.2 Theoretical Approach to Incoherent Charge Separation 207

7.3.3 Parameterization of the Model Hamiltonian 210

7.4 Numerical Results 216

7.4.1 Charge Separation from the Strongly Bound CT State 218

7.4.2 Charge Separation from a Donor Exciton State 231

7.5 Discussion and Significance of Our Results 238

8 Conclusion 242

A Proofs of the Expansion and Truncation Theorems in the Phonon-Free Case 247

A.1 Proof of the Expansion Theorem 247

A.2 Proof of the Truncation Theorem 249

B Contraction Relations Relevant for the Second-Order Dynamics 251

C Markov and Adiabatic Approximations 254

D Further Details about Closing the Hierarchy of Equations 256

D.1 Closing the Phonon Branch of the Hierarchy 256

D.2 Comments on the Energy Conservation 258

***Curriculum Vitae*–Veljko Janković 281**

List of Figures

1.1 Fuel shares of the total primary energy supply in 1973 and 2015. 2

1.2 General scheme of a solar cell. 3

1.3 Benzene molecule and its π-electron molecular orbitals. Series of oligoacenes. Crystal structure of pentacene molecular crystal. 9

1.4 Molecular orbitals of two isolated molecules and their dimer. 11

1.5 Chemical formulae of fullerene and PCBM molecules. 12

1.6 Structure of trans-polyacetylene and Peierls instability. 13

1.7 Chemical formulae of monomer units of P3HT and PCPDTBT polymers. Unit cell of the ideally ordered P3HT polymer. 15

1.8 Schematic view of active layers of different types of OSCs. 19

1.9 Band alignment in a D/A OSC. 19

1.10 Pictorial view of the sequential mechanism of light-to-charge conversion in OSCs. 21

1.11 Pictorial view of “hot” and “cold” charge separation mechanisms in OSCs. . . . 27

3.1 Schematic picture of the hierarchy of equations for density matrices. 82

4.1 Schematic view of the parallelization scheme implemented in our own `C` program that performs integration of the system of quantum kinetic equations. . . . 101

4.2 Exciton spectrum in the model of a neat organic semiconductor. 103

4.3 Time evolution of the number of bound excitons in the model of a neat organic semiconductor for different central frequencies of the excitation. 105

4.4 Time evolution of the number of bound excitons in the model of a neat organic semiconductor for different temperatures. 106

4.5 Time evolution of exciton populations in particular exciton bands in the model of a neat organic semiconductor for different temperatures. 107
4.6 Time evolution of the number of coherent excitons for different temperatures. . 107
4.7 Time evolution of the number of bound excitons in the model of a neat organic semiconductor for different carrier-phonon interaction strengths. 108
4.8 Time evolution of the number of bound excitons in the model of a neat organic semiconductor for different values of the on-site Coulomb interaction. 109
4.9 Exciton spectrum in the model of a neat inorganic semiconductor. 111
4.10 Exciton dynamics in the model of a neat inorganic semiconductor. 113

5.1 Schematic view of ultrafast optical experiments performed by Bakulin et al. [48]. 118
5.2 Schematic view of ultrafast optical experiments performed by Jailaubekov et al. [37]. 119
5.3 Schematic view of ultrafast optical experiments performed by Grancini et al. [36]. 120
5.4 Schematic view of the two-band model of a D/A heterojunction. 125
5.5 Time evolution of populations of various groups of exciton states, together with the probability of an electron being in the acceptor, in the two-band model of a D/A heterojunction. 135
5.6 Ultrafast exciton dynamics in the two-band model of a D/A heterojunction for different values of the D/A electronic coupling. 137
5.7 Ultrafast exciton dynamics in the two-band model of a D/A heterojunction for different values of the LUMO–LUMO offset. 138
5.8 Ultrafast exciton dynamics in the two-band model of a D/A heterojunction for different values of the electronic coupling in the acceptor. 138
5.9 Ultrafast exciton dynamics in the two-band model of a D/A heterojunction for different carrier–phonon interaction strengths. 139
5.10 Ultrafast exciton dynamics in the two-band model of a D/A heterojunction for different ratios of the carrier–phonon coupling constants with high- and low-frequency phonon modes. 141

5.11 Ultrafast exciton dynamics in the two-band model of a D/A heterojunction for different temperatures. 142
5.12 Principal scheme of an ultrafast time-resolved TA spectroscopy experiment. . . 144
5.13 Time evolution of theoretical DTSs emerging from our dynamics for different wave lengths of pump and probe pulses. 153

6.1 Schematic view of the multiband model of a D/A heterojunction. 166
6.2 Schematic view of the classification of exciton states in the model of a D/A heterojunction. 170
6.3 Exciton spectrum and ultrafast photophysical pathways in the multiband model of a D/A heterojunction. 173
6.4 Time evolution of populations of various groups of exciton states in the multiband and two-band model of a D/A heterojunction. 177
6.5 Time- and energy-resolved numbers of coherent excitons in various groups of exciton states in the multiband model of a D/A heterojunction. 179
6.6 Time- and energy-resolved numbers of excitons in various groups of exciton states in the multiband model of a D/A heterojunction. 181
6.7 Electron and hole distributions in representative exciton states participating in the ultrafast dynamics of the multiband model of a D/A heterojunction. 183
6.8 Ultrafast exciton dynamics in the multiband model of a D/A heterojunction for different central frequencies of the excitation. 185
6.9 Influence of small variations in the LUMO–LUMO offset on the ultrafast exciton dynamics in the multiband model of a D/A heterojunction. 187
6.10 Ultrafast exciton dynamics in the multiband model of a D/A heterojunction for different carrier–phonon interaction strengths. 188
6.11 Time- and energy-resolved numbers of excitons is various groups of exciton states for different strengths of the carrier–phonon interaction in the multiband model of a D/A heterojunction. 190

7.1 Electron energy levels relevant for the operation of an OSC under different working conditions. 196
7.2 Current-voltage characteristic of a solar cell in the dark and under illumination. 198
7.3 Schematic view of the model of a D/A bilayer. 211
7.4 Disorder-averaged densities of states for various groups of exciton states. 216
7.5 Field-dependent yield of charge separation from the strongly bound CT state. Relative position of the low-energy edges of the densities of CT and contact exciton states. 219
7.6 Distributions of the yield of charge separation from the strongly bound CT state for different strengths of the electric field. 220
7.7 Distribution of energies of the intermediate and initial CT state. 223
7.8 Yield of charge separation from the strongly bound CT state as a function of the disorder strength. Disorder-averaged energy barrier opposing the separation of the strongly bound CT state as a function of the disorder strength. 226
7.9 Field-dependent separation yield from the strongly bound CT state for different degrees of carrier delocalization and Coulomb interaction strengths. 228
7.10 Yield of charge separation from the strongly bound CT state as a function of the temperature and LUMO–LUMO offset. 229
7.11 Field-dependent yield of charge separation starting from donor exciton states of different energies. 232
7.12 Yield of the donor exciton separation as a function of the disorder strength. . . 234
7.13 Field-dependent separation yield from the closely separated donor state for different degrees of carrier delocalization and Coulomb interaction strengths. . . . 236
7.14 Yield of the separation from the closely separated donor state as a function of the temperature and LUMO–LUMO offset. 236

List of Tables

4.1 Values of model parameters used in computations on the model of a neat semiconductor. 98

4.2 Active density matrices, their total numbers in the most general case and the case specific to our model. 99

5.1 Values of model parameters used in computations on the two-band model of a D/A heterojunction. 128

6.1 Values of model parameters used in computations on the multiband model of a D/A heterojunction. 165

7.1 Values of model parameters used in computations on the model of a D/A bilayer. 213

List of Abbreviations

PCE	power conversion efficiency
IQE	internal quantum efficiency
OSC	organic solar cell
OPV	organic photovoltaic
LUMO	lowest unoccupied molecular orbital
HOMO	highest occupied molecular orbital
D/A	donor/acceptor
PCBM	[6,6]-phenyl-C_{61} butyric acid methyl ester
P3HT	poly(3-hexylthiophene)
PCPDTBT	poly[2,6-(4,4-bis-(2-ethylhexyl)-4H-cyclopenta [2,1-*b*;3,4-*b*'] dithiophene)--alt-4,7(2,1,3-benzothiadiazole)]
CT	charge transfer (state, exciton)
CS	charge separated (state, exciton)
DCT	dynamics controlled truncation (scheme)
TA	transient absorption (spectroscopy, experiment)
DTS	differential transmission signal
VB	valence band
CB	conduction band
SBE	semiconductor Bloch equation
TR-FU	time-resolved fluorescence up-conversion
NLO	nonlinear optical (crystal)
LAPACK	Linear Algebra Package
HPC	high performance computing

MPI	Message Passing Interface
(TR-)SHG	(time-resolved) second harmonic generation
XD	donor exciton (state)
XA	acceptor exciton (state)
GSB	ground state bleaching
SE	stimulated emission
PIA	photoinduced absorption
kMC	kinetic Monte Carlo

Physical Constants

Elementary Charge	$e = 1.602 \times 10^{-19}\,\mathrm{C}$
Vacuum Permittivity	$\varepsilon_0 = 8.854 \times 10^{-12}\,\mathrm{F\,m^{-1}}$
Electron Mass	$m_e = 9.109 \times 10^{-31}\,\mathrm{kg}$
Boltzmann Constant	$k_B = 1.380 \times 10^{-23}\,\mathrm{J\,K^{-1}}$
Vacuum Permeability	$\mu_0 = 4\pi \times 10^{-7}\,\mathrm{T\,m\,A^{-1}}$

List of Symbols

ε_r	relative dielectric permittivity
r_{CT}	electron–hole separation in the “cold” CT exciton
$\epsilon_{\mathrm{b}}^{\mathrm{CT}}$	binding energy of the “cold” CT exciton
$\Psi\left(\mathbf{r}\right)\ \left[\Psi^{\dagger}\left(\mathbf{r}\right)\right]$	Fermi field operators annihilating [creating] a particle in $\mathbf{r}$
$b_{\mu}\ \left[b_{\mu}^{\dagger}\right]$	Bose operators annihilating [creating] a phonon in mode μ
$\hbar\omega_{\mu}$	energy of phonon mode μ
$\mathbf{E}(t)$, $E(t)$, E	external electric field
$a_p\ \left[a_p^{\dagger}\right]$	Fermi operators annihilating [creating] a particle in single-particle state p
E_g	semiconductor single-particle gap
$c_p\ \left[c_p^{\dagger}\right]$	Fermi operators annihilating [creating] an electron in conduction-band state $p \in \mathrm{CB}$
$d_p\ \left[d_p^{\dagger}\right]$	Fermi operators annihilating [creating] a hole in valence-band state $p \in \mathrm{VB}$
$\epsilon_p^{\mathrm{c}}\ [\epsilon_p^{\mathrm{v}}]$	energy of conduction-band state $p \in \mathrm{CB}$ [valence-band state $p \in \mathrm{VB}$]
$V_{pqkl}^{\lambda_p\lambda_q\lambda_k\lambda_l}$	matrix element of the Coulomb interaction in the electron–hole picture
γ_{pq}^{μ}	matrix element of the carrier-phonon interaction in the electron–hole picture
$\mathbf{M}_{pq}^{\lambda_p\lambda_q}$	matrix element of the dipole-moment operator in the electron–hole picture
$\vert 0\rangle_e$	vacuum state in the particle picture
$\vert GS\rangle$	semiconductor ground state in the particle picture
$\vert 0\rangle$	semiconductor ground state in the electron–hole picture
$\vert x\rangle$	exciton state x (eigenstate x of an electron–hole pair)
$\hbar\omega_x$	energy of exciton state x
$X_x\ \left[X_x^{\dagger}\right]$	operators annihilating [creating] an exciton in state x
ψ_{ab}^{x}	exciton “wavefunction”, i.e., scalar product $\langle ab \vert x\rangle$ ($a \in \mathrm{VB}, b \in \mathrm{CB}$)
m_e^* (m_h^*)	electron (hole) effective mass

$\epsilon_{\mathrm{b}}^{X}$	binding energy of the Wannier exciton $(\mathbf{K}=0, n=1)$
$a_{0,X}$	electron–hole separation in the Wannier exciton $(\mathbf{K}=0, n=1)$
Y_{ab}	interband polarizations in the single-particle basis
C_{ab} (D_{ab})	electron (hole) populations and intraband polarizations in the single-particle basis
$\hat{N}_e$	electron number operator
N_e	electron number
$\hat{N}_h$	hole number operator
N_h	hole number
N_{tot}	total exciton number
N_{abcd}	exciton populations and exciton–exciton coherences in the single-particle basis
y_x	interband polarizations in the exciton basis
$y_{x\mu^\pm}$	single-phonon-assisted interband polarizations in the exciton basis
$n_{\bar{x}x}$	exciton populations and exciton–exciton coherences in the exciton basis
$n_{\bar{x}x\mu^+}$	single-phonon-assisted exciton populations and exciton–exciton coherences in the exciton basis
$\bar{n}_{\bar{x}x}$	incoherent part of exciton populations and exciton–exciton coherences in the exciton basis
$\mathbf{M}_x$, M_x	matrix elements of the dipole-moment operator in the exciton basis
$\Gamma^{\mu}_{\bar{x}x}$, $\Gamma^{i\lambda_i}_{\bar{x}x}$	matrix elements of the carrier–phonon interaction in the exciton basis
n^{ph}_{μ} $\left[n^{\mathrm{ph}}(E)\right]$	equilibrium number of phonons in phonon mode μ [of energy E]
T	temperature
U	on-site Coulomb interaction
$\epsilon_{\mathrm{b}}^{\mathrm{pol}}$	polaron binding energy
ω_c	central frequency of the excitation
$\mathbf{F}$	vector of the internal electric field in the cell

To my childhood and my youth
To the only one that has never abandoned me

Chapter 1

Introduction

1.1 Global Energy Issue

Finding economically viable and efficient ways of utilizing renewable resources of energy to satisfy an ever-increasing global energy demand is one of the major challenges of the 21st century. According to the definition provided by the International Energy Agency [1],

"Renewable energy is derived from natural processes that are replenished constantly. In its various forms, it derives directly from the Sun, or from heat generated deep within the Earth. Included in the definition is electricity and heat generated from solar, wind, ocean, hydropower, biomass, geothermal resources, and biofuels and hydrogen derived from renewable resources."

The amount of energy produced during one year on the global level, as measured by the world total primary energy supply, has more than doubled in the last forty years, rising from ca. 70,000 TWh in 1973 to ca. 160,000 TWh in 2015 [2]. The largest part of the energy is generated by using fossil fuels, such as oil, coal, and natural gas, see the fuel shares of the total primary energy supply in Fig. 1.1. These resources of energy are limited, unevenly distributed, and cause excessive emissions of CO_2 in the Earth's atmosphere, thus promoting the global warming. The participation of the energy generated from fossil fuels in the total produced energy has somewhat decreased (from 86.7% in 1973 to 81.4% in 2015, see Fig. 1.1), mainly due to an increase in the contribution of the nuclear energy. At the same time, the share of the energy from all renewable resources has risen from 0.1% in 1973 to 1.5% in 2015. The nuclear energy, however, cannot be

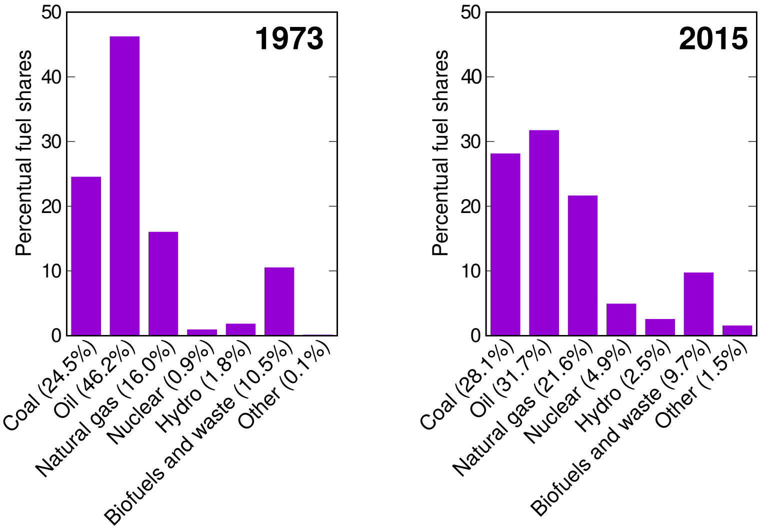

FIGURE 1.1: Fuel shares of the total primary energy supply in 1973 and 2015. The resources denoted by “Other” include geothermal, solar, wind, ocean, and other resources. The data are extracted from Ref. [2].

regarded as a sustainable solution to the global energy problem because of the risks related to the operation of nuclear power plants, the issue of the nuclear waste, and the latent threat of its military use. Having in mind the predicted growth of both the global population and the average income in the near future, as well as the fact that the fossil fuels are slowly but surely running out, a sustainable and long-term solution to the global energy problem has to be formulated. To this end, governments and companies throughout the world are providing more and more funding for fundamental and applied research that would lead to a large-scale and cost-effective exploitation of the energy from renewable resources.

Among all of the renewable energy resources, the energy of the Sun, together with the wind energy, has the greatest theoretical potential to resolve the global energy issue. To understand this, it is enough to remember that the intensity of the orthogonally incident solar radiation just outside the Earth atmosphere is approximately 1.36 kW/m^2 (the so-called solar constant). Remembering that the solar power reaching the Earth is distributed over the illuminated Earth hemisphere, and that every point on the surface of the Earth is, on average, illuminated for 12 hours every day, one can calculate that, on average and disregarding the influence of the Earth atmosphere, each square meter of the Earth receives the solar power of 340 W [3]. The total energy that we receive from the Sun during one year is approximately 1.5×10^9 TWh, which is around 10,000 times larger than the global annual energy consumption in 2015 [2].

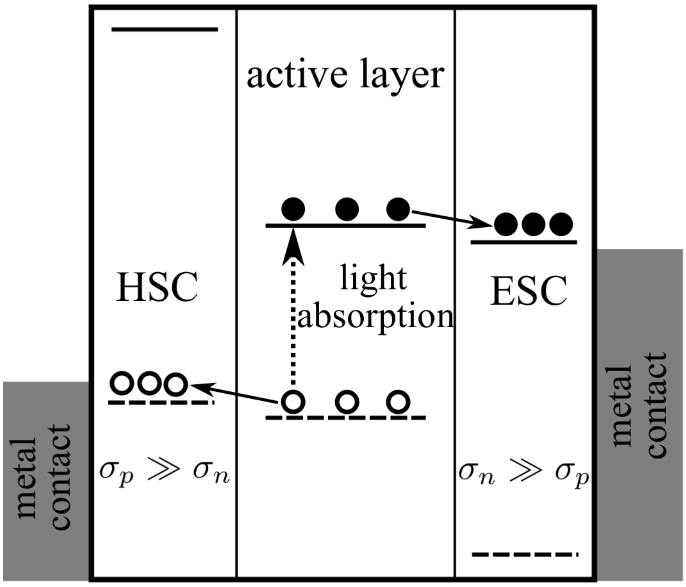

FIGURE 1.2: General scheme of a solar cell. HSC stands for the hole-selective contact, in which the hole conductivity σ_p is much larger than the electron conductivity σ_n. ESC stands for the electron-selective contact, in which the inequality $\sigma_n \gg \sigma_p$ holds. The solid (dashed) horizontal lines in the HSC, active layer, and ESC, are meant to represent the edges of the conduction (valence) band. The dashed vertical arrow in the active layer represents the light absorption generating electrons (full circles) in the conduction band and holes (empty circles) in the valence band.

1.2 Photovoltaic Effect and Solar Cell

The conversion of solar energy to electricity is based on the photovoltaic effect whose discovery in 1839 is commonly attributed to Alexandre-Edmond Becquerel [4]. In essence, the photovoltaic effect is a physical and chemical phenomenon consisting of the creation of voltage and electric current in a material upon its irradiation by light. Solar cells (or photovoltaic cells) are electric devices that convert sunlight into electricity by means of the photovoltaic effect. A solar cell typically consists of the active layer (usually made of a semiconductor material) that is sandwiched between two carrier-selective contacts. The material constituting the active layer can absorb light and convert the energy of the photons absorbed into excess carriers, whose number is determined by the competition between the rates of their generation and recombination. A very general scheme of a solar cell is presented in Fig. 1.2. The basic features of the solar cell operation mechanism are:

(a) the absorption of light of sufficient energy by a semiconductor material promotes an electron from the valence band to the conduction band, leaves a hole in the valence band, and generates an electron–hole pair (exciton);

(b) the oppositely charged electron and hole thus generated are separated, either spontaneously or by some other means;

(c) the separated charge carriers should be separately extracted at the carrier-selective contacts and can then be used to generate photocurrent in the external circuit.

The aforementioned carrier-selectivity of the contacts is crucial to the production of the photocurrent [5]. An electron-selective contact is permeable for electrons and blocks the holes, i.e., it is a good conductor of electrons and a poor conductor of holes. On the other hand, a hole-selective contact is impermeable for electrons, i.e., it has a large conductivity for holes and a small conductivity for electrons. Typical electron-selective contact is made of an n-type semiconductor, whereas p-type semiconductors are used as hole-selective contacts. In order to prevent hole (electron) injection from the absorber into the electron-selective (hole-selective) contact, the energy band gaps of the contacts are generally larger than the energy band gap of the active layer. The contacts, therefore, transmit almost all of the incident photons, which are then absorbed in the active layer. Metal contacts, by means of which the carriers are finally extracted to the external circuit, are in contact with carrier-selective layers.

There are numerous ways to quantify the performance of a solar cell (see, e.g., Ch. 4 of Ref. [6]). The solar cell efficiency may be assessed by computing the so-called power conversion efficiency (PCE), which is given by the ratio of the maximum electrical power delivered by the solar cell per unit device area and the intensity of the incident light (i.e., the light power incident onto the unit device area)

$$\mathrm{PCE} = \frac{\text{electrical power delivered}}{\text{incident light power}}. \tag{1.1}$$

The PCE of a solar cell is directly relevant for applications, in which the solar cell delivers power to the external load by maintaining its ends at different electric potentials and forcing the electric current through it. For scientific analyses, other figures of merit may be more useful. Let us here introduce the so-called internal quantum efficiency (IQE) of the solar cell, which quantifies the efficiency with which the photons absorbed by the active layer are converted into free charges capable of producing photocurrent. Differently from the PCE, the IQE is measured under the so-called short-circuit conditions, when the voltage (and consequently the power) delivered by the solar cell is equal to zero. Formally, the IQE is the ratio of the electron flux in the circuit (the number of electrons obtained per unit device area and per unit time) and the flux of absorbed photons (the number of photons absorbed per unit device area and per unit time)

$$\mathrm{IQE} = \frac{\text{electron flux in the circuit}}{\text{absorbed photon flux}}. \tag{1.2}$$

In the most efficient solar cells, the IQE can reach unity [7], meaning that essentially every absorbed photon is converted to free charges.

The world solar photovoltaic electricity production has substantially risen in the last decade, from 4 TWh in 2005 to 247 TWh in 2015 [2]. The largest part of this electricity is generated by silicon solar cells. The silicon, either in the form of single crystals or a polycrystalline material, has been the preferred material used in photovoltaics ever since the first inorganic solar cell based on it was constructed at Bell Laboratories in 1954 [8]. A common inorganic solar cell is configured as a large-area *p*–*n* junction and its basic working principles are very well known (see, e.g., Ch. 29 of Ref. [9] or Ch. 6 of Ref. [5]). In this sense, silicon is unarguably the most mature photovoltaic material, and the silicon technology features globally spread infrastructures in both the photovoltaic and integrated circuit industries. However, the production of inorganic solar cells typically requires a multitude of expensive and energy-consuming processing steps, making their efficiency-to-price ratio not good enough to promote them to a globally dominant source of energy. Therefore, in search for alternative materials that could compose the active region of a solar cell, the focus of the scientific and engineering communities has been placed on organic semiconductor materials.

1.3 Organic Semiconductors

The aforementioned interest in solar cells based on organic semiconductors (organic solar cells, OSCs) is driven by the unique features of this class of materials, which offer the prospect of mechanically flexible, light-weight, and low-cost solar cells [10]. The basic building blocks of organic semiconductors are carbon and hydrogen atoms along with a few other atoms (the so-called heteroatoms) such as oxygen, nitrogen, phosphorous, or sulfur. These compounds combine favorable electronic properties of inorganic semiconductor materials with mechanical (flexibility) and chemical (non-toxicity) advantages of organic materials. Organic semiconductors can absorb and emit light in the visible range of the electromagnetic spectrum, and are sufficiently good at conducting electricity, so that they can be used as the active material in devices such as solar cells, light-emitting diodes, and field-effect transistors. Another positive feature of organic semiconductors is the possibility of a relatively easy manipulation of their electronic (e.g., tuning the position of the maximum of the emission or absorption spectrum), chemical (e.g., making the material soluble), and mechanical properties by chemical synthesis. Having all these facts considered, vigorous and interdisciplinary research activities undertaken in the last thirty years in the field of organic photovoltaics (OPVs) are not surprising. The field has experienced a rapid progress and PCEs of OSCs have risen from less than 1% in the 1980s [11, 12] to somewhat above 13% nowadays [13] (for comparison, the current record efficiencies of silicon solar cells are above 25%). This progress can be attributed to a fortuitous synergy between rational design and trial and error. As stated by Bässler and Köhler [14], “it is indeed fortunate that OSCs are so efficient but it is unfortunate that the reason is unclear.” The fundamental physical processes underlying the operation of OSCs are heavily debated and poorly understood, which prevents us from rationally designing more efficient OSCs. Any conclusive description of basic physical processes at play in OSCs should take into account the above-mentioned unique features of organic semiconductors, which is by no means an easy task. Even though the fundamental physical laws that govern the behavior of both inorganic and organic semiconductors under a photoexcitation are the same, they may seem quite different, just because key material parameters that govern the relevant processes assume very different values. The apparent difference in the physical pictures used to describe organic and inorganic semiconductors is essentially related to the relative importance of the electron–hole interaction with respect to the bandwidth and the carrier–phonon interaction. Let us now briefly review the origin of the semiconducting properties of organic semiconductors, outline their basic classification , and summarize the main differences between inorganic and organic semiconductors. The discussion to be presented is based on Refs. [6, 15, 16].

1.3.1 Electronic Configuration of Carbon in Organic Semiconductors

The origin of the semiconducting properties of organic semiconductors can be traced back to the electronic configuration of their main ingredient, the carbon atom. It possesses six electrons in total, four of which are valence electrons that actually participate in the formation of chemical bonds with other atoms. According to the Hund's rule, the ground-state electronic configuration of the carbon atom reads as $(1s)^2\ (2s)^2\ (2p_x)^1\ (2p_y)^1\ (2p_z)^0$. In organic semiconductors, it is common that the $2s$ orbital and the two partially filled $2p$ orbitals $2p_x$ and $2p_y$ exhibit the so-called sp^2 hybridization and form three sp^2 orbitals, each of which is occupied by a single electron. The three sp^2 orbitals are located within one plane, accommodate one electron each, and participate in the so-called σ bonds, which are arranged so that the angle between neighboring bonds is $2\pi/3$. At the same time, the third $2p$ orbital, i.e., the $2p_z$ orbital, remains unchanged. It is perpendicular to the plane hosting the three sp^2 orbitals and accommodates one electron. The $2p_z$ orbitals of the two C atoms laterally overlap in the region out of the plane and form the so-called π bond, which is much weaker than the in-plane σ bond. Nevertheless, this overlap between p orbitals makes the electrons occupying them (the so-called π electrons) delocalized, which is the crux of the conductivity of organic semiconductors. The lateral overlap of p orbitals of two adjacent carbon atoms that are also bonded by a σ bond is known as the π conjugation. A π-conjugated system possesses a region in which the π conjugation is at play. The hallmarks of the π conjugation are, therefore, the alternation of single and double bonds between neighboring C atoms and the delocalization of π electrons.

The simplest example of the π conjugation is encountered in the simplest aromatic molecule, benzene. It consists of six carbon atoms arranged in a ring, each C atom featuring one single (σ) bond with one H atom, as well as one single (π bond) and one double (σ and π) bond with the two neighboring C atoms, see Fig. 1.3(a). There are two possible structures meeting the above-introduced requirements, the so-called resonance structures, but the symmetry considerations do not prefer any of them. The six π electrons are shared among all six C atoms and, in this sense, they are delocalized over the perimeter of the molecule. In the picture of molecular orbitals, the overlap between six atomic p_z orbitals results in six molecular π orbitals whose energies are different and dependent on the phase overlap between different atomic orbitals, i.e., on the number of nodal planes in molecular orbitals, see Fig. 1.3(b). In the ground state of the benzene molecule, the three lower-energy bonding π orbitals are completely filled with six electrons, whereas the three higher-energy antibonding π^* orbitals are empty. The energy difference between the lowest unoccupied molecular orbital (LUMO) and the highest occupied molecular orbital (HOMO) is commonly referred to as the HOMO–LUMO gap, and its value for the benzene molecule is around 6 eV.

The HOMO–LUMO gap of aromatic molecules can be tuned by extending (in electron number and space) the system of π electrons, which can be accomplished by adding more benzene rings. We thus obtain the series of the so-called oligoacenes, which starts with naphthalene (2 rings), anthracene (3 rings), tetracene (4 rings), and pentacene (5 rings). Their chemical structures are depicted in Fig. 1.3(c). The HOMO–LUMO gap decreases with increasing the number of benzene rings forming the molecule, and this trend can be reproduced by treating the π electrons as noninteracting particles in a one-dimensional infinitely deep potential well whose linear size is determined by the perimeter of the molecule [6]. This feature supports the notion of well-delocalized π electrons. Aromatic molecules can form regular crystal structures, the so-called molecular crystals, which will be introduced in the following section.

The alternation of single and double bonds between C atoms is not specific to aromatic systems. The C atoms may be arranged in a conjugated chain $= \mathrm{C} - \mathrm{C} = \mathrm{C} - \mathrm{C} = \mathrm{C} - \leftrightarrow - \mathrm{C} = \mathrm{C} - \mathrm{C} = \mathrm{C} - \mathrm{C} =$ in which each C atom contributes one π electron that is delocalized throughout the chain. Such a situation is typical of the so-called conjugated polymers.

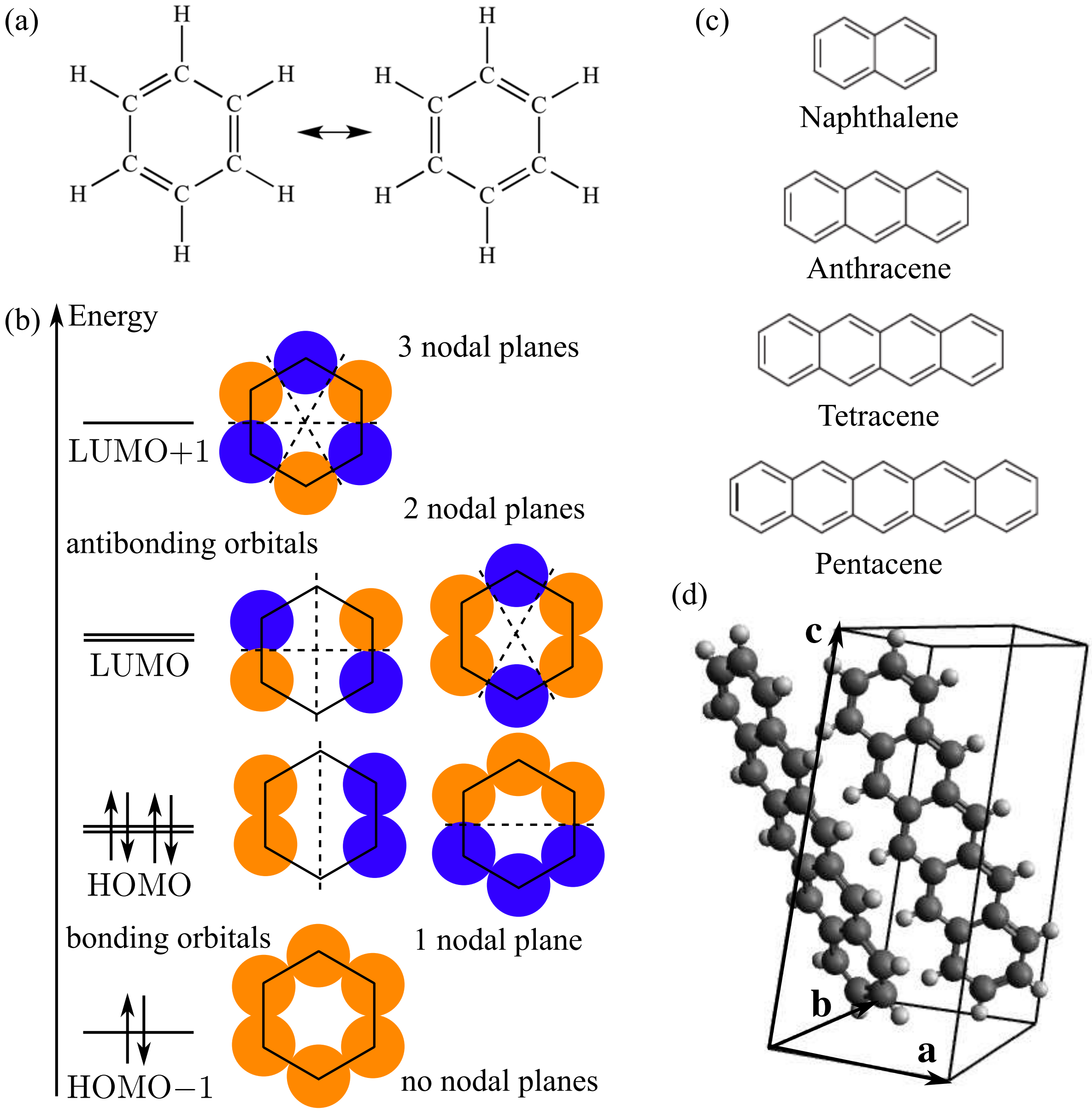
(a)
H
C
(b)
Energy
3 nodal planes
LUMO+1
2 nodal planes
antibonding orbitals
LUMO
HOMO
bonding orbitals
1 nodal plane
HOMO−1
no nodal planes
(c)
Naphthalene
Anthracene
Tetracene
Pentacene
(d)
c
b
a

FIGURE 1.3: (a) Resonance structures of benzene molecule. (b) Energy and occupation diagram of the π-electron molecular orbitals of benzene molecule. A schematic above-view of each molecular orbital is provided on the right. Different colors (yellow and blue) correspond to different phases (positive and negative) of the electronic wave function. The three lower-energy orbitals are bonding, while the three higher-energy orbitals are antibonding orbitals. As the number of nodal planes (planes on which the phase of the electronic wave function exhibits a change in sign) of the orbital increases, its energy also increases. (c) Chemical structures of oligoacenes, from naphthalene to pentacene. H atoms are customarily omitted. (d) Unit cell of pentacene molecular crystal comprises two pentacene molecules. The crystal possesses triclinic symmetry, while the unit cell parameters are $|\mathbf{a}| = 6.28$ Å, $|\mathbf{b}| = 7.71$ Å, $|\mathbf{c}| = 14.44$ Å, $\alpha = 76.75°$, $\beta = 88.01°$, and $\gamma = 84.52°$.

1.3.2 Different Types of Organic Semiconductors

The preceding discussion on the origin of the semiconducting properties of certain organic materials suggests that organic semiconductors may be divided into two broad categories:

(a) small molecule-based organic semiconductors, and

(b) conjugated polymers.

Particularly important class of organic semiconductors based on small molecules are molecular crystals. They feature a perfectly ordered lattice at whose sites the basis, consisting of one or more molecules, is placed. The molecules forming molecular crystals are in general planar, aromatic molecules, such as the above-introduced oligoacenes, see the crystal structure of the pentacene molecular crystal in Fig. 1.3(d). These molecules are electrically neutral and their HOMO orbitals are delocalized, meaning that the electrons occupying them are quite free to move throughout the molecule. The neutral and nonpolar molecules are kept together in the crystal by weak van-der-Waals forces. Although a single molecule possesses no permanent dipole moment, its charge distribution exhibits temporal fluctuations and produces a time-fluctuating dipole moment. The fluctuating dipole moment of one molecule causes the appearance of fluctuating dipoles on its neighbors. The attractive van-der-Waals interaction between the two molecules originates from the electrostatic interaction between the corresponding correlated fluctuating dipoles. The associated potential energy is proportional to r^{-6}, where r is the distance between the molecules, and the force is then proportional to r^{-7}. Since molecular crystals are highly ordered materials, they boast quite high charge mobilities (ranging from 1 to 50 $\mathrm{cm}^2/(\mathrm{Vs})$, see Ref. [15] and references therein), rendering them interesting for applications in organic field-effect transistors. However, due to their brittleness (that is ultimately induced by the weak intermolecular bonds), they are not suitable for applications in organic light-emitting diodes and organic solar cells, which require quite thin semiconductor layers.

The main spectroscopic properties of a molecular crystal can be directly traced back to the properties of the underlying individual molecules [17]. The intermolecular interactions cause

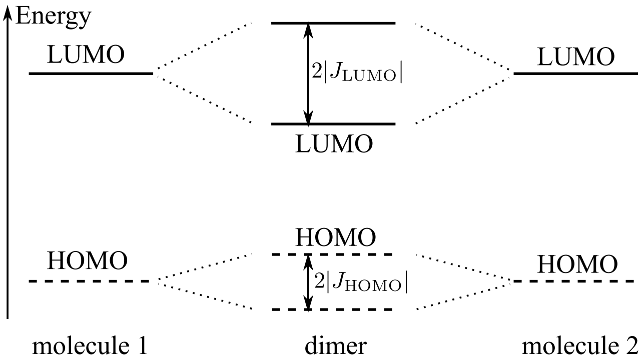

FIGURE 1.4: Molecular orbitals of two isolated molecules (on the left- and right-hand side) and molecular orbitals of the dimer formed by two interacting molecules (central part). The splitting between the molecular orbitals of the dimer that stem from the HOMO (LUMO) of individual isolated molecules is twice the magnitude of the electronic coupling J_{HOMO} (J_{LUMO}) between the respective orbitals. HOMO and LUMO of the dimer are indicated. The electronic coupling reduces the HOMO–LUMO gap of the dimer with respect to the HOMO–LUMO gap of the single molecule.

the broadening of the molecular energy levels into electronic bands. The bandwidths are then determined by the strengths of these interactions, i.e., by the electronic couplings between (neighboring) molecules. This effect is clearly noticed already at the level of two interacting molecules. The left- and right-hand sides of Fig. 1.4 present the energies of the HOMO and LUMO of individual isolated molecules, while the central part shows molecular orbitals of the dimer, in which the intermolecular interactions are considered. The splitting between molecular orbitals of the dimer is directly proportional to the electronic coupling between the molecules. The electronic coupling may be formally defined as the matrix element of the electronic Hamiltonian between the molecular orbitals of the two isolated molecules [18]. The electronic band stemming from the HOMO level is the highest occupied band of the crystal and is commonly denoted as the valence band, while the LUMO level of single molecules gives rise to the lowest unoccupied band of the crystal or the conduction band. The bandwidths of the conduction and valence bands in oligoacene molecular crystals are of the order of 500 meV [19]. The (single-particle) band gap of the solid is defined as the energy difference between the lowest-energy state (the bottom) of the conduction band and the highest-energy state (the top) of the valence band. The band gap of the solid is generally reduced in comparison with the HOMO–LUMO band gap of the molecule. This feature can be understood already on the level of a dimer, where the electronic coupling

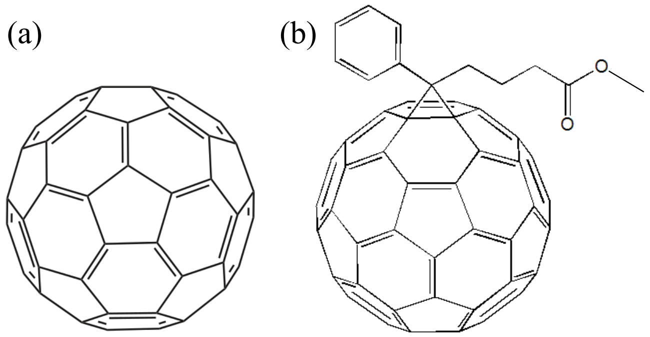

FIGURE 1.5: Chemical formula of (a) fullerene (C_{60}) molecule, and (b) [6,6]-phenyl-C_{61} butyric acid methyl ester (PCBM) molecule.

makes the HOMO–LUMO gap of the dimer smaller than the HOMO–LUMO gap of the single molecule, see Fig. 1.4.

The films of small molecule-based materials that are widely used is OSCs are not in the form of a molecular crystal, but are rather partially disordered. These films do not exhibit long-range order, and their electronic properties cannot be described in terms of energy bands and wave-like carriers that are delocalized throughout the system. The disorder present in these materials tends to localize carrier wave functions over a number of neighboring molecules, which are then said to form a molecular aggregate, or even on one molecule. The degree of carrier (de)localization is then determined by the competition between the strength and spatial extent of the disorder, which promotes carrier localization, and the magnitude of the intermolecular electronic coupling, which is responsible for carrier delocalization. Therefore, small molecule-based films usually contain both disordered and ordered regions. Let us mention here that molecules of fullerene [C_{60}, see Fig. 1.5(a)] and its functionalized derivatives [e.g., [6,6]-phenyl-C_{61} butyric acid methyl ester, widely known as PCBM, see Fig. 1.5(b)] form partially disordered films that are used as electron-accepting materials in the most efficient donor/acceptor (D/A) OSCs. A comprehensive account of morphology, electronic structure, and charge localization properties of partially disordered PCBM can be found in Ref. [20].

A polymer is an organic macromolecule characterized by the existence of the basic building block, commonly denoted as a monomer, which is periodically repeated. Conjugated polymers are organic macromolecules comprising a backbone chain of carbon atoms that exhibits the π conjugation. The symmetry of the chain determines the electronic structure of the polymer,

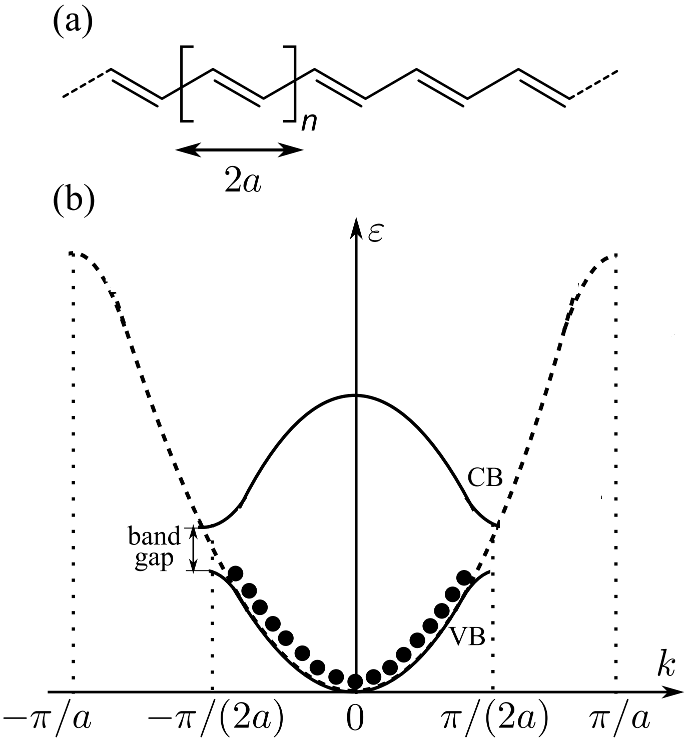

FIGURE 1.6: (a) Structure of trans-polyacetylene $(C_2H_2)_n$. (b) Peierls instability opens up the band gap between the fully occupied valence band (VB) and the completely empty conduction band (CB).

which is commonly similar to the electronic structure of semiconductors. Here, the band gap stems from the alternation of bond lengths along the polymer chain. To understand this, let us concentrate on a particularly important example of the simplest conjugated polymer, polyacetylene $(C_2H_2)_n$, whose monomers are C_2H_2 units that are arranged in a quasi-one-dimensional lattice, see Fig. 1.6(a). Due to the sp^2 hybridization of C atoms, the three valence electrons form σ bonds with the two neighboring carbon atoms and the hydrogen atom. The remaining fourth electron is formally unpaired. If the distances between any two adjacent carbon atoms were equal to a, the π electrons would be completely delocalized along the chain, making the polymer metal-like, see the dashed $\varepsilon(k)$ curve in Fig. 1.6(b). However, due to the Peierls instability [21], an equidistantly spaced chain of ions with one unpaired electron per ion tends to distort spontaneously in such a way that the distances between successive ions along the chain alternate, i.e., the chain is dimerized. Because of the alternating distances in the chain, the lattice period of the dimerized chain is two times larger than the lattice period of the undimerized chain. The change in the chain periodicity opens the band gap at $\pi/(2a)$, meaning that the electronic band is now fully occupied, analogously to the fully occupied valence band in a semiconductor, see Fig. 1.6(b). This indicates that the chain with alternating bond lengths shows semiconducting properties. Theoretically, single-particle excitations of such a chain are described within the framework of the famous Su-Schrieffer-Heeger model [22], which regards them as delocalized wave-like entities, just as in the standard Bloch theory of solids.

Films made of a conjugated polymer comprise both crystalline and amorphous regions, so that there is a strong dependence of their electronic properties on the morphology. One of the most widely used polymers in OSCs is poly(3-hexylthiophene) (P3HT), since it can be easily fabricated in form of a film that features ordered regions in which the charge transport properties are much better than in amorphous regions. The backbone of P3HT consists of thiophene rings, to each of which a hexyl side chain is attached, see the chemical formula in Fig. 1.7(a). Polymer chains in ordered regions are arranged in two-dimensional planes of parallel aligned chains [24], see the unit cell of the ordered P3HT polymer in Fig. 1.7(c). In the main-chain direction, whose unit vector is vector $\mathbf{c}$ in Fig. 1.7(c), the bond between monomers is covalent, which leads to strong electronic coupling in the so-called intrachain direction. The direction in the planes that is perpendicular to the chain direction [the so-called interchain direction or the $\pi - \pi$ stacking direction, whose unit vector is vector $\mathbf{b}$ in Fig. 1.7(c)] sees weak van-der-Waals interchain bonds and weak electronic couplings between chains. Nevertheless, the interchain coupling is still sufficient to cause delocalization of carrier wave function among different chains in one plane [the plane is determined by vectors $\mathbf{b}$ and $\mathbf{c}$ in Fig. 1.7(c)]. The planes are separated by insulating alkyl side chains, meaning that the electronic coupling, as well as the conduction, between different planes [in the direction determined by vector $\mathbf{a}$ in Fig. 1.7(c)] is entirely negligible. In first approximation, the ordered polymer region can be conceived as an array of identical, mutually parallel, polymer chains, with the electronic couplings inside a chain being much larger than the electronic couplings among different chains. The value of the intrachain transfer integral may be estimated as a quarter of the bandwidth of HOMO (or LUMO) band of a straight polymer chain. Typically, these bandwidths assume values of the order of 2 eV [24, 25], so that the intrachain transfer integral is of the order of 0.5 eV. As an estimate of the value of the interchain transfer integral, we may use a quarter of the bandwidth in the $\pi - \pi$ stacking direction, which is of

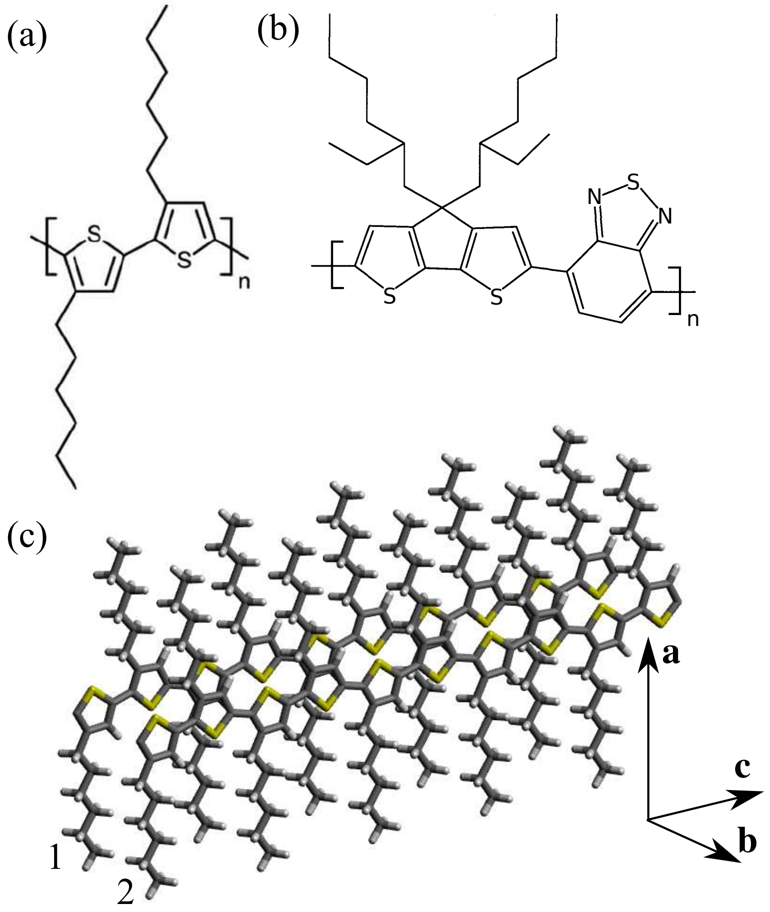

FIGURE 1.7: (a) Chemical formula of the monomer unit of the P3HT polymer. (b) Chemical formula of the monomer unit of the low-band-gap polymer PCPDTBT, which consists of the electron-rich 4,4'-bis-(2-ethylhexyl)-4H-cyclopenta[2,1-*b*;3,4-*b*']-dithiophene (CPDT) unit and the electron-deficient 2,1,3-benzothiadiazole (BT) unit. (c) Unit cell of the ordered P3HT polymer. The interchain (main-chain) direction is the direction of vector $\mathbf{c}$, the intrachain ($\pi - \pi$ stacking) direction is the direction of vector $\mathbf{b}$, whereas the side-chain direction is the direction of vector $\mathbf{a}$. The parameters of the unit cell determined in Ref. [23] are $|\mathbf{a}|/2 = 15.7$ Å, $|\mathbf{b}| = 8.2$ Å, and $|\mathbf{c}| = 7.77$ Å, $\alpha = \beta = \gamma = 90°$.

the order of 0.2 eV [24, 25], so that the interchain transfer integral is of the order of 0.05 eV. Amorphous polymer regions generally appear as fully disordered spaghetti-like regions formed by intertwined polymer chains. Such an irregular structure appears due to the irregular shape of polymer chains, which is caused by the monomers' rotational freedom around the bond that connects them. The disorder originating from the irregular shape of the chains is referred to as the static disorder. The term "static" is due to the fact that the chains retain their shape on at least nanosecond time scales, which is much longer than time scales relevant for charge transport processes. The presence of the static disorder generally influences both on-site energies (diagonal static disorder) and electronic couplings (off-diagonal static disorder).

For applications in OSCs, it is important that the absorption spectrum of a conjugated polymer overlap well with the solar radiation spectrum. The absorption onset of P3HT is at around 2 eV [26], which means that the absorption spectrum of P3HT does not overlap with the infrared region of the solar spectrum. In order to harvest the solar energy more efficiently, recently, a number of the so-called low-band-gap polymers, whose absorption edge is shifted towards the infrared, have been synthesized. In Fig. 1.7(b), the chemical formula of the monomer unit of the low-band-gap polymer PCPDTBT [27], which consists of the electron-donating (electron-rich) CPDT unit and the electron-accepting (electron-deficient) BT unit, is depicted.

1.3.3 Comparison between Inorganic and Organic Semiconductors

Typical inorganic semiconductors, such as silicon, germanium, or gallium-arsenide, are crystalline, and their constitutive elements are held together by covalent or ionic chemical bonds. In other words, the electronic coupling between them is quite strong. Consequently, the highest occupied and lowest unoccupied atomic orbitals of the individual constituents are broadened into wide valence and conduction bands in which electrons move coherently, as Bloch waves. The bandwidths in inorganic semiconductors are typically of the order of several electronvolts. The coupling of the electronic excitations of inorganic semiconductors to lattice vibrations (the carrier–phonon coupling) is not particularly strong and does not destroy the above-mentioned band picture, i.e., it can be reasonably treated perturbatively. The dielectric screening in a typical inorganic semiconductor is very good, which is best seen in the high value of the relative dielectric constant ε_r, which is of the order of 10 (in silicon, $\varepsilon_r = 11$). Such a high value of ε_r has far-reaching consequences for the function of inorganic solar cells. As already mentioned in Sec. 1.2, the absorption of a photon of sufficient energy generates a pair of oppositely charged carriers, an electron in the conduction band and a hole in the valence band. The very good dielectric screening reduces the range of the electron–hole interaction by an order of magnitude compared to its range in the vacuum. The thermal fluctuations alone are very likely to split the pair into free electron and hole. To understand this, it is sufficient to compare the Coulomb binding energy that keeps together an electron and a hole (the so-called exciton binding energy) to the thermal energy k_BT at room temperature. The exciton model appropriate for inorganic semiconductors is the Wannier exciton model, which is presented in greater detail in Sec. 2.3.1. It is suitable to describe weakly bound, large-radius excitons, for the description of which it is equally important to consider both good carrier delocalization (described in terms of rather small effective masses for electrons and holes) and rather weak Coulomb interaction between them (due to large ε_r). The binding energy of the large-radius exciton, as given in Eq. (2.77), is typically of the order of 10 meV (in silicon, it is approximately 15 meV), which is smaller than the thermal energy at room temperature [$(k_BT)_{T=300\text{ K}} \approx 25$ meV]. Therefore, an optical excitation across the band gap of a typical inorganic semiconductor generates essentially free charge carriers. In other words, the electronic processes triggered by an optical excitation across the band gap of an inorganic semiconductor can be reasonably described starting from the usual energy-band picture.

The situation is dramatically different in organic semiconductors, whose constitutive units exhibit much weaker mutual binding. Due to weak electronic couplings between the constitutive units, the electronic bands in organic semiconductors are typically much narrower than in inorganic semiconductors, the bandwidths being of the order of a couple of tenths of an electronvolt. The dielectric screening is much weaker compared to the case of inorganic semiconductors. Generally speaking, the relative dielectric constant ε_r in a typical organic semiconductor ranges between 2 and 4. The carrier–phonon coupling is typically stronger in organic than in inorganic semiconductors. Contrarily to the case of inorganic semiconductors, in which the carriers are well delocalized and the Coulomb interaction between them is weak, carriers in organic semiconductors are poorly delocalized, while the Coulomb interaction between them is strong. These features of organic semiconductors suggest that an optical excitation across the band gap creates strongly bound excitons. Excitons in organic semiconductors are typically described using the Frenkel exciton model, which is introduced in Sec. 2.3.2. In brief, the Frenkel exciton model assumes that electron–hole pairs are tightly bound and localized around single lattice sites (the translational symmetry of the lattice requires that true stationary states of an electron–hole pair be linear combinations of these localized pair states). The exciton binding energy is then primarily determined by the magnitude of the on-site direct Coulomb interaction. The exciton binding energy in organic semiconductors typically ranges between 0.5 and 1 eV [6, 28], which is much larger than the thermal energy at room temperature. The thermal excitations alone are not sufficient to split the photogenerated electron–hole pair into free electrons and holes. As discussed in the following, the last conclusion has an enormous impact on the design and geometry of OSCs.

1.4 Organic Solar Cells

The active layer of the simplest possible OSC would consist of only a single organic semiconductor, see Fig. 1.8(a). Since the exciton binding energy in organic semiconductors is much larger than the thermal energy at room temperature, the overwhelming part of the excitons photogenerated in the bulk do not separate into free carriers, but recombine. The PCEs of these so-called single-layer OSCs, which were first tested in the 1970s, were significantly below 1% [11].

The improvement in the PCE was made by introducing another organic semiconductor in the active layer and constructing the so-called D/A OSCs. The presence of the D/A interface, at which the electronic properties of the active layer exhibit a discontinuous change, is the crucial ingredient in the working mechanism of D/A OSCs. The other semiconductor was first added as a layer in the planar geometry [12], so that the D/A interface was planar and localized in the central part of the active layer, see Fig. 1.8(b). The PCEs of these bilayer D/A OSCs were around 1%. Further increase in the PCE required that the interface between the two semiconductors be

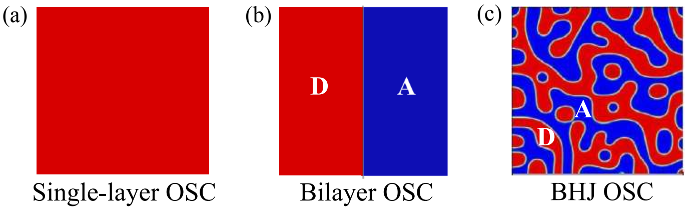

FIGURE 1.8: Schematic view of the active layer of (a) a single-layer OSC, (b) a bilayer OSC, (c) an OSC based on the BHJ morphology. In panels (b) and (c), the donor material is depicted in red, while the acceptor material is depicted in blue.

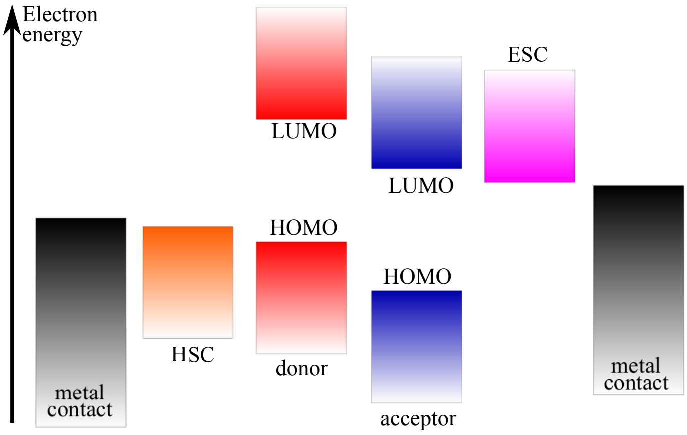

FIGURE 1.9: Scheme of the band alignment in a D/A OSC. Apart from the levels of the active layer, the levels of the ESC and HSC relevant for the operation of the solar cell, as well as the Fermi levels of metal contacts, are shown, see also Fig. 1.2.

developed and evenly distributed throughout the volume of the active layer of the solar cell. The so-called bulk heterojunction (BHJ) D/A OSC was first realized in 1995 [29], and the BHJ morphology, see Fig. 1.8(c), has remained the preferred morphology for D/A OSCs up to now.

The two organic semiconductors composing D/A OSCs differ in their electron affinities and ionization potentials, i.e., there is an energy offset between the two bottoms of the conduction bands and the two tops of the valence bands. The light is primarily absorbed in the semiconductor of lower electron affinity. This semiconductor acts as electron donor (in further text, donor), with holes as its majority carriers. The other semiconductor acts as electron acceptor (in further text, acceptor), its majority carriers being electrons. Heterojunctions of two organic semiconductors are most often the so-called type II heterojunctions [6], in which both the energy offset between the bottoms of the conduction bands and the energy offset between the tops of the valence bands are of the same sign (generally, they are not equal), see Fig. 1.9. The offset between the two bottoms of the conduction bands is commonly referred to as the LUMO–LUMO offset, whereas the offset between the two tops of the valence bands is widely known as the HOMO–HOMO offset. A suitable LUMO–LUMO offset between the donor and acceptor material makes the dissociation of the exciton photogenerated in the donor material (in further text, the donor exciton) by the electron transfer to the acceptor material energetically favorable (energetically downhill). The materials that are most often used as donors are based on conjugated polymers, whereas the fullerene and its soluble derivatives are commonly used as electron acceptors. This choice has not been changed since 1992, when the photoinduced electron transfer from the excited state of a conjugated polymer onto the fullerene was observed for the first time [30]. The light-to-charge conversion in a D/A OSC is commonly considered to be a sequential process comprising [28, 31]:

(1) the light absorption in the donor material and the generation of the donor exciton;

(2) the diffusion of the photogenerated donor exciton through the donor material to the D/A interface;

(3) the dissociation of the photogenerated donor exciton at the D/A interface by means of the electron transfer from the donor to the acceptor material that produces the so-called charge transfer (CT) exciton; the electron of the CT exciton is located in the acceptor, whereas the hole is accommodated by the donor material; the interfacial electron transfer takes place as a consequence of the favorable value of the LUMO–LUMO offset;

(4) further spatial separation of the electron (which is in the acceptor material) and the hole (which is in the donor material) and the formation of the so-called charge separated (CS) exciton;

(5) carrier transport throughout the respective materials towards the respective contacts, at which they can be extracted.

These steps are schematically presented on the energy diagram in Fig. 1.10(a) and on the typical conjugated polymer/fullerene interface in Fig. 1.10(b).

Let us now discuss which steps of the above-described sequential view of the light-to-charge conversion process in D/A OSCs may be critical to their operation. We start with the exciton

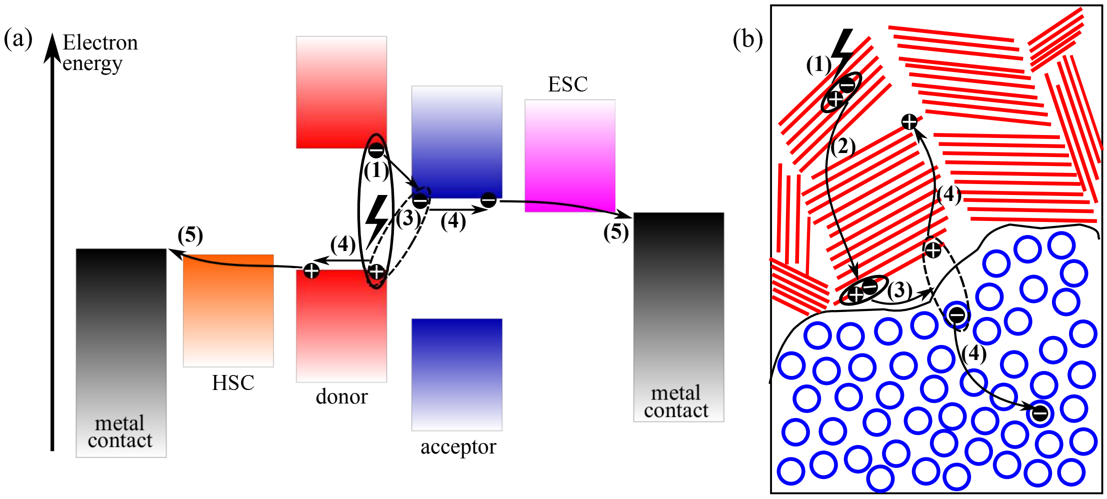

FIGURE 1.10: Steps (1)–(5) of the sequential mechanism of light-to-charge conversion in a D/A OSC depicted on (a) the energy diagram, and (b) a conjugated polymer/fullerene interface. While panel (a) shows steps (1), (3), (4) and (5), panel (b) shows steps (1)–(4). On panel (b), red rods represent conjugated polymer chains, while blue cricles represent fullerene molecules.

diffusion to the D/A interface, which presents the crucial step that limits the efficiency of bilayer OSCs. Experimental data suggest that the distance the donor exciton can cover before its recombination is of the order of a couple of tens of nanometers [32]. Having in mind that the absorption coefficient of organic semiconductors in the vicinity of the absorption edge is typically $\alpha \sim 10^5$ cm^{-1} [5, 6], we conclude that linear dimensions of the donor region of a bilayer OSC that are required to absorb the major part of the incoming light are of the order of $\alpha^{-1} \sim 100$ nm, which is at least an order of magnitude larger than the exciton diffusion length. We conclude that only donor excitons that are generated in the proximity of the D/A interface may have the chance to reach it and dissociate. The donor excitons that are generated deep in the donor material (measured from the D/A interface) are certain to recombine, since the distance they have to cover in order to dissociate is much larger than the distance they can cover within their lifetime. That is the reason why the introduction of the BHJ morphology presented a major step forward in the efficiencies of D/A OSCs. In a BHJ OSC, the two materials are finely intertwined, the interface between them is distributed throughout the whole active region, and the linear dimensions of phase-segregated domains of pure donor and acceptor materials are comparable to the donor exciton diffusion length. In the most efficient BHJ OSCs, they range between 10 and 20 nm [33], meaning that almost all of the donor excitons are photogenerated in the vicinity of the

D/A interface and, consequently, may potentially be converted into free carriers.

The initially photogenerated donor exciton is strongly bound, its binding energy ranging from 0.5 to 1 eV. After its dissociation at the D/A interface, the electron and hole in thus formed CT exciton are still tightly bound and localized at the interface. To understand this, let us estimate the binding energy of the CT exciton. Since the electron and hole in the CT state are pinned to the D/A interface, it seems reasonable to assume that they are point charges. The intrapair separation r_{CT} may be taken to be comparable to the typical separation between constituents of the donor and acceptor materials, and we take $r_{\mathrm{CT}} = 1$ nm. Using the relative dielectric constant $\varepsilon_r = 3$, the binding energy of the CT exciton is estimated to be [28, 34]

$$\epsilon_{\mathrm{b}}^{\mathrm{CT}} = \frac{1}{4\pi\varepsilon_0\varepsilon_r}\frac{e^2}{r_{\mathrm{CT}}}, \tag{1.3}$$

where $e > 0$ is the elementary charge, and ε_0 is the vacuum permittivity. Upon insertion of the numerical values, we obtain $\epsilon_{\mathrm{b}}^{\mathrm{CT}} = 0.5$ eV. We see that $\epsilon_{\mathrm{b}}^{\mathrm{CT}}$ is comparable to the binding energy of the initial donor exciton and is still much larger than the thermal energy at room temperature. This back-of-the-envelope calculation suggests that the introduction of the acceptor material should not be expected to drastically improve the efficiency of OSCs, since the electron transfer from the donor to the acceptor results in charges that are still quite strongly bound and cannot be spontaneously separated into free carriers. Considering these facts, the experimental evidence that, in the most efficient OSCs, virtually all of the absorbed photons are eventually converted into free charges capable of producing photocurrent [7], seems surprising. These pieces of evidence suggest that the above-described sequential mechanism of the OSC operation be critically reassessed. In the following section, based on the existing experimental, as well as theoretical developments, we provide a critical view of the sequential mechanism.

1.5 Critical View of the Sequential Mechanism of OSC Operation

Let us return to the first experimental observation [30] of the photoinduced electron transfer from a conjugated polymer onto the fullerene. The authors reported that the electron transfer takes place on a picosecond time scale. The fact that one of the processes leading to free charge carriers occurs on such short time scales has motivated numerous time-resolved experimental studies of exciton dissociation and charge separation on ultrashort time scales [35–39]. The advances in the techniques used to generate ultrashort laser pulses enabled experimentalists to probe the very initial stages of carrier dynamics in photoexcited OSCs with time resolution as good as 10 fs. There is a multitude of available time-resolved nonlinear spectroscopic techniques. However, in all of them, the system of interest is first exposed to an energetic optical pulse (the so-called pump pulse) that initiates nonequilibrium microscopic dynamics of the system. The information on the state of the system some time after its initial excitation is then extracted by irradiating the system by a weak optical pulse (the so-called probe pulse), which is followed by a comparison of a certain property of the excited system (e.g., the absorption spectrum) to the same property of the unexcited system (in the absence of the pump pulse). From such a comparison, nonequilibrium features of the dynamics can be inferred and their time evolution can be followed with temporal resolution that is limited by pulse duration. Irrespective of the particular technique used, the ultrafast spectroscopic signals obtained in experiments on the most efficient OSCs point towards the presence of essentially free charges on 100-fs time scales following the excitation of the system [36–39]. These results are difficult to reconcile with the commonly accepted sequential mechanism of free-charge generation for at least two reasons:

(a) for typical values of the exciton diffusion coefficient in organic semiconductors, which are of the order of 10^{-3} cm^2/(Vs) [32], the distance the initially photogenerated donor exciton can cover in 100 fs is of the order of 0.1 nm; this distance is much smaller than the characteristic linear dimension (10–20 nm) of phase-segregated domains in the most efficient BHJ OSCs; it is then unclear how the donor exciton manages to reach the D/A interface and perform all the subsequent steps in the sequential mechanism in such a short amount of time;

(b) even if the exciton dissociation occurs, it is not obvious what drives the transition from the CT state towards the CS state and eventually the free-charge state on such short time scales; this is especially controversial having in mind our estimate [Eq. (1.3)] of the binding energy of the CT exciton, which is also a measure of the energy barrier that the electron and hole have to overcome in order to become free.

The actual mechanism of ultrafast free-charge generation in OSCs is under intense debate that has recently inspired a great number of studies concerning exciton dissociation and charge separation that occur on ultrashort time scales, see the review articles [40–42]. The consensus on what drives such a fast generation of free carriers, as well as on the relevance of the ultrafast processes for the actual functioning of OSCs as electronic devices, has not been reached yet [14, 43]. In the following, we mention some of the hypotheses that have been used to explain how OSCs perform an efficient conversion of photons to free charges despite apparently unfavorable material characteristics.

One hypothesis is motivated by the long-lasting debate on the nature of primary photoexcitations in conjugated polymers that reached its culmination during the last decade of the 20th century. As discussed in more detail in Ch. 4, there are two conflicting standpoints. On the one hand, Heeger and coworkers suggest that a photoexcitation across the band gap of a conjugated polymer produces the so-called free polarons, i.e., mobile charge carriers that do not exhibit strong mutual Coulomb attraction (they are free from one another), but each of them is accompanied by the deformation of the chain configuration [44]. On the other hand, Bässler and coworkers highlight experimental evidence supporting the notion that strongly bound, localized, and electrically neutral excitons residing on conjugated segments that are determined by disorder [45] are the primary photoexcitations. Actual primary photoexcitations in conjugated polymers are in between these two limits, and their nature strongly depends on the time scale on which they are observed. Therefore, describing the excited state of conjugated polymers as a single species without invoking its time evolution may present a huge oversimplification of the actual physical situation [33]. The last point became obvious in experimental investigations of the very initial stages of the electronic dynamics in photoexcited neat conjugated polymers performed by Heeger and coworkers [46, 47]. In essence, these studies shed light onto the complex charge relaxation processes taking place in the excited state of conjugated polymers on time scales ranging from femtoseconds to hundreds of picoseconds. It was observed that the photoexcitation initially generates delocalized and essentially free charges that localize on 100-fs time scales to form a weakly bound exciton state and then relax to a strongly bound exciton state within approximately 1 ps following the photoexcitation. Therefore, in a polymer/fullerene BHJ blend, the charge separation at the polymer/fullerene interface is concurrent and competes with the charge relaxation in the pure polymer phase. It is conceivable that the observed ultrafast charge separation at a D/A interface occurs from a state of highly delocalized charges prior to the formation of the bound donor exciton [33].

According to the above-introduced sequential mechanism, upon reaching the D/A interface, the strongly bound donor exciton transforms into localized and strongly bound CT exciton [see Eq. (1.3)], which presents the starting point for further charge separation and eventual formation of free charges. Many experimental [36, 37, 48] and theoretical [49–53] studies have critically reassessed this assumption of the sequential mechanism. These studies have emphasized the importance of electronically "hot" (energetically higher) CT states that act as intermediate states in the subpicosecond conversion of the initial donor excitons to CS excitons. While in the electronically "cold" CT state (the strongly bound CT state, the lowest-energy CT state) the electron and hole are pinned to the D/A interface, the electronically "hot" CT states feature exceptionally good charge delocalization [37, 48, 49]. The "hot" CT states are kinetically more accessible from the initial donor states than the "cold" CT state [48, 49]. Due to such a strong charge delocalization, a direct transition from "hot" CT states to CS states, which circumvents the "cold" CT state, is possible. The charge separation by virtue of "hot" CT states is concurrent and competes with the exciton relaxation towards the "cold" CT state, which occurs on a picosecond time scale [37, 53]. Any conclusive description of ultrafast charge separation dynamics should also treat the carrier–phonon interaction [54–59]. The carrier–phonon interaction mediates the conversion of initial donor excitons to CS excitons, which may either be direct [57], or involve some sort of "hot" CT states [59].

The proposals put forward in the last paragraph are motivated by the ultrafast time-resolved spectroscopic studies on the most efficient OSCs. All of them implicitly assume that all of the photogenerated charges separate on subpicosecond time scales by exploiting some form of quantum mechanical coherence. These mechanisms of charge separation are thus collectively denoted as coherent charge separation mechanisms. The coherent mechanisms imply that the efficiency of the conversion of the absorbed photons to free charges should strongly depend on the energy of the photoexcitation. In other words, the selective excitation of the "cold" CT state should result in practically no free charges, since "hot" CT states are energetically far above the excited "cold" CT state. Moreover, the IQE as a function of the excitation energy should exhibit a pronounced increase once the "hot" CT states become accessible from the states in which initially photogenerated excitons reside. Even though such conclusions have been obtained [36], there are also other studies that have suggested that the IQE is practically independent on the excitation energy [60] and is almost equal to 100% all the way down to the selective excitation of the "cold" CT state [61]. Such studies, therefore, reinforce the notion that the "cold" CT state is involved in charge separation, without the need to invoke higher-energy, ultrafast routes towards free charges. Due to the aforementioned ultrafast relaxation of "hot" CT excitons towards the "cold" CT state, the majority of photoexcitations into higher energy states actually relax to the "cold" CT state, from which further separation may be achieved on much longer time scales. According to the results of Vandewal et al. [61], despite the existence of "hot" and ultrafast charge separation pathways at all-organic heterointerfaces, the major part of free charges is obtained on much longer time scales, starting from the strongly bound and localized CT state, and not via population and subsequent separation of "hot" CT states. This long-time charge separation proceeds as a sequence of incoherent hops between localized states, typically occurs in tens to hundreds of picoseconds, and is possibly assisted by the internal electric field at the D/A interface [62, 63].[1] The mechanisms of this sort are therefore collectively referred to as incoherent charge separation mechanisms. However, what drives the incoherent charge separation out of localized "cold" CT state remains elusive and there have been many attempts

---

[1] The notion of the internal electric field at the D/A interface is introduced in Sec. 7.1.

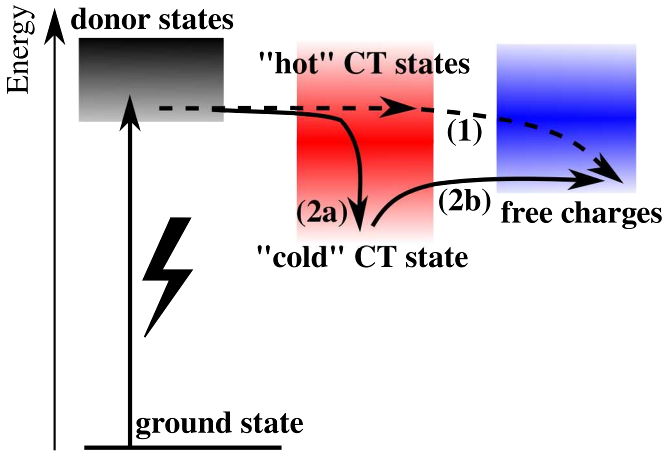

FIGURE 1.11: Energy diagram illustrating the controversy over the actual charge separation mechanism in D/A OSCs. The color gradients within the manifolds of donor, CT, and free-charge states are meant to be schematic representations of the respective densities of states. A photoexcitation of sufficient energy (black bolt) generates the donor exciton. The electron transfer at the D/A interface converts the donor exciton into the exciton in a "hot" CT state. The exciton in a "hot" CT state can (1) exhibit further separation that produces free charges, or (2a) first relax to the "cold" CT state and then (2b) separate into free charges. Note that the time scale characteristic of pathway (1) is comparable to the time scale of the "hot" CT exciton relaxation (2a) (which occurs on a picosecond time scale), but is much shorter than the time scale on which (2b) occurs (tens to hundreds of picoseconds).

to unveil the fundamental physical mechanisms that enable it. The problem has been tackled by the Onsager–Braun model [64, 65] and its amendments, which conceive charge separation from the "cold" CT state as a kinetic competition between charge recombination to the ground state and their thermal- and electric field-assisted escape from the mutual Coulomb barrier to the free-charge state. However, the Onsager–Braun model has been recognized as unsuitable to describe charge separation in D/A OSCs [66], mainly because it does not include neither the effects induced by disorder nor carrier delocalization. In recent years, there has been a multitude of theoretical proposals regarding the driving force for "cold" CT separation, see review articles [14, 41, 67], and a number of theoretical studies emphasizing that "utilizing coherent phenomena is not necessarily required for highly efficient charge separation in organic solar cells" [68–70]. The debate on "hot" and "cold" charge separation mechanisms is schematically summarized in Fig. 1.11.

1.6 Organization of the Thesis

The discussion conducted in Sec. 1.5 clearly demonstrates the need for a more solid understanding of fundamental physical effects that govern the light-to-charge conversion in OSCs, both on ultrafast and on much longer time scales. To this end, the focus of this thesis will not be on one particular material system, but rather on a detailed examination of relatively simple, yet physically plausible, model systems that capture all the physical effects that are regarded as relevant for the phenomena of interest.

Chapter 2 introduces the so-called standard semiconductor Hamiltonian, which will be used as a basic theoretical model throughout the thesis. We provide a formal definition of an exciton and introduce the so-called exciton basis, which consists of the eigenstates of an electron–hole pair that are supported by the model system. The adopted framework for description of excitons is quite general and comprises as limiting cases the widely known Wannier and Frenkel exciton models, which is explicitly demonstrated.

The basic theoretical tool used to investigate the ultrafast exciton dynamics within the standard semiconductor model is presented in Ch. 3. The infinite hierarchy of dynamical equations within the density matrix formalism is truncated by means of the so-called dynamics controlled truncation (DCT) scheme. Such a treatment is particularly suitable to describe the dynamics of electronic excitations generated by applying an optical pulse to an initially unexcited semiconductor, whose state is the vacuum of electron–hole pairs. In such a setup, many-body correlations are ultimately induced by the applied optical field and may, therefore, be systematically classified according to the powers with which they scale in the applied field. Such a classification enables one to perform a systematic truncation of the carrier branch of the hierarchy of equations of motion for density matrices. Previous theoretical developments in the field of inorganic semiconductors established that a conclusive description of exciton dynamics in photoexcited semiconductors is achieved already in the second order in the applied field. We, thus, truncate the carrier branch of the hierarchy at the second order in the applied field, and describe our method of the truncation of the phonon branch of the hierarchy. Our approach to the truncation of the phonon branch of the hierarchy consists in proposing the form of coupling among single-phonon-assisted and higher-order phonon-assisted density matrices that is compatible with the energy and particle-number conservation after a pulsed optical excitation of an initially unexcited semiconductor. The proposed treatment of the ultrafast exciton dynamics is fully quantum and statistical.

The essence of the proposal put forward by the Heeger's group is that subpicosecond charge separation at a photoexcited D/A interface is possible because it happens before the formation of bound excitons in the donor material. This proposal calls for a theoretical investigation of the exciton formation and relaxation dynamics taking place on femtosecond to picosecond time scales in a (neat) photoexcited semiconductor. Chapter 4 of this thesis is devoted to such an investigation, which is performed on a one-dimensional two-band lattice model of a semiconductor. The main aim of the study is the extraction of time scales relevant for the formation of the bound excitons and their subsequent relaxation and the comparison of the time scales thus obtained with relevant experimental data. The generality of our model enables us to study the photoinduced exciton dynamics for two sets of the values of model parameters, namely for the values typical of organic and inorganic semiconductors. The exciton basis states are divided into bound and unbound exciton states, the latter being counterparts of free-carrier states within our model. The time scales characteristic of the exciton formation and relaxation following the excitation of a neat semiconductor are obtained by following the time evolution of the numbers of bound excitons and free charges. The time scales thus obtained are compared to those emerging from subpicosecond time-resolved experiments. Furthermore, we vary different model parameters and identify the influence of different physical effects on the time scales of interest.

In Ch. 5, we move our focus to the ultrafast exciton dynamics at photoexcited D/A interfaces, striving to unveil the origin of spatially separated charges that have been experimentally observed on $\lesssim$ 100-fs time scales after the photoexcitation of the most efficient OSCs. We adjust the theoretical model presented in Ch. 2 to the case of interest and construct a one-dimensional lattice model of a D/A heterojunction. The theoretical method developed in Ch. 3 enables us to treat exciton photogeneration, exciton dissociation, and further charge separation equally and on a fully quantum level. The exciton basis states at a model D/A heterointerface are classified as donor, acceptor, and space-separated states. The space-separated states are further divided into CT and CS states according to the value of the mean electron–hole distance. Tracking the time evolution of the numbers of excitons in donor, acceptor, CT, and CS states provides us with a quantitative insight into the efficiency of ultrafast exciton dissociation and further charge separation, as well as into the underlying time scales. While the conventional interpretation of experimental results ascribes the presence of space-separated charges on ultrafast time scales to the ultrafast population transfer from donor to space-separated states, our results suggest that the major part of space-separated charges present on ultrafast time scales is directly optically generated from the ground state. The direct accessibility of space-separated states from the ground state is possible due to the resonant mixing between single-electron states in the donor and acceptor moieties, which leads to the redistribution of oscillator strengths between donor and space-separated states. The robustness of the principal conclusion is checked by varying different model parameters. We also theoretically investigate ultrafast transient absorption (TA) experiments, whose results are commonly interpreted in terms of populations only. We derive an analytical formula for the differential transmission signal (DTS) that demonstrates that, apart from populations, coherences should also be taken into account on such short time scales. We find that the signal on subpicosecond time scales is actually dominated by coherences rather than by state populations. Our findings, therefore, challenge the usual interpretation of experimental signals on subpicosecond time scales.

The aforementioned resonant mixing, which brings about the possibility of directly reaching space-separated states from the ground state, is studied in greater detail in Ch. 6, in which we focus upon individuating the photophysical pathways that photogenerated excitations follow on subpicosecond time scales after the photoexcitation. We find that, depending on the energy region of the exciton spectrum, there are two ways in which the resonant mixing mechanism can occur. The resonant mixing among single-particle states in the two materials leads to the formation of the so-called photon-absorbing charge-bridging states, which enhance the number of space-separated charges on ultrafast time scales by their direct optical generation, as in Ch. 5. On the other hand, the resonant mixing among two-particle (exciton) states of donor and space-separated character is responsible for the formation of the so-called bridge states that enhance the ultrafast generation of separated charges by acting as intermediate states in phonon-assisted transitions from donor states towards space-separated states. We conclude that, on subpicosecond time scales, free-charge generation is governed by the competition between transitions from the donor to the space-separated manifold and transitions within the donor manifold. While the former type of transitions may enhance free-charge generation, the latter type of transitions leads to the relaxation towards the lowest-energy donor state, which acts as a trap for charge separation. Our numerical results demonstrate that, at ~ 1 ps following the excitation, the major part of photogenerated excitons remains in the donor exciton manifold. Moreover, on the same time scales, we also observe some relaxation within the space-separated manifold towards the strongly bound CT state.

While indicating that there is some build-up of the populations of space-separated states on ultrafast time scales, the results obtained in Ch. 6 strongly suggest that, if the charge separation at a D/A interface is effective, it is expected to predominantly occur on time scales that are much longer than the picosecond one, from the strongly bound and localized donor or CT states. As we have already discussed, such a scenario is typical of incoherent ("cold") separation mechanisms, which, however, do not provide us with the driving force enabling charge separation from localized initial conditions. Our efforts summarized in Ch. 7 are aimed at identifying the physical effects that are responsible for the experimentally observed efficient and electric field- and temperature-independent separation of strongly bound charge pairs. The model is essentially the same as in Chapter 6, but in Ch. 7 it also takes into account the presence of the disorder, which is ubiquitous in organic semiconductors. Differently from many proposed models of incoherent charge separation, our model fully and properly takes into account charge delocalization effects, whose relevance has been repeatedly recognized. We find that the combination of charge delocalization and disorder is at the heart of efficient and weakly field- and temperature-dependent charge separation from both the strongly bound CT and donor exciton states.

Chapter 8 is devoted to a summary of the most important conclusions emerging from the investigations presented in this thesis.

Chapter 2

Standard Semiconductor Model

Here, we introduce the standard semiconductor model, which is the basic theoretical model that will be used throughout this thesis. Since this model should provide us with insights into microscopic processes taking place in photoexcited semiconductors on ultrafast time scales, it has to account for relevant physical effects such as

(a) the charge delocalization, which leads to the formation of bands,

(b) the electron–hole interaction, which is responsible for exciton formation,

(c) the carrier–phonon interaction, which determines the relaxation properties of the system, and

(d) the interaction of carriers with the external electromagnetic field that creates interband (electron–hole) excitations.

In Sec. 2.1, we introduce the two-band semiconductor model, consisting of one conduction band and one valence band. The generalization to the multiband case is straightforward and will be used in certain parts of the thesis. The standard semiconductor model is thoroughly presented from various viewpoints in a number of review articles [71–73] and books [74, 75]. Here, we follow the analysis presented in Ref. [71]. Section 2.2 defines an exciton as the simplest excitation above the ground state of a semiconductor. While the developments in Secs. 2.1 and 2.2 are quite general, in Sec. 2.3 we are more specific and demonstrate that, under appropriate approximations, the model we use can reduce to the widely known Wannier and Frenkel exciton models.

2.1 Two-Band Semiconductor Model

The Hamiltonian of a system of nonrelativistic valence electrons interacting with lattice vibrations (phonons) and with an external optical field can be expressed as

$$H = H_{\mathrm{mat}} + H_{\mathrm{p}} + H_{\mathrm{mat-p}} + H_{\mathrm{mat-f}}. \tag{2.1}$$

The first and the second term describe isolated carriers and phonons, the third term is the carrier–phonon interaction, while the fourth term represents the interaction of carriers with the external electromagnetic field. For the sake of simplicity, unless otherwise stated, we will not explicitly consider the electron spin, but assume that the spin quantum number is absorbed into the generic quantum number for electronic excitations. Using the second-quantized field operators $\Psi(\mathbf{r})$ and $\Psi^\dagger(\mathbf{r})$, the part of the Hamiltonian that describes isolated carriers reads as

$$H_{\mathrm{mat}} = \int \mathrm{d}\mathbf{r}\ \Psi^\dagger(\mathbf{r}) H_0(\mathbf{r}) \Psi(\mathbf{r}) + \frac{1}{2} \int \mathrm{d}\mathbf{r}_1\, \mathrm{d}\mathbf{r}_2\ \Psi^\dagger(\mathbf{r}_1)\Psi^\dagger(\mathbf{r}_2) V_{\mathrm{c-c}}(\mathbf{r}_1 - \mathbf{r}_2)\Psi(\mathbf{r}_2)\Psi(\mathbf{r}_1). \tag{2.2}$$

$H_0(\mathbf{r})$ is the single-electron Hamiltonian, which comprises the kinetic energy of an electron and the single-particle potential created by the nuclei and core electrons. $V_{\mathrm{c-c}}(\mathbf{r}_1 - \mathbf{r}_2)$ denotes the Coulomb interaction potential screened by the core electrons and lattice degrees of freedom that are not accounted for dynamically. The Fermi field operators $\Psi(\mathbf{r})$ [$\Psi^\dagger(\mathbf{r})$] annihilate [create] an electron in $\mathbf{r}$ and satisfy the anticommutation relations

$$\{\Psi(\mathbf{r}), \Psi(\mathbf{r}')\} = 0, \quad \left\{\Psi(\mathbf{r}), \Psi^\dagger(\mathbf{r}')\right\} = \delta(\mathbf{r} - \mathbf{r}'). \tag{2.3}$$

The free-phonon part of the Hamiltonian is

$$H_{\mathrm{p}} = \sum_\mu \hbar\omega_\mu b_\mu^\dagger b_\mu, \tag{2.4}$$

where b_μ ($b_\mu^\dagger$) are Bose operators destroying (creating) a phonon in mode μ with energy $\hbar\omega_\mu$ and obeying the commutation relations

$$[b_\mu, b_\nu] = 0, \quad \left[b_\mu, b_\nu^\dagger\right] = \delta_{\mu\nu}. \tag{2.5}$$

The coupling between carriers and lattice vibrations is described by

$$H_{\mathrm{mat-p}} = \int \mathrm{d}\mathbf{r}\ \Psi^\dagger(\mathbf{r}) V_{\mathrm{c-p}}(\mathbf{r}) \Psi(\mathbf{r}), \tag{2.6}$$

where

$$V_{\mathrm{c-p}}(\mathbf{r}) = \sum_\mu \left(\tilde{g}_\mu(\mathbf{r}) b_\mu^\dagger + \tilde{g}_\mu^*(\mathbf{r}) b_\mu\right) \tag{2.7}$$

is the potential induced by the lattice vibrations, in which only terms linear in the displacements of the nuclei have been retained. Finally, the interaction with the optical field $\mathbf{E}(t)$ is of the form

$$H_{\mathrm{mat-f}} = -\mathbf{E}(t) \int \mathrm{d}\mathbf{r}\ \Psi^\dagger(\mathbf{r})\left(-e\mathbf{r}\right)\Psi(\mathbf{r}). \tag{2.8}$$

Since our main aim is to study time-dependent phenomena in semiconductors (and their heterojunctions) excited by a laser pulse, we assume that the electric field is spatially homogeneous. The spatial dependence of the field can be included in a straightforward manner, see, e.g., Ref. [72].

Let us study in more detail the ground state of the interacting-carrier Hamiltonian [Eq. (2.2)]. The simplest possible approximation to the true ground state of a system of interacting fermions is the Hartree–Fock ground state, which is a single Slater determinant consisting of occupied single-particle states that are determined by the variational approach. Namely, by requiring that the ground-state energy be minimal, we obtain the set of Hartree–Fock equations, the solution to which provides us with the aforementioned single-particle states. We introduce new Fermi operators $a_p, a_p^\dagger$ by

$$\Psi(\mathbf{r}) = \sum_p \phi_p(\mathbf{r}) a_p, \tag{2.9}$$

where $\phi_p(\mathbf{r})$ are orthonormal single-particle wave functions labeled by index p. Operators a_p, $a_p^\dagger$ obey the following anticommutation laws

$$\{a_p, a_{p'}\} = 0, \quad \left\{a_p, a_{p'}^\dagger\right\} = \delta_{pp'}, \tag{2.10}$$

and will be further referred to as particle operators, while computations performed using particle operators are said to be performed in the particle picture. The ground state of H_{mat} is then approximated as

$$|GS\rangle = \prod_{p\in\text{occ}} a_p^\dagger |0\rangle_e, \tag{2.11}$$

where $|0\rangle_e$ is the particle vacuum, and "occ" denotes the set of occupied single-particle states. The wave functions $\phi_p(\mathbf{r})$ are determined by requiring that the energy of the ground state $|GS\rangle$,

$$\langle GS|H_{\text{mat}}|GS\rangle = \sum_{p\in\text{occ}} t_{pp} + \frac{1}{2}\sum_{pq\in\text{occ}} \left(V_{ppqq} - V_{pqqp}\right), \tag{2.12}$$

be minimal. In other words, these wave functions satisfy the Hartree–Fock equations

$$H_0(\mathbf{r})\phi_p(\mathbf{r}) + \sum_{p'\in\text{occ}} \int \mathrm{d}\mathbf{r}' \phi_{p'}^*(\mathbf{r}') V_{\text{c}-\text{c}}(\mathbf{r}-\mathbf{r}') \left[\phi_{p'}(\mathbf{r}')\phi_p(\mathbf{r}) - \phi_p(\mathbf{r}')\phi_{p'}(\mathbf{r})\right] = \epsilon_p\, \phi_p(\mathbf{r}), \tag{2.13}$$

where ϵ_p are the energies of Hartree–Fock orbitals. In Eq. (2.12), we introduce matrix elements t_{pq} of the single-particle Hamiltonian H_0

$$t_{pq} = \int \mathrm{d}\mathbf{r}\; \phi_p^*(\mathbf{r}) H_0(\mathbf{r}) \phi_q(\mathbf{r}), \tag{2.14}$$

as well as matrix elements V_{pqkl} of the Coulomb interaction

$$V_{pqkl} = \int \mathrm{d}\mathbf{r}_1\, \mathrm{d}\mathbf{r}_2\; \phi_p^*(\mathbf{r}_1)\phi_q(\mathbf{r}_1) V_{\text{c}-\text{c}}(\mathbf{r}_1 - \mathbf{r}_2) \phi_k^*(\mathbf{r}_2)\phi_l(\mathbf{r}_2). \tag{2.15}$$

The energy difference between the lowest unoccupied and the highest occupied single-particle states (in the ground state of the carrier subsystem)

$$E_g = \min_{p\notin\mathrm{occ}} \epsilon_p - \max_{p\in\mathrm{occ}} \epsilon_p \tag{2.16}$$

in a typical semiconductor is $E_g \sim 1$ eV and is denoted as the single-particle band gap. Since E_g is much larger than the thermal energy at room temperature, we may safely assume that, in the absence of an optical excitation of sufficient energy, the carrier subsystem is in the Hartree–Fock ground state [Eq. (2.11)].

The preceding developments make it easy to differentiate between occupied and unoccupied states with respect to the Hartree–Fock ground state. In other words, we may transfer the description of a semiconductor from the particle picture to the so-called electron–hole picture. The particles in initially unoccupied states are further referred to as electrons. The absence of a particle in an initially occupied state is further denoted as a hole. We define creation ($d_p^\dagger$) and annihilation (d_p) operators for holes as

$$d_p^\dagger = a_p, \quad d_p = a_p^\dagger, \quad \text{for } p \in \mathrm{occ}. \tag{2.17}$$

The definitions of electron creation ($c_p^\dagger$) and annihilation (c_p) operators are

$$c_p^\dagger = a_p^\dagger, \quad c_p = a_p, \quad \text{for } p \notin \mathrm{occ}. \tag{2.18}$$

In a semiconductor, the band gap separates the valence band, which is fully occupied, from the conduction band, which is completely empty. We assume that the spectrum of both occupied and unoccupied single-particle states is dense, i.e., occupied states form a single band of states that is further denoted as the valence band, while unoccupied states also form a single band further referred to as the conduction band. In further analysis, single-particle states $p \in \mathrm{occ}$ that are occupied in the ground state $|GS\rangle$ will be considered as valence-band states and denoted as $p \in \mathrm{VB}$, while single-particle states $p \notin \mathrm{occ}$ that are empty in the ground state $|GS\rangle$ will be considered as conduction-band states and denoted as $p \in \mathrm{CB}$. The electron and hole operators satisfy the following anticommutation relations that stem from Eqs. (2.10), (2.17), and (2.18):

$$\{c_p, c_q\} = 0, \quad \left\{c_p, c_q^\dagger\right\} = \delta_{pq}, \quad \text{for } p, q \in \text{CB}; \tag{2.19}$$

$$\{d_p, d_q\} = 0, \quad \left\{d_p, d_q^\dagger\right\} = \delta_{pq}, \quad \text{for } p, q \in \text{VB}; \tag{2.20}$$

$$\{c_p, d_q\} = \left\{c_p, d_q^\dagger\right\} = 0, \quad \text{for } p \in \text{CB and } q \in \text{VB}. \tag{2.21}$$

The Hamiltonian of isolated carriers H_{mat} should now be expressed in terms of electron and hole operators. Enforcing the normal order of operators, the interacting-carrier part of the Hamiltonian reads as

$$H_{\text{mat}} = E_{GS} + H^{(0)}_{\text{mat}} + H^{(1)}_{\text{mat}} + H^{(2)}_{\text{mat}}, \tag{2.22}$$

where

$$E_{GS} = \sum_{p\in\text{VB}} \epsilon^{\text{v}}_p - \frac{1}{2} \sum_{pq\in\text{VB}} \left(V^{\text{vvvv}}_{ppqq} - V^{\text{vvvv}}_{pqqp}\right), \tag{2.23}$$

$$\begin{aligned} H^{(0)}_{\text{mat}} = &\sum_{p\in\text{CB}} \epsilon^{\text{c}}_p\, c^\dagger_p c_p - \sum_{p\in\text{VB}} \epsilon^{\text{v}}_p\, d^\dagger_p d_p + \sum_{\substack{pq\in\text{VB}\\ kl\in\text{CB}}} \left(V^{\text{vccv}}_{plkq} - V^{\text{vvcc}}_{pqkl}\right) c^\dagger_k d^\dagger_q d_p c_l \\ &+\frac{1}{2}\left[\sum_{pqkl\in\text{CB}} V^{\text{cccc}}_{pqkl}\, c^\dagger_p c^\dagger_k c_l c_q + \sum_{pqkl\in\text{VB}} V^{\text{vvvv}}_{pqkl}\, d^\dagger_q d^\dagger_l d_k d_p\right], \end{aligned} \tag{2.24}$$

$$\begin{aligned} H^{(1)}_{\text{mat}} = &\frac{1}{2} \sum_{\substack{qkl\in\text{VB}\\ p\in\text{CB}}} \left(V^{\text{vvcv}}_{kqpl} - V^{\text{cvvv}}_{pqkl}\right) c^\dagger_p d^\dagger_q d^\dagger_l d_k + \frac{1}{2} \sum_{\substack{pkl\in\text{VB}\\ q\in\text{CB}}} \left(V^{\text{vcvv}}_{pqkl} - V^{\text{vvvc}}_{plkq}\right) d^\dagger_l d_p d_k c_q \\ &+\frac{1}{2} \sum_{\substack{pql\in\text{CB}\\ k\in\text{VB}}} \left(V^{\text{ccvc}}_{pqkl} - V^{\text{vccc}}_{kqpl}\right) c^\dagger_p c_q d_k c_l + \frac{1}{2} \sum_{\substack{pkl\in\text{CB}\\ q\in\text{VB}}} \left(V^{\text{cvcc}}_{pqkl} - V^{\text{cccv}}_{plkq}\right) c^\dagger_p d^\dagger_q c^\dagger_k c_l, \end{aligned} \tag{2.25}$$

$$H^{(2)}_{\text{mat}} = \frac{1}{2}\left[\sum_{\substack{pk\in\text{CB}\\ ql\in\text{VB}}} V^{\text{cvcv}}_{pqkl}\, c^\dagger_p d^\dagger_q c^\dagger_k d^\dagger_l + \sum_{\substack{pk\in\text{VB}\\ ql\in\text{CB}}} V^{\text{vcvc}}_{pqkl}\, d_p c_q d_k c_l\right]. \tag{2.26}$$

In order to facilitate the interpretation of the result, in Eqs. (2.24)–(2.26) we have indicated the information on the particle type (electron or hole) as upper indices of the matrix elements. Equation (2.22) tells us that H_{mat} can be decomposed into the constant part E_{GS}, which represents the total energy of filled valence-band states, and three contributions $H^{(j)}_{\text{mat}}$ ($j = 0, 1, 2$) that change the number of electron–hole pairs by j pairs. Apart from the constant part, which amounts to a shift of the energy axis, in this thesis we will also disregard all the contributions that do not conserve the number of electron–hole pairs and focus our attention on the pair-conserving part $H^{(0)}_{\mathrm{mat}}$. The approximation that neglects contributions that do not preserve the number of electron–hole pairs will be viewed from somewhat different perspective in Sec. 2.3.2 devoted to the Frenkel exciton model.

The Coulomb matrix elements appearing in Eq. (2.24) can be divided into direct and exchange terms. If the arguments in the Coulomb matrix element can be grouped to give electron or hole densities of the respective single-particle states, as is the case in terms V^{vvcc}_{pqkl}, V^{cccc}_{pqkl}, and V^{vvvv}_{pqkl}, this matrix element represents a direct term. On the other hand, Coulomb matrix element V^{vccv}_{plkq} is an example of an exchange term.

The carrier–phonon interaction is expressed in terms of electron and hole operators as

$$H_{\mathrm{mat-p}} = H^{(0)}_{\mathrm{mat-p}} + H^{(1)}_{\mathrm{mat-p}} + H^{(f)}_{\mathrm{mat-p}}, \tag{2.27}$$

where

$$H^{(0)}_{\mathrm{mat-p}} = \sum_{pq\in\mathrm{CB}} \sum_{\mu} \left(\gamma^{\mu}_{pq}\, c^{\dagger}_{p} c_{q} b^{\dagger}_{\mu} + \gamma^{\mu *}_{pq} c^{\dagger}_{q} c_{p} b_{\mu}\right) + \sum_{pq\in\mathrm{VB}} \sum_{\mu} \left(\gamma^{\mu}_{pq} d^{\dagger}_{q} d_{p} b^{\dagger}_{\mu} + \gamma^{\mu *}_{pq} d^{\dagger}_{p} d_{q} b_{\mu}\right), \tag{2.28}$$

$$H^{(1)}_{\mathrm{mat-p}} = \sum_{\substack{p\in\mathrm{VB}\\ q\in\mathrm{CB}}} \sum_{\mu} \left(\gamma^{\mu}_{pq} d_{p} c_{q} b^{\dagger}_{\mu} + \gamma^{\mu *}_{pq} c^{\dagger}_{q} d^{\dagger}_{p} b_{\mu}\right) + \sum_{\substack{p\in\mathrm{CB}\\ q\in\mathrm{VB}}} \sum_{\mu} \left(\gamma^{\mu}_{pq} c^{\dagger}_{p} d^{\dagger}_{q} b^{\dagger}_{\mu} + \gamma^{\mu *}_{pq} d_{q} c_{p} b_{\mu}\right), \tag{2.29}$$

$$H^{(f)}_{\mathrm{mat-p}} = \sum_{pq\in\mathrm{VB}} \delta_{pq} \left(\gamma^{\mu}_{pq} b^{\dagger}_{\mu} + \gamma^{\mu *}_{pq} b_{\mu}\right). \tag{2.30}$$

The carrier–phonon matrix element between two single-particle states reads as

$$\gamma^{\mu}_{pq} = \int \mathrm{d}\mathbf{r}\; \phi^{*}_{p}(\mathbf{r})\; \tilde{g}(\mathbf{r})\; \phi_{q}(\mathbf{r}). \tag{2.31}$$

The decomposition of the carrier–phonon interaction Hamiltonian embodied in Eq. (2.27) is similar to the decomposition of the purely carrier Hamiltonian in Eq. (2.22). The contribution $H^{(f)}_{\mathrm{mat-p}}$ represents the carrier–phonon interaction energy in the Hartree–Fock ground state.

Since its action is limited to phonon degrees of freedom, this term does not contribute to the hole–phonon coupling and will not be considered in further discussion. The contributions $H^{(j)}_{\mathrm{mat-p}}$ ($j = 0$, 1) change the number of electron–hole pairs by j pairs. $H^{(1)}_{\mathrm{mat-p}}$ describes phonon-induced transitions among occupied and unoccupied states. Having in mind that the energy gap separating these two groups of states is of the order of 1 eV, such transitions are not very probable in common semiconductor materials. Therefore, we further consider only contribution $H^{(0)}_{\mathrm{mat-p}}$, which conserves the number of electron–hole pairs.

The interaction with the optical field can be recast in terms of electron and hole operators as

$$\begin{aligned} H_{\mathrm{mat-f}} =& -\mathbf{E}(t)\left(\sum_{\substack{p\in\mathrm{VB}\\ q\in\mathrm{CB}}} \mathbf{M}^{\mathrm{vc}}_{pq} d_p c_q + \sum_{\substack{p\in\mathrm{CB}\\ q\in\mathrm{VB}}} \mathbf{M}^{\mathrm{cv}}_{pq} c^\dagger_p d^\dagger_q\right) \\ & -\mathbf{E}(t)\left(\sum_{pq\in\mathrm{CB}} \mathbf{M}^{\mathrm{cc}}_{pq} c^\dagger_p c_q + \sum_{pq\in\mathrm{VB}} \mathbf{M}^{\mathrm{vv}}_{pq} d^\dagger_q d_p\right), \end{aligned} \tag{2.32}$$

where the dipole-moment matrix elements are defined as

$$\mathbf{M}_{pq} = \int \mathrm{d}\mathbf{r}\; \phi^*_p(\mathbf{r})\,(-e\mathbf{r})\,\phi_q(\mathbf{r}). \tag{2.33}$$

The first term in Eq. (2.32) describes the so-called interband transitions, in which the optical field of sufficient frequency promotes an electron from the valence band to the conduction band and creates an electron–hole pair. On the other hand, the second term in Eq. (2.32) describes the so-called intraband transitions that take place within the conduction or valence band. In this thesis, the focus is on the detailed understanding of processes occurring during and after the excitation of a neat semiconductor (or a heterojunction of two semiconductors) that creates electron–hole pair excitations. Therefore, in the major part of the thesis, the second term in Eq. (2.32) will not be considered. An exception will be made in our theoretical treatment of a transient absorption experiment in Sec. 5.4.2.

In summary, we explicitly write down the model Hamiltonian that will be used throughout this thesis

$$H = H_{\mathrm{c}} + H_{\mathrm{p}} + H_{\mathrm{c-p}} + H_{\mathrm{c-f}}, \tag{2.34}$$

$$
\begin{aligned}
H_{\mathrm{c}} = & \sum_{p\in\mathrm{CB}} \epsilon_p^{\mathrm{c}}\, c_p^\dagger c_p - \sum_{p\in\mathrm{VB}} \epsilon_p^{\mathrm{v}}\, d_p^\dagger d_p + \sum_{\substack{pq\in\mathrm{VB}\\ kl\in\mathrm{CB}}} \left(V_{plkq}^{\mathrm{vccv}} - V_{pqkl}^{\mathrm{vvcc}}\right) c_k^\dagger d_q^\dagger d_p c_l \\
& + \frac{1}{2}\left[\sum_{pqkl\in\mathrm{CB}} V_{pqkl}^{\mathrm{cccc}}\, c_p^\dagger c_k^\dagger c_l c_q + \sum_{pqkl\in\mathrm{VB}} V_{pqkl}^{\mathrm{vvvv}}\, d_q^\dagger d_l^\dagger d_k d_p\right],
\end{aligned}
\tag{2.35}
$$

$$
H_{\mathrm{p}} = \sum_\mu \hbar\omega_\mu b_\mu^\dagger b_\mu, \tag{2.36}
$$

$$
\begin{aligned}
H_{\mathrm{c-p}} = & \sum_{pq\in\mathrm{CB}} \sum_\mu \left(\gamma_{pq}^\mu\, c_p^\dagger c_q b_\mu^\dagger + \gamma_{pq}^{\mu *} c_q^\dagger c_p b_\mu\right) \\
& + \sum_{pq\in\mathrm{VB}} \sum_\mu \left(\gamma_{pq}^\mu d_q^\dagger d_p b_\mu^\dagger + \gamma_{pq}^{\mu *} d_p^\dagger d_q b_\mu\right),
\end{aligned}
\tag{2.37}
$$

$$
H_{\mathrm{c-f}} = -\mathbf{E}(t)\left(\sum_{\substack{p\in\mathrm{VB}\\ q\in\mathrm{CB}}} \mathbf{M}_{pq}^{\mathrm{vc}} d_p c_q + \sum_{\substack{p\in\mathrm{CB}\\ q\in\mathrm{VB}}} \mathbf{M}_{pq}^{\mathrm{cv}} c_p^\dagger d_q^\dagger\right). \tag{2.38}
$$

The model Hamiltonian given in Eqs. (2.34)–(2.38) is known in literature as the standard semiconductor Hamiltonian.

The derivation of the model Hamiltonian has produced the diagonal single-particle contribution in Eq. (2.35). In actual modeling, this part does not have to be diagonal, so that it may be replaced by

$$
\sum_{p\in\mathrm{CB}} \epsilon_p^{\mathrm{c}}\, c_p^\dagger c_p - \sum_{p\in\mathrm{VB}} \epsilon_p^{\mathrm{v}}\, d_p^\dagger d_p \to \sum_{pq\in\mathrm{CB}} \epsilon_{pq}^{\mathrm{c}}\, c_p^\dagger c_q - \sum_{pq\in\mathrm{VB}} \epsilon_{qp}^{\mathrm{v}}\, d_p^\dagger d_q. \tag{2.39}
$$

The last point will be useful in the construction of models describing charge separation at interfaces between two semiconductors.

All the interactions present in the model Hamiltonian embodied in Eqs. (2.34)–(2.38) are spin-independent. Let us now explicitly separate the spin quantum number σ_p out of the generic quantum number p, $p = (p_o, \sigma_p)$, where p_o is the orbital quantum number. This step has to be accompanied by a more specific definition of the hole creation and annihilation operators [Eq. (2.17)]. Namely, the annihilation of an electron with spin σ in a valence-band state can also be seen as the creation of a hole with spin $\overline{\sigma} = -\sigma$ in the same valence-band state, i.e., $d_{p_o,\sigma_p}^\dagger = a_{p_o,\overline{\sigma_p}}$. Moreover, if valence-band states are labeled by wave vector $\mathbf{k}$, the annihilation of an electron in the valence-band state $(\mathbf{k}, \sigma)$ can be conceived as the creation of a hole with wave vector $-\mathbf{k}$ and spin $-\sigma$,[1]

$$d^{\dagger}_{-\mathbf{k},-\sigma} = a_{\mathbf{k},\sigma}. \tag{2.40}$$

Taking the last fact into account, the terms H_{c} [Eq. (2.35)], $H_{\mathrm{c-p}}$ [Eq. (2.37)], and $H_{\mathrm{c-f}}$ [Eq. (2.38)] of the standard semiconductor Hamiltonian, in which the spin quantum number is explicitly considered, read as

$$\begin{aligned} H_{\mathrm{c}} = &\sum_{p_o \in \mathrm{CB}} \sum_{\sigma} \epsilon^{\mathrm{c}}_{p_o}\, c^{\dagger}_{p_o\sigma} c_{p_o\sigma} - \sum_{p_o \in \mathrm{VB}} \sum_{\sigma} \epsilon^{\mathrm{v}}_{p_o}\, d^{\dagger}_{p_o\sigma} d_{p_o\sigma} \\ &+ \sum_{\substack{p_o q_o \in \mathrm{VB} \\ k_o l_o \in \mathrm{CB}}} \sum_{\sigma_p \sigma_k} \left(V^{\mathrm{vccv}}_{p_o l_o k_o q_o} c^{\dagger}_{k_o\sigma_k} d^{\dagger}_{q_o\overline{\sigma_k}} d_{p_o\sigma_p} c_{l_o\overline{\sigma_p}} - V^{\mathrm{vvcc}}_{p_o q_o k_o l_o} c^{\dagger}_{k_o\sigma_k} d^{\dagger}_{q_o\sigma_p} d_{p_o\sigma_p} c_{l_o\sigma_k} \right) \\ &+ \frac{1}{2} \sum_{p_o q_o k_o l_o \in \mathrm{CB}} \sum_{\sigma_p \sigma_k} V^{\mathrm{cccc}}_{p_o q_o k_o l_o}\, c^{\dagger}_{p_o\sigma_p} c^{\dagger}_{k_o\sigma_k} c_{l_o\sigma_k} c_{q_o\sigma_p} \\ &+ \frac{1}{2} \sum_{p_o q_o k_o l_o \in \mathrm{VB}} \sum_{\sigma_p \sigma_k} V^{\mathrm{vvvv}}_{p_o q_o k_o l_o}\, d^{\dagger}_{q_o\sigma_p} d^{\dagger}_{l_o\sigma_k} d_{k_o\sigma_k} d_{p_o\sigma_p}, \end{aligned} \tag{2.41}$$

$$\begin{aligned} H_{\mathrm{c-p}} = &\sum_{p_o q_o \in \mathrm{CB}} \sum_{\sigma} \sum_{\mu} \left(\gamma^{\mu}_{p_o q_o}\, c^{\dagger}_{p_o\sigma} c_{q_o\sigma} b^{\dagger}_{\mu} + \gamma^{\mu *}_{p_o q_o} c^{\dagger}_{q_o\sigma} c_{p_o\sigma} b_{\mu} \right) \\ &+ \sum_{p_o q_o \in \mathrm{VB}} \sum_{\sigma} \sum_{\mu} \left(\gamma^{\mu}_{p_o q_o} d^{\dagger}_{q_o\sigma} d_{p_o\sigma} b^{\dagger}_{\mu} + \gamma^{\mu *}_{p_o q_o} d^{\dagger}_{p_o\sigma} d_{q_o\sigma} b_{\mu} \right), \end{aligned} \tag{2.42}$$

$$H_{\mathrm{c-f}} = -\mathbf{E}(t) \left(\sum_{\substack{p_o \in \mathrm{VB} \\ q_o \in \mathrm{CB}}} \sum_{\sigma} \mathbf{M}^{\mathrm{vc}}_{p_o q_o} d_{p_o\overline{\sigma}} c_{q_o\sigma} + \sum_{\substack{p_o \in \mathrm{CB} \\ q_o \in \mathrm{VB}}} \sum_{\sigma} \mathbf{M}^{\mathrm{cv}}_{p_o q_o} c^{\dagger}_{p_o\sigma} d^{\dagger}_{q_o\overline{\sigma}} \right). \tag{2.43}$$

Let us also notice that the above-presented developments are quite general and do not rely on specific assumptions regarding indices that label single-particle states. The model Hamiltonian is, therefore, flexible, as will be shown in greater detail in Secs. 2.3.1 and 2.3.2, where we explicitly demonstrate that it can be applied to study Wannier and Frenkel excitons.

---

[1] The hole operators may be formally introduced by applying a time reversal transformation to particle operators, see, e.g., Ref. [76]. The time reversal introduces a minus sign in front of the momentum (and spin), so that the wave vector (and spin) associated with a hole acquire an additional minus sign.

2.2 Definition of Exciton

The ground state $|GS\rangle$ of a semiconductor in the Hartree–Fock approximation [Eq. (2.11)] can also be regarded as the vacuum of electron–hole pairs and will be further denoted as $|0\rangle$. In a singly excited state, an electron is promoted to the conduction band, leaving behind a hole in the valence band, i.e., there is an electron–hole pair. The excited electron and hole are coupled by the Coulomb interaction. The most general electron–hole pair state is the superposition

$$|x\rangle = \sum_{\substack{a\in\mathrm{VB}\\ b\in\mathrm{CB}}} \psi^x_{ab}\, c^\dagger_b d^\dagger_a |0\rangle, \tag{2.44}$$

where the amplitude ψ^x_{ab} describes the contribution of the pair state in which an electron initially in valence-band state a is promoted to conduction-band state b. The exciton basis is defined by the eigenvalue problem

$$H_\mathrm{c}|x\rangle = \hbar\omega_x|x\rangle, \tag{2.45}$$

which, due to the linear independence of different pair states $c^\dagger_b d^\dagger_a|0\rangle$, can be written as the following equation for amplitudes ψ^x_{ab}

$$\left(\epsilon^\mathrm{c}_b - \epsilon^\mathrm{v}_a\right)\psi^x_{ab} + \sum_{\substack{p\in\mathrm{VB}\\ q\in\mathrm{CB}}} \left(V^\mathrm{vccv}_{pqba} - V^\mathrm{vvcc}_{pabq}\right)\psi^x_{pq} = \hbar\omega_x\psi^x_{ab}. \tag{2.46}$$

The amplitude ψ^x_{ab} may also be expressed as the scalar product $\psi^x_{ab} = \langle a_h b_e|x\rangle$ of two vectors in the space of single electron–hole excitations. Since exciton states $\{|x\rangle\}$ are orthonormal, the following identity holds

$$\sum_{\substack{a\in\mathrm{VB}\\ b\in\mathrm{CB}}} \psi^{x'*}_{ab}\psi^x_{ab} = \delta_{x'x}. \tag{2.47}$$

Exciton states $\{|x\rangle\}$ constitute a basis in the space of single electron–hole excitations, so that the decomposition of unity in this space gives the following relation

$$\sum_x \psi^{x*}_{a'b'}\psi^x_{ab} = \delta_{a'a}\delta_{b'b}. \tag{2.48}$$

The operator that creates an exciton in state $|x\rangle$ is denoted as $X_x^\dagger$ and introduced by $|x\rangle = X_x^\dagger|0\rangle$. In terms of electron and hole operators,

$$X_x^\dagger = \sum_{\substack{a\in\mathrm{VB}\\ b\in\mathrm{CB}}} \psi_{ab}^x \, c_b^\dagger d_a^\dagger. \tag{2.49}$$

Using the anticommutation relations of electron and hole operators [Eqs. (2.19)–(2.21)], we obtain that exciton operators $X_x, X_x^\dagger$ satisfy the following relations

$$[X_x, X_{x'}] = \left[X_x^\dagger, X_{x'}^\dagger\right] = 0, \tag{2.50}$$

$$\left[X_x, X_{x'}^\dagger\right] = \delta_{xx'} - \sum_{a'a\in\mathrm{VB}} \left(\sum_{b\in\mathrm{CB}} \psi_{ab}^{x*}\psi_{a'b}^{x'}\right) d_{a'}^\dagger d_a - \sum_{b'b\in\mathrm{CB}} \left(\sum_{a\in\mathrm{VB}} \psi_{ab}^{x*}\psi_{ab'}^{x'}\right) c_{b'}^\dagger c_b. \tag{2.51}$$

When the density of electronic excitations is small, Eqs. (2.50) and (2.51) suggest that excitons can be regarded as bosons.

Let us now complete our discussion on excitons by explicitly considering the spin quantum number. According to their spin multiplicity, exciton states can be classified as singlet or triplet states. The space of single electron–hole excitations, which is spanned by vectors

$$\left\{|(a_o\sigma_a)_h(b_o\sigma_b)_e\rangle = c_{b_o\sigma_b}^\dagger d_{a_o\sigma_a}^\dagger|0\rangle\right\}, \tag{2.52}$$

can be divided into subspaces with well-defined spin multiplicity according to the eigenvalues of operators $\mathbf{S}^2$ and S_z, where the operator of the total spin $\mathbf{S}$ is defined as

$$\mathbf{S} = \sum_{\sigma'\sigma} \left\langle \sigma' \left| \frac{\hbar}{2}\boldsymbol{\tau} \right| \sigma \right\rangle \left(\sum_{p_o\in\mathrm{CB}} c_{p_o\sigma'}^\dagger c_{p_o\sigma} - \sum_{p_o\in\mathrm{VB}} d_{p_o\overline{\sigma}}^\dagger d_{p_o\overline{\sigma'}}\right). \tag{2.53}$$

In the last equation, $\boldsymbol{\tau}$ are Pauli matrices. In the subspace of singlet excitons, both $\mathbf{S}^2$ and S_z reduce to zero, and the corresponding basis vectors are [77, 78]

$$\left\{|(a_o)_h(b_o)_e\rangle_S = \frac{1}{\sqrt{2}}\left(c_{b_o,\uparrow}^\dagger d_{a_o,\downarrow}^\dagger + c_{b_o,\downarrow}^\dagger d_{a_o,\uparrow}^\dagger\right)|0\rangle\right\}. \tag{2.54}$$

In the subspace of triplet excitons, operator $\mathbf{S}^2$ reduces to 2, while, according to the eigenvalue of S_z, we have the following groups of basis vectors

$$\left\{|(a_o)_h(b_o)_e\rangle_{T,0} = \frac{1}{\sqrt{2}}\left(c^\dagger_{b_o,\uparrow}d^\dagger_{a_o,\downarrow} - c^\dagger_{b_o,\downarrow}d^\dagger_{a_o,\uparrow}\right)|0\rangle\right\}, \tag{2.55a}$$

$$\left\{|(a_o)_h(b_o)_e\rangle_{T,1} = c^\dagger_{b_o,\uparrow}d^\dagger_{a_o,\uparrow}|0\rangle\right\}, \tag{2.55b}$$

$$\left\{|(a_o)_h(b_o)_e\rangle_{T,-1} = c^\dagger_{b_o,\downarrow}d^\dagger_{a_o,\downarrow}|0\rangle\right\}. \tag{2.55c}$$

Therefore, the most general singlet exciton state is of the form

$$|x\rangle_S = \sum_{\substack{a_o\in\mathrm{VB}\\ b_o\in\mathrm{CB}}} \psi^{x,S}_{a_ob_o}\,|(a_o)_h(b_o)_e\rangle_S\,, \tag{2.56}$$

where the expansion coefficients $\psi^{x,S}_{a_ob_o}$ satisfy an equation analogous to Eq. (2.46) that reads as

$$\left(\epsilon^{\mathrm{c}}_{b_o} - \epsilon^{\mathrm{v}}_{a_o}\right)\psi^{x,S}_{a_ob_o} + \sum_{\substack{p_o\in\mathrm{VB}\\ q_o\in\mathrm{CB}}}\left(2V^{\mathrm{vccv}}_{p_oq_ob_oa_o} - V^{\mathrm{vvcc}}_{p_oa_ob_oq_o}\right)\psi^{x,S}_{p_oq_o} = \hbar\omega_{x,S}\psi^{x,S}_{a_ob_o}. \tag{2.57}$$

Similarly, the most general triplet exciton state with a fixed value of S_z is

$$|x\rangle_{T,S_z} = \sum_{\substack{a_o\in\mathrm{VB}\\ b_o\in\mathrm{CB}}} \psi^{x,(T,S_z)}_{a_ob_o}\,|(a_o)_h(b_o)_e\rangle_{T,S_z}\,, \tag{2.58}$$

and the expansion coefficients satisfy

$$\left(\epsilon^{\mathrm{c}}_{b_o} - \epsilon^{\mathrm{v}}_{a_o}\right)\psi^{x,(T,S_z)}_{a_ob_o} - \sum_{\substack{p_o\in\mathrm{VB}\\ q_o\in\mathrm{CB}}} V^{\mathrm{vvcc}}_{p_oa_ob_oq_o}\psi^{x,(T,S_z)}_{p_oq_o} = \hbar\omega_{x,(T,S_z)}\psi^{x,(T,S_z)}_{a_ob_o}. \tag{2.59}$$

Let us mention that Eqs. (2.57) and (2.59) are usually written as a single equation for the expansion coefficients $\psi^x_{a_ob_o}$ in the orbital space

$$\left(\epsilon^{\mathrm{c}}_{b_o} - \epsilon^{\mathrm{v}}_{a_o}\right)\psi^x_{a_ob_o} + \sum_{\substack{p_o\in\mathrm{VB}\\ q_o\in\mathrm{CB}}}\left(2\delta_M V^{\mathrm{vccv}}_{p_oq_ob_oa_o} - V^{\mathrm{vvcc}}_{p_oa_ob_oq_o}\right)\psi^x_{p_oq_o} = \hbar\omega_x\psi^x_{a_ob_o}, \tag{2.60}$$

where $\delta_M = 1$ for singlet excitons and $\delta_M = 0$ for triplet excitons. A photoexcitation of a semiconductor whose form is given in Eq. (2.38) [or Eq. (2.43)] can generate only singlet excitons. We usually say that singlet excitons are optically active, while triplet excitons are optically inactive. Since the time evolution driven by the standard semiconductor Hamiltonian cannot change spin multiplicity of photogenerated singlet excitons, we conclude that, in all of our theoretical developments concerning exciton dynamics, we will have to deal exclusively with singlet excitons. In reality, however, the spin–orbit coupling, i.e., the interaction between the spin and orbital motion of an electron, brings about mixing between singlet and triplet excitations [79]. An excitation transfer from the singlet to the triplet manifold is commonly denoted as the intersystem crossing. Our focus in the forthcoming chapters will be on exciton dynamics occurring on femtosecond to picosecond time scales following the photoexcitation of organic semiconductors and their heterojunctions. However, the intersystem crossing in these systems typically takes place on much longer time scales, spanning the range from nanoseconds to microseconds [79, 80]. Therefore, the intersystem crossing is not active on time scales of our interest, and confining the investigations to the singlet subspace provides us with relevant insights into ultrafast exciton dynamics.

We will not further dwell on the spin multiplicity of exciton states. To compute the (singlet) exciton basis states, we will use Eq. (2.46) remembering that, according to Eq. (2.57), a factor of 2 should be inserted in front of the exchange term.

2.3 Wannier and Frenkel Exciton Models

In this section, we discuss which approximations should be employed in order to obtain the widely known Wannier [81] and Frenkel [82, 83] exciton models. The analysis concerning the Wannier model is mainly based on Ch. 2 of Ref. [76] and Ch. 23 of Ref. [84], while the microscopic model for Frenkel excitons is developed in Ch. 24 of Ref. [84] and also in Ref. [85]. An excellent classical text on these two models of excitons can be found Ref. [86].

2.3.1 Wannier Exciton Model

Let us now specialize to the case of a crystalline semiconductor consisting of N_{uc} periodically repeated unit cells. The single-particle states in both the valence and the conduction band can then be counted by wave vector $\mathbf{k}$, and the corresponding wave functions are ($\lambda \in \{\mathrm{v}, \mathrm{c}\}$)

$$\phi^{\lambda}_{\mathbf{k}}(\mathbf{r}) = \frac{1}{\sqrt{N_{uc}}}\, u^{\lambda}_{\mathbf{k}}(\mathbf{r})\, \mathrm{e}^{\mathrm{i}\mathbf{k}\cdot\mathbf{r}}, \tag{2.61}$$

where Bloch functions $u^{\lambda}_{\mathbf{k}}(\mathbf{r})$ have the periodicity of the lattice. The explicit separation of the factor $1/\sqrt{N_{uc}}$ out of the wave function $\phi^{\lambda}_{\mathbf{k}}(\mathbf{r})$ ensures that Bloch functions are normalized to 1 within a unit cell

$$\int_{v_{uc}} \mathrm{d}\mathbf{r}\, \left|u^{\lambda}_{\mathbf{k}}(\mathbf{r})\right|^2 = 1, \tag{2.62}$$

where v_{uc} is the volume of the unit cell. We further assume that we deal with a direct semiconductor with isotropic effective masses m_e^* and m_h^* for electrons and holes, respectively, so that the single-particle energies in the vicinity of the valence-band maximum (and conduction-band minimum) $\mathbf{k} = 0$ can be expressed as

$$\epsilon^{\mathrm{c}}_{\mathbf{k}} = E_g + \frac{\hbar^2\mathbf{k}^2}{2m_e^*}, \quad \epsilon^{\mathrm{v}}_{\mathbf{k}} = -\frac{\hbar^2\mathbf{k}^2}{2m_h^*}, \tag{2.63}$$

where E_g is the single-particle gap of the semiconductor (at $\mathbf{k} = 0$), see also Eq. (2.16). The eigenvalue problem that should be solved to obtain exciton basis states [Eq. (2.46)] can be specialized to the case of interest to give

$$\left(\epsilon^{\mathrm{c}}_{\mathbf{k}_e} - \epsilon^{\mathrm{v}}_{-\mathbf{k}_h}\right)\psi^{x}_{\mathbf{k}_h\mathbf{k}_e} + \sum_{\mathbf{l}_h\mathbf{l}_e}\left(V^{\mathrm{vccv}}_{-\mathbf{l}_h\mathbf{l}_e\mathbf{k}_e-\mathbf{k}_h} - V^{\mathrm{vvcc}}_{-\mathbf{l}_h-\mathbf{k}_h\mathbf{k}_e\mathbf{l}_e}\right)\psi^{x}_{\mathbf{l}_h\mathbf{l}_e} = \hbar\omega_x\psi^{x}_{\mathbf{k}_h\mathbf{k}_e}. \tag{2.64}$$

Let us analyze in more detail the direct term of the electron–hole interaction

$$\begin{aligned} V^{\mathrm{vvcc}}_{-\mathbf{l}_h-\mathbf{k}_h\mathbf{k}_e\mathbf{l}_e} = \frac{1}{N_{uc}^2}\int_{\Omega} &\mathrm{d}\mathbf{r}_h\,\mathrm{d}\mathbf{r}_e\, \mathrm{e}^{\mathrm{i}(\mathbf{l}_h-\mathbf{k}_h)\cdot\mathbf{r}_h}\, \mathrm{e}^{\mathrm{i}(\mathbf{l}_e-\mathbf{k}_e)\cdot\mathbf{r}_e}\, V_{\mathrm{c-c}}(\mathbf{r}_e-\mathbf{r}_h) \\ &\times u^{\mathrm{v}*}_{-\mathbf{l}_h}(\mathbf{r}_h)\, u^{\mathrm{v}}_{-\mathbf{k}_h}(\mathbf{r}_h)\, u^{\mathrm{c}*}_{\mathbf{k}_e}(\mathbf{r}_e)\, u^{\mathrm{c}}_{\mathbf{l}_e}(\mathbf{r}_e), \end{aligned} \tag{2.65}$$

where the integrations are performed over the entire volume Ω of the crystal. The exchange term can be written in a similar manner. For electronic excitations in the vicinity of the band extrema ($\mathbf{k} = 0$), the plane-wave factors, as well as the Coulomb potential, are slowly varying functions whose changes within one unit cell are very small. These simplifying assumptions are due to Wannier [81] and are appropriate for weakly bound pair states, in which the electron–hole separation is large compared to the lattice constant and the wave vector of the relative motion of the electron and hole is small compared to the inverse lattice constant. The integrations in Eq. (2.67) can be split into the summations over all unit cells and the integrations over the volume of a unit cell v_{uc}. The Bloch functions are then be expanded around $\mathbf{k} = 0$ and only the first, constant in $\mathbf{k}$, term is retained. Using the aforementioned assumptions together with the lattice periodicity of the Bloch functions, we obtain the following integrals

$$\int_{v_{uc}} \mathrm{d}\mathbf{r}\; u^{\mathrm{c}*}_{\mathbf{k}\simeq 0}(\mathbf{r})\; u^{\mathrm{c}}_{\mathbf{l}\simeq 0}(\mathbf{r}) \simeq 1, \qquad \int_{v_{uc}} \mathrm{d}\mathbf{r}\; u^{\mathrm{c}*}_{\mathbf{k}\simeq 0}(\mathbf{r})\; u^{\mathrm{v}}_{\mathbf{l}'\simeq 0}(\mathbf{r}) \simeq 0. \tag{2.66}$$

Therefore, in this approximation, the exchange term vanishes. Since the length scales of relevance are much larger than the lattice constant, in the direct term we can transfer to the continuum representation and obtain

$$V^{\mathrm{vvcc}}_{-\mathbf{l}_h - \mathbf{k}_h \mathbf{k}_e \mathbf{l}_e} = \frac{1}{\Omega^2} \int_{\Omega} \mathrm{d}\mathbf{r}_e\, \mathrm{d}\mathbf{r}_h\; \mathrm{e}^{\mathrm{i}(\mathbf{l}_h - \mathbf{k}_h)\cdot \mathbf{r}_h}\; \mathrm{e}^{\mathrm{i}(\mathbf{l}_e - \mathbf{k}_e)\cdot \mathbf{r}_e}\; V_{\mathrm{c-c}}(\mathbf{r}_e - \mathbf{r}_h). \tag{2.67}$$

Equation (2.67) shows us that the total wave vector of the pair,

$$\mathbf{K} = \mathbf{k}_e + \mathbf{k}_h = \mathbf{l}_e + \mathbf{l}_h, \tag{2.68}$$

is a good quantum number, and that the direct term $V^{\mathrm{vvcc}}_{-\mathbf{l}_h - \mathbf{k}_h \mathbf{k}_e \mathbf{l}_e}$ is proportional to the Fourier transformation $V_{\mathrm{c-c}}\left(|\mathbf{l}_h - \mathbf{k}_h|\right)$ of the Coulomb potential.

Having substituted the results given in Eqs. (2.63) and (2.67) into Eq. (2.64), further manipulations in Eq. (2.64) are facilitated by introducing the Fourier transformation of amplitudes

$\psi^x_{\mathbf{k}_h\mathbf{k}_e}$

$$\psi^x_{\mathbf{r}_h\mathbf{r}_e} = \sum_{\mathbf{k}_h\mathbf{k}_e} \mathrm{e}^{\mathrm{i}\mathbf{k}_h\cdot\mathbf{r}_h}\, \mathrm{e}^{\mathrm{i}\mathbf{k}_e\cdot\mathbf{r}_e}\, \psi^x_{\mathbf{k}_h\mathbf{k}_e}. \tag{2.69}$$

The Fourier transformation of Eq. (2.64) then gives

$$\left(-\frac{\hbar^2}{2m_e^*}\nabla_e^2 - \frac{\hbar^2}{2m_h^*}\nabla_h^2 + E_g - V_{\mathrm{c-c}}(\mathbf{r}_e - \mathbf{r}_h)\right)\psi^x_{\mathbf{r}_h\mathbf{r}_e} = \hbar\omega_x\psi^x_{\mathbf{r}_h\mathbf{r}_e}. \tag{2.70}$$

Since Eq. (2.70) is actually a two-body problem, it is convenient to separate the motion of the center of mass of the pair (coordinate $\mathbf{R}$) and the relative motion of the electron and hole composing the pair (coordinate $\mathbf{r}$) by introducing

$$\mathbf{R} = \frac{m_e^*}{m_e^* + m_h^*}\mathbf{r}_e + \frac{m_h^*}{m_e^* + m_h^*}\mathbf{r}_h, \quad \mathbf{r} = \mathbf{r}_e - \mathbf{r}_h. \tag{2.71}$$

The motion of the center of mass can be described by a plane wave with wave vector $\mathbf{K}$. The relative motion is described by quantity $\psi^{x,\mathrm{rel}}_{\mathbf{r}}$ which is defined as

$$\psi^x_{\mathbf{r}_h\mathbf{r}_e} = \frac{1}{\sqrt{\Omega}}\,\mathrm{e}^{\mathrm{i}\mathbf{K}\cdot\mathbf{R}}\,\psi^{x,\mathrm{rel}}_{\mathbf{r}}, \tag{2.72}$$

and satisfies

$$\left(-\frac{\hbar^2}{2m_{\mathrm{red}}}\nabla^2 - V_{\mathrm{c-c}}(\mathbf{r})\right)\psi^{x,\mathrm{rel}}_{\mathbf{r}} = \left(\hbar\omega_x - E_g - \frac{\hbar^2\mathbf{K}^2}{2(m_e^* + m_h^*)}\right)\psi^{x,\mathrm{rel}}_{\mathbf{r}}. \tag{2.73}$$

In the last equation, $m_{\mathrm{red}} = \frac{m_e^* m_h^*}{m_e^* + m_h^*}$ is the reduced mass of the pair. If we model the Coulomb interaction potential as

$$V_{\mathrm{c-c}}(\mathbf{r}) = \frac{1}{4\pi\varepsilon_0}\,\frac{e^2}{\varepsilon_r|\mathbf{r}|}, \tag{2.74}$$

where ε_r is the relative dielectric constant of the medium, we see that Eq. (2.73) is analogous to the equation satisfied by the stationary states of the hydrogen atom. Therefore, the solutions to Eq. (2.73) are counted by quantum number $n = 1, 2, \ldots$, and pair states can be uniquely identified by specifying the wave vector of the center of mass $\mathbf{K}$ and n, i.e., label x can be replaced by $(\mathbf{K}, n)$. In other words, there is the internal motion of an electron around a hole (described by the quantum number n) that is accompanied by the motion of the pair as a whole throughout the crystal (characterized by the center-of-mass wave vector $\mathbf{K}$). The total energy of state $(\mathbf{K}, n)$ is given as

$$\hbar\omega_{\mathbf{K},n} = E_g + \frac{\hbar^2\mathbf{K}^2}{2(m_e^* + m_h^*)} + \epsilon_n, \tag{2.75}$$

where

$$\epsilon_n = -\frac{m_{\text{red}}e^4}{32\pi^2\varepsilon_0^2\varepsilon_r^2}\,\frac{1}{n^2}. \tag{2.76}$$

The energy spectrum of an electron–hole pair contains a number of bound pair states and the continuum of ionized (unbound) states. The binding energy of the lowest-energy exciton state $(\mathbf{K} = 0, n = 1)$ is usually referred to as the exciton binding energy and is given as

$$\epsilon_{\text{b}}^X = \frac{m_{\text{red}}e^4}{32\pi^2\varepsilon_0^2\varepsilon_r^2}, \tag{2.77}$$

while the corresponding Bohr radius, which is a measure of the electron–hole separation in bound states, is

$$a_{0,X} = \frac{4\pi\varepsilon_0\varepsilon_r\hbar^2}{m_{\text{red}}e^2}. \tag{2.78}$$

Compared to the hydrogen atom, the exciton binding energy is reduced because the reduced mass of the pair is smaller than the free-electron mass and the Coulomb interaction is screened, so that

$$\epsilon_{\text{b}}^X = \frac{m_{\text{red}}}{m_e}\,\frac{1}{\varepsilon_r^2}\,\frac{m_e e^4}{32\pi^2\varepsilon_0^2} = \frac{m_{\text{red}}}{m_e}\,\frac{1}{\varepsilon_r^2} \times 13.6\,\text{eV}, \tag{2.79}$$

and

$$a_{0,X} = \varepsilon_r\left(\frac{m_{\text{red}}}{m_e}\right)^{-1}\frac{4\pi\varepsilon_0\hbar^2}{m_e e^2} = \varepsilon_r\left(\frac{m_{\text{red}}}{m_e}\right)^{-1} \times 52.9\,\text{pm}, \tag{2.80}$$

where m_e is the free-electron mass. In a typical inorganic semiconductor, $\varepsilon_r \sim 10$, while the reduced mass m_{red} is smaller than the electron effective mass $m_e^* \sim \frac{1}{10}m_e$, so that $m_{\text{red}} \lesssim \frac{1}{10}m_e$. Therefore, the typical binding energy of the Wannier exciton is of the order of 1–10 meV, while the corresponding exciton radius is of the order of 10–100 nm.

The creation operator of an exciton in pair state $(\mathbf{K}, n)$ is

$$X^{\dagger}_{\mathbf{K},n} = \sum_{\mathbf{k}_h \mathbf{k}_e} \delta_{\mathbf{K},\mathbf{k}_h+\mathbf{k}_e} \, \psi^{n,\mathrm{rel}}_{\mathbf{l}} c^{\dagger}_{\mathbf{k}_e} d^{\dagger}_{\mathbf{k}_h}, \tag{2.81}$$

where $\mathbf{l} = \frac{m_h^*}{m_e^*+m_h^*}\mathbf{k}_e - \frac{m_e^*}{m_e^*+m_h^*}\mathbf{k}_h$, and

$$\psi^{n,\mathrm{rel}}_{\mathbf{l}} = \int \mathrm{d}\mathbf{r} \; \mathrm{e}^{-\mathrm{i}\mathbf{l}\cdot\mathbf{r}} \, \psi^{n,\mathrm{rel}}_{\mathbf{r}}. \tag{2.82}$$

2.3.2 Frenkel Exciton Model

Let us now assume that the single-particle states appearing in Eq. (2.46) are localized around lattice sites $\mathbf{R}$, i.e., the corresponding single-particle eigenfunctions are the Wannier functions

$$\phi^{\lambda}_{\mathbf{R}}(\mathbf{r}) = w^{\lambda}(\mathbf{r} - \mathbf{R}). \tag{2.83}$$

Instead of directly solving the exciton eigenvalue problem given in Eq. (2.46), as we did for Wannier excitons, we introduce the Frenkel exciton model by rewriting the interacting-carrier part H_{c} of the Hamiltonian [Eq. (2.35)] in the localized basis. At the same time, such a derivation will shed new light on the approximation of retaining only the pair-conserving contribution to the full interacting-carrier part of the Hamiltonian [Eqs. (2.22)–(2.26)].

Let us start by examining matrix elements of the Coulomb interaction in the localized basis

$$\begin{aligned} V^{\lambda_1'\lambda_1\lambda_2'\lambda_2}_{\mathbf{R}_1'\mathbf{R}_1\mathbf{R}_2'\mathbf{R}_2} = \int \mathrm{d}\mathbf{r}_1 \, \mathrm{d}\mathbf{r}_2 \, & w^{\lambda_1' *}\left(\mathbf{r}_1 - \mathbf{R}_1'\right) w^{\lambda_1}\left(\mathbf{r}_1 - \mathbf{R}_1\right) V_{\mathrm{c-c}}\left(\mathbf{r}_1 - \mathbf{r}_2\right) \times \\ & w^{\lambda_2' *}\left(\mathbf{r}_2 - \mathbf{R}_2'\right) w^{\lambda_2}\left(\mathbf{r}_2 - \mathbf{R}_2\right). \end{aligned} \tag{2.84}$$

We assume that the only nontrivial matrix elements are those featuring maximal overlap between Wannier functions, which is attained for $\mathbf{R}_1' = \mathbf{R}_1$ and $\mathbf{R}_2' = \mathbf{R}_2$. In other words, we approximate

$$V^{\lambda_1'\lambda_1\lambda_2'\lambda_2}_{\mathbf{R}_1'\mathbf{R}_1\mathbf{R}_2'\mathbf{R}_2} \approx \delta_{\mathbf{R}_1'\mathbf{R}_1} \, \delta_{\mathbf{R}_2'\mathbf{R}_2} \, V^{\lambda_1'\lambda_1\lambda_2'\lambda_2}_{\mathbf{R}_1\mathbf{R}_1\mathbf{R}_2\mathbf{R}_2}. \tag{2.85}$$

Under this assumption, the full carrier–carrier interaction [which comprises the last three summations on the right-hand side of Eq. (2.24), as well as Eqs. (2.25) and (2.26)] may be regarded as a multipolar expansion of the Coulomb interaction. Namely, as shown in greater detail in, e.g., Ref. [87], the direct terms in Eq. (2.24) are the monopole–monopole interaction, Eq. (2.25) describes the monopole–dipole interaction, whereas the two terms in Eq. (2.26) together with the exchange term in Eq. (2.24) represent the dipole–dipole interaction. The monopole–monopole interaction is the only long-range contribution and thus the most important one. Retaining only pair-conserving contributions to the Coulomb interaction, we actually fully capture its long-range part and, in addition, keep an exchange (dipole–dipole) contribution, which is essential to the derivation of the Frenkel exciton Hamiltonian.

The interacting-carrier part of the Hamiltonian in Eq. (2.35) may be rewritten in the localized basis as

$$\begin{aligned} H_{\mathrm{c}} = & \sum_{\mathbf{R}} \epsilon^{\mathrm{c}}_{\mathbf{R}}\, c^\dagger_{\mathbf{R}} c_{\mathbf{R}} - \sum_{\mathbf{R}} \epsilon^{\mathrm{v}}_{\mathbf{R}}\, d^\dagger_{\mathbf{R}} d_{\mathbf{R}} \\ & + \sum_{\mathbf{R}\mathbf{R}'} V^{\mathrm{vccv}}_{\mathbf{R}\mathbf{R}\mathbf{R}'\mathbf{R}'}\, c^\dagger_{\mathbf{R}'} d^\dagger_{\mathbf{R}'} d_{\mathbf{R}} c_{\mathbf{R}} - \sum_{\mathbf{R}\mathbf{R}'} V^{\mathrm{vvcc}}_{\mathbf{R}\mathbf{R}\mathbf{R}'\mathbf{R}'}\, c^\dagger_{\mathbf{R}'} d^\dagger_{\mathbf{R}} d_{\mathbf{R}} c_{\mathbf{R}'} \\ & + \frac{1}{2}\left(\sum_{\mathbf{R}\mathbf{R}'} V^{\mathrm{cccc}}_{\mathbf{R}\mathbf{R}\mathbf{R}'\mathbf{R}'}\, c^\dagger_{\mathbf{R}'} c^\dagger_{\mathbf{R}} c_{\mathbf{R}} c_{\mathbf{R}'} + \sum_{\mathbf{R}\mathbf{R}'} V^{\mathrm{vvvv}}_{\mathbf{R}\mathbf{R}\mathbf{R}'\mathbf{R}'}\, d^\dagger_{\mathbf{R}'} d^\dagger_{\mathbf{R}} d_{\mathbf{R}} d_{\mathbf{R}'} \right). \end{aligned} \tag{2.86}$$

Equation (2.86) implicitly assumes that the single-particle orbitals centered around different lattice sites do not overlap, so that carriers exhibit strong localization and are confined to single lattice sites. In the case of Frenkel excitons, electrons and holes are located around the same lattice site. Such a scenario is typically realized in molecular crystals, in which the carrier–carrier interaction prevails over carrier delocalization. We now introduce the operator $X^\dagger_{\mathbf{R}}$ creating an electron–hole pair at lattice site $\mathbf{R}$

$$X^\dagger_{\mathbf{R}} = c^\dagger_{\mathbf{R}} d^\dagger_{\mathbf{R}}, \tag{2.87}$$

and limit further discussion to the two-particle (single-exciton) subspace spanned by states $\left\{ X^\dagger_{\mathbf{R}} |0\rangle \right\}$. The electron–electron and hole–hole interaction reduce to zero in this subspace. The exchange term of the electron–hole interaction may be readily rewritten as

$$\sum_{\mathbf{R}\mathbf{R}'} V^{\mathrm{vccv}}_{\mathbf{R}\mathbf{R}\mathbf{R}'\mathbf{R}'}\, c^\dagger_{\mathbf{R}'} d^\dagger_{\mathbf{R}'} d_{\mathbf{R}} c_{\mathbf{R}} = \sum_{\mathbf{R}\mathbf{R}'} V_{\mathrm{exch}}\left(\mathbf{R}-\mathbf{R}'\right) X^\dagger_{\mathbf{R}'} X_{\mathbf{R}}, \tag{2.88}$$

where we introduce the exchange potential $V_{\mathrm{exch}}\left(\mathbf{R}-\mathbf{R}'\right) = V^{\mathrm{vccv}}_{\mathbf{R}\mathbf{R}\mathbf{R}'\mathbf{R}'}$. In the subspace of interest, the action of the direct electron–hole interaction is nontrivial only for $\mathbf{R}=\mathbf{R}'$, meaning that it can be recast in terms of operators $X_{\mathbf{R}}, X^\dagger_{\mathbf{R}}$ as

$$\sum_{\mathbf{R}\mathbf{R}'} V^{\mathrm{vvcc}}_{\mathbf{R}\mathbf{R}\mathbf{R}'\mathbf{R}'}\, c^\dagger_{\mathbf{R}'} d^\dagger_{\mathbf{R}} d_{\mathbf{R}} c_{\mathbf{R}'} \to \sum_{\mathbf{R}} V_{\mathrm{dir}}(0)\, X^\dagger_{\mathbf{R}} X_{\mathbf{R}}, \tag{2.89}$$

where we have introduced the on-site (direct) electron–hole interaction $V_{\mathrm{dir}}(0) = V^{\mathrm{vvcc}}_{\mathbf{R}\mathbf{R}\mathbf{R}\mathbf{R}}$. The number operators of electrons and holes, $c^\dagger_{\mathbf{R}} c_{\mathbf{R}}$ and $d^\dagger_{\mathbf{R}} d_{\mathbf{R}}$, can be reduced in the subspace of single localized electron–hole excitations to

$$c^\dagger_{\mathbf{R}} c_{\mathbf{R}},\, d^\dagger_{\mathbf{R}} d_{\mathbf{R}} \to X^\dagger_{\mathbf{R}} X_{\mathbf{R}}. \tag{2.90}$$

Therefore, the reduction of the Hamiltonian given in Eq. (2.86) to the subspace spanned by vectors $\left\{X^\dagger_{\mathbf{R}}|0\rangle\right\}$ is expressed (in terms of operators $X_{\mathbf{R}}, X^\dagger_{\mathbf{R}}$) as

$$H_{\mathrm{c}} = \sum_{\mathbf{R}} \left[\epsilon^{\mathrm{c}}_{\mathbf{R}} - \epsilon^{\mathrm{v}}_{\mathbf{R}} - V_{\mathrm{dir}}(0)\right] X^\dagger_{\mathbf{R}} X_{\mathbf{R}} + \sum_{\mathbf{R}\mathbf{R}'} V_{\mathrm{exch}}\left(\mathbf{R}-\mathbf{R}'\right) X^\dagger_{\mathbf{R}'} X_{\mathbf{R}}. \tag{2.91}$$

This is the Frenkel exciton Hamiltonian. We see that the direct contribution to the electron–hole interaction binds an electron and a hole at the same site into an exciton, while the exchange contribution $V_{\mathrm{exch}}\left(\mathbf{R}-\mathbf{R}'\right)$ is responsible for the excitation transfer between sites. The Frenkel exciton Hamiltonian may be diagonalized by exploiting the translational symmetry of the problem to introduce new operators $X_{\mathbf{k}}, X^\dagger_{\mathbf{k}}$ by

$$X^\dagger_{\mathbf{k}} = \frac{1}{\sqrt{N_{uc}}} \sum_{\mathbf{R}} \mathrm{e}^{\mathrm{i}\mathbf{k}\cdot\mathbf{R}} X^\dagger_{\mathbf{R}}, \tag{2.92}$$

where N_{uc} is the number of unit cells in the crystal, while $\mathbf{k}$ is the wave vector. The Frenkel exciton Hamiltonian is diagonal in $X_{\mathbf{k}}, X_{\mathbf{k}}^\dagger$

$$H_{\mathrm{c}} = \sum_{\mathbf{k}} E(\mathbf{k}) X_{\mathbf{k}}^\dagger X_{\mathbf{k}}, \tag{2.93}$$

with the exciton dispersion

$$E(\mathbf{k}) = \epsilon_{\mathbf{R}}^{\mathrm{c}} - \epsilon_{\mathbf{R}}^{\mathrm{v}} - V_{\mathrm{dir}}(0) + \frac{1}{N_{uc}} \sum_{\mathbf{R}\mathbf{R}'} \mathrm{e}^{\mathrm{i}\mathbf{k}\cdot(\mathbf{R}-\mathbf{R}')}\, V_{\mathrm{exch}}\left(\mathbf{R}-\mathbf{R}'\right). \tag{2.94}$$

Let us note in passing that the excitation transfer mediated by the nonradiative exchange coupling is important in describing the energy transfer between two organic molecules and is known as the Förster energy transfer [88]. In more detail, when the Coulomb interaction potential assumes the form given in Eq. (2.74), the potential of the exchange interaction can be expressed as [see Eq. (2.84)]

$$\begin{aligned} V_{\mathrm{exch}}\left(\mathbf{R}-\mathbf{R}'\right) = \int \mathrm{d}\mathbf{r}\,\mathrm{d}\mathbf{r}'\, w^{\mathrm{v}*}\left(\mathbf{r}-\mathbf{R}\right) w^{\mathrm{c}}\left(\mathbf{r}-\mathbf{R}\right) \frac{e^2}{4\pi\varepsilon_0\varepsilon_r\left|\mathbf{r}-\mathbf{r}'\right|} \times \\ w^{\mathrm{c}*}\left(\mathbf{r}'-\mathbf{R}'\right) w^{\mathrm{v}}\left(\mathbf{r}'-\mathbf{R}'\right). \end{aligned} \tag{2.95}$$

Introducing vectors $\boldsymbol{\rho} = \mathbf{r}-\mathbf{R}$ and $\boldsymbol{\rho}' = \mathbf{r}'-\mathbf{R}'$ and assuming that the inequality $\left|\boldsymbol{\rho}-\boldsymbol{\rho}'\right| \ll \left|\mathbf{R}-\mathbf{R}'\right|$ holds, we can perform the multipolar expansion of $\left|\mathbf{r}-\mathbf{r}'\right|^{-1}$ up to the second order in $\left|\boldsymbol{\rho}-\boldsymbol{\rho}'\right| / \left|\mathbf{R}-\mathbf{R}'\right|$ to obtain

$$\frac{1}{\left|\mathbf{r}-\mathbf{r}'\right|} = \frac{1}{\left|\mathbf{R}-\mathbf{R}'\right|} + \frac{\left(\mathbf{R}-\mathbf{R}'\right)\cdot\left(\boldsymbol{\rho}'-\boldsymbol{\rho}\right) - \frac{1}{2}\left(\boldsymbol{\rho}'-\boldsymbol{\rho}\right)^2}{\left|\mathbf{R}-\mathbf{R}'\right|^3} + \frac{3}{2}\frac{\left[\left(\mathbf{R}-\mathbf{R}'\right)\cdot\left(\boldsymbol{\rho}'-\boldsymbol{\rho}\right)\right]^2}{\left|\mathbf{R}-\mathbf{R}'\right|^5}. \tag{2.96}$$

Bearing in mind the orthogonality of Wannier functions and the definition of the dipole-moment matrix element

$$\int \mathrm{d}\boldsymbol{\rho}\, w^{\mathrm{c}*}\left(\boldsymbol{\rho}\right) w^{\mathrm{v}}\left(\boldsymbol{\rho}\right) \approx 0, \tag{2.97a}$$

$$\boldsymbol{\mu} = \int \mathrm{d}\boldsymbol{\rho}\, w^{\mathrm{c}*}\left(\boldsymbol{\rho}\right)\left(-e\boldsymbol{\rho}\right) w^{\mathrm{v}}\left(\boldsymbol{\rho}\right), \tag{2.97b}$$

we conclude that the monopole term in Eq. (2.96) reduces to zero, while isolating the nontrivial contributions from the other two terms in Eq. (2.96) gives us the familiar expression for the dipole–dipole interaction energy

$$V_{\text{exch}}\left(\mathbf{R}-\mathbf{R}'\right)=\frac{1}{4\pi\varepsilon_0\varepsilon_r}\left(\frac{\boldsymbol{\mu}^*\cdot\boldsymbol{\mu}}{\left|\mathbf{R}-\mathbf{R}'\right|^3}-3\frac{\left[\boldsymbol{\mu}^*\cdot\left(\mathbf{R}-\mathbf{R}'\right)\right]\left[\boldsymbol{\mu}\cdot\left(\mathbf{R}-\mathbf{R}'\right)\right]}{\left|\mathbf{R}-\mathbf{R}'\right|^5}\right). \tag{2.98}$$

Since $V_{\text{exch}}\left(\mathbf{R}-\mathbf{R}'\right)$ is proportional to $\left|\mathbf{R}-\mathbf{R}'\right|^{-3}$, the rate of the transition of a localized molecular excitation is then proportional to $\left|\mathbf{R}-\mathbf{R}'\right|^{-6}$, as predicted by the Förster theory.

Chapter 3

Theoretical Approach to Ultrafast Exciton Dynamics in Photoexcited Semiconductors

In this chapter, we describe the theoretical formalism that we employ to investigate the dynamics of semiconductors and their heterojunctions excited by a pulsed laser excitation. We focus our attention on the time evolution of semiconductor state on ultrafast (femtosecond to picosecond) time scales following the photoexcitation. These time scales may be of particular relevance for the operation of OSCs, as has been extensively reviewed in Ch. 1. A detailed understanding of the ultrafast exciton dynamics provides us with insights into the fundamental physical processes taking place on these time scales. Moreover, it enables us to decide whether or not the secret of the efficiency of OSCs is hidden in the very initial stages of the light-to-charge conversion process.

Section 3.1 provides a quite general view of the semiconductor dynamics triggered by a photoexcitation. The basics of the density matrix theory and the hierarchy problem are introduced in Sec. 3.2, while Sec. 3.3 introduces some of the existing strategies to truncate the aforementioned hierarchy. In Sec. 3.4, we lay out the theoretical foundations of the dynamics controlled truncation scheme in its most general form. Our focus in Sec. 3.5 moves to the particular case of the truncation up to the second order in the exciting field. In that section, we perform our specific truncation of the phonon branch of the hierarchy, which was published in Ref. [89], by conducting a comprehensive discussion on the energy and particle-number conservation after a pulsed excitation of a semiconductor.

3.1 General Picture of the Dynamics of Photoexcited Semiconductors

A pulsed photoexcitation of a semiconductor leaves it in a highly nonequilibrium state. In general, such an excitation induces both interband coherences (also known as interband polarizations, optical polarizations, exciton amplitudes)

$$Y_{ab} = \langle d_a c_b \rangle, \tag{3.1}$$

and intraband excitations, i.e., electron (C_{ab}) and hole (D_{ab}) populations ($a = b$) and intraband polarizations ($a \neq b$)

$$C_{ab} = \langle c_a^\dagger c_b \rangle, \quad D_{ab} = \langle d_a^\dagger d_b \rangle. \tag{3.2}$$

The subsequent time evolution of the semiconductor state is governed by the complex interplay between phase coherence, many-body correlations, and energy relaxation. Many-body correlations are primarily induced by the Coulomb interaction, which correlates electrons and holes and thereby produces a new type of stable quasiparticles, excitons. On the other hand, the carrier–phonon scattering processes destroy the coherence and lead to the dephasing of interband and intraband polarizations. Moreover, they promote the relaxation of carrier populations towards the values predicted by the equilibrium distribution. The time scale on which interband coherences dephase is governed by the energy gap E_g, which in typical semiconductors is of the order of 1 eV or larger. The dephasing of the interband coherences thus typically occurs on a femtosecond time scale. Depending on the particular value of the phonon energy, the time scale typical of phonon-assisted transitions, which lead to the dephasing of intraband polarizations, ranges from hundreds of femtoseconds to picoseconds. The resulting semiconductor dynamics, taking place on femtosecond to picosecond time scales following the excitation, is generally referred to as ultrafast dynamics. Theoretical approaches for treating ultrafast semiconductor dynamics are most often based on the density matrix theory [72, 73, 90, 91] or the nonequilibrium Green's functions formalism [92–97]. The density matrix theory has become the preferred technique in the treatment of experiments with ultrashort pulses, since it deals with quantities that depend on one time argument and are directly related to observables, thus providing an intuitive picture (in the language of elementary interaction processes) of the nonequilibrium dynamics in such setups. In the following, we restrict ourselves to the density matrix theory and, in particular, its applications on the very initial stages of exciton formation and relaxation dynamics.

3.2 Density Matrix Theory

The central quantities in the density matrix theory are expectation values of (normal ordered) products of creation and annihilation operators describing electronic excitations, quanta of lattice vibrations, quanta of electromagnetic field, etc. These quantities are referred to as density matrices. Quantities $Y_{ab},\ C_{ab},$ and D_{ab} defined in Eqs. (3.1) and (3.2) are the simplest examples of purely electronic density matrices and they are the so-called single-particle (two-point) density matrices.[1] In this thesis, we will also deal with the so-called phonon-assisted density matrices, which, apart from electron and hole operators, contain arbitrary numbers of phonon creation and annihilation operators.

The dynamics is then studied by establishing the equations of motion for density matrices. This is done by setting up the Heisenberg equations for the corresponding operators O, which is followed by taking the expectation values of the obtained operator-valued equations,

$$\mathrm{i}\hbar\,\partial_t\langle O\rangle = \langle[O,H]\rangle. \tag{3.3}$$

The expectation value should be taken in the Heisenberg picture and is defined with respect to the time-independent statistical operator, i.e., the statistical operator at the initial instant. Equivalently, one may evaluate the expectation values in the Schrödinger picture, in which operators are time-independent, while the averaging is performed with respect to the time-dependent statistical operator. The dynamics governed by the standard semiconductor Hamiltonian introduced in

---

[1] Let us note here that the purely electronic density matrix defined as the expectation value of the normal ordered product of N creation ($a_p^\dagger$) and N annihilation (a_p) operators in the particle picture is denoted as $2N$-point or N-particle density matrix.

Ch. 2 exhibits genuine many-body effects, which are induced by the carrier–carrier and carrier–phonon interactions. Therefore, the described procedure of establishing the equations of motion for density matrices does not result in a closed set of equations, but rather involves density matrices containing an ever-larger number of operators. We are thus confronted by an infinite hierarchy of equations for density matrices, the levels of the hierarchy being defined by the number of operators that participate in density matrices. The main feature of this hierarchy is the coupling of the density matrices at any given level to the density matrices at higher levels. Such a hierarchy is the quantum-mechanical analogue of the Bogoliubov–Born–Green–Kirkwood–Yvon (BBGKY) hierarchy encountered in the classical statistical physics of interacting particles [98]. Let us here formulate the equations of motion for single-particle electronic density matrices Y_{ab} and C_{ab} defined in Eqs. (3.1) and (3.2). Using the prescription given in Eq. (3.3), we obtain

$$\begin{aligned}
\mathrm{i}\hbar\,\partial_t Y_{ab} = {} & (\epsilon^{\mathrm{c}}_b - \epsilon^{\mathrm{v}}_a)\,Y_{ab} + \sum_{\substack{p\in\mathrm{VB}\\ q\in\mathrm{CB}}} \left(V^{\mathrm{vccv}}_{pqba} - V^{\mathrm{vvcc}}_{pabq}\right) Y_{pq} \\
& + \sum_{pqk\in\mathrm{CB}} V^{\mathrm{cccc}}_{bqkp}\langle c^\dagger_k c_p d_a c_q\rangle - \sum_{\substack{pq\in\mathrm{CB}\\ k\in\mathrm{VB}}} \left(V^{\mathrm{vvcc}}_{kapq} - V^{\mathrm{vccv}}_{kqpa}\right)\langle c^\dagger_p c_q d_k c_b\rangle \\
& + \sum_{pqk\in\mathrm{VB}} V^{\mathrm{vvvv}}_{kpqa}\langle d^\dagger_p d_k d_q c_b\rangle - \sum_{\substack{pq\in\mathrm{VB}\\ k\in\mathrm{CB}}} \left(V^{\mathrm{vvcc}}_{pqbk} - V^{\mathrm{vccv}}_{pkbq}\right)\langle d^\dagger_q d_p d_a c_k\rangle \\
& - \mathbf{E}(t)\left(\mathbf{M}^{\mathrm{cv}}_{ba} - \sum_{k\in\mathrm{VB}} \mathbf{M}^{\mathrm{cv}}_{bk} D_{ka} - \sum_{k\in\mathrm{CB}} \mathbf{M}^{\mathrm{cv}}_{ka} C_{kb}\right) + \mathrm{i}\hbar\left(\partial_t Y_{ab}\right)_{\mathrm{p}}\,,
\end{aligned} \tag{3.4}$$

$$\begin{aligned}
\mathrm{i}\hbar\,\partial_t C_{ab} = {} & (\epsilon^{\mathrm{c}}_b - \epsilon^{\mathrm{c}}_a)\,C_{ab} \\
& + \sum_{\substack{pq\in\mathrm{VB}\\ k\in\mathrm{CB}}} \left(V^{\mathrm{vccv}}_{pkbq} - V^{\mathrm{vvcc}}_{pqbk}\right)\langle c^\dagger_a d^\dagger_q d_p c_k\rangle - \sum_{\substack{pq\in\mathrm{VB}\\ k\in\mathrm{CB}}} \left(V^{\mathrm{vccv}}_{pakq} - V^{\mathrm{vvcc}}_{pqka}\right)\langle c^\dagger_k d^\dagger_q d_p c_b\rangle \\
& + \sum_{pqk\in\mathrm{CB}} \left(V^{\mathrm{cccc}}_{bpqk}\langle c^\dagger_a c^\dagger_q c_k c_p\rangle - V^{\mathrm{cccc}}_{pqka}\langle c^\dagger_p c^\dagger_k c_q c_b\rangle\right) \\
& - \mathbf{E}(t)\sum_{k\in\mathrm{VB}} \left(\mathbf{M}^{\mathrm{cv}}_{bk} Y^*_{ka} - \mathbf{M}^{\mathrm{vc}}_{ka} Y_{kb}\right) + \mathrm{i}\hbar\left(\partial_t C_{ab}\right)_{\mathrm{p}}\,.
\end{aligned} \tag{3.5}$$

The equation for hole densities and intraband coherences D_{ab} is formally similar to Eq. (3.5). We concentrate on presenting the coupling to higher-order purely electronic density matrices, and consequently absorb all density matrices with single-phonon assistance (which stem from commutators with the carrier–phonon interaction) in terms $\mathrm{i}\hbar\left(\partial_t Y_{ab}\right)_{\mathrm{p}}$ and $\mathrm{i}\hbar\left(\partial_t C_{ab}\right)_{\mathrm{p}}$. Apart from the couplings of Y_{ab}, C_{ab}, and D_{ab} among themselves, Eqs. (3.4) and (3.5) contain four-particle (two-point quantities) of the type $\langle c^\dagger cdc\rangle$, $\langle d^\dagger ddc\rangle$, $\langle c^\dagger d^\dagger dc\rangle$, $\langle c^\dagger c^\dagger cc\rangle$, and $\langle d^\dagger d^\dagger dd\rangle$, which are known as the electron-screened interband transition amplitude, hole-screened interband transition amplitude, exciton occupation and exciton–exciton coherence, electron density–correlation, and hole density–correlation, respectively.

In order to obtain a problem amenable to at least an approximate solution, one has to find a reasonable and physically grounded way to truncate the hierarchy at a finite level. The truncation should address both purely electronic branch of the hierarchy and the branch containing phonon assistance. There are various truncation strategies based on different physical arguments and some of them will be discussed in the following text.

3.3 Brief Review of Theoretical Approaches to Ultrafast Exciton Dynamics

Previous theoretical studies of the exciton formation after an ultrafast optical excitation of a semiconductor were typically focused on inorganic semiconductors. Early studies were conducted in the framework of the semiclassical Boltzmann approach. The state of the system is entirely described in terms of the populations (distribution functions) of carriers and other quasiparticles, e.g., phonons and excitons. The initial nonequilibrium electron and hole distributions, generated by means of an above-gap pulsed photoexcitation, relax by various interaction mechanisms, e.g., carrier–phonon interaction, the carriers being scattered to lower-energy bound exciton states. The scattering events are point-like in space and time. In this approach, electrons, holes and excitons are treated as different particle species and a set of coupled semiclassical Boltzmann equations for the k-space occupations of these species is established [99, 100].

The most complete formalism capable of treating a wide variety of optical and excitonic effects after an ultrafast optical excitation of a semiconductor is presented in Refs. [101, 102], where the fully microscopic and quantum theory for the interacting system of electrons, holes, photons, and phonons was elaborated. This approach is based on the density matrix theory and the resulting hierarchy of equations was systematically truncated using the so-called cluster-expansion scheme, in which one determines all consistent factorizations of an N-particle quantity in terms of independent single particles (singlets), correlated two-particle clusters (doublets), three-particle clusters (triplets), up to correlated N-particle clusters. The physical picture of the truncation is then based on the fact that correlations that involve an increasing number of particles should become less and less important. For example, such factorizations of purely electronic two-particle quantities appearing in Eqs. (3.4) and (3.5) read as

$$\langle c_p^\dagger c_q d_k c_l\rangle = C_{pq}Y_{kl} - C_{pl}Y_{kq} + \delta\langle c_p^\dagger c_q d_k c_l\rangle, \tag{3.6}$$

$$\langle d_p^\dagger d_q d_k c_l\rangle = D_{pq}Y_{kl} - D_{pk}Y_{ql} + \delta\langle d_p^\dagger d_q d_k c_l\rangle, \tag{3.7}$$

$$\langle c_p^\dagger d_q^\dagger d_k c_l\rangle = Y_{qp}^{*}Y_{kl} + C_{pl}D_{qk} + \delta\langle c_p^\dagger d_q^\dagger d_k c_l\rangle, \tag{3.8}$$

$$\langle c_p^\dagger c_q^\dagger c_k c_l\rangle = C_{pl}C_{qk} - C_{pk}C_{ql} + \delta\langle c_p^\dagger c_q^\dagger c_k c_l\rangle, \tag{3.9}$$

where $\delta\langle\dots\rangle$ denotes correlated (in this case, two-particle) clusters. Neglecting these two-particle correlations in Eqs. (3.4) and (3.5) closes the electronic branch of the hierarchy at the singlet level and the equations thus obtained are the semiconductor Bloch equations (SBEs) [103]. The SBEs can correctly describe the linear response of a semiconductor. In particular, solving the SBEs in the linear regime, in which carrier densities vanish, while the interband polarizations are linear in the applied field, we can recover the Elliott formula [104] that expresses the linear semiconductor absorption as a function of strongly peaked resonances at bound exciton states. However, in order to describe the exciton formation and the subsequent dynamics of thus created exciton populations, the singlet level of the theory is not appropriate and one has to retain in the formalism the two-particle correlations. Namely, the two-particle correlation $\delta\langle c_p^\dagger d_q^\dagger d_k c_l\rangle$ can describe the Coulomb correlation that binds together an electron and a hole into an exciton. The theoretical development presented in [101] retains all correlations up to four-point level (correlated doublets). In equations of motion for correlated doublets, three-particle quantities appear; the purely electronic branch of the hierarchy is truncated by performing factorizations of the three-particle quantities into all possible combinations of singlets and (correlated) doublets, i.e., by neglecting genuine three-particle correlations. A similar approach is applied to truncate the phonon-assisted branch of the hierarchy. This formalism was also used to study exciton formation from an initial incoherent charge distribution [105–107].

Apart from the cluster-expansion-based truncation scheme, the exciton dynamics in photoexcited inorganic semiconductors has also been studied by employing the DCT scheme [71, 108–112]. The DCT scheme is particularly suitable to describe exciton dynamics in systems that are initially unexcited (prior to the action of an external electromagnetic field, the carrier subsystem is described by the vacuum of electron–hole pairs). A crucial prerequisite to successfully apply the DCT scheme is that the only part of the system's Hamiltonian that can change the number of electron–hole pairs is the interaction with the external electromagnetic field. In other words, electrons and holes always occur in pairs. The standard semiconductor Hamiltonian presented in Ch. 2 meets this requirement. The nontrivial dynamics of all density matrices is, therefore, ultimately induced by the system's coupling to the external field, so that there is an intimate connection between the expansion of the system's state in powers of the optical field and the expansion of the system's state into states with definite numbers of electrons and holes. Translated into the language of the density matrix theory, the last statement implies a close relation between the leading order with which each density matrix scales with the external optical field and the level at which it appears for the first time in the hierarchy. One can, therefore, classify the (nonlinear) response of a semiconductor to an optical excitation according to an expansion in powers of the applied field. The truncation of the hierarchy then consists of selecting a set of dynamic variables that contribute to the response up to any given order in the applied field. This approach is reminiscent of the introduction of nonlinear susceptibilities when analyzing the nonlinear optical response in atomic systems and is discussed in greater detail in the following text.

3.4 Fundamentals of the DCT Scheme

The DCT scheme was initially developed to describe the nonlinear optical response of semiconductors. Prior to the action of the external electromagnetic field, the semiconductor is unexcited, i.e., the state of its electronic subsystem is the vacuum of electron–hole pairs. Let us for the moment ignore the phonon bath, which is responsible for dephasing and relaxation, and concentrate on the so-called coherent electronic dynamics, i.e., the dynamics of the purely electronic system. Early developments of the DCT scheme were motivated by the invention of femtosecond laser systems in the last quarter of the 20th century [113]. This breakthrough enables experimentalists to investigate the very initial stages of optical experiments performed by irradiating a semiconductor with an ultrashort laser pulse. The typical signal obtained in such an experiment on femtosecond time scales following the excitation is dominated by coherent features, since the incoherent parts of the signal have not yet built up (see also the discussion in Sec. 3.5.4).

The initial state of the semiconductor is the zero-particle state (in the electron–hole picture), while its subsequent time evolution triggered by the external optical field generates a state of genuine many-body character. If the optical excitation is weak, a systematic classification of many-body effects may be achieved by performing an expansion of density matrices in powers of the exciting field. The many-body correlations may be consistently described by a finite set of density matrices with an error that is of desired order in the optical field. Such an approach was first presented in 1994 by Axt and Stahl [108, 109] and Lindberg et al. [112]. These works focused on the truncation up to the third order in the exciting field with the aim of describing the experimental results that could not be explained on the level of SBEs, but their understanding required an explicit inclusion of biexciton resonances [109] or biexciton continuum [112]. Later on, it was demonstrated that the coherent semiconductor optics may be formulated with accuracy up to any given order in the exciting field by following the time evolution of a finite set of density matrices [110]. Following Ref. [110], we now formulate the basic theorems of the DCT scheme that are applicable to the phonon-free case.

The relevant Hamiltonian is the purely electronic part of the standard semiconductor Hamiltonian given in Eq. (2.34)

$$H_{\mathrm{coh}} = H_{\mathrm{c}} + H_{\mathrm{c-f}}, \tag{3.10}$$

where the Hamiltonian describing interacting carriers H_{c} is given in Eq. (2.35), while the interaction of carriers with an exciting electromagnetic field is governed by the Hamiltonian in Eq. (2.38).

If $|\psi(0)\rangle = |0\rangle$ is the initial state (at $t = 0$) of the semiconductor, the time-dependent perturbation theory (see, e.g., Ref. [114]) gives that the Schrödinger state $|\psi(t)\rangle$ at time t can be expanded in powers n of the optical field E as follows:

$$|\psi(t)\rangle = \sum_{n=0}^{+\infty} |\psi(t)\rangle^{(n)}, \tag{3.11}$$

$$|\psi(t)\rangle^{(0)} = \mathrm{e}^{-\mathrm{i}H_{\mathrm{c}}t/\hbar}|0\rangle, \tag{3.12}$$

$$|\psi(t)\rangle^{(n)} = \frac{1}{\mathrm{i}\hbar}\int_0^t \mathrm{d}t'\, \mathrm{e}^{-\mathrm{i}H_{\mathrm{c}}(t-t')/\hbar} H_{\mathrm{c-f}}(t')|\psi(t')\rangle^{(n-1)}. \tag{3.13}$$

The state $|\psi(t)\rangle^{(n)}$, which scales as E^n in the optical field, may be expanded in the basis of states $\{|n_e, n_h, n, t\rangle\}$ having a fixed number of electrons (n_e) and holes (n_h),

$$|\psi(t)\rangle^{(n)} = \sum_{n_e=0}^{+\infty}\sum_{n_h=0}^{+\infty} |n_e, n_h, n, t\rangle, \tag{3.14}$$

with $\hat{N}_{e/h}|n_e, n_h, n, t\rangle = n_{e/h}|n_e, n_h, n, t\rangle$, where the electron ($\hat{N}_e$) and hole ($\hat{N}_h$) number operators are defined as

$$\hat{N}_e = \sum_{p\in\mathrm{CB}} c_p^\dagger c_p \tag{3.15a}$$

$$\hat{N}_h = \sum_{p\in\mathrm{VB}} d_p^\dagger d_p. \tag{3.15b}$$

The states $|n_e, n_h, n, t\rangle$ are not normalized, but rather scale as E^n in the optical field. Since electrons and holes are generated in pairs, and since state $|\psi(t)\rangle^{(n)}$, being proportional to E^n, may accommodate at most n electron–hole pairs, the above expansion involves only a finite number of terms, each of which contains an equal number of electrons and holes. This is summarized in the following

Expansion Theorem: Each of the contributions $|\psi(t)\rangle^{(n)}$ to the Schrödinger state of the semiconductor at time t may be expressed solely in terms of states with definite total numbers of electrons and holes in which the total number of electrons is equal to the total number of holes, $n_e = n_h = n_p$, and is smaller than or equal to n, $n_p \leq n$. Moreover, the difference $n - n_p$ is even, so that

$$|\psi(t)\rangle^{(n)} = \sum_{n_p=n,n-2,\ldots,\geq 0} |n_p, n_p, n, t\rangle. \tag{3.16}$$

The formal proof of the expansion theorem is deferred for Appendix A.1. The physical meaning of the expansion theorem is that the many-body effects in coherent dynamics of optically excited semiconductors can be classified by employing an expansion in powers of E. The many-body effects that are relevant up to the nth order in the exciting field are captured by accounting for the states containing at most n pairs.

Let us now discuss on intuitive level the other aspect of the expansion theorem, namely the fact that the difference $n - n_p$ is even. The generation of any state accommodating n_p pairs may be imagined as the n_p-fold application of the optical field that is further followed by $k \geq 0$ creation and k annihilation processes. Only one and the same particle type (either electrons or holes) may participate in these additional k processes, *vide infra*. Since the creation (and also annihilation) of a single carrier requires a single application of the electric field, we conclude that the above-described generation of an n_p-pair state is a process of order n_p+2k in the exciting field. If this process is to result in a contribution of order n in the exciting field, the difference $n - n_p = 2k$ has to be even.

The discussion in the preceding paragraph puts forward another important point. Namely, since Hamiltonian H_{coh} conserves the total number of particles (in the particle picture), only the density matrices whose underlying operators commute with the total number of particles can acquire nontrivial values in the course of the system's evolution. The most general density matrix obeying this condition is of the form

$$\langle \underbrace{c^\dagger \dots c^\dagger}_{n_u} \underbrace{c^\dagger d^\dagger \dots c^\dagger d^\dagger}_{n_p^+ \text{ pairs}} \underbrace{dc \dots dc}_{n_p^- \text{ pairs}} \underbrace{c \dots c}_{n_u} \rangle, \tag{3.17}$$

or

$$\langle \underbrace{d^\dagger \dots d^\dagger}_{n_u} \underbrace{c^\dagger d^\dagger \dots c^\dagger d^\dagger}_{n_p^+ \text{ pairs}} \underbrace{dc \dots dc}_{n_p^- \text{ pairs}} \underbrace{d \dots d}_{n_u} \rangle. \tag{3.18}$$

n_p^+ pairs are created, n_p^- pairs are annihilated, and additionally there are $2n_u$ unpaired electron or hole operators. The number of effectively annihilated pairs $n_g = n_p^- - n_p^+$ determines the energies at which many-particle resonances corresponding to these density matrices should be observed; these energies are of the order of $n_g E_g$, where E_g is the single-particle band gap. On the other hand, the density matrix in Eq. (3.17) contains in total $n_c = n_p^+ + n_p^- + 2n_u$ electron creation and annihilation operators $c^\dagger$ and c, while the total number of hole operators $d^\dagger, d$ is $n_d = n_p^+ + n_p^-$. The density matrix in Eq. (3.18) comprises $n_c = n_p^+ + n_p^-$ electron operators $c^\dagger, c$ and $n_d = n_p^+ + n_p^- + 2n_u$ hole operators $d^\dagger, d$.

Given a normally ordered n-particle operator, we know that its expectation value in a state containing less than n particles is identically equal to zero. According to the expansion theorem, the number of particles in the states relevant for the description of the system is connected to the order to which the interaction with the optical field is taken into account. As a consequence, the expectation values of operators involving a large number of creation and annihilation operators are nontrivial only in high enough orders in the optical field. Therefore, to a given order in the optical field, only a finite subset of all possible density matrices of the form given in Eqs. (3.17) and (3.18) exhibit nontrivial evolution. This is the essential content of the following

Truncation Theorem: Let A denote the normal-ordered product of electron and hole operators $c,\ c^\dagger,\ d,\ d^\dagger$ an let it be of the form given in Eq. (3.17) or Eq. (3.18). The operator A comprises n_c electron operators $c^\dagger, c$ and n_d hole operators $d^\dagger, d$. If the initial state of the system is the vacuum of electron–hole pairs, then the expectation value of operator A is at least of order $m = \max\{n_c, n_d\}$ in the optical field. Furthermore, the expansion of $\langle A \rangle$ in powers of the optical field contains either only even or only odd terms:

$$\langle A\rangle = \mathcal{O}(E^m), \quad m = \max\{n_c, n_d\}, \tag{3.19}$$

$$\langle A\rangle = \sum_{l=0}^{+\infty} \langle A\rangle^{(m+2l)}, \quad \text{where } \langle A\rangle^{(k)} \propto E^k. \tag{3.20}$$

The proof of the truncation theorem is given in Appendix A.2. The set of density matrices needed to describe the optical response up to the nth order in the applied field is limited to those containing at most n electron and n hole operators. The truncation theorem provides us with the following prescription to truncate the electronic branch of the hierarchy up to a certain order in the optical field:

(a) formulate the Heisenberg equations of motion [Eq. (3.3)] for density matrices whose leading order in the applied field is less than or equal to the given order;

(b) in the equations thus obtained, neglect all source terms whose leading order in the optical field is greater than the given order.

The physical origin of the relation between the leading order in the expansion of a density matrix in the optical field and the number of fermion operators comprising the density matrix is the fact that all excitations above the ground state are generated by the optical field. This property, however, is not influenced by the coupling to phonons. Therefore, all the results derived from this feature of the system, and in particular the expansion and truncation theorems, can be readily generalized to the case when the carrier–phonon coupling is active, i.e., the Hamiltonian of the system is given by Eqs. (2.34)–(2.38). This has been done in Ref. [111].

In the presence of the carrier–phonon coupling, we assume that, at $t = 0$, the state of the system is described by the statistical operator

$$\rho(0) = |0\rangle\langle 0|\rho_{\mathrm{p}}. \tag{3.21}$$

Prior to the excitation, the state of the electronic subsystem is the vacuum $|0\rangle$ of electron–hole pairs, while the phonon subsystem is described by the statistical operator

$$\rho_{\mathrm{p}} = \frac{\mathrm{e}^{-\beta H_{\mathrm{p}}}}{\mathrm{Tr}\ \mathrm{e}^{-\beta H_{\mathrm{p}}}}. \tag{3.22}$$

In Eq. (3.22), we assume that the phonon subsystem, described by Hamiltonian H_{p} in Eq. (2.36), is in thermal equilibrium at temperature $T = (k_B \beta)^{-1}$, where k_B is the Boltzmann constant. The system is, at any instant t, described by statistical operator $\rho(t)$, whose time evolution is governed by the Liouville–von Neumann equation. Similarly to the case of the purely electronic system, statistical operator $\rho(t)$ can be expanded in powers of the optical field

$$\rho(t) = \sum_{n=0}^{+\infty} \rho^{(n)}(t), \text{ where } \rho^{(n)} \propto E^n. \tag{3.23}$$

The generalization of the expansion theorem [111] states that the nth order contribution $\rho^{(n)}(t)$, when expressed in terms of number states $|n_e, n_h, n, t\rangle$, contains only states with equal numbers of electrons and holes in which the total number of particles is smaller than or equal to n. The most general density matrix exhibiting nontrivial dynamics is of the form similar to the one given in Eqs. (3.17) and (3.18) and may comprise a number of phonon creation and annihilation operators $b^\dagger$ and b:

$$\langle \underbrace{c^\dagger \dots c^\dagger}_{n_u} \underbrace{c^\dagger d^\dagger \dots c^\dagger d^\dagger}_{n_p^+ \text{ pairs}} \underbrace{dc \dots dc}_{n_p^- \text{ pairs}} \underbrace{c \dots c}_{n_u} \underbrace{b^\dagger \dots b^\dagger}_{n_{\mathrm{ph}}^+} \underbrace{b \dots b}_{n_{\mathrm{ph}}^-} \rangle, \tag{3.24}$$

or

$$\langle \underbrace{d^\dagger \dots d^\dagger}_{n_u} \underbrace{c^\dagger d^\dagger \dots c^\dagger d^\dagger}_{n_p^+ \text{ pairs}} \underbrace{dc \dots dc}_{n_p^- \text{ pairs}} \underbrace{d \dots d}_{n_u} \underbrace{b^\dagger \dots b^\dagger}_{n_{\mathrm{ph}}^+} \underbrace{b \dots b}_{n_{\mathrm{ph}}^-} \rangle. \tag{3.25}$$

As a consequence of the expansion theorem, one can prove the following

Central Theorem of the DCT Scheme: Let A denote the normal-ordered product of electron, hole, and phonon operators of the form given in Eqs. (3.24) and (3.25) that contains n_e electron operators $c^\dagger$, c, n_h hole operators $d^\dagger$, d, and an arbitrary number of phonon operators $b^\dagger$, b. If the initial state of the system is given in Eqs. (3.21) and (3.22), then the expectation value $\langle A\rangle$ is at least of order $m = \max\{n_e, n_h\}$ in the optical field, i.e.,

$$\langle A\rangle = \mathcal{O}(E^m), \quad m = \max\{n_e, n_h\}. \tag{3.26}$$

Furthermore, the expansion of $\langle A\rangle$ in powers of the optical field contains either only even or only odd terms:

$$\langle A\rangle = \sum_{l=0}^{+\infty} \langle A\rangle^{(m+2l)}, \text{ where } A^{(k)} \propto E^k. \tag{3.27}$$

This theorem is proved in Ref. [111] and, analogously to the truncation theorem in the phonon-free case, enables the systematic truncation of the electronic branch of the density-matrix hierarchy up to any given order in the optical field. However, the density matrices containing different numbers of phonon creation and annihilation operators are dynamically coupled to one another. Therefore, having truncated the carrier branch of the hierarchy, we still face an infinite phonon branch of the hierarchy due to the many-body nature of the carrier–phonon coupling. Approaches to truncate the phonon branch of the hierarchy are numerous and the DCT scheme, employed to truncate the carrier branch of the hierarchy, can in principle be combined with any of these approaches. It is, however, crucial that the DCT scheme and the strategy to deal with the phonon-assisted density matrices be compatible with the particle-number and energy conservation when the exciting field vanishes. In the following, we will pay special attention to meet these two requirements.

3.5 The DCT Scheme up to the Second Order in Applied Field

Let us now demonstrate how the DCT scheme introduced in the previous chapter can be employed to describe exciton formation and initial stages of exciton dynamics in photoexcited semiconductors. We limit ourselves to the case of weak optical field and low carrier densities, in which it is justified to neglect biexciton effects and keep only contributions up to the second order in the optical field. It is in principle clear that the second order is the lowest order in the optical field in which a meaningful description of excitons can be performed. The definition of the exciton creation operator $X_x^\dagger$ [Eq. (2.49)] reveals that the exciton population is expressed as the expectation value of the type $\langle c^\dagger d^\dagger dc\rangle$. This expectation value is, according to the central theorem of the DCT scheme, of the second order in the exciting field. The DCT scheme up to the second order in the optical field was successfully applied to study the dynamics of exciton formation in inorganic semiconductors for near-band-gap excitations and low excitation densities [115–117]. Here, we will adopt the same strategy to truncate the carrier branch of the hierarchy, while the phonon branch of the hierarchy will be truncated so as to explicitly satisfy the particle-number and energy conservation laws in the absence of the exciting field.

According to the central theorem of the DCT scheme, there are five types of purely electronic density matrices that should be considered when studying the system's response up to the second order in the optical field. These are exciton amplitudes Y_{ab} defined in Eq. (3.1), electron and hole populations and intraband polarizations C_{ab} and D_{ab} defined in Eq. (3.2), exciton populations

$$N_{abcd} = \langle c_a^\dagger d_b^\dagger d_c c_d\rangle, \tag{3.28}$$

and biexciton amplitudes

$$B_{abcd} = \langle d_a c_b d_c c_d\rangle. \tag{3.29}$$

Apart from these purely electronic contributions, we also have to consider (in principle all) their phonon-assisted counterparts. In order to facilitate further discussion, let us introduce the following generation functions for phonon-assisted density matrices

$$Y_{ab}^{\alpha\beta} = \left\langle d_a c_b \hat{F}^{\alpha\beta}\right\rangle, \tag{3.30}$$

$$N_{abcd}^{\alpha\beta} = \left\langle c_a^\dagger d_b^\dagger d_c c_d \hat{F}^{\alpha\beta}\right\rangle, \tag{3.31}$$

$$C_{ab}^{\alpha\beta} = \left\langle c_a^\dagger c_b \hat{F}^{\alpha\beta}\right\rangle, \tag{3.32}$$

$$D_{ab}^{\alpha\beta} = \left\langle d_a^\dagger d_b \hat{F}^{\alpha\beta}\right\rangle, \tag{3.33}$$

$$B_{abcd}^{\alpha\beta} = \left\langle d_a c_b d_c c_d \hat{F}^{\alpha\beta}\right\rangle, \tag{3.34}$$

$$F^{\alpha\beta} = \left\langle \hat{F}^{\alpha\beta} \right\rangle = \left\langle \exp\left(\sum_{\mu} \alpha_\mu b_\mu^\dagger\right) \exp\left(\sum_{\mu} \beta_\mu b_\mu\right) \right\rangle, \tag{3.35}$$

where $\{\alpha_\mu\}$ and $\{\beta_\mu\}$ are two sets of arbitrary real parameters. The condensed notation $\alpha\beta$ in the arguments of these functions is meant to denote these two sets of parameters. By virtue of the generating-function property, any phonon-assisted density matrix can be obtained by differentiating these functions with respect to the indices of interest and then taking $\alpha_\mu = \beta_\mu = 0$, e.g.,

$$\left\langle d_a c_b b^\dagger_{\rho_1} \dots b^\dagger_{\rho_{n^+_{\text{ph}}}} b_{\sigma_1} \dots b_{\sigma_{n^-_{\text{ph}}}} \right\rangle = \left(\frac{\partial^k}{\partial\alpha_{\rho_1} \dots \partial\alpha_{\rho_{n^+_{\text{ph}}}}} \frac{\partial^l}{\partial\beta_{\sigma_1} \dots \partial\beta_{\sigma_{n^-_{\text{ph}}}}} Y^{\alpha\beta}_{ab} \right)_{\alpha=\beta=0}. \tag{3.36}$$

While exciton amplitudes scale as E, all quantities C_{ab}, D_{ab}, N_{abcd}, and B_{abcd} scale as E^2 in the exciting field E. The number of relevant types of density matrices may further be reduced by noting that biexciton amplitudes B_{abcd}, despite being of the second order in the exciting field, do not participate as source terms in equations of motion (that contain only contributions up to the second order in the field) for Y_{ab} [see Eq. (3.4)], C_{ab} [see Eq. (3.5)], D_{ab}, and N_{abcd} (more details can be found in Refs. [71, 108]). Therefore, quantities B_{abcd} do not have to be regarded as independent variables in the formalism up to the second order in the optical field.

Another way to avoid explicit consideration of some density matrices that at first sight seem relevant is to employ the so-called contraction theorem that is formulated in Refs. [110, 111]. The contraction theorem states that density matrices with a nonvanishing number of unpaired particles ($n_u \neq 0$) can be entirely expressed in terms of density matrices containing only pair creation ($c^\dagger d^\dagger$) and annihilation (dc) operators. Up to the second order in the optical field, the contraction theorem suggests that variables C_{ab} and D_{ab} be eliminated from the formalism in favor of Y_{ab} and N_{abcd}. Using different arguments, which rely on the constancy of the total number of particles, in Appendix B we prove that the following identities hold:

$$C^{\alpha\beta}_{ab} = \sum_{k\in\text{VB}} N^{\alpha\beta}_{akkb} + \mathcal{O}(E^4), \tag{3.37}$$

$$D_{ab}^{\alpha\beta} = \sum_{k\in\mathrm{CB}} N_{kabk}^{\alpha\beta} + \mathcal{O}(E^4). \tag{3.38}$$

These identities permit us to avoid explicit consideration of $C_{ab}^{\alpha\beta}$ and $D_{ab}^{\alpha\beta}$ in the formalism up to the second order in the optical field. Further discussion will justify the elimination of C_{ab} and D_{ab} in favor of N_{abcd} from another viewpoint. Finally, we remain with only two types of density matrices that should be considered, namely $Y_{ab}^{\alpha\beta}$ and $N_{abcd}^{\alpha\beta}$.

The differential equations for variables $Y_{ab}^{\alpha\beta}$ and $N_{abcd}^{\alpha\beta}$, in which we keep only contributions that are at most of the second order in the optical field, read as

$$\begin{aligned}
\mathrm{i}\hbar\,\partial_t Y_{ab}^{\alpha\beta} = {} & (\epsilon_b^{\mathrm{c}} - \epsilon_a^{\mathrm{v}})Y_{ab}^{\alpha\beta} + \sum_{\substack{p\in\mathrm{VB}\\ q\in\mathrm{CB}}} \left(V_{pqba}^{\mathrm{vccv}} - V_{pabq}^{\mathrm{vvcc}}\right) Y_{pq}^{\alpha\beta} + \sum_{\mu} \hbar\omega_\mu \left(\beta_\mu \partial_{\beta_\mu} - \alpha_\mu \partial_{\alpha_\mu}\right) Y_{ab}^{\alpha\beta} \\
& + \sum_{\substack{k\in\mathrm{CB}\\ \mu}} \left(\gamma_{bk}^{\mu}(\partial_{\alpha_\mu} + \beta_\mu) + \gamma_{kb}^{\mu*}\partial_{\beta_\mu}\right) Y_{ak}^{\alpha\beta} - \sum_{\substack{k\in\mathrm{VB}\\ \mu}} \left(\gamma_{ka}^{\mu}(\partial_{\alpha_\mu} + \beta_\mu) + \gamma_{ak}^{\mu*}\partial_{\beta_\mu}\right) Y_{kb}^{\alpha\beta} \\
& - \mathbf{E}(t)\mathbf{M}_{ba}^{\mathrm{cv}} F^{\alpha\beta},
\end{aligned} \tag{3.39}$$

$$\begin{aligned}
\mathrm{i}\hbar\,\partial_t N_{abcd}^{\alpha\beta} = {} & (\epsilon_d^{\mathrm{c}} - \epsilon_c^{\mathrm{v}} + \epsilon_b^{\mathrm{v}} - \epsilon_a^{\mathrm{c}})N_{abcd}^{\alpha\beta} \\
& + \sum_{\substack{p\in\mathrm{VB}\\ q\in\mathrm{CB}}} \left(\left(V_{pqdc}^{\mathrm{vccv}} - V_{pcdq}^{\mathrm{vvcc}}\right) N_{abpq}^{\alpha\beta} - \left(V_{baqp}^{\mathrm{vccv}} - V_{bpqa}^{\mathrm{vvcc}}\right) N_{qpcd}^{\alpha\beta} \right) \\
& + \sum_{\mu} \hbar\omega_\mu \left(\beta_\mu \partial_{\beta_\mu} - \alpha_\mu \partial_{\alpha_\mu}\right) N_{abcd}^{\alpha\beta} \\
& + \sum_{\substack{k\in\mathrm{CB}\\ \mu}} \left(\left(\gamma_{dk}^{\mu}(\partial_{\alpha_\mu} + \beta_\mu) + \gamma_{kd}^{\mu*}\partial_{\beta_\mu}\right) N_{abck}^{\alpha\beta} - \left(\gamma_{ka}^{\mu}\partial_{\alpha_\mu} + \gamma_{ak}^{\mu*}(\partial_{\beta_\mu} + \alpha_\mu)\right) N_{kbcd}^{\alpha\beta} \right) \\
& - \sum_{\substack{k\in\mathrm{VB}\\ \mu}} \left(\left(\gamma_{kc}^{\mu}(\partial_{\alpha_\mu} + \beta_\mu) + \gamma_{ck}^{\mu*}\partial_{\beta_\mu}\right) N_{abkd}^{\alpha\beta} - \left(\gamma_{bk}^{\mu}\partial_{\alpha_\mu} + \gamma_{kb}^{\mu*}(\partial_{\beta_\mu} + \alpha_\mu)\right) N_{akcd}^{\alpha\beta} \right) \\
& - \mathbf{E}(t) \left(\mathbf{M}_{dc}^{\mathrm{cv}} Y_{ba}^{\beta\alpha*} - \mathbf{M}_{ba}^{\mathrm{vc}} Y_{cd}^{\alpha\beta} \right).
\end{aligned} \tag{3.40}$$

Let us stop for a moment and, using Eq. (3.40), formulate the equation of motion for variable $\sum\limits_{k\in\mathrm{VB}} N_{akkb}$, disregarding for simplicity its phonon-assisted part

$$\begin{aligned}\mathrm{i}\hbar\left(\partial_t \sum_{k\in\mathrm{VB}} N_{akkb}\right)_{\mathrm{carrier}} &= \left(\epsilon_b^{\mathrm{v}} - \epsilon_a^{\mathrm{c}}\right)\sum_{k\in\mathrm{VB}} N_{akkb} \\ &+ \sum_{\substack{pk\in\mathrm{VB}\\ q\in\mathrm{CB}}}\left(V_{pqbk}^{\mathrm{vccv}} - V_{pkbq}^{\mathrm{vvcc}}\right)N_{akpq} - \sum_{\substack{pk\in\mathrm{VB}\\ q\in\mathrm{CB}}}\left(V_{kaqp}^{\mathrm{vccv}} - V_{kpqa}^{\mathrm{vvcc}}\right)N_{qpkb} \\ &- \mathbf{E}(t)\sum_{k\in\mathrm{VB}}\left(\mathbf{M}_{bk}^{\mathrm{cv}} Y_{ka}^{*} - \mathbf{M}_{ka}^{\mathrm{vc}} Y_{kb}\right).\end{aligned} \tag{3.41}$$

We now compare Eq. (3.41) to Eq. (3.5) in which the phonon-assisted part $\mathrm{i}\hbar\left(\partial_t C_{ab}\right)_{\mathrm{p}}$, along with the fourth-order contributions of type $\langle c^\dagger c^\dagger c c\rangle$, are neglected. We see that, within the second order treatment, the carrier part of the time evolution of quantities $\sum\limits_{k\in\mathrm{VB}} N_{akkb}$ and C_{ab} is governed by the same differential equation. Since similar conclusion also holds for the phonon-assisted part of the dynamics, and since both quantities start from the same initial condition (at $t = 0$, both are equal to zero), we conclude that, within the second-order treatment,

$$C_{ab} = \sum_{k\in\mathrm{VB}} N_{akkb}.$$

Generalization to the respective phonon-assisted density matrices is immediate. Therefore, we have proven the contraction relation given in Eq. (3.37) by an explicit calculation.

Now, we take advantage of the fact that carrier parts of both $Y_{ab}^{\alpha\beta}$ and $N_{abcd}^{\alpha\beta}$ consist of creations and annihilations of electron–hole pairs. Therefore, all equations of motion will be formulated in the exciton basis, defined by the eigenvalue problem given in Eq. (2.46), by expanding relevant density matrices in this basis. Instead of working with quantities Y_{ab} and N_{abcd}, which are given in the single-particle basis, we will work with the corresponding quantities y_x and $n_{\bar{x}x}$ in the exciton basis, whose relations to Y_{ab} and N_{abcd} read as

$$Y_{ab} = \sum_x \psi_{ab}^x y_x, \quad y_x = \sum_{\substack{a\in\mathrm{VB}\\ b\in\mathrm{CB}}} \psi_{ab}^{x*} Y_{ab} = \langle X_x\rangle, \tag{3.42}$$

$$N_{abcd} = \sum_{\bar{x}x} \psi_{ba}^{\bar{x}*} \psi_{cd}^{x} n_{\bar{x}x}, \quad n_{\bar{x}x} = \sum_{\substack{ad \in \mathrm{CB} \\ bc \in \mathrm{VB}}} \psi_{ba}^{\bar{x}} \psi_{cd}^{x*} N_{abcd} = \langle X_{\bar{x}}^{\dagger} X_x \rangle. \tag{3.43}$$

Similar relations hold for the corresponding phonon-assisted electronic density matrices; in the case of single-phonon assistance, the definitions are

$$Y_{ab\mu^+} \equiv \langle d_a c_b b_\mu^\dagger \rangle = \sum_x \psi_{ab}^x y_{x\mu^+}, \tag{3.44a}$$

$$N_{abcd\mu^+} \equiv \langle c_a^\dagger d_b^\dagger d_c c_d b_\mu^\dagger \rangle = \sum_{\bar{x}x} \psi_{ba}^{\bar{x}*} \psi_{cd}^{x} n_{\bar{x}x\mu^+}. \tag{3.44b}$$

The number of excitons in state x is

$$n_{xx} = \langle X_x^\dagger X_x \rangle. \tag{3.45}$$

Using the definition of exciton creation and annihilation operators [Eq. (2.49)], performing the decoupling embodied in Eq. (3.8), and neglecting the product of electron and hole densities (since it is of the fourth order in the applied field), the number of excitons in state x can be expressed as

$$\langle X_x^\dagger X_x \rangle = |y_x|^2 + \bar{n}_{xx}. \tag{3.46}$$

In Eq. (3.46), we define new quantities $\bar{n}_{\bar{x}x}$

$$\bar{n}_{\bar{x}x} = n_{\bar{x}x} - y_{\bar{x}}^* y_x. \tag{3.47}$$

The first term in Eq. (3.46) is the number of the so-called coherent excitons, whereas the second term is the number of incoherent excitons, i.e., truly bound electron–hole pairs. Namely, as we have already noted in Sec. 3.1, the interband polarizations Y_{ab} (or, after transferring to the exciton basis, y_x), decay very fast after the pulsed excitation due to various scattering mechanisms present. Their squared moduli $|y_x|^2$, which are commonly referred to as coherent exciton populations [115], do not provide information about the real populations of exciton states, which are the consequence of Coulomb-induced correlations between electrons and holes and which typically exist in the system for a long time after the decay of the interband polarizations. In order to describe true excitons, which are atomlike complexes of electrons and holes bound by the Coulomb attraction, we have to consider two-particle correlations among them rather than single-particle quantities [102]. The last conclusion justifies the identification of $\bar{n}_{xx}$ with the true exciton population in state x.

The equations of motion for the purely electronic relevant variables y_x and $n_{\bar{x}x}$ are

$$\begin{aligned} \partial_t y_x &= -\mathrm{i}\omega_x y_x - \frac{1}{\mathrm{i}\hbar}\mathbf{E}(t)\mathbf{M}_x \\ &+ \frac{1}{\mathrm{i}\hbar}\sum_{\mu x'} \Gamma^{\mu}_{xx'}\, y_{x'\mu^+} + \frac{1}{\mathrm{i}\hbar}\sum_{\mu x'} \Gamma^{\mu *}_{x'x}\, y_{x'\mu^-}, \end{aligned} \tag{3.48}$$

$$\begin{aligned} \partial_t n_{\bar{x}x} &= -\mathrm{i}(\omega_x - \omega_{\bar{x}}) n_{\bar{x}x} - \frac{1}{\mathrm{i}\hbar}\mathbf{E}(t)\left(y^*_{\bar{x}}\mathbf{M}_x - \mathbf{M}^*_{\bar{x}} y_x\right) \\ &+ \frac{1}{\mathrm{i}\hbar}\sum_{\mu x'} \Gamma^{\mu}_{xx'} n_{\bar{x}x'\mu^+} - \frac{1}{\mathrm{i}\hbar}\sum_{\mu \bar{x}'} \Gamma^{\mu}_{\bar{x}'\bar{x}} n_{\bar{x}'x\mu^+} \\ &+ \frac{1}{\mathrm{i}\hbar}\sum_{\mu x'} \Gamma^{\mu *}_{x'x} n^*_{x'\bar{x}\mu^+} - \frac{1}{\mathrm{i}\hbar}\sum_{\mu \bar{x}'} \Gamma^{\mu *}_{\bar{x}\bar{x}'} n^*_{x\bar{x}'\mu^+}. \end{aligned} \tag{3.49}$$

In Eqs. (3.48) and (3.49), we introduce dipole-moment matrix elements in the exciton basis

$$\mathbf{M}_x = \sum_{\substack{a\in\mathrm{VB}\\ b\in\mathrm{CB}}} \psi^{x*}_{ab} \mathbf{M}^{\mathrm{cv}}_{ba}, \tag{3.50}$$

as well as matrix elements of the carrier–phonon interaction in the exciton basis, which describe the coupling to the phonon mode μ (the transition from exciton state x' to exciton state x mediated by the emission of a phonon from mode μ):

$$\Gamma^{\mu}_{xx'} = \sum_{\substack{a\in\mathrm{VB}\\ b\in\mathrm{CB}}} \psi^{x*}_{ab} \left(\sum_{k\in\mathrm{CB}} \gamma^{\mu}_{bk}\psi^{x'}_{ak} - \sum_{k\in\mathrm{VB}} \gamma^{\mu}_{ka}\psi^{x'}_{kb} \right). \tag{3.51}$$

Equations (3.48) and (3.49) contain coupling to single-phonon-assisted density matrices $y_{x\mu^\pm}$ and $n_{\bar{x}x\mu^+}$. There are different possibilities to close the phonon branch of the hierarchy. Our approach to closing the phonon branch of the hierarchy is motivated by the physical requirements of the particle-number and energy conservation following the pulsed optical excitation.

3.5.1 Energy and Particle-Number Conservation

The dynamics should conserve the particle number after the external field has vanished, since all the other terms in the Hamiltonian given by Eqs. (2.34)–(2.38) commute with the number operators for electrons and holes defined in Eqs. (3.15a) and (3.15b). The number of electrons is

$$N_e = \sum_{p\in \mathrm{CB}} \langle c_p^\dagger c_p \rangle, \tag{3.52}$$

and the number of holes is

$$N_h = \sum_{p\in \mathrm{VB}} \langle d_p^\dagger d_p \rangle. \tag{3.53}$$

The equality $N_e = N_h$ holds, since carriers are generated in pairs in our model. Using the contraction identities and retaining only terms up to the second order in the optical field, we obtain that

$$N_{\mathrm{tot}} = N_e = N_h = \sum_x n_{xx}. \tag{3.54}$$

Even at this level, without specifying the form of equations for one-phonon-assisted electronic density matrices, using Eq. (3.49) with vanishing electric field it is easily shown that, in the absence of external fields, our dynamics conserves the total number of particles.

The dynamic equations for the relevant variables should also be compatible with the energy conservation in a system without external fields. Our system, however, interacts with an external optical field, but, since we consider a pulsed excitation, the energy of the system should be conserved after the field has vanished. The total energy of the system, i.e., the expectation value of the Hamiltonian $\langle H \rangle$ defined in Eqs. (2.34)–(2.38), is expressed as

$$\mathcal{E} = \mathcal{E}_{\mathrm{c}} + \mathcal{E}_{\mathrm{p}} + \mathcal{E}_{\mathrm{c-p}} + \mathcal{E}_{\mathrm{c-f}}, \tag{3.55}$$

where the carrier energy is

$$\mathcal{E}_{\mathrm{c}} = \sum_x \hbar\omega_x n_{xx}, \tag{3.56}$$

the phonon energy is

$$\mathcal{E}_{\mathrm{p}} = \sum_{\mu} \hbar\omega_{\mu} \, \langle b_{\mu}^{\dagger} b_{\mu} \rangle, \tag{3.57}$$

the carrier–phonon interaction energy is

$$\mathcal{E}_{\mathrm{c-p}} = 2 \sum_{\bar{x}x\mu} \mathrm{Re}\{\Gamma_{\bar{x}x}^{\mu} n_{\bar{x}x\mu^{+}}\}, \tag{3.58}$$

and the carrier–field interaction energy is

$$\mathcal{E}_{\mathrm{c-f}} = -\mathbf{E}(t) \sum_{x} \left(\mathbf{M}_{x}^{*} y_{x} + y_{x}^{*} \mathbf{M}_{x} \right). \tag{3.59}$$

In Eqs. (3.55)–(3.59), we have kept only contributions up to the second order in the external field and transferred to the exciton basis. The fact that the energy of the system under consideration (carriers and phonons) should be conserved after the pulsed photoexcitation means that

$$\partial_t \left(\mathcal{E}_{\mathrm{c}} + \mathcal{E}_{\mathrm{p}} + \mathcal{E}_{\mathrm{c-p}} \right) = 0 \text{ when } \mathbf{E} = 0. \tag{3.60}$$

3.5.2 Closing the Phonon Branch of the Hierarchy

Let us now form the equations of motion for single-phonon-assisted density matrices $y_{x\mu^{\pm}}$ and $n_{\bar{x}x\mu^{+}}$. We do so by performing an appropriate differentiation of Eqs. (3.39) and (3.40), setting $\alpha_{\rho} = \beta_{\rho} = 0$, and transforming the equations thus obtained to the exciton basis. Here, we neglect the coupling to the light field, i.e., we neglect contributions arising from the combined action of the phonon coupling and the interaction with the light field (the so-called cross terms) [71, 118]. The equations governing time evolution of single-phonon-assisted density matrices exhibit coupling to two-phonon-assisted density matrices. These two-phonon-assisted density matrices are factorized [similarly to the factorizations embodied in Eqs. (3.6)–(3.9)] into products of density matrices with lower-order phonon assistance and the correlated parts.

In equation for $y_{x\mu^+}$, two-phonon-assisted density matrices of the form $y_{x'\mu^+\rho^-} = \langle X_{x'} b_\mu^\dagger b_\rho \rangle$ and $y_{x'\mu^+\rho^+} = \langle X_{x'} b_\mu^\dagger b_\rho^\dagger \rangle$ appear. We adopt the following factorizations of these density matrices

$$y_{x'\mu^+\rho^-} = \langle X_{x'} \rangle \langle b_\mu^\dagger b_\rho \rangle + \delta \langle X_{x'} b_\mu^\dagger b_\rho \rangle = y_{x'} \delta_{\mu\rho} n_\mu^{\mathrm{ph}} + \delta y_{x'\mu^+\rho^-}, \tag{3.61}$$

$$y_{x'\mu^+\rho^+} = \langle X_{x'} \rangle \langle b_\mu^\dagger b_\rho^\dagger \rangle + \delta \langle X_{x'} b_\mu^\dagger b_\rho^\dagger \rangle = \delta y_{x'\mu^+\rho^+}. \tag{3.62}$$

In Eq. (3.61), we assume that $\langle b_\mu^\dagger b_\rho \rangle = \delta_{\mu\rho} n_\mu^{\mathrm{ph}}$, where $n_\mu^{\mathrm{ph}} = \left(\mathrm{e}^{\beta \hbar \omega_\mu} - 1 \right)^{-1}$ is the equilibrium number of phonons in mode μ at temperature $T = (k_B \beta)^{-1}$. Similarly, in Eq. (3.62), we take that $\langle b_\mu^\dagger b_\rho^\dagger \rangle = 0$. In other words, we neglect hot phonon effects, i.e., we assume that the phonon numbers do not significantly deviate from the values predicted by the equilibrium distribution. Since the phonon distribution function $\langle b_\mu^\dagger b_\mu \rangle$ appears in the expression for the total energy of the system [see Eqs. (3.55) and (3.57)], we will explicitly formulate the equation governing its time evolution

$$\partial_t \langle b_\mu^\dagger b_\mu \rangle = \frac{2}{\hbar} \sum_{\bar{x}x} \mathrm{Im}\{ \Gamma_{\bar{x}x}^\mu n_{\bar{x}x\mu^+} \}. \tag{3.63}$$

However, in view of small differences between the phonon number predicted by Eq. (3.63) and the equilibrium phonon number, we take that in all the equations for y_x, $n_{\bar{x}x}$, and their phonon-assisted counterparts, phonon numbers assume their equilibrium values.

The equation for $n_{\bar{x}x\mu^+}$ exhibits couplings to two-phonon-assisted density matrices of the form $n_{\bar{x}'x'\mu^+\rho^-} = \langle X_{\bar{x}'}^\dagger X_{x'} b_\mu^\dagger b_\rho \rangle$ and $n_{\bar{x}'x'\mu^+\rho^+} = \langle X_{\bar{x}'}^\dagger X_{x'} b_\mu^\dagger b_\rho^\dagger \rangle$. Since density matrix $n_{\bar{x}x\mu^+}$ participates in the equation describing time evolution of exciton populations and coherences, we treat an exciton as the basic entity and accordingly perform factorizations

$$n_{\bar{x}'x'\mu^+\rho^-} = \langle X_{\bar{x}'}^\dagger X_{x'} \rangle \langle b_\mu^\dagger b_\rho \rangle + \delta \langle X_{\bar{x}'}^\dagger X_{x'} b_\mu^\dagger b_\rho \rangle = n_{\bar{x}'x'} \delta_{\mu\rho} n_\mu^{\mathrm{ph}} + \delta n_{\bar{x}'x'\mu^+\rho^-}, \tag{3.64}$$

$$n_{\bar{x}'x'\mu^+\rho^+} = \langle X_{\bar{x}'}^\dagger X_{x'} \rangle \langle b_\mu^\dagger b_\rho^\dagger \rangle + \delta \langle X_{\bar{x}'}^\dagger X_{x'} b_\mu^\dagger b_\rho^\dagger \rangle = \delta n_{\bar{x}'x'\mu^+\rho^+}. \tag{3.65}$$

Using decompositions of two-phonon-assisted density matrices in Eqs. (3.61)–(3.65), the following equations for single-phonon-assisted density matrices are obtained:

$$\begin{aligned}\partial_t n_{\bar{x}x\mu^+} &= -\mathrm{i}(\omega_x - \omega_{\bar{x}} - \omega_\mu) n_{\bar{x}x\mu^+} \\ &+ \frac{n_\mu^{\mathrm{ph}}}{\mathrm{i}\hbar} \sum_{x'} \Gamma^{\mu *}_{x'x} n_{\bar{x}x'} - \frac{1+n_\mu^{\mathrm{ph}}}{\mathrm{i}\hbar} \sum_{\bar{x}'} \Gamma^{\mu *}_{\bar{x}\bar{x}'} n_{\bar{x}'x} + \left(\partial_t n_{\bar{x}x\mu^+}\right)_{\mathrm{higher}} ,\end{aligned} \tag{3.66}$$

$$\partial_t y_{x\mu^+} = -\,\mathrm{i}(\omega_x - \omega_\mu)\, y_{x\mu^+} + \frac{n_\mu^{\mathrm{ph}}}{\mathrm{i}\hbar} \sum_{x'} \Gamma^{\mu *}_{x'x}\, y_{x'} + \left(\partial_t y_{x\mu^+}\right)_{\mathrm{higher}} , \tag{3.67}$$

$$\partial_t y_{x\mu^-} = -\,\mathrm{i}(\omega_x + \omega_\mu)\, y_{x\mu^-} + \frac{1+n_\mu^{\mathrm{ph}}}{\mathrm{i}\hbar} \sum_{x'} \Gamma^{\mu}_{xx'}\, y_{x'} + \left(\partial_t y_{x\mu^-}\right)_{\mathrm{higher}} . \tag{3.68}$$

The last summands on the right-hand sides of Eqs. (3.66)–(3.68) represent the rates at which the corresponding density matrices change due to the coupling to the correlated parts of density matrices with higher-order phonon assistance. Their explicit forms are

$$\begin{aligned}\left(\partial_t n_{\bar{x}x\mu^+}\right)_{\mathrm{higher}} = &- \frac{1}{\mathrm{i}\hbar} \sum_{\rho\bar{x}'} \Gamma^{\rho *}_{\bar{x}\bar{x}'} \delta n_{\bar{x}'x\mu^+\rho^-} - \frac{1}{\mathrm{i}\hbar} \sum_{\rho\bar{x}'} \Gamma^{\rho}_{\bar{x}'\bar{x}} \delta n_{\bar{x}'x\mu^+\rho^+} \\ &+ \frac{1}{\mathrm{i}\hbar} \sum_{\rho x'} \Gamma^{\rho *}_{x'x} \delta n_{\bar{x}x'\mu^+\rho^-} + \frac{1}{\mathrm{i}\hbar} \sum_{\rho x'} \Gamma^{\rho}_{xx'} \delta n_{\bar{x}x'\mu^+\rho^+} ,\end{aligned} \tag{3.69}$$

$$\left(\partial_t y_{x\mu^+}\right)_{\mathrm{higher}} = \frac{1}{\mathrm{i}\hbar} \sum_{\rho x'} \Gamma^{\rho}_{xx'} \delta y_{x'\mu^+\rho^+} + \frac{1}{\mathrm{i}\hbar} \sum_{\rho x'} \Gamma^{\rho *}_{x'x} \delta y_{x'\mu^+\rho^-} , \tag{3.70}$$

$$\left(\partial_t y_{x\mu^-}\right)_{\mathrm{higher}} = \frac{1}{\mathrm{i}\hbar} \sum_{\rho x'} \Gamma^{\rho}_{xx'} \delta y_{x'\rho^+\mu^-} + \frac{1}{\mathrm{i}\hbar} \sum_{\rho x'} \Gamma^{\rho *}_{x'x} \delta y_{x'\rho^-\mu^-} . \tag{3.71}$$

One manner to truncate the phonon branch of the hierarchy is to neglect the coupling to correlated parts of two-phonon-assisted density matrices in Eqs. (3.66)–(3.68), and solve the equations thus obtained using Markov and adiabatic approximations. Such an approach, which has been applied in Refs. [71, 115], results in the elimination of phonon-assisted density matrices from the formalism. Single-phonon-assisted density matrices $y_{x\mu^\pm}$ are then entirely expressed in terms of y_x, whereas density matrices $n_{\bar{x}x\mu^+}$ are expressed in terms of $n_{\bar{x}x}$. However, it can be shown that the total energy under these approximations is not exactly conserved after the external electric field has vanished.

Here, however, motivated by the fact that the total energy explicitly depends on single-phonon-assisted density matrices $n_{\bar{x}x\mu^+}$, we retain all density matrices $y_{x\mu^\pm}$ and $n_{\bar{x}x\mu^+}$ as active variables in the formalism. The truncation of the phonon branch of the hierarchy is, therefore, performed on the level of two-phonon-assisted density matrices. Let us now concentrate on eliminating correlated parts $\delta n_{\bar{x}x\mu^+\rho^-}$ and $\delta n_{\bar{x}x\mu^+\rho^+}$ from the formalism. The strategy to accomplish this goal is essentially similar to the one used to eliminate single-phonon-assisted density matrices in Refs. [71, 115]. Namely, in equations of motion for $\delta n_{\bar{x}x\mu^+\rho^-}$ and $\delta n_{\bar{x}x\mu^+\rho^+}$, three-phonon-assisted density matrices are present. In order to close the phonon branch of hierarchy, we factorize them into all possible combinations of phonon distribution functions and phonon-assisted electronic density matrices and neglect their correlated parts. The strategy is similar to the one employed in Eqs. (3.64) and (3.65), for example,

$$\langle X^\dagger_{\bar{x}'} X_{x'} b^\dagger_\mu b^\dagger_\rho b_\sigma \rangle = \delta_{\rho\sigma} n_{\bar{x}'x'\mu^+} n^{\mathrm{ph}}_\rho + \delta_{\mu\sigma} n_{\bar{x}'x'\rho^+} n^{\mathrm{ph}}_\mu . \tag{3.72}$$

The evolution of $\delta n_{\bar{x}x\rho^+\sigma^-}$ is then governed by

$$\begin{aligned}
\partial_t \, \delta n_{\bar{x}x\rho^+\sigma^-} &= -\mathrm{i}(\omega_x - \omega_{\bar{x}} + \omega_\sigma - \omega_\rho)\delta n_{\bar{x}x\rho^+\sigma^-} \\
&\quad + \frac{1+n^{\mathrm{ph}}_\sigma}{\mathrm{i}\hbar} \sum_{x'} \Gamma^\sigma_{xx'} n_{\bar{x}x'\rho^+} - \frac{n^{\mathrm{ph}}_\sigma}{\mathrm{i}\hbar} \sum_{\bar{x}'} \Gamma^\sigma_{\bar{x}'\bar{x}} n_{\bar{x}'x\rho^+} \\
&\quad - \frac{1+n^{\mathrm{ph}}_\rho}{\mathrm{i}\hbar} \sum_{\bar{x}'} \Gamma^{\rho*}_{\bar{x}\bar{x}'} n^*_{x\bar{x}'\sigma^+} + \frac{n^{\mathrm{ph}}_\rho}{\mathrm{i}\hbar} \sum_{x'} \Gamma^{\rho*}_{x'x} n^*_{x'\bar{x}\sigma^+} .
\end{aligned} \tag{3.73}$$

A similar equation describes the evolution of $\delta n_{\bar{x}x\rho^+\sigma^+}$. We now solve Eq. (3.73) in Markov and adiabatic approximations [118, 119] to obtain

$$\begin{aligned}
\delta n_{\bar{x}x\rho^+\sigma^-} &= (1+n^{\mathrm{ph}}_\sigma) \sum_{x'} \Gamma^\sigma_{xx'} \mathcal{D}(\hbar\omega_{x'} - \hbar\omega_x - \hbar\omega_\sigma) n_{\bar{x}x'\rho^+} \\
&\quad - n^{\mathrm{ph}}_\sigma \sum_{\bar{x}'} \Gamma^\sigma_{\bar{x}'\bar{x}} \mathcal{D}(\hbar\omega_{\bar{x}} - \hbar\omega_{\bar{x}'} - \hbar\omega_\sigma) n_{\bar{x}'x\rho^+} \\
&\quad + (1+n^{\mathrm{ph}}_\rho) \sum_{\bar{x}'} \Gamma^{\rho*}_{\bar{x}\bar{x}'} \mathcal{D}^*(\hbar\omega_{\bar{x}'} - \hbar\omega_{\bar{x}} - \hbar\omega_\rho) n^*_{x\bar{x}'\sigma^+} \\
&\quad - n^{\mathrm{ph}}_\rho \sum_{x'} \Gamma^{\rho*}_{x'x} \mathcal{D}^*(\hbar\omega_x - \hbar\omega_{x'} - \hbar\omega_\rho) n^*_{x'\bar{x}\sigma^+} ,
\end{aligned} \tag{3.74}$$

where

$$\mathcal{D}(\epsilon) = -\mathrm{i}\pi\delta(\epsilon) + \mathcal{P}\left(\frac{1}{\epsilon}\right) . \tag{3.75}$$

The details on the application of Markov and adiabatic approximations to solve Eq. (3.73) can be found in Appendix C. We thus expressed two-phonon-assisted electronic density matrices in terms of one-phonon-assisted electronic density matrices. When these results are inserted in Eq. (3.69), we neglect all terms involving principal values which, in principle, lead to polaron shifts in energies [90, 119]. Furthermore, we note that the inserted terms involve multiple summations over exciton indices x, which are cumbersome to evaluate, and we use the so-called random phase approximation to simplify the expression obtained. In essence, the random phase approximation consists of neglecting sums over correlated parts of one-phonon-assisted electronic density matrices (which are complex-valued quantities) due to random phases at different arguments of these density matrices [90]. This approximation is easier to understand and justify when we transfer to a particular representation for the exciton index x. Appendix D.1 is devoted to a detailed discussion on the application of the random phase approximation. Here, we only cite the final expression for $(\partial_t n_{\bar{x}x\mu^+})_{\text{higher}}$ under the approximations employed

$$(\partial_t n_{\bar{x}x\mu^+})_{\text{higher}} = -\gamma_{\bar{x}x\mu} n_{\bar{x}x\mu^+} , \tag{3.76}$$

where $\gamma_{\bar{x}x\mu}$ is given as

$$\gamma_{\bar{x}x\mu} = \frac{1}{2}\left(\Gamma_x + \Gamma_{\bar{x}}\right) , \tag{3.77}$$

$$\Gamma_x = \frac{2\pi}{\hbar}\sum_{\tilde{x}\rho}\left(|\Gamma^{\rho}_{x\tilde{x}}|^2\delta(\hbar\omega_x - \hbar\omega_{\tilde{x}} + \hbar\omega_\rho)n^{\text{ph}}_\rho + |\Gamma^{\rho}_{\tilde{x}x}|^2\delta(\hbar\omega_x - \hbar\omega_{\tilde{x}} - \hbar\omega_\rho)(1 + n^{\text{ph}}_\rho)\right) . \tag{3.78}$$

It was recognized that this form of the coupling to higher-order phonon-assisted electronic density matrices is at variance with the energy conservation [72, 90, 120]. In this work, we will use the following form of the coupling to higher-order phonon-assisted density matrices:

$$(\partial_t n_{\bar{x}x\mu^+})_{\text{higher}} = -\gamma_{\bar{x}x\mu} n_{\bar{x}x\mu^+} + \gamma_{\bar{x}x\mu} n^{*}_{\bar{x}x\mu^+} , \tag{3.79}$$

where $\gamma_{\bar{x}x\mu}$ is, as before, defined by Eqs. (3.77) and (3.78). This form of $(\partial_t n_{\bar{x}x\mu^+})_{\text{higher}}$ is compatible with the energy conservation, as long as the matrix elements of the carrier–phonon interaction $\Gamma^{\mu}_{\bar{x}x}$ are purely real, which is the case relevant for our numerical investigations in the following chapters. Here, let us only mention that the rate at which the total energy changes after the pulse is equal to the rate at which the carrier–phonon interaction energy changes due to the coupling of the single–phonon–assisted electronic density matrices $n_{\bar{x}x\mu^+}$ to density matrices with higher-order phonon assistance,

$$\partial_t\,\mathcal{E} = (\partial_t\,\mathcal{E}_{\text{c-p}})_{\text{higher}} = 2\sum_{\bar{x}x\mu}\text{Re}\left\{\Gamma^{\mu}_{\bar{x}x}\,(\partial_t\,n_{\bar{x}x\mu^+})_{\text{higher}}\right\}. \tag{3.80}$$

It is then clear that, if all $\Gamma^{\mu}_{\bar{x}x}$ are real, the form of $(\partial_t\,n_{\bar{x}x\mu^+})_{\text{higher}}$ given in Eq. (3.79) does not violate the energy conservation. Furthermore, as $n_{\bar{x}x\mu^+}$ describes the elementary process in which an exciton initially in the state x is scattered to the state $\bar{x}$ emitting a phonon from the mode μ, the reverse microscopic process, described by $n_{x\bar{x}\mu^-} = n^*_{\bar{x}x\mu^+}$, is also possible, so in the differential equation for $n_{\bar{x}x\mu^+}$ the quantity $n^*_{\bar{x}x\mu^+}$ may appear. Further comments on the energy conservation are given in Appendix D.2.

Similar strategy can be adopted to simplify the coupling to electronic density matrices with higher-order phonon assistance in Eqs. (3.67) and (3.68), with the final result

$$(\partial_t y_{x\mu^\pm})_{\text{higher}} = -\gamma_{x\mu}\,y_{x\mu^\pm}, \tag{3.81}$$

where

$$\gamma_{x\mu} = \frac{1}{2}\Gamma_x, \tag{3.82}$$

and Γ_x is defined in Eq. (3.78).

The interrelations between relevant density matrices in the resulting hierarchy of equations, which consists of Eqs. (3.48), (3.49), (3.66), (3.67), (3.68), (3.79), and (3.81), are schematically presented in Fig. 3.1.

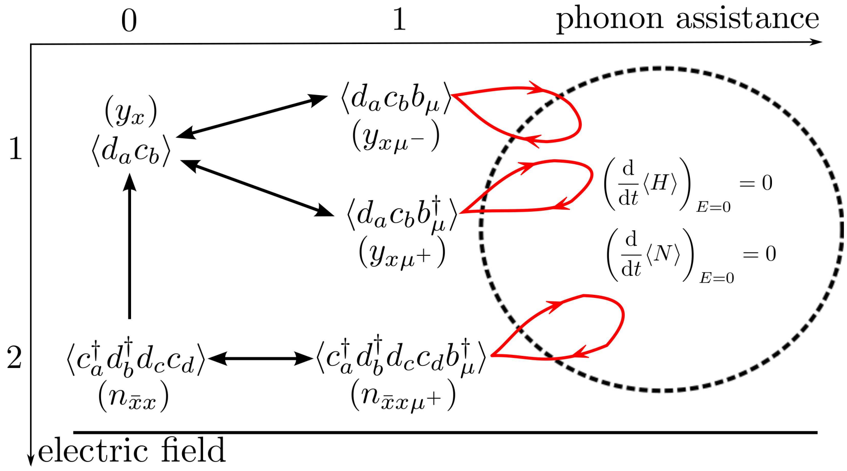
0
1
phonon assistance
1
2
electric field
(y_x)
$\langle d_a c_b \rangle$
$\langle d_a c_b b_\mu \rangle$
$(y_{x\mu^-})$
$\langle d_a c_b b_\mu^\dagger \rangle$
$(y_{x\mu^+})$
$\langle c_a^\dagger d_b^\dagger d_c c_d \rangle$
$(n_{\bar{x}x})$
$\langle c_a^\dagger d_b^\dagger d_c c_d b_\mu^\dagger \rangle$
$(n_{\bar{x}x\mu^+})$
$\left(\frac{\mathrm{d}}{\mathrm{d}t}\langle H \rangle\right)_{E=0} = 0$
$\left(\frac{\mathrm{d}}{\mathrm{d}t}\langle N \rangle\right)_{E=0} = 0$

FIGURE 3.1: Active variables in the density matrix formalism and their mutual relations in the resulting hierarchy of equations. The direction of a straight arrow indicates that in the equation for the variable at its start appears the variable at its end. Loops represent couplings to higher-order phonon-assisted density matrices [see Eqs. (3.69), (3.70) and (3.71)] which are truncated so that the particle number and energy of the free system are conserved.

3.5.3 Another View of the Second-Order Semiconductor Dynamics

This section presents another standpoint from which the semiconductor dynamics up to the second order in the exciting field may be regarded. We have already emphasized that we work in the approximation of weak exciting field and low carrier densities. Let us now demonstrate that retaining only contributions up to the second order in the optical field is essentially equivalent to confining our description to the subspace of two-particle, i.e., single-exciton states. This demonstration also provides us with a technically less demanding procedure of obtaining the equations of motion for relevant density matrices.

The interacting-carrier part of the Hamiltonian H_c [Eq. (2.35)] commutes with the exciton number operator $\sum_x X_x^\dagger X_x$, meaning that subspaces of n-exciton states are invariant under the action of H_c. In other words, H_c, as well as the commutation relations of exciton operators [Eq. (2.51)], can be expressed in terms of an infinite series of normally ordered products of exciton creation and annihilation operators $X_x^\dagger$ and X_x [121]. The nth term of this series contains n exciton creation and n exciton annihilation operators, i.e.,

$$H_\mathrm{c} = \sum_{n=0}^{+\infty} \sum_{\substack{\bar{x}_1 \ldots \bar{x}_n \\ x_1 \ldots x_n}} h_{x_1 \ldots x_n}^{\bar{x}_1 \ldots \bar{x}_n} X_{\bar{x}_1}^\dagger \ldots X_{\bar{x}_n}^\dagger X_{x_1} \ldots X_{x_n}. \tag{3.83}$$

The expansion coefficients $h_{x_1\dots x_n}^{\bar{x}_1\dots\bar{x}_n}$ are then determined order by order, starting from the zero-order term, and using the fact that the normal-ordered product of n exciton creation and n exciton annihilation operators reduces to zero in all m-exciton subspaces in which $m < n$. This procedure enables one to reduce the description of the dynamics to a subspace containing at most $n \geq 1$ excitons.

Having in mind that the relevant purely electronic density matrices within the second-order formalism are $y_x = \langle X_x \rangle$ and $n_{\bar{x}x} = \langle X_{\bar{x}}^\dagger X_x \rangle$, it is clear that the part of H_c relevant for the formulation of the second-order dynamics is its reduction up to the single-exciton subspace. H_c then reduces to

$$H_\mathrm{c} = \sum_x \hbar\omega_x X_x^\dagger X_x, \tag{3.84}$$

while the corresponding reduction of the carrier–phonon interaction $H_\mathrm{c-p}$ [Eq. (2.37)] reads as

$$H_\mathrm{c-p} = \sum_{\mu\bar{x}x} \left(\Gamma_{\bar{x}x}^{\mu} X_{\bar{x}}^\dagger X_x b_\mu^\dagger + \Gamma_{\bar{x}x}^{\mu *} X_x^\dagger X_{\bar{x}} b_\mu \right). \tag{3.85}$$

The Hamiltonian $H_\mathrm{c-f}$ [Eq. (2.38)] of the interaction with optical field is responsible for exciton generation, it couples the n-exciton subspace to $(n+1)$- and $(n-1)$-exciton subspaces, and its form is

$$H_\mathrm{c-f} = -\mathbf{E}(t) \sum_x \left(\mathbf{M}_x^* X_x + \mathbf{M}_x X_x^\dagger \right). \tag{3.86}$$

The reduction of the commutation relations up to the single-exciton subspace reads as

$$\left[X_x, X_{\bar{x}}^\dagger \right] = \delta_{x\bar{x}} - \sum_{\bar{x}'x'} C_{\bar{x}x}^{\bar{x}'x'} X_{\bar{x}'}^\dagger X_{x'}, \tag{3.87}$$

where four-index coefficients $C_{\bar{x}x}^{\bar{x}'x'}$ are given as

$$\begin{aligned} C_{\bar{x}x}^{\bar{x}'x'} = & \sum_{\bar{q}q\in\mathrm{CB}} \left(\sum_{p\in\mathrm{VB}} \psi_{p\bar{q}}^{\bar{x}'*} \psi_{pq}^{x'} \right) \left(\sum_{p\in\mathrm{VB}} \psi_{p\bar{q}}^{\bar{x}} \psi_{pq}^{x*} \right) \\ & + \sum_{\bar{p}p\in\mathrm{VB}} \left(\sum_{q\in\mathrm{CB}} \psi_{\bar{p}q}^{\bar{x}'*} \psi_{pq}^{x'} \right) \left(\sum_{q\in\mathrm{CB}} \psi_{\bar{p}q}^{\bar{x}} \psi_{pq}^{x*} \right). \end{aligned} \tag{3.88}$$

Equations of motion for the density matrices relevant for the second-order semiconductor dynamics are then obtained by considering the time evolution with respect to the total Hamiltonian [Eqs. (2.34)–(2.38)] that is reduced up to the single-exciton subspace [122] and expressed in terms of exciton creation and annihilation operators as

$$\begin{aligned} H = &\sum_{x} \hbar\omega_x X_x^\dagger X_x + \sum_{\mu} \hbar\omega_\mu b_\mu^\dagger b_\mu + \sum_{\mu\bar{x}x} \left(\Gamma^{\mu}_{\bar{x}x} X_{\bar{x}}^\dagger X_x b_\mu^\dagger + \Gamma^{\mu *}_{\bar{x}x} X_x^\dagger X_{\bar{x}} b_\mu \right) \\ &- \mathbf{E}(t) \sum_{x} \left(\mathbf{M}_x^* X_x + \mathbf{M}_x X_x^\dagger \right) . \end{aligned} \tag{3.89}$$

At the same time, it is sufficient to retain only the zero-order term in the commutation relations [Eq. (3.87)], $\left[X_x, X_{\bar{x}}^\dagger\right] = \delta_{x\bar{x}}$, i.e., to consider excitons as noninteracting bosons. The viewpoint on the second-order semiconductor dynamics presented here will be used in our treatment of a transient absorption experiment in Sec. 5.4.2.

3.5.4 Schematic Picture of the Second-Order Semiconductor Dynamics

This section is devoted to a general qualitative analysis of the semiconductor dynamics described by Eqs. (3.48), (3.49), (3.66), (3.67), (3.68), (3.79), and (3.81). The analysis is aimed at providing a schematic picture of carrier dynamics induced by a pulsed optical excitation of a semiconductor.

Coherent and Incoherent Quantities

Let us start from the general observations we made in Sec. 3.1. Namely, we mentioned that interband polarizations Y_{ab} typically decay very fast following a pulsed semiconductor excitation, whereas the electron (C_{ab}) and hole (D_{ab}) populations and coherences typically exist for a long time after the decay of interband polarizations (and the vanishing of the external excitation). In other words, quantities Y_{ab} are of transient character and their presence in the system requires the action of an external driving field with energy on the scale of the band gap E_g. On the other hand, quantities C_{ab} and D_{ab} are long-living.

It seems plausible to classify semiconductor excitations on the basis of whether or not they remain in the system at times (measured from the end of the exciting pulse) exceeding the dephasing lifetime of the interband polarizations [102]. Generally speaking, coherent quantities assume nontrivial values only if an external excitation is present, whereas incoherent quantities are also present after the excitation on time scales that are much longer than the lifetime of the interband polarizations. In this sense, density matrices Y_{ab} are coherent quantities, while C_{ab} and D_{ab} are incoherent quantities.

In order to decide whether a given density matrix belongs to the group of coherent or incoherent quantities, one should analyze its free propagation. In the case of Y_{ab}, Eq. (3.4) gives

$$\mathrm{i}\hbar\left(\partial_t Y_{ab}\right)_{\mathrm{free}} = \left(\epsilon_b^{\mathrm{c}} - \epsilon_a^{\mathrm{v}}\right) Y_{ab}, \tag{3.90}$$

while using Eq. (3.5) we obtain that the free evolution of C_{ab} is governed by

$$\mathrm{i}\hbar\left(\partial_t C_{ab}\right)_{\mathrm{free}} = \left(\epsilon_b^{\mathrm{c}} - \epsilon_a^{\mathrm{c}}\right) C_{ab}. \tag{3.91}$$

While the energy difference $E_Y = |\epsilon_b^{\mathrm{c}} - \epsilon_a^{\mathrm{v}}|$ appearing in Eq. (3.90) is of the order of E_g (it describes the promotion of an electron from the valence to the conduction band), the energy difference $E_C = |\epsilon_b^{\mathrm{c}} - \epsilon_a^{\mathrm{c}}|$ is typically at least an order of magnitude smaller than E_g (it describes the electron transition between two conduction-band states). Since quantities Y_{ab} describe processes involving substantial energy exchanges, they need external driving to be sustained. After the external excitation fades out, scattering mechanisms (e.g., the carrier–phonon interaction) lead to a rapid decay of Y_{ab}. On the contrary, quantities C_{ab} describe processes involving only minor energy exchanges, and as such do not need external driving to be sustained. They can exist within the system for a long time after the excitation, since scattering processes may equilibrate them, but do not destroy them.

The preceding discussion enables us to establish the following criterion for the coherence or incoherence of a given density matrix $\langle A\rangle$, where A is a (normal-ordered) product of creation and annihilation operators of carriers and phonons. The free evolution of $\langle A\rangle$ is governed by

$$\mathrm{i}\hbar\left(\partial_t\langle A\rangle\right)_{\text{free}} = E_A\langle A\rangle. \tag{3.92}$$

If $|E_A|$ approximately equals $n_g = 1, 2, \ldots$ times the band gap E_g, density matrix $\langle A\rangle$ involves n_g interband transitions and is classified as a coherent quantity. If, on the contrary, $E_A \approx 0$, density matrix $\langle A\rangle$ is classified as an incoherent quantity. It is worth noting that this definition of coherence is not formal, and as such it requires certain knowledge about the band structure of the solid and its phonon spectrum. In this regard, we assume that the typical phonon energy is at least an order of magnitude smaller than the band gap E_g and is, therefore, comparable to the typical carrier intraband transition energy.

Let us now decide which of the quantities $y_x,\ y_{x\mu^\pm},\ n_{\bar{x}x}$,and $n_{\bar{x}x\mu^+}$ are coherent, and which are incoherent. The free evolution of y_x [Eq. (3.39)] and $y_{x\mu^\pm}$ [Eqs. (3.67) and (3.68)] suggests that these three quantities are coherent. On the contrary, the free evolution of $n_{\bar{x}x}$ [Eq. (3.40)] and $n_{\bar{x}x\mu^+}$ [Eq. (3.66)] points towards the incoherent nature of these two quantities.

The discrimination among transient and long-living quantities can be utilized to efficiently integrate Eqs. (3.48), (3.49), (3.66), (3.67), (3.68), (3.79), and (3.81). Namely, coherent quantities have to be resolved on very short time scales, while they do not have to be followed on longer time scales due to their fast decay. On the other hand, the time scales on which incoherent quantities have to be resolved are much longer. The time step for the numerical integration of Eqs. (3.48), (3.67), (3.68), and (3.81) can be substantially reduced if we explicitly separate out the free evolutions of coherent quantities y_x and $y_{x\mu^\pm}$, i.e., we integrate equations of motion for quantities $\tilde{y}_x$ and $\tilde{y}_{x\mu^\pm}$ defined as (compare to Appendix C)

$$y_x(t) = \mathrm{e}^{-\mathrm{i}\omega_x t}\tilde{y}_x(t), \tag{3.93a}$$

$$y_{x\mu^\pm}(t) = \mathrm{e}^{-\mathrm{i}(\omega_x\mp\omega_\mu)t}\tilde{y}_{x\mu^\pm}(t). \tag{3.93b}$$

The explicitly separated free rotations are quite fast (their frequencies are of the order of $E_g/\hbar$), while the time scales on which quantities $\tilde{y}_x$ and $\tilde{y}_{x\mu^\pm}$ exhibit appreciable changes are typically orders of magnitude slower, meaning that the time step with which their evolution should be followed is much longer than h/E_g.

Analysis of the Semiconductor Dynamics

An optical excitation of sufficient energy (of the order of the band gap E_g) initially creates coherent quantities y_x and $y_{x\mu^\pm}$. Let us cite here the source term (the term proportional to the exciting field) of interband polarizations y_x

$$(\partial_t y_x)_{\text{source}} = -\frac{1}{\mathrm{i}\hbar}\mathbf{E}(t)\mathbf{M}_x, \tag{3.94}$$

and exciton populations and exciton–exciton coherences $n_{\bar{x}x}$

$$(\partial_t n_{\bar{x}x})_{\text{source}} = -\frac{1}{\mathrm{i}\hbar}\mathbf{E}(t)\left(y_{\bar{x}}^*\mathbf{M}_x - \mathbf{M}_{\bar{x}}^* y_x\right). \tag{3.95}$$

Comparing the last two equations, we see that the source term in equation for $n_{\bar{x}x}$ is identical to the source term for quantity $y_{\bar{x}}^* y_x$ which, according to Eq. (3.47), represents the coherent part of quantity $n_{\bar{x}x}$. Therefore, during the action of the pulse, exciton populations n_{xx} and exciton–exciton coherences $n_{\bar{x}x}$ ($\bar{x} \neq x$) start to build up, their sources being interband polarizations. The next sequence of the dynamics sees the decline of coherent densities due to the scattering with phonons, while incoherent exciton populations and exciton–exciton coherences increase. The scattering mechanisms typically become active already during the excitation, so that the decay of coherent quantities is almost completed by the end of the pulse. Moreover, scattering events also lead to a redistribution of exciton populations and a slow decay of exciton–exciton coherences, which is taken into account by the nontrivial time evolution of phonon-assisted density matrices $n_{\bar{x}x\mu^+}$. After the pulse has vanished, due to the constancy of the total number of excitons [Eq. (3.54)], coherent exciton populations $|y_x|^2$ are converted into incoherent exciton populations $\bar{n}_{xx}$ on a time scale that ranges from a couple of femtoseconds to a couple of tens of femtoseconds. On the other hand, density matrices $n_{\bar{x}x}$ and $n_{\bar{x}x\mu^+}$ influence the dynamics on much longer time scales after the end of the excitation. Eventually, single-phonon-assisted density matrices $n_{\bar{x}x\mu^+}$ are expected to vanish, while exciton–exciton coherences may vanish or, more generally, reach some steady-state values. The exciton populations are then expected to reach their equilibrium or, more generally, steady-state values [71].

Chapter 4

Ultrafast Dynamics of Exciton Formation and Relaxation in Photoexcited Neat Semiconductors

This chapter is devoted to a detailed investigation of exciton formation and early stages of exciton relaxation in a neat semiconductor excited by a pulsed optical excitation. As has been discussed in Ch. 1, the findings obtained in such a study are not only interesting *per se*, but may also have a broader impact on our understanding of the very initial stages of the light-to-current conversion in OSCs. A brief summary of existing experimental and theoretical results that are relevant for the topic is provided in Sec. 4.1. In Secs. 4.2 and 4.3, we present our results regarding picosecond exciton dynamics in a photoexcited neat semiconductor. The content of these two sections is based upon our article [89]. Further discussion on our results and their broader significance are topics of Sec. 4.4.

4.1 Theoretical and Experimental Background

The nature of primary photoexcitations in pristine semiconducting polymers has been a subject of intense scientific debate. Historically, there are two different standpoints from which the origin of semiconducting properties of conjugated polymers has been considered [15, 44, 45].

The energy-band picture of electrons in semiconducting polymers, epitomized by the Su–Schrieffer–Heeger model, was developed for a perfect, infinite, one-dimensional polymer chain, as has been discussed in Ch. 1. The energy band gap arises due to the alternation of single and double bonds between consecutive carbon atoms in the polymer chain. Then, the Peierls instability in a one-dimensional system at half-filling opens up the energy gap between the completely filled π band and the completely empty π^* band, therefore the polymer chain shows semiconducting properties. However, such a view of conjugated polymers entirely neglects the electron–electron correlation and the electron–hole interaction, thus interpreting the optical absorption as an electronic transition from the valence band to the conduction band and generation of essentially free charges, just as in typical inorganic semiconductors.[1]

Semiconducting properties of a polymer chain may also be understood by using the molecular picture. Successive molecular repeat units along the chain are mutually coupled. Therefore, due to the translational symmetry of the chain, this coupling of neighboring molecular units leads to the broadening of molecular energy levels and formation of bands. The π and π^* bands arise from HOMO and LUMO orbitals of molecular repeat units and represent the valence and conduction band, respectively. Let us point out that, in the molecular picture, it is the electronic coupling between repeat units that is at the heart of the semiconducting properties of a perfectly ordered polymer chain. They are independent on whether or not the system shows bond alternation or aromaticity. The molecular picture considers the Coulomb interaction to be strong, so that an optical excitation of a conjugated polymer results in the formation of a neutral excited state, i.e., a strongly bound electron–hole pair.

Time-resolved studies of the dynamics of photoinduced electronic excitations in neat conjugated polymers on multiple time scales [46, 47] suggest that the nature of excitations is complex and dependent on the time scale on which they are observed. Experimental insights into the temporal evolution of photoexcitations are provided by studying the time-dependent emission following the initial light absorption. A suitable experimental technique is embodied in the so-called time-resolved fluorescence up-conversion (TR-FU) spectroscopy, which extracts information of interest from the fluorescence decay. TR-FU spectroscopy presents a selective probe of neutral photoexcitations and is thus well suited to gain insight into the dynamics of exciton formation and relaxation. The major part of the fluorescence decay occurs on time scales spanning the range from 100 fs to 1 ns, so that the time-resolved fluorescence spectroscopy requires short laser pulses and instrumentation featuring high temporal resolution. We now describe the essence of the TR-FU technique [46, 123]. The sample is first excited by means of an ultrashort pump pulse, which triggers its fluorescence. After a certain time delay τ, the sample is irradiated by the probe laser pulse, which is then, together with the fluorescence, confocused on a nonlinear optical (NLO) crystal. The NLO crystal serves to enhance the fluorescence of the sample by the sum-frequency generation with the probe pulse, which results in the up-converted fluorescence signal (the down-converted signal would be generated by the difference-frequency generation). The up-converted signal is then spectrally analyzed and its intensity and polarization are measured. The fluorescence dynamics at different emission wavelengths can be studied by a suitable reorientation of the NLO crystal. The time evolution of the fluorescence signal can be obtained by performing the described measurement for different time delays τ of the probe laser pulse with respect to the pump laser pulse. By identifying the time scales involved in the fluorescence decay at various emission wavelengths, one can gain a detailed insight into the photophysics of the material of the sample.

---

[1] Let us note that present discussion emphasizes the importance of the Coulomb interaction and does not consider the role of the carrier–phonon interaction in this process. In this sense, having in mind that, within the energy-band picture, the carrier–phonon coupling is strong, it is more appropriate to say that the optical absorption across the band gap creates a pair of positively and negatively charged polarons.

Let us now summarize (without going into materials-specific details) the main results presented in Refs. [46, 47]. The experiments provide evidence that, directly ($\lesssim$ 100 fs) after the photoexcitation across the band gap, delocalized electrons and holes in their respective energy bands are formed. This is followed by the relaxation of electrons and holes towards the band edges and the formation of bound electron–hole pair states on a time scale of $\sim$ 500 fs–1 ps. Further relaxation of excitons thus formed occurs on multiple time scales, ranging from hundreds of femtoseconds to tens of picoseconds. Therefore, the experiments suggest that the exciton formation, i.e., the build-up of the Coulomb correlation between electrons and holes, is not an instantaneous process (as assumed in the molecular picture), but a rather complex process happening over a range of time scales.

Theoretical investigations of the dynamics of exciton formation in organic semiconductors are rather scarce. In the literature, there are reports on the dynamics of exciton formation from an initial state of two opposite charges in organic semiconductors. It was typically modeled by simulating the time evolution of empirical Hamiltonians applied to small systems, where the effects of the lattice are not included at all or are treated classically [124, 125]. These studies were motivated by applications in organic light-emitting diodes, whose working mechanism is in some sense the reverse of the working mechanism of OSCs. The dynamics of light-induced exciton formation in organic semiconductors has not received wider theoretical attention, mainly because of the challenges related to the treatment of strong carrier–carrier and carrier–phonon interactions. One should explicitly and simultaneously consider the interaction with the optical field generating electronic excitations, the Coulomb interaction causing the binding of electrons and holes into excitons, the carrier delocalization, and the carrier–phonon coupling that is responsible for relaxation processes. Apart from the treatment of the rather strong Coulomb interaction, a matter of concern to the theoretical modeling is also the carrier–phonon coupling, which is commonly considered to be quite strong in organic semiconductors. As a result, carriers are expected to undergo strong phonon-induced renormalization and have polaronic character, meaning that the treatment of the carrier–phonon coupling should be essentially unperturbative. However, in Ref. [126], a microscopic treatment of the carrier–phonon coupling in a crystalline organic semiconductor provided evidence for nonpolaronic nature of charge carriers. With this result in mind, in this thesis, we content ourselves with the essentially perturbative treatment of the carrier–phonon coupling that has been presented in Ch. 3. The treatment of the Coulomb interaction in Ch. 3 effectively neglects electron–electron and hole–hole interactions, which is a sufficiently good approximation in the low-density regime we are concentrated on. It, however, treats the electron–hole interaction, which is the most important ingredient in the exciton formation process, properly in the low-density limit. On subpicosecond and picosecond time scales, which are of our main interest, the effects of exciton recombination can safely be neglected, since the exciton lifetime in most organic semiconductors is of the order of hundreds of picoseconds [127]. Therefore, we are confident that the theoretical treatment introduced in Ch. 3 can provide us with meaningful insights into the dynamics of exciton formation and relaxation on ultrafast time scales.

4.2 Model Description

4.2.1 One-Dimensional Semiconductor Model

The exciton formation and relaxation dynamics are studied in a two-band one-dimensional semiconductor model. We use a tight-binding model on a one-dimensional lattice with N sites and lattice spacing a to describe the semiconductor. Periodic boundary conditions are used. The Hamiltonian describing interacting carriers is given as

$$\begin{aligned} H_\mathrm{c} = &\sum_{i=0}^{N-1} \epsilon_0^\mathrm{c}\, c_i^\dagger c_i - \sum_{i=0}^{N-1} J^\mathrm{c}(c_i^\dagger c_{i+1} + c_{i+1}^\dagger c_i) - \sum_{i=0}^{N-1} \epsilon_0^\mathrm{v}\, d_i^\dagger d_i + \sum_{i=0}^{N-1} J^\mathrm{v}(d_i^\dagger d_{i+1} + d_{i+1}^\dagger d_i) \\ &+ \frac{1}{2}\sum_{i,j=0}^{N-1} (c_i^\dagger c_i - d_i^\dagger d_i) V_{ij} (c_j^\dagger c_j - d_j^\dagger d_j). \end{aligned} \tag{4.1}$$

Operators $c_i^\dagger$ and c_i ($d_i^\dagger$ and d_i) create and annihilate an electron (a hole) at lattice site i. It is assumed that the carrier transfer integrals J^c, J^v are nonzero only among nearest-neighbor pairs of sites. The Coulomb interaction is taken into account in the lowest monopole–monopole approximation [87], and the interaction potential V_{ij} is taken to be the Ohno potential

$$V_{ij} = \frac{U}{\sqrt{1 + \left(\frac{|i-j|a}{a_0}\right)^2}}. \tag{4.2}$$

The Ohno potential is commonly used to describe the electron–electron interaction in conjugated polymers [77]. U is the on-site carrier–carrier interaction, while a_0 is the characteristic length given as $a_0 = e^2/(4\pi\varepsilon_0\varepsilon_r U)$, where ε_r is the static relative dielectric constant. This form of carrier–carrier interaction is an interpolation between the on-site Coulomb interaction U and the ordinary Coulomb potential (in which the static relative dielectric constant is taken) $e^2/(4\pi\varepsilon_0\varepsilon_r r)$ when $r \to \infty$ (see, e.g., the discussion on the effective electron–hole interaction in Ref. [86]). The interaction with phonons is taken to be of the Holstein form, where a charge carrier is locally and linearly coupled to a dispersionless optical mode

$$H_\mathrm{c-p} = \sum_{i=0}^{N-1} g^\mathrm{c}\, c_i^\dagger c_i (b_i + b_i^\dagger) - \sum_{i=0}^{N-1} g^\mathrm{v}\, d_i^\dagger d_i (b_i + b_i^\dagger), \tag{4.3}$$

where the free-phonon Hamiltonian describes noninteracting oscillators localized at single lattice sites

$$H_{\mathrm{p}} = \sum_{i=0}^{N-1} \hbar\omega_{\mathrm{ph}} b_i^\dagger b_i. \tag{4.4}$$

Despite the fact that the carrier–phonon interaction in real materials has a more complicated form, we choose for our numerical investigations its simplest possible form [Eq. (4.3)] capable of providing the energy relaxation of the electronic subsystem. The interaction with the electric field is

$$H_{\mathrm{c-f}} = -d^{\mathrm{cv}} E(t) \sum_{i=0}^{N-1} (d_i c_i + c_i^\dagger d_i^\dagger), \tag{4.5}$$

where d^{cv} denotes the interband dipole matrix element.

As the system described is translationally symmetric, we can transfer to the momentum space and obtain the same Hamiltonian as described in Eqs. (2.34)–(2.38) with the following values of parameters:

$$\epsilon_k^{\mathrm{c/v}} = \epsilon_0^{\mathrm{c/v}} - 2J^{\mathrm{c/v}} \cos(ka), \tag{4.6a}$$

$$\gamma_{k_1 k_2}^q = \delta_{k_2, k_1+q} \frac{g^{\mathrm{c}}}{\sqrt{N}} \, \mathrm{for} \, k_1, k_2 \in \mathrm{CB}, \tag{4.6b}$$

$$\gamma_{k_1 k_2}^q = \delta_{k_1, k_2+q} \frac{g^{\mathrm{v}}}{\sqrt{N}} \, \mathrm{for} \, k_1, k_2 \in \mathrm{VB}, \tag{4.6c}$$

$$V_{pqkl}^{\mathrm{vvcc}} = \delta_{k+q, p+l} V_{k-l}, \quad V_{plkq}^{\mathrm{vccv}} = 0. \tag{4.6d}$$

There are exactly N allowed values of wave vector k that are consistent with the periodic boundary conditions,

$$k = \frac{2\pi}{Na} n, \tag{4.7}$$

where n is an integer. Within the first Brillouin zone, the upper limit of n is $\left\lfloor \frac{N}{2} \right\rfloor$, while its lower limit is $-\left\lfloor \frac{N}{2} \right\rfloor$. We take that the signs of the transfer integrals are $J^{\mathrm{c}} > 0$, $J^{\mathrm{v}} < 0$. The constant energy $\epsilon_0^{\mathrm{c}} > 0$, while $\epsilon_0^{\mathrm{v}} < 0$ is chosen so that the maximum of the valence band is the zero of the energy scale. V_{k-l} is the Fourier transformation of the Ohno potential and it is computed numerically as

$$V_k = \frac{1}{N^2} \sum_{i,j=0}^{N-1} V_{ij}\, \mathrm{e}^{-\mathrm{i}ka(i-j)}. \tag{4.8}$$

The translational symmetry of our model enables us to efficiently solve the eigenvalue problem [Eq. (2.46)] that defines the exciton basis. Using Eq. (4.6), Eq. (2.46) can be rewritten as

$$\left(\epsilon^{\mathrm{c}}_{k_e} - \epsilon^{\mathrm{v}}_{k_h}\right) \psi^{x}_{k_h k_e} - \sum_{k'_e} V_{k_e - k'_e} \psi^{x}_{k_h + k_e - k'_e, k'_e} = \hbar\omega_x \psi^{x}_{k_h k_e}. \tag{4.9}$$

Equation (4.9) shows that each exciton state x is characterized by the sum $Q = k_h + k_e$, which can be interpreted as the center-of-mass wave vector of the electron–hole pair. The wave vector Q can assume N possible values that are of the type given in Eq. (4.7). Therefore, instead of regarding Eq. (4.9) as the eigenvalue problem of an $N^2 \times N^2$ matrix, we can regard it as N independent eigenvalue problems (one for each allowed value of Q) of matrices of dimension $N \times N$. We thus obtain N^2 exciton eigenstates, which are counted by Q and the so-called band index $\nu = 0, 1, \ldots, N-1$. The band index enumerates the distinct eigenstates of the aforementioned $N \times N$ matrix. While Q characterizes the motion of the pair as a whole, ν describes the internal motion of the pair, see also a more general discussion in Appendix D.1. As an efficient and numerically accurate tool to solve the eigenvalue problem embodied in Eq. (4.9), we used routines provided by the Linear Algebra Package (LAPACK), which is a standard software library for numerical linear algebra. In our computations, N is of the order of 100, and the solution of 100 eigenvalue problem of matrices of dimension 100×100 takes a couple of seconds on a single processor. The numerical complexity lies in the integration of the system of quantum kinetic equations, which will be addressed in more detail in Sec. 4.3.

The general index of an exciton state x should be, in all practical calculations, replaced by combination (Q, ν). This has the following consequences on the matrix elements in the exciton basis: dipole matrix elements [Eq. (3.50)] reduce to

$$M_{(Q\nu)} = \delta_{Q,0}\, d^{\mathrm{cv}} \sum_{k_e} \psi^{(Q\nu)*}_{Q-k_e, k_e}, \tag{4.10}$$

whereas carrier–phonon interaction matrix elements [Eq. (3.51)] reduce to

$$\Gamma^{q}_{(Q\nu)(Q'\nu')} = \delta_{Q',Q+q}\frac{1}{\sqrt{N}}\sum_{k_e}\psi^{(Q\nu)*}_{Q-k_e,k_e}\left(g^{\mathrm{c}}\psi^{(Q'\nu')}_{Q-k_e,Q'-Q+k_e} - g^{\mathrm{v}}\psi^{(Q'\nu')}_{Q'-k_e,k_e}\right). \tag{4.11}$$

Due to the translational symmetry of our model, only the dynamic variables for which the total created wave vector is equal to the total annihilated wave vector will acquire nontrivial values in the course of the system's evolution. For example, from all the density matrices $y_{(Q\nu)}$, only those with $Q = 0$ can have nonzero values.

Our objective is to analyze, within the framework of this relatively simple model, the characteristic time scales of exciton formation and relaxation in a photoexcited semiconductor, along with the impact that various model parameters have on these processes. Basic parameters in our model are transfer integrals J^{c} and J^{v} (which determine bandwidths of the conduction and valence bands), electron–phonon coupling constants g^{c} and g^{v}, the phonon energy $\hbar\omega_{\mathrm{ph}}$, the dielectric constant ε_r, and the on-site Coulomb interaction U. We will, throughout the computations, assume for simplicity that $|J^{\mathrm{c}}| = |J^{\mathrm{v}}| = J$ and $g^{\mathrm{c}} = g^{\mathrm{v}} = g$.

4.2.2 Parametrization of the Model Hamiltonian

As has been discussed in more detail in Ch. 1, the main differences between a typical organic and inorganic semiconductor can be expressed in terms of bandwidths, dielectric constant, and the carrier–phonon interaction strength, see, e.g., Ref. [6]. Namely, inorganic semiconductors are characterized by wide bands and high value of dielectric constant (good dielectric screening), whereas organic semiconductors have narrow bands and small value of dielectric constant (the Coulomb interaction is poorly screened). The carrier–phonon interaction is generally stronger in organic than in inorganic semiconductors. Having all these facts in mind, we propose two sets of model parameters which assume values typical of an organic and inorganic semiconductor. Values of our model parameters are adjusted to material parameters of bulk GaAs for the inorganic case and pentacene crystal for the organic case. Values of carrier–phonon coupling constants are chosen to correspond to typical values of mobility and/or typical values of the polaron binding energy.

The lattice constant is fixed to $a = 1$ nm for both organic and inorganic parameter sets. Typical bandwidths in organic semiconductors are $W \sim 500$ meV [6], which corresponds to the transfer integral of $J \sim 125$ meV in our one-dimensional model. On the other hand, inorganic semiconductors usually exhibit bandwidths of several electronvolts [6], and we take in our calculations the value of the transfer integral $J = 500$ meV. The dielectric constant in a typical inorganic semiconductor is of the order of 10 and in the calculations we take the value of static dielectric constant of GaAs $\varepsilon_r = 12.9$. For a representative value of the dielectric constant in organic semiconductors we take $\varepsilon_r = 3.0$. The value of the on-site Coulomb interaction U is chosen to give the correct order of magnitude for the exciton binding energy, which is calculated numerically as the energy difference between the lowest-lying exciton state $(Q = 0, \nu = 0)$[2] and the single-particle band gap at $Q = 0$, cf. Eqs. (2.75)–(2.77). For the organic parameter set, we set $U = 480$ meV, which gives the exciton binding energy of around 320 meV, while for the inorganic parameter set $U = 15$ meV and the corresponding exciton binding energy is roughly 10 meV.

The carrier–phonon coupling constants for the inorganic case are estimated from the mobility values. The mobility of carriers is estimated using the relation $\mu = e\tau/m^*$, where τ is the inelastic scattering time, $e > 0$ is the elementary charge, and m^* is the effective mass of a carrier. For cosine bands considered here, $m^* = \hbar^2/\left(2|J|a^2\right)$ in the vicinity of the band extremum. The scattering time is estimated from the expression for the carrier–phonon inelastic scattering rate based on the Fermi's golden rule, which around the band extremum $k = 0$ assumes the following form:

$$\frac{1}{\tau(k)} = \frac{g^2}{\hbar|J|} \frac{n^{\mathrm{ph}}}{\sqrt{1 - \left(\cos(ka) - \frac{\hbar\omega_{\mathrm{ph}}}{2|J|}\right)^2}}, \tag{4.12}$$

where $n^{\mathrm{ph}} = (\mathrm{e}^{\beta\hbar\omega_{\mathrm{ph}}} - 1)^{-1}$. Therefore, the carrier–phonon coupling constant in terms of the carrier mobility reads as

$$g = |J|\sqrt{\frac{2ea^2}{\hbar\mu n^{\mathrm{ph}}}} \left(1 - \left(1 - \frac{\hbar\omega_{\mathrm{ph}}}{2|J|}\right)^2\right)^{1/4}. \tag{4.13}$$

---

[2] Here, the lowest band of exciton states is $\nu = 0$, while the integer index of the lowest-energy Wannier exciton in Sec. 2.3.1 is $n = 1$.

TABLE 4.1: Values of model parameters that are representative of a typical organic and inorganic semiconductor. References from which the values of material parameters are extracted are indicated.

Parameter	Inorganic	Organic
E_g (meV)	1519 [115]	2000 [130]
J (meV)	500	125
ε_r	12.9 [115]	3.0 [6]
g (meV)	25	40
$\hbar\omega_{\mathrm{ph}}$ (meV)	36.4 [115]	10.0 [131, 132]
U (meV)	15	480

Using the value of the electron mobility in GaAs at 300 K, $\mu_{\mathrm{e}} \approx 8500$ cm^2/(Vs) [128], we obtain $g \approx 25$ meV.

We can also estimate the carrier–phonon coupling constants from the polaron binding energy. As an estimate of this quantity, we use the result of the second-order weak-coupling perturbation theory at $T = 0$ in the vicinity of the point $k = 0$ [129]:

$$\epsilon_{\mathrm{b}}^{\mathrm{pol}}(k) = \frac{g^2}{2|J|} \frac{1}{\sqrt{\left(\cos(ka) + \frac{\hbar\omega_{\mathrm{ph}}}{2|J|}\right)^2 - 1}}. \tag{4.14}$$

It is known that polaron binding energies in typical inorganic semiconductors are $\epsilon_{\mathrm{b}}^{\mathrm{pol}} \sim 1$ meV and we use this fact along with Eq. (4.14) to check our estimate for g from the value of mobility; for $g \approx 25$ meV, we obtain $\epsilon_{\mathrm{b}}^{\mathrm{pol}} \approx 2$ meV. The polaron binding energies in polyacenes lie in the range between 21 and 35 meV [17]. The value of g in the set of model parameters representative of organic semiconductors was estimated from the polaron binding energy in pentacene, which is around 20 meV. We obtain that $g \approx 40$ meV. The values used for the organic/inorganic set of parameters are summarized in Table 4.1.

The form of the electric field is assumed to be a rectangular cosine pulse

$$E(t) = E_0 \cos(\omega_c t)\theta(t + t_0)\theta(t_0 - t), \tag{4.15}$$

where ω_c is the central frequency of the field and $\theta(t)$ is the Heaviside step function. Time t_0 is chosen large enough so that the pulse is so spectrally narrow that the notion of the central

TABLE 4.2: Numbers of active density matrices in the most general case (the first two columns) and the case specific to our model (the last two columns). The wave vectors appearing as arguments of the density matrices listed in the third column assume the form given in Eq. (4.7).

General Form	Total Number	Specific Form	Actual Number
y_x	N^2	$y_{(Q=0,\nu)}$	n_{band}
$y_{x\mu^+}$	N^3	$y_{(q\nu)q^+}$	$N \times n_{\text{band}}$
$y_{x\mu^-}$	N^3	$y_{(-q\nu)q^-}$	$N \times n_{\text{band}}$
$n_{\bar{x}x}$	N^4	$n_{(Q\bar{\nu})(Q\nu)}$	$N \times n_{\text{band}}^2$
$n_{\bar{x}x\mu^+}$	N^5	$n_{(Q-q,\bar{\nu})(Q\nu)q^+}$	$N^2 \times n_{\text{band}}^2$

frequency makes sense. On the other hand, the pulse should be as short as possible, so that after its end we observe the intrinsic dynamics of our system, the one which is not accompanied by the carrier generation process, but merely shows how initially generated populations are redistributed among various states. Trying to reconcile the aforementioned requirements, we choose $t_0 = 250$ fs. The amplitude of the electric field E_0 and the interband dipole matrix element d^{cv} are chosen so that we stay in the low-density regime; particularly, we choose them so that the corresponding Rabi frequency $\hbar\omega_R = d^{\text{cv}}E_0$ assumes the value of 0.2 meV, which is smaller than any energy scale in our problem and ensures that the excitation is weak.

4.3 Numerical Results

In order to quantitatively study the process of exciton formation during and after a pulsed excitation of a semiconductor, we solve the system of quantum kinetic equations for electronic density matrices y_x and $n_{\bar{x}x}$, and their single-phonon-assisted counterparts [Eqs. (3.48), (3.49), (3.66), (3.67), and (3.68) supplemented with Eqs. (3.79) and (3.81)] using the fourth-order Runge–Kutta algorithm [133]. The model described in Sec. 4.2.1 features N^2 exciton states and N phonon modes in total. The total numbers of density matrices of various types are presented in the second column of Table 4.2. However, in actual computations, the number of active density matrices is further reduced by combining the translational symmetry of the model with the fact that the central frequency of the excitation and the thermal energy crucially determine the number of exciton states that can be involved in the ultrafast dynamics. For the sake of convenience in numerical implementation, in our computations, we do not select a certain number of lowest-lying exciton states, but deal only with whole exciton bands, and consider only $n_{\rm band}$ lowest-lying bands. For the given central frequency ω_c of the excitation, we take into account all the bands whose minima lie below $\hbar\omega_c + \alpha k_B T$, where $\alpha \sim 5$ is a numerical constant. We have explicitly checked that employing higher values of α does not significantly change our numerical results. The forms of the active density matrices that take into account the translational symmetry of our model are summarized in the third column of Table 4.2. The fourth column of Table 4.2 lists the numbers of various types of density matrices that are actually considered in computations. In the computations whose results are presented in Sec. 4.3.1, we take $N = 101$, while $n_{\rm band}$ is typically around 25, so that the total number of single-phonon-assisted density matrices $n_{(Q-q,\bar{\nu})(Q\nu)q^+}$ typically ranges between 5×10^6 and 10^7. Since the numbers of the active density matrices of other types are much smaller, see the fourth column of Table 4.2, the system of mutually coupled differential equations that we have to solve contains around ten million equations in total. It is then clear that high performance computing (HPC) resources play a crucial role in solving such a large system of equations in a reasonable amount of time. Our computations are performed on the PARADOX supercomputing facility at the Scientific Computing Laboratory of the Institute of Physics Belgrade. We construct our own `C` program that can be run in parallel on a number of processors. The communication between different processors is accomplished by using Message Passing Interface (MPI) routines. In order to keep this communication at a reasonable level, at each time step, all of the processors keep information about all of the active density matrices.[3] The parallelization scheme that we adopt, therefore, does not involve the reduction in size of the memory space used by individual processors, but rather reduces the execution time by evenly dividing numerical effort between processors. Namely, each of the processors effectively computes time evolution of only a portion of the total number of each of the five types of active density matrices listed in Table 4.2, while the values of all the other density matrices are set to zero. This is schematically depicted in Fig. 4.1, in which processor P$_i$ computes only portion i (in gray) of the active density matrices. After the calculations in one time step have

---

[3] Since one time step in fourth-order Runge–Kutta method consists of four substeps, this also holds in individual substeps.

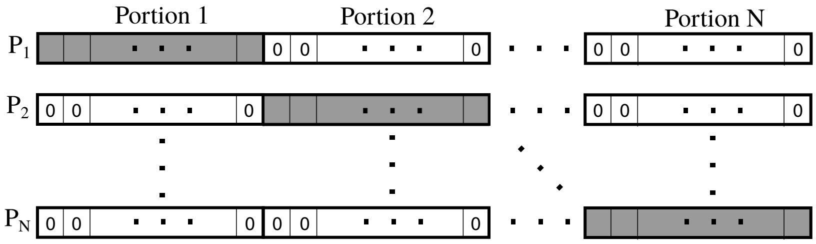

FIGURE 4.1: Schematic view of the parallelization scheme implemented in our own `C` program that performs integration of the system of quantum kinetic equations. Each row shows the memory space allocated by individual processors. Columns show the division of the memory space into portions. In row i, only the density matrices in the portion in gray (Portion i) are actually propagated in time by processor P_i.

been completed, a simple column-wise summation of the results obtained on individual processor ensures that all of the processors have information on all of the active density matrices. Our computations were typically performed on 64 or 128 CPU cores. Regarding the time step for numerical integration of the system of quantum kinetic equations, after separating out the fast free evolution of coherent quantities y_x and $y_{x\mu^\pm}$ [see Eq. (3.93)], the equations for quantities $\tilde{y}_x$, $\tilde{y}_{x\mu^\pm}$, $n_{\bar{x}x}$, and $n_{\bar{x}x\mu^+}$ can be integrated with the same time step $\Delta t = 0.8$ fs. Therefore, computing 5 fs of exciton dynamics requires 6250 time steps. In the computations whose results are presented in Sec. 4.3.1, each time step lasts for around 2.5 s, meaning that 5 fs of exciton dynamics is typically computed within ca. 5 hours.

If not explicitly states otherwise, the computations are performed for the temperature $T =$ 300 K and the central frequency of the pulse equal to the single-particle gap ($\hbar\omega_c = E_g$).

The exciton state characterized by pair (Q, ν) is considered bound (unbound) if its energy $\hbar\omega_{(Q\nu)}$ is smaller (larger) than the smallest (with respect to k_e) single-particle energy difference $\epsilon^{\mathrm{c}}_{k_{\mathrm{e}}} - \epsilon^{\mathrm{v}}_{Q-k_{\mathrm{e}}}$ [130]. The equation of the boundary line that separates bound from unbound pair states reads as

$$\epsilon_{\mathrm{sep}}(Q) = \epsilon^{\mathrm{c}}_0 - \epsilon^{\mathrm{v}}_0 - 2\sqrt{(J^{\mathrm{c}})^2 + (J^{\mathrm{v}})^2 - 2J^{\mathrm{c}}J^{\mathrm{v}}\cos(Qa)}. \tag{4.16}$$

An unbound exciton may be considered as (quasi)free electron and hole, so this way it is possible to distinguish between bound excitons and free carriers.

The exciton formation and the initial stages of exciton relaxation are examined by following the decay of the coherent pair occupation

$$N_{\mathrm{coh}} = \sum_{\nu} |y_{(Q=0,\nu)}|^2, \tag{4.17}$$

and the build-up of the total number of incoherent bound excitons

$$N_{\mathrm{incoh,b}} = \sum_{x \in \mathrm{bound}} \bar{n}_{xx}. \tag{4.18}$$

The quantity $N_{\mathrm{incoh,b}}$ represents the number of truly bound electron–hole pairs that exist even after the optical field has vanished and, as such, is the direct measure of the efficiency of the exciton formation process. We will, when useful, also consider the number of incoherent excitons in a particular band ν,

$$N_{\mathrm{incoh},\nu} = \sum_{Q} \bar{n}_{(Q\nu)(Q\nu)}. \tag{4.19}$$

The quantities $N_{\mathrm{incoh,b}}$ and $N_{\mathrm{incoh},\nu}$ will be normalized to the total number of excitons N_{tot} defined in Eq. (3.54), which is conserved after the excitation.

4.3.1 Organic Set of Parameters

We start this section by an overview of the properties of the exciton spectrum shown in Fig. 4.2(a) that will be relevant for further discussion of the exciton formation process. The lowest band of exciton states is energetically well separated from the rest of the spectrum, the energy separation between the minima of the bands $\nu = 0$ and $\nu = 1$ being around 200 meV, which is much larger than both the value of $k_B T$ at room temperature and the phonon energy in our model (see Table 4.1). As a consequence, downward transitions that end on the lowest exciton band start almost exclusively from the states on $\nu = 1$ band and an exciton, which is at some instant in a state on the $\nu = 0$ band, cannot be scattered to an unbound exciton state.

We briefly comment on the size of the exciton for these values of model parameters. From the exciton wave function $\psi^{(Q\nu)}_{Q-k_e,k_e}$ in k space, we can obtain the exciton wave function in real

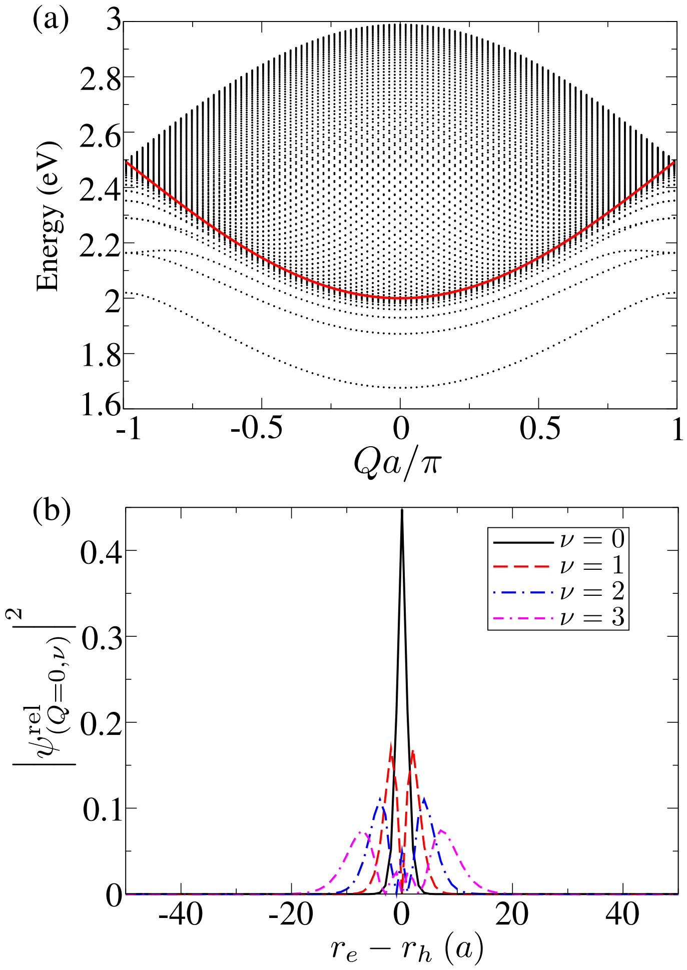

Figure 4.2: (a) Exciton spectrum for the organic set of parameters. Dots represent individual exciton states (Q, ν), while thick red line is the boundary between bound and unbound exciton states computed using Eq. (4.16). (b) Squared modulus of the wave function that describes the relative motion of an electron–hole pair [Eq. (4.21)] calculated for different states $(Q = 0, \nu)$. Mean electron–hole separations in these states are 0.7 a ($\nu = 0$), 2.5 a ($\nu = 1$), 4.6 a ($\nu = 2$), and 7.8 a ($\nu = 3$). Computations are performed for $N = 101$.

space by performing the Fourier transformation [compare to Eq. (2.69)]

$$\begin{aligned}\psi_{r_h r_e}^{(Q\nu)} &= \sum_{k_e} \mathrm{e}^{\mathrm{i}(Q-k_e)r_h} \mathrm{e}^{\mathrm{i}k_e r_e} \psi_{Q-k_e,k_e}^{(Q\nu)} \\ &= \mathrm{e}^{\mathrm{i}Q(r_e+r_h)/2} \sum_{k_e} \mathrm{e}^{-\mathrm{i}(Q-2k_e)(r_e-r_h)/2} \psi_{Q-k_e,k_e}^{(Q\nu)}.\end{aligned} \tag{4.20}$$

The exciton wave function in real space is a product of the plane wave that describes the motion of the center of mass with the wave vector Q and the wave function of the relative motion of an electron and a hole:

$$\psi_{(Q\nu)}^{\mathrm{rel}} = \sum_{k_e} \mathrm{e}^{-\mathrm{i}(Q-2k_e)(r_e-r_h)/2} \psi_{Q-k_e,k_e}^{(Q\nu)}. \tag{4.21}$$

The latter part is directly related to the exciton size. We calculated squared modulus of the wave function of the relative motion of a pair for states $(Q = 0, \nu)$ in various bands. The result is shown in Fig. 4.2(b). It is clearly seen that an electron and a hole are tightly bound in these states and their relative separations are of the order of lattice constant, which is the typical value for the exciton radius in organic semiconductors. We point out that this does not mean that an exciton is localized; due to the translational symmetry of our system, it is delocalized over the whole lattice, as described by the plane-wave factor in the total wave function of a pair. Moreover, we note that the system size $N = 101$ is large enough for the results to be numerically accurate, as it is much larger than the typical size of the exciton in a bound state.

Let us first discuss the exciton formation process for different central frequencies of the exciting pulse. We have considered central frequencies in resonance with $(Q = 0, \nu = 1)$ state, $(Q = 0, \nu = 2)$ state, single-particle gap E_g, and the central frequency which is 100 meV above the band gap. As can be noted from Fig. 4.3, raising the central frequency of the laser field leads to lower relative number of incoherent bound excitons. Namely, the higher is the central frequency, the higher (in energy) are the bands in which the initial coherent exciton populations are created and the slower is the conversion of these coherent populations to incoherent populations in lower exciton bands. However, in the long-time limit, the relative number of incoherent bound excitons should not depend on the central frequency of the laser, but tend to the value predicted by the Maxwell–Boltzmann distribution, which is above 99%. Such a high value is due to the

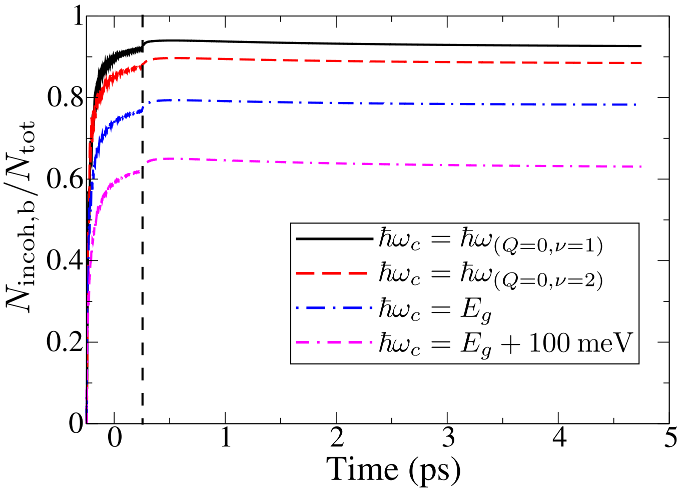

FIGURE 4.3: Time dependence of the relative number of incoherent bound excitons for different central frequencies of the pulse. The dashed vertical line marks the end of the pulsed excitation.

large energy separation between the lowest exciton band and the rest of the spectrum. We can thus infer, based on Fig. 4.3, that the semiconductor dynamics right after the pulsed excitation shows highly nonequilibrium features. Relaxation towards equilibrium occurs on a time scale longer than the picosecond one.

Next, we consider the dependence of the exciton formation process on temperature. The temperature enters our model only through phonon numbers n^{ph}. The overall behavior of the relative number of incoherent bound excitons for different temperatures is presented in Fig. 4.4. During the pulse, the relative number of incoherent bound excitons is highest for $T = 300$ K and lowest for $T = 100$ K, which is the consequence of the fact that scattering processes from higher-lying exciton bands (in which initial coherent exciton populations are created and which are situated both in the pair continuum and below it) towards lower-lying exciton bands are most efficient at $T = 300$ K. After the generation of carriers has been completed, phonon-mediated processes lead to the redistribution of created incoherent excitons among different exciton states and the relative number of incoherent bound excitons increases with decreasing the temperature, which is the expected trend. In the inset of Fig. 4.4 we also note that the relative number of incoherent bound excitons after the pulse experiences an initial growth followed by a slow decay at $T = 300$ K, whereas at $T = 100$ K it monotonically rises. The initial growth at $T = 300$ K is attributed to downward scattering processes, but since at this temperature upward scattering

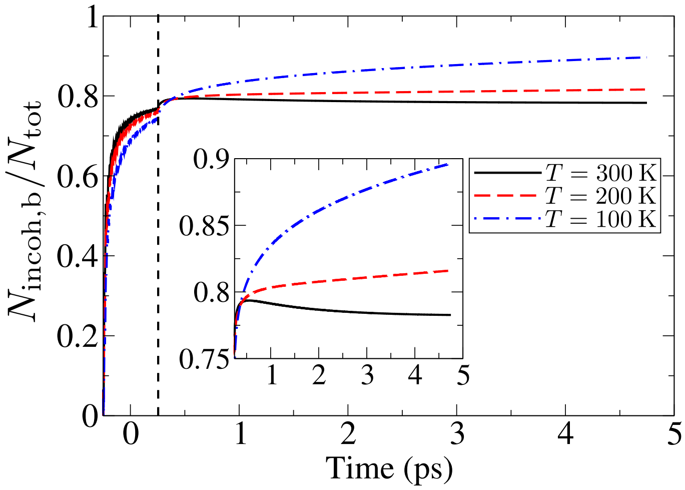

FIGURE 4.4: Time dependence of the relative number of incoherent bound excitons for different temperatures. The dashed vertical line marks the end of the pulsed excitation. The inset shows the portions of the same curves after the pulse.

events cannot be neglected, the following slow decay is due to the fact that some exciton bands situated well below the pair continuum (bands $\nu = 1, 2, 3$) lose excitons both by downward scattering and upward scattering to exciton states which are near to or belong to the pair continuum [see Figs. 4.5(a) and 4.5(b)]. At $T = 100$ K, these upward processes are much less probable than downward processes, thus the decay of the relative number of incoherent bound excitons is not observed; in Figs. 4.5(c) and 4.5(d) we see that lowest exciton bands ($\nu = 0, 1, 2$) gain excitons, whereas bands that are near to or belong to the pair continuum (ν = 9, 11, 13 ,15) lose excitons. The population of the lowest exciton band $\nu = 0$ continually grows at all the temperatures studied, due to the large energetic separation between this band and the rest of the spectrum.

We briefly comment on the behavior of the number of coherent excitons N_{coh} and its temperature dependence. Right after the start of the pulse, coherent excitons comprise virtually the total exciton population, see Fig. 4.6. Due to the carrier–phonon interaction, the relative number of coherent excitons decays during the pulse, so that at its end coherent excitons comprise around 1% of the total exciton population. The conversion from coherent to incoherent populations is thus almost completed by the end of the pulse. From the inset of Fig. 4.6, we note that $N_{\text{coh}}/N_{\text{tot}}$ exhibits a very fast decay after the pulse has vanished. The time it takes for the ratio $N_{\text{coh}}/N_{\text{tot}}$ to decay ten times is of the order of 50 fs or less. Therefore, we infer that the transformation from coherent to incoherent exciton populations takes place on a 50-fs time scale. Based on Fig. 4.6,

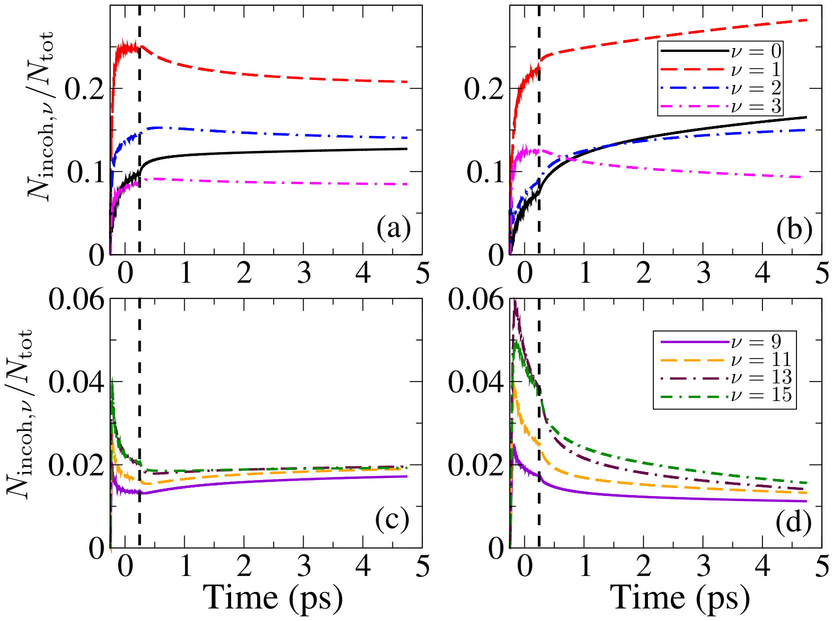

FIGURE 4.5: Time dependence of the relative population of various exciton bands for different temperatures, $T = 300$ K for panels (a) and (c) and $T = 100$ K for panels (b) and (d). Panels (a) and (b) concern bands which are well below the pair continuum ($\nu = 0$, 1, 2, 3), whereas panels (c) and (d) deal with the bands which are near the continuum ($\nu = 9$) or in the continuum ($\nu = 11$, 13, 15).

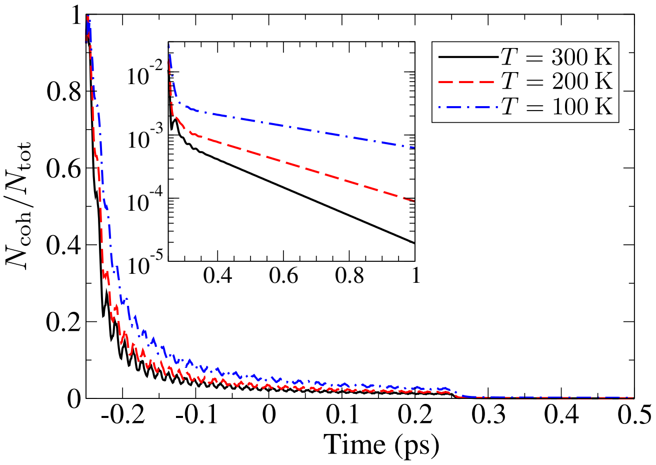

FIGURE 4.6: Time dependence of the relative number of coherent excitons for different temperatures. The inset shows the portions of the same curves (note the logarithmic scale on the vertical axis) after the pulse.

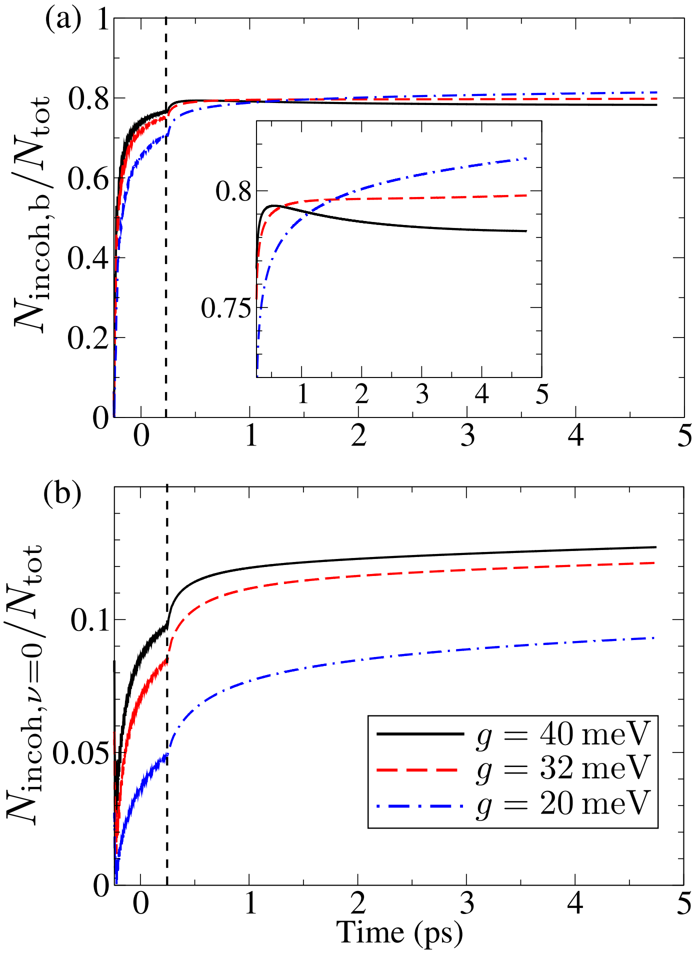

FIGURE 4.7: Time dependence of: (a) the relative number of incoherent bound excitons, (b) the relative number of incoherent excitons in the $\nu = 0$ band, for various values of g. The inset in the panel (a) shows the portions of the same curves after the pulse.

we also note that the lower is the temperature, the slower is the transformation from coherent to incoherent exciton populations, which is the expected trend.

We continue our investigation by examining the effects that changes in the carrier–phonon coupling constant g have on the exciton formation process. Since increasing (lowering) g increases (lowers) semiclassical transition rates, just as increasing (lowering) T does, the changes in g and T should have, in principle, similar effects on the exciton formation process. Considering first the relative number of incoherent bound excitons, whose time dependence for different values of g is shown in Fig. 4.7(a), we note that, after the end of the pulse, it increases with decreasing g. However, during the pulse, higher values of g lead to more incoherent bound excitons, as is expected since scattering processes which populate low-energy states are more

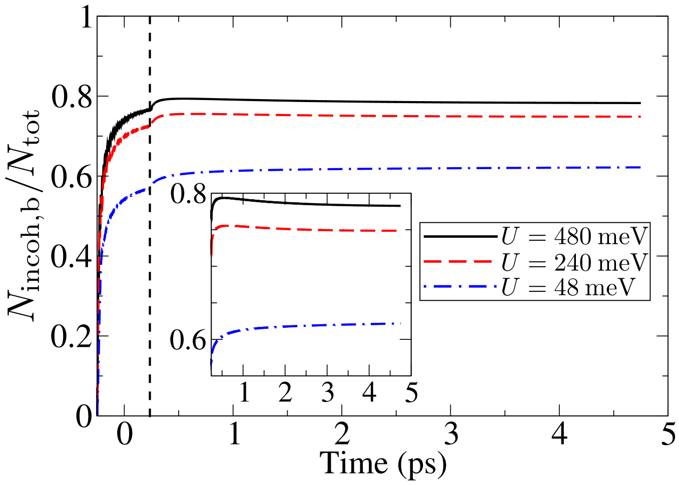

FIGURE 4.8: Time dependence of the relative number of incoherent bound excitons for various values of U. The inset shows the portions of the same curves after the pulse.

intensive for larger g. We also show the time dependence of the relative number of excitons in $\nu = 0$ band in Fig. 4.7(b). It is observed that the lower is g, the lower is the number of excitons in the lowest exciton band. This is due to the fact that populations on the lowest band are generated mainly via scattering processes from the $\nu = 1$ band and these processes are less efficient for smaller g.

We conclude this section by studying the effects that changes in the on-site Coulomb interaction U have on the process of exciton formation. Changing U has profound effects on the exciton spectrum. Exciton binding energy lowers with lowering U along with the energy separation between the band $\nu = 0$ and the rest of the spectrum. We studied the impact of U on the exciton formation process for three values of U, $U = 480$, 240, and 48 meV, for which the exciton binding energy is $\sim$ 320, $\sim$ 175, and $\sim$ 40 meV, respectively. Lowering U lowers the relative number of incoherent bound excitons, as is shown in Fig. 4.8. Smaller energy separation between the lowest exciton band and the rest of the spectrum means that phonon-mediated transitions which start/end on the band $\nu = 0$ can end/start not predominantly on the band $\nu = 1$, but also on higher exciton bands, which, for lower U, are more certain to belong to the electron–hole pair continuum than to the part of the spectrum that contains bound pair states. Thus, the lower is U, the more likely are the dissociation processes in which an exciton, initially in a bound state, after a phonon-mediated transition ends in an unbound pair state, which explains the observed trend in the relative number of incoherent bound excitons. This agrees with the usual picture according to which thermal fluctuations are likely to dissociate loosely bound electron–hole pairs. For $U = 48$ meV, in the long-time limit and according to the Maxwell–Boltzmann distribution, around 78% of the total number of excitons should be in bound states, whereas for the other two values of U this number is above 99%. Thus, the dynamics observed is highly nonequilibrium, but unlike the cases $U = 480$ meV and $U = 240$ meV, in which we cannot observe that the relative number of incoherent bound excitons starts to tend to its equilibrium value, for $U = 48$ meV we observe such a behavior (see the inset of Fig. 4.8).

Let us now list the time scales of the exciton formation and and initial stages of their relaxation that emerge from our computations. These time scales are obtained by fitting the normalized number of incoherent bound excitons $N_{\mathrm{incoh,b}}/N_{\mathrm{tot}}$ after the carrier generation has been completed to a sum of three exponentially decaying terms. The decay constants provided by the fitting procedure then indicate time scales on which changes in $N_{\mathrm{incoh,b}}/N_{\mathrm{tot}}$ occur. For model parameters representative of organic semiconductors, we obtain characteristic time scales of ~ 50 fs, ~ 500 fs, and $\gtrsim 1$ ps. These time scales are largely robust to the variations of model parameters that are performed in this section. Our discussion on the time evolution of the normalized number of coherent excitons (see the text accompanying Fig. 4.6) suggests that the fastest time scale be attributed to decoherence processes that are responsible for conversion from coherent ($|y_x|^2$) to incoherent ($\bar{n}_{xx}$) populations due to the interaction with phonons. The time scale of ~ 500 fs may be associated with the build-up of the Coulomb-induced correlations between electrons and holes by formation of bound incoherent electron–hole pairs via phonon-assisted scattering processes. After this time scale, however, intraband coherences $\bar{n}_{\bar{x}x}$ ($\bar{x} \neq x$), as well as single-phonon-assisted density matrices $n_{\bar{x}x\mu^+}$, still have significant values. In the long-time limit, these variables are expected to asymptotically vanish, and we remain only with incoherent populations whose dynamics will eventually lead to thermalized distribution of excitons [71]. As our computations are certainly not long enough to observe these effects, we speculate that the slowest time scale we obtain may be related to the decay of the intraband coherences and/or phonon-assisted variables.

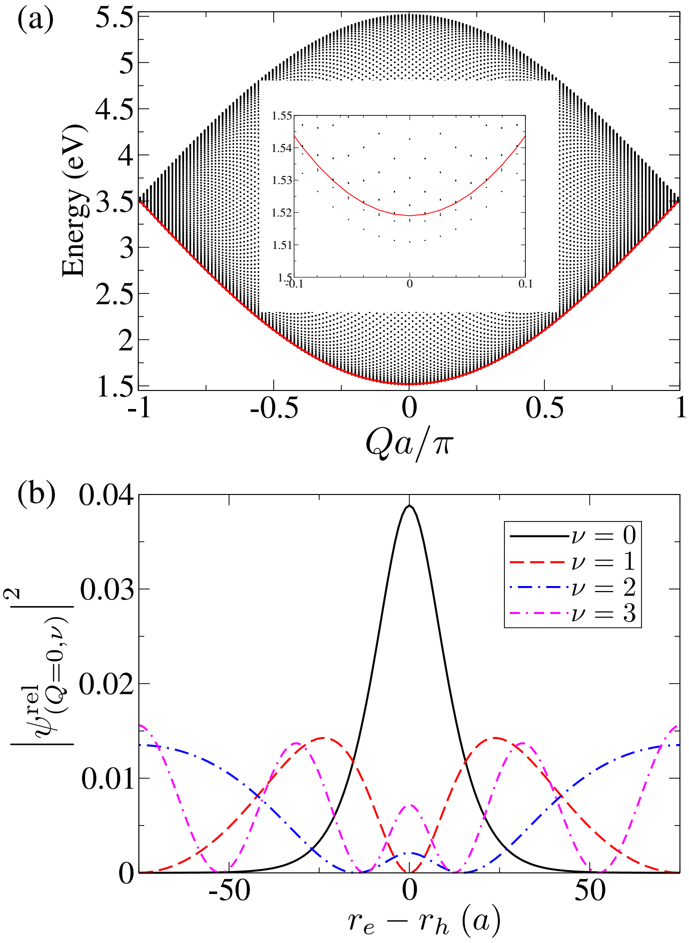

FIGURE 4.9: (a) Exciton spectrum for the inorganic set of parameters. Dots represent individual exciton states (Q, ν), while thick red line is the boundary between bound and unbound exciton states computed using Eq. (4.16). The inset shows the same spectrum in the range of energies around the single-particle gap. (b) Squared modulus of the wave function which describes the relative motion of an electron–hole pair [Eq. (4.21)] calculated for different states $(Q = 0, \nu)$. Mean electron–hole separations are 9.1 a $(\nu = 0)$ and 29.4 a $(\nu = 1)$, while states $(Q = 0, \nu = 2)$ and $(Q = 0, \nu = 3)$ are not bound. Computations are performed for $N = 151$.

4.3.2 Inorganic Set of Parameters

Here, we investigate the exciton formation process in the case when material parameters assume values typical of inorganic semiconductors, i.e., relatively large bandwidths, large dielectric constant (weak Coulomb interaction), and weak carrier–phonon interaction. The exciton spectrum is shown in Fig. 4.9(a). We see that almost all exciton bands belong to the pair continuum, except for a couple of lowest bands, which is more clearly seen in the inset of Fig. 4.9(a). This is an entirely different situation from the one that we encounter for the organic set of parameters, where large energy separation of the lowest exciton band from the rest of the spectrum was crucial to understand the exciton formation process. As a consequence, excitons in bound states are likely to scatter to states in the pair continuum, in contrast to the situation for the model parameters representative of an organic semiconductor.

Having noted the important characteristics of the exciton spectrum, we move on to comment briefly on the exciton size for the inorganic set of parameters. We plot in Fig. 4.9(b) the squared modulus of the wave function of the relative motion of the pair, which is defined in Eq. (4.21). We note that for the inorganic set of parameters, electron and hole are not as tightly bound as for the organic set of parameters, which is in accord with the fact that excitons in a typical inorganic semiconductor have large radii, typically of the order of 10 lattice constants [86]. From Fig. 4.9(b), it is also clear that, if we are to see the lowest exciton state $(Q = 0, \nu = 0)$ as a bound pair, we should take the system size $N \gtrsim 120$. We opt for $N = 151$ because this value makes a good compromise between the minimal size of the system needed for the results to be numerically accurate and the computational time.

For the inorganic set of parameters, we note that incoherent unbound excitons comprise the major part of the total exciton population [see Fig. 4.10(a)], which is different from the case when model parameters assume values representative of an organic semiconductor, when excitons in bound states prevail. Considering an unbound exciton as quasifree electron and hole, we interpret the last observation in the following manner: after an optical excitation of an organic semiconductor, (strongly) bound electron–hole pairs (excitons) are mainly generated, whereas in the case of an inorganic semiconductor an optical excitation predominantly generates (quasi)free charges. In Fig. 4.10(a), we also note that for higher central frequency of the laser field, the relative number of bound excitons is lower. However, in the long-time limit the number of incoherent bound excitons should assume the value predicted by the Maxwell–Boltzmann distribution, which is around 36.5$\%$, irrespectively of the central frequency of the pulse. The values of the relative number of incoherent bound excitons at the end of our computations do not strongly deviate from the value predicted by the Maxwell–Boltzmann distribution, in contrast to the situation for the organic set of parameters, where this deviation was more pronounced (see Fig. 4.3). It can thus be inferred that nonequilibrium features of the semiconductor dynamics after a pulsed excitation are more pronounced for the organic than for the inorganic set of parameters.

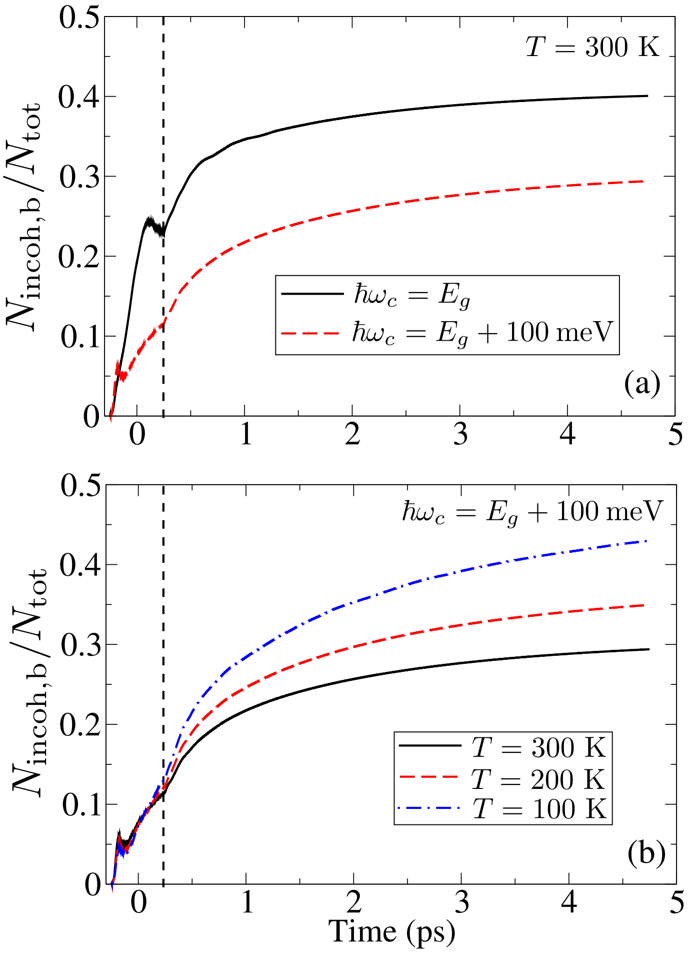

FIGURE 4.10: (a) Time dependence of the relative number of incoherent bound excitons for the excitation resonant with the single-particle gap E_g and the one that is 100 meV above it. The temperature in both cases is $T = 300$ K. (b) Time dependence of the relative number of incoherent bound excitons for various temperatures. The central frequency of the laser pulse is 100 meV above the single-particle gap.

Finally, we comment on the temperature dependence of the exciton formation process for the excitation whose central frequency is 100 meV above the single-particle gap. The lower is the temperature, the higher is the relative number of the incoherent bound excitons [see Fig. 4.10(b)]. During the pulse, higher temperature leads to higher relative number of incoherent bound excitons, which has already been explained in the section dealing with the organic set of parameters. The long-time limit values of the relative number of incoherent bound excitons are 44.7% for $T = 200$ K and 62.7% for $T = 100$ K. In all three cases, the dynamics is highly nonequilibrium, but it displays the trend of a slow, but monotonic, approach towards the equilibrium.

4.4 Discussion and Significance of Our Results

We perform an investigation of exciton dynamics taking place on picosecond time scales following a pulsed excitation of the model semiconductor. Despite the fact that our Hamiltonian does not include the effects of disorder that are present in real materials and uses an oversimplified form of the carrier–phonon interaction, the time scales of exciton formation and relaxation processes that we obtain using the organic parameter set are consistent with experimental data on conjugated polymer-based materials [46, 47]. The formation of strongly bound excitons is characterized by multiple time scales that are concurrent with the time scale of the electron transfer in most efficient D/A OSCs. In particular, our results indicate that, if the charge transfer from the photoexcited donor to the acceptor took place on $\sim$ 100 fs time scales after the photoexcitation, it would predominantly occur from higher-lying donor exciton states, prior to the formation of strongly bound donor excitons, which we find to occur on a $\sim$ 500-fs time scale. In this sense, our results may be considered to support the hypothesis put forward by Heeger and coworkers [33], according to which the ultrafast charge transfer in most efficient D/A blends is possible because it takes place before the formation of strongly bound donor excitons.

Instead of focusing on details of one particular material system, we work with the model Hamiltonian whose parameters have clear physical interpretation and can be varied, which enables us to identify the influence of different physical effects on relevant time scales. We find that the exciton formation strongly depends on the central frequency of the excitation, higher-energy excitations leading to more free carriers on picosecond time scales. Stronger carrier-phonon and carrier-carrier couplings promote more efficient binding of electrons and holes into excitons. As the temperature is decreased, the relative participation of strongly bound excitons in the total exciton population increases.

Chapter 5

Origin of Space-Separated Charges in Photoexcited Organic Heterojunctions on Ultrafast Time Scales

The aim of this chapter is to unveil the fundamental physical mechanisms behind the experimentally observed presence of spatially separated charges on subpicosecond time scales following the photoexcitation of the most efficient D/A OSCs. As has been described in Ch. 1, these experimental findings challenge the conventional picture of light-to-charge conversion in OSCs and call for its amendments. We start this chapter with an overview (Sec. 5.1) of recent experimental and theoretical activities that have influenced the topic of our interest. Our results regarding subpicosecond exciton dynamics at photoexcited D/A heterojunctions are presented in Secs. 5.2 and 5.3, whose content is based on our publication [134]. Section 5.4 introduces our theoretical treatment of ultrafast transient absorption spectroscopy, which is followed by the discussion of the differential transmission signal computed by using the expression we derive. The results of Sec. 5.4 were also disseminated in Ref. [134].

5.1 Experimental and Theoretical Background

Here, we provide an overview of the experimental and theoretical results that are relevant for the topic of ultrafast charge separation at all-organic D/A heterointerfaces. The manner of the presentation of the experimental results is similar to that in Refs. [40, 135].

5.1.1 Overview of Recent Experimental Results

The authors of Ref. [35] performed one of the pioneering TA experiments in the femtosecond time regime on a conjugated polymer/fullerene blend. They succeeded in time-resolving the photoinduced electron transfer from the excited polymer onto the fullerene with time resolution of the order of 10 fs. Basically, the blend is first excited by a pump pulse, and thus created nonequilibrium state of the blend is examined by comparing the absorption spectrum of the pumped blend to the absorption spectrum of the blend in equilibrium. This comparison is performed at various times after the action of the pump pulse by exposing the sample to a probe pulse. The central experimental quantity, the DTS, may be resolved in time and/or frequency domain, providing one with a wealth of information on photophysical processes in the blend. A more detailed discussion of this experimental technique is deferred for Sec. 5.4. The charge transfer was observed to be ultrafast ($\sim$ 45 fs), but the nature of its product (whether it produces the strongly bound CT state or free charge carriers), as well as its physical mechanism, remained unclear. Later on, time-resolved TA experiments on the blend of the low-band-gap polymer PCPDTBT and the fullerene suggested that free carriers can be generated directly from the initial donor excitons in less than 200 fs following the photoexcitation [27]. On the same time scale, the electron transfer may also produce an electron–hole pair in the intermediate CT state, which converts to long-lived free carriers in less than 10 ps. Similar conclusions were also obtained in the P3HT/PCBM blend [136] by employing the same experimental technique.

The study by Bakulin et al. [48] shed new light on the experimentally observed presence of free charge carriers on subpicosecond time scales after photoexcitation. The authors suggest that the long-range charge separation in OSCs is facilitated by charge delocalization. In essence, the presence of high-energy (“hot”) CT states, which feature quite good charge delocalization, may enable a conversion of the initial donor exciton into a pair of free charges via a “hot” CT state, see the separation pathway outlined by arrows (1) and (4) in Fig. 5.1, without involving the strongly bound and localized interfacial CT state. Their proposal is based on the experimental results obtained on a variety of material combinations by using the so-called pump–push photocurrent technique. The blend is first excited by visible light, see the black bolt in Fig. 5.1, and, as a result,

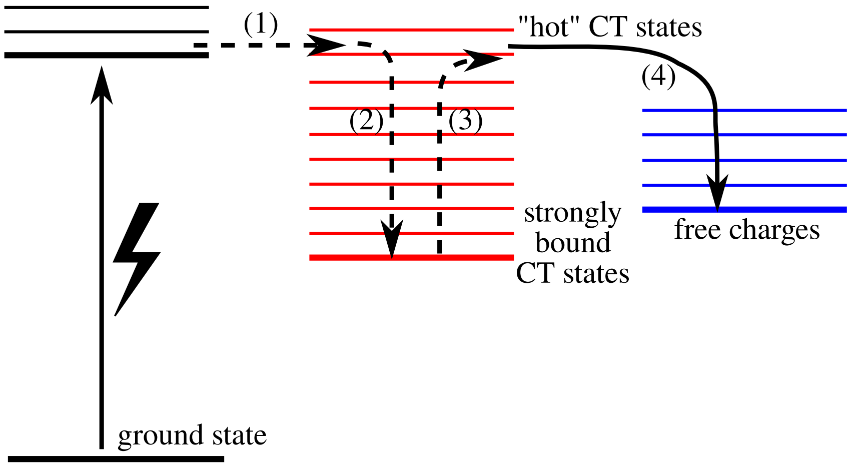

FIGURE 5.1: Schematic view of ultrafast optical experiments performed by Bakulin et al. [48]. An excitation by visible light (black bolt) generates donor excitons. Upon ultrafast electron transfer [arrow (1)], excitons in “hot” CT states are produced, which may either escape to the manifold of free-charge states [arrow (4)], or exhibit relaxation towards the strongly bound CT state [arrow (2)]. An infrared push pulse [arrow (3)] then reexcites excitons from the strongly bound CT state to “hot” CT states and provides them with another opportunity to separate [arrow (4)].

donor excitons, strongly bound CT excitons [see arrows (1) and (2)], and free carriers capable of producing photocurrent [see arrows (1) and (4)] are generated. The blend is then exposed to an infrared push pulse, whose frequency is tuned to the difference between the energies of the initially excited donor state and the strongly bound CT state, see arrow (3) in Fig. 5.1. In other words, the push pulse is supposed to reexcite an exciton in the strongly bound CT state to a higher-energy CT state that is in some sense similar to the CT state formed right after the electron transfer from the donor to the acceptor, see arrow (1) in Fig. 5.1. The change in the photocurrent induced by the push pulse in registered as a function of the delay between pump and push pulses. When the push pulse arrives immediately after the pump pulse, a sharp increase in the photocurrent (occurring within ~ 200 fs) is observed. This sharp rise is interpreted to originate from strongly bound CT excitons that, under the action of the push pulse, are reexcited in the CT exciton manifold to “hot” CT states, giving them another chance to separate, see arrows (3) and (4) in Fig. 5.1. In other words, strongly bound CT states, which are reached by the relaxation of the initial “hot” CT population, constitute an important loss channel, whereas delocalized “hot” CT states can separate with high efficiency. Complementary atomistic simulations revealed that “hot” CT states are characterized by good hole delocalization along polymer chains.

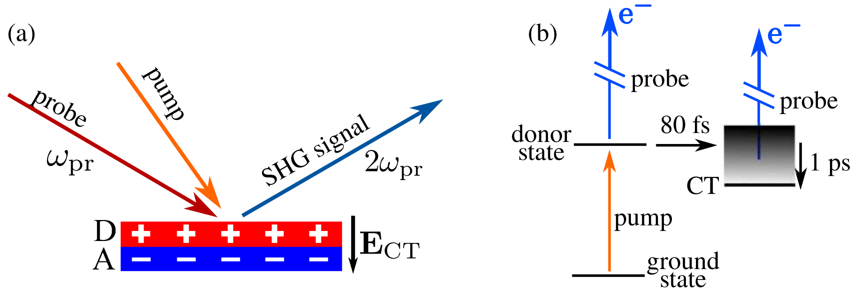

FIGURE 5.2: Schematic view of ultrafast optical experiments performed by Jailaubekov et al. [37]. (a) Time-resolved second harmonic generation. $\mathbf{E}_{\rm CT}$ denotes the electric field created by separating charges, while $\omega_{\rm pr}$ is the probe frequency. (b) Time-resolved two-photon photoemission spectroscopy. Ultrafast charge transfer from the initial donor state toward a "hot" CT state occurs in ~ 80 fs after pumping, while the relaxation of "hot" excitons takes place on a picosecond time scale.

The results of Ref. [48] suggest that a successful charge separation via "hot" CT states has to occur prior to the relaxation of the initial CT excitons to localized and strongly bound CT states. The ultrafast charge separation and the relaxation of CT excitons are thoroughly examined by Jailaubekov et al. in Ref. [37]. The formation of CT excitons is studied on the well-defined heterojunction between copper phthalocyanine (CuPc) and fullerene (C_{60}) by employing the time-resolved second harmonic generation (TR-SHG), whose principal scheme is depicted Fig. 5.2(a). The TR-SHG follows the emergence of the transient interfacial electric field $\mathbf{E}_{\rm CT}$ resulting from charge separation at the D/A interface. The ultrashort pump laser pulse generates excitons in the CuPc layer, and, after a time delay, the probe pulse (whose frequency $\omega_{\rm pr}$ is different from the frequency of the pump pulse) is applied to the sample. As charges separate, the electric field they create produces a signal at the second harmonic $2\omega_{\rm pr}$ of the probe frequency, and this signal is recorded as a function of the pump–probe delay. The rise-time of the TR-SHG signal gives information on the time scale on which charges separate. The experimental results point towards an extremely fast ($\lesssim 100$ fs) charge separation following the direct excitation of the bulk CuPc. A more detailed investigation of the population dynamics and energetics of exciton states on femtosecond time scales is performed by using the time-resolved two-photon photoemission spectroscopy, see Fig. 5.2(b). The pump pulse generates excitons in CuPc, while the probe pulse causes photoemission of electrons from exciton states. Based on an analysis of the kinetic energy of the photoelectrons thus obtained, one can identify the nature of the photoexcited state

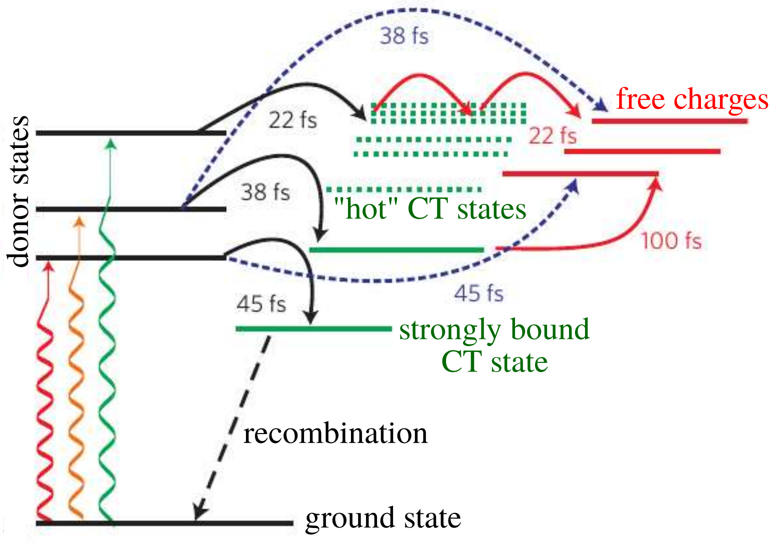

FIGURE 5.3: Summary of the photophysical pathways obtained by Grancini et al. [36] along which initially generated donor excitons are converted into free charges. Each pathway contains information on time scales of processes involved. Solid black arrows represent transitions of donor excitons into the CT manifold, while the conversion of CT excitons into free charges is represented by solid red arrows. Dashed blue arrows denote direct pathways from donor to free-charge states. The recombination of the strongly bound CT state is represented by dashed black arrow. Adapted with permission from Springer Customer Service Centre GmbH: Springer Nature, Nature Materials, Ref. [36] © (2013).

from which the electron has been emitted. The "hot" CT excitons produced in ~ 80 fs after the dissociation of CuPc excitons are observed to relax within ~ 1 ps to the strongly bound CT state. The authors propose that, on a picosecond time scale following the excitation by the pump, there is a competition between free-carrier generation via weakly bound and delocalized "hot" CT states and their relaxation towards strongly bound and localized CT states. This relaxation sets the time limit for efficient charge separation at organic D/A interfaces, which is ultimately aided by carrier delocalization.

Similar conclusions have emerged from the study by Grancini et al. [36], who performed ultrafast TA measurements to examine the very first stages of free-charge generation in the PCPDTBT/PCBM blend. The photoexcitation dynamics is tracked with sub-10-fs time resolution and its dependence on the pump energy is discussed in great detail. The principal finding is that initially generated donor excitons are converted into "hot" CT states, from which free-charge states are readily accessible, in $\lesssim 50$ fs following the photoexcitation, see Fig. 5.3. The precise time in which free-charge states become populated depends on the energy of the pump pulse, higher-lying donor states exhibiting a more rapid transformation into free charges. Such a path from donor excitons to free charges is opened up by the strong resonant coupling between donor states and “hot” CT states. Being of a more delocalized nature than the lowest-energy strongly bound CT state, “hot” CT states are more likely to transform into free-charge states than to experience the relaxation within the CT manifold. Grancini et al. have also obtained that the IQE is strongly dependent on the pump photon energy and exhibits a two-fold increase on the excitation energy increase from the optical band gap to well above the lowest-energy donor exciton. The excitation energy-dependent IQE strongly suggests that the light-to-charge conversion in OSCs occurs via “hot” CT states.

While the study by Bakulin et al. [48] points towards the importance of hole delocalization for ultrafast charge separation, the beneficial effect of electron delocalization was first demonstrated by Gélinas et al. [38]. The temporal evolution of the distance between separating charges is followed by tracking the changes in the optical absorption spectrum brought about by the electric field that is generated as charges separate. In other words, they measured the electro-absorption signal, i.e., the Stark effect, with sub-30-fs precision by employing the time-resolved TA spectroscopy. The results demonstrate that a large portion of the Coulomb barrier between the oppositely charged electron and hole is overcome within the first 40 fs following the excitation, during which the linear extension of the pair reaches 4 nm. At this electron–hole separation, the magnitude of the Coulomb interaction between the electron and hole is smaller than or of the order of the thermal energy at room temperature, so that further charge separation proceeds without kinetic obstacles. By studying blends featuring different fullerene mass ratios, the authors conclude that high fullerene loadings, which promote fullerene aggregation in ordered domains, positively influence ultrafast charge separation due to electron delocalization across aggregates.

5.1.2 Overview of Recent Theoretical Results

The experimental results outlined in previous paragraphs have led to a number of theoretical proposals aiming to unravel the origin of such a fast charge separation in OPVs. In the following, we provide a more detailed description of some of them.

Troisi and coworkers have investigated exciton dissociation at model OPV interfaces [49, 50]. They concluded that, contrarily to the widespread view, the dissociation of initially generated donor excitons does not generate tightly bound electron–hole pairs that are localized at the D/A interface, but rather "hot" CT excitons in which charges are relatively delocalized and predominantly located far from the interface. The accessibility of "hot" CT states from initial donor exciton states stems from the resonant coupling between these two groups of states. The higher degree of carrier delocalization in the respective materials is important not because the "hot" CT states are more delocalized, but because the resonant coupling between the initial states of donor excitons and "hot" CT states is stronger. Their conclusions are robust against the introduction of the disorder, which is ubiquitous in organic materials. Similar conclusions emerge from Ref. [51], whose results suggest that efficient free-charge generation in a polymer/fullerene blend is achieved through the resonant coupling of photogenerated polymer excitons to a high-energy manifold of CS states in which the electron is delocalized across fullerene aggregates. The authors of Ref. [51] emphasize that ultrafast charge separation leans on the energy alignment between initial donor states and "hot" CT states, which is achieved as a result of the specific electronic structure of the molecules of soluble fullerene derivatives used in most efficient OSCs. The origin of the supremacy of fullerene derivatives over other electron-accepting materials used in OSCs has been traced back to its particular electronic properties that originate from the presence of higher-than-LUMO orbitals energetically close to the LUMO orbital [137].

Further evidence that charge delocalization is crucial for the electron and hole in the CT state to overcome the Coulomb barrier on subpicosecond time scales has also been provided by other studies [52, 56, 58, 138]. In essence, all of them construct a model of a D/A interface that is suitably parameterized on the basis of literature data or quantum chemical calculations. The dynamics of ultrafast charge separation within such a model is then studied by various approaches, ranging from the nonadiabatic Ehrenfest dynamics [52] to sophisticated quantum dynamical simulations of the coupled electron–phonon system [56]. The carrier that is delocalized is either the hole [52] (along polymer chains) or the electron [52, 58, 138] (within fullerene aggregates). The role of the carrier–phonon coupling in exciton dissociation and charge separation has remained elusive. Troisi has suggested that the exciton dissociation can be conceived as a purely electronic process mainly because the coupling of charges to the nuclear degrees of freedom is effectively weakened due to charge delocalization [49]. On the other hand, there is experimental [139] and theoretical [56, 140] evidence that the carrier–phonon coupling is crucial to ultrafast exciton dissociation at D/A interfaces. Following the generation of the donor exciton, the coupling between electronic and nuclear degrees of freedom leads to electron delocalization across the D/A interface [139]. The last conclusion stems from the observed correlated oscillations of both charge density and the nuclei that occur with period that matches the frequency of prominent high-frequency phonon modes. The full charge separation is facilitated by the presence of an intermediate CT state that exhibits a good phonon-assisted coupling to the donor exciton state [56, 140]. It has also been proposed that the carrier coupling to lattice vibrations can make free-carrier states directly accessible from initial donor states on ~ 100 fs time scales [57]. There are also reports indicating that too strong carrier–phonon coupling suppresses charge separation on subpicosecond time scales by promoting a fast formation of strongly bound and localized CT pairs [141, 142].

There is another proposal that can readily rationalize the presence of spatially separated charges on ultrafast time scales following a photoexcitation of a D/A interface. As demonstrated by Vandewal et al. [61], the lowest-energy CT state, which is strongly bound and localized at the D/A interface, is directly accessible from the ground state by means of a suitable photoexcitation. The direct accessibility of the strongly bound CT state has its origin in the very small, but sufficient, overlap of between electron and hole wave functions in this state. On the other hand, it is widely believed that high-energy CT states, in which carriers mainly reside far from the interface, are not directly reachable from the ground state by a photoexcitation, since the overlap between electron and hole wave functions in these states is essentially equal to zero. However, the above-mentioned resonant coupling between the donor exciton states and "hot" CT states may challenge this simplistic view. Using a combination of quantum chemical calculations on realistic small-size systems and calculations on model systems, Ma and Troisi observe that states of spatially separated electron–hole pairs contribute nontrivially to the absorption spectrum of a D/A interface [143], suggesting that they may be populated by a direct optical excitation from the ground state. The fundamental physical effect responsible for their observation is the combination of carrier delocalization in "hot" CT states with the resonance between donor and "hot" CT states. Similar conclusions were also reported by D'Avino et al. [144], whose results point towards the absorption intensity transfer from donor exciton states to high-energy CT states that is brought about by their resonant mixing.

These studies, however, do not discuss the actual relevance of the direct optical generation of space-separated charges for experimentally observed ultrafast light-to-charge conversion in OSCs. In particular, there is no assessment of the relative importance of direct optical generation of space-separated charges in comparison with other hypothesized mechanisms of their generation. However, such an assessment requires that exciton generation by means of a photoexcitation, exciton dissociation, and further charge separation be treated on equal footing. The vast majority of existing theoretical studies on charge separation at heterointerfaces does not treat explicitly the interaction with the exciting field that creates excitons from an initially unexcited system [52, 58], but rather assumes that the exciton has been already generated and then follows its evolution at the interface between two materials. If we are to explore the possibility of direct optical generation of spatially separated charges, we should certainly monitor the initial process of exciton generation by means of a photoexcitation. The general method presented in Ch. 3 is, therefore, a suitable approach to unveil the impact of direct optical generation of space-separated charges on subpicosecond dynamics at a D/A interface. The semiconductor model presented in Ch. 2 should be modified and appropriately parameterized so as to describe the interface between two semiconductors, which is done in Sec. 5.2.

5.2 Model Description

5.2.1 One-Dimensional Lattice Model of a Heterojunction

To describe a heterojunction, we employ a one-dimensional two-band lattice semiconductor model, which is formally similar to the model of a neat semiconductor material that we used in Ch. 4. There are $2N$ sites in total and the separation between adjacent sites is a. First N sites

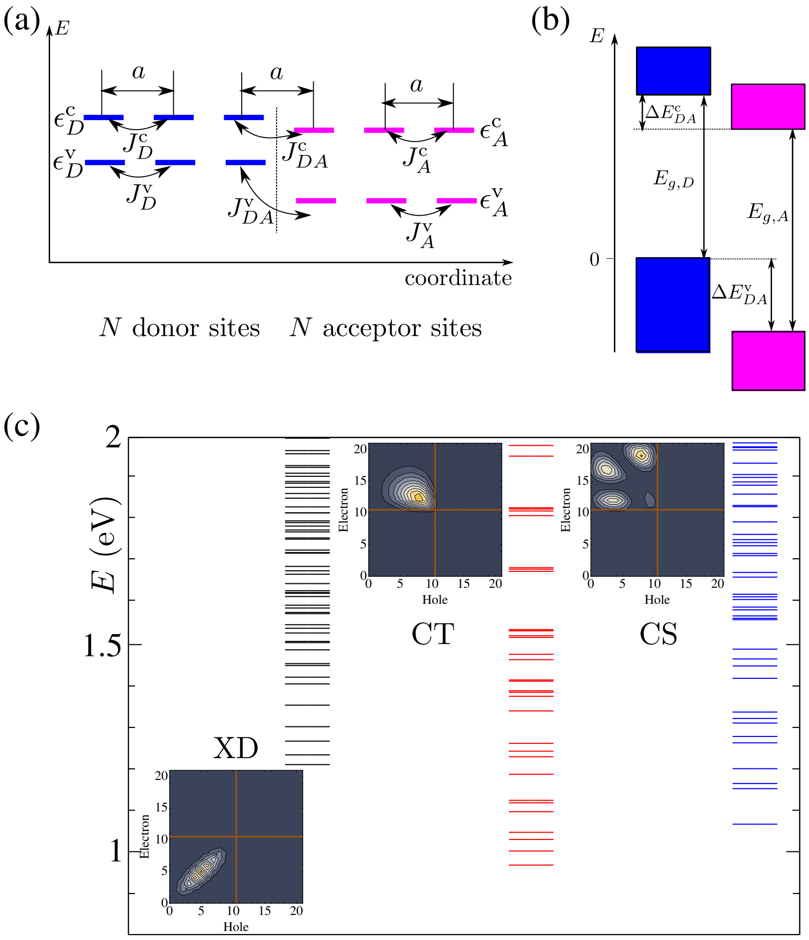
(a)
E
a
a
a
ϵ_D^c
ϵ_D^v
J_D^c
J_D^v
J_{DA}^c
J_{DA}^v
J_A^c
J_A^v
ϵ_A^c
ϵ_A^v
coordinate
N donor sites
N acceptor sites
(b)
E
ΔE_{DA}^c
$E_{g,D}$
$E_{g,A}$
0
ΔE_{DA}^v
(c)
E (eV)
2
1.5
1
XD
CT
CS
Electron
Hole
0
5
10
15
20

FIGURE 5.4: (a) One-dimensional lattice model of a heterojunction. Various types of electronic couplings (in the donor, in the acceptor, and among them) are indicated. There is an energy offset between single-electron/hole levels in the donor and acceptor, which translates into the LUMO–LUMO and HOMO–HOMO offsets between the two parts of the heterojunction. (b) Band alignment produced by our model. (c) Energies of exciton states, in particular of donor excitons (black lines), CT (red lines) and CS (blue lines) states. Exciton wave function square moduli are shown for the lowest donor, CT and CS state.

(labeled by $0, \ldots, N-1$) belong to the donor part, while sites labeled by $N, \ldots, 2N-1$ belong to the acceptor part of the heterojunction. The model is schematically presented in Fig. 5.4(a). Each site i has one valence-band and one conduction-band orbital and also contributes a number of localized phonon modes counted by index λ_i. The total Hamiltonian is given in Eq. (2.34), in which the interacting-carrier part of the Hamiltonian H_c reads as

$$H_c = \sum_{ij} \epsilon_{ij}^c c_i^\dagger c_j - \sum_{ij} \epsilon_{ij}^v d_i^\dagger d_j + \frac{1}{2} \sum_{ij} \left(c_i^\dagger c_i - d_i^\dagger d_i \right) V_{ij} \left(c_j^\dagger c_j - d_j^\dagger d_j \right), \tag{5.1}$$

the free-phonon Hamiltonian H_p is

$$H_\mathrm{p} = \sum_{i\lambda_i} \hbar\omega_{i\lambda_i} b_{i\lambda_i}^\dagger b_{i\lambda_i}, \tag{5.2}$$

the carrier–phonon interaction $H_{\mathrm{c-p}}$ is

$$H_{\mathrm{c-p}} = \sum_{i\lambda_i} g_{i\lambda_i}^\mathrm{c} c_i^\dagger c_i \left(b_{i\lambda_i}^\dagger + b_{i\lambda_i}\right) - \sum_{i\lambda_i} g_{i\lambda_i}^\mathrm{v} d_i^\dagger d_i \left(b_{i\lambda_i}^\dagger + b_{i\lambda_i}\right), \tag{5.3}$$

while the interaction of carriers with the external exciting field $E(t)$, $H_{\mathrm{c-f}}$, is given as

$$H_{\mathrm{c-f}} = -\sum_i d_i^\mathrm{cv} E(t) \left(c_i^\dagger d_i^\dagger + d_i c_i\right). \tag{5.4}$$

We assume that quantities ϵ_{ij}^c $\left(\epsilon_{ij}^\mathrm{v}\right)$, which represent electron (hole) on-site energies (for $i = j$) and transfer integrals (for $i \neq j$), are different from zero only for certain values of indices i and j. In more detail, the quantity ϵ_{ij}^c assumes nonzero values when it represents

(1) on-site energy of an electron on donor site i, ϵ_D^c, for $i = j$ and $i \leq N - 1$,

(2) on-site energy of an electron on acceptor site i, ϵ_A^c, for $i = j$ and $i \geq N$,

(3) negative electron transfer integral between neighboring sites in the donor part of the heterojunction, $-J_D^\mathrm{c}$, for $i \leq N - 1$, $j \leq N - 1$, and $|i - j| = 1$,

(4) negative electron transfer integral between neighboring sites in the acceptor part of the heterojunction, $-J_A^\mathrm{c}$, for $i \geq N$, $j \geq N$, and $|i - j| = 1$,

(5) negative electron transfer integral between the donor and acceptor part of the heterojunction, $-J_{DA}^\mathrm{c}$, for $i = N - 1$ and $j = N$ or vice versa.

Similarly, depending on the values of indices i and j, ϵ_{ij}^v stands for the hole on-site energies in the donor ϵ_D^v and acceptor ϵ_A^v, negative hole transfer integral $-J_D^\mathrm{v}$ between adjacent sites in the donor, negative hole transfer integral $-J_A^\mathrm{v}$ between adjacent sites in the acceptor, or negative hole transfer integral $-J_{DA}^\mathrm{v}$ between the donor and acceptor part of the heterojunction. The meaning of all of these quantities is illustrated in Fig. 5.4(a). The carrier–carrier interaction potential V_{ij} is assumed to be the Ohno potential given in Eq. (4.2), whose parameters are the on-site Coulomb interaction U and the relative dielectric constant ε_r. It is assumed that the frequency of the exciting field $E(t)$ is sufficient to create electron–hole pairs. Interband matrix elements of the dipole moment are denoted as d_i^{cv}, while its intraband matrix elements are neglected.

The model defined in Eqs. (5.1)–(5.4) is constructed to represent the interface of two semiconductors of different electronic properties. However, it may also be formally regarded as a model of a single semiconductor whose electronic properties are position-dependent. Therefore, the theoretical approach to ultrafast exciton dynamics presented in Ch. 3 may be used to study the dynamics of the model D/A interface triggered by a pulsed photoexcitation. We assume that the heterojunction is initially unexcited, i.e., initially, there are no electrons and holes in either part of the heterojunction. The general form of the eigenvalue problem defining the exciton basis [Eq. (2.46)], when used in the context of the above-introduced model of a D/A heterojunction, gives the following eigenvalue problem

$$\sum_{i'j'} \left(\delta_{i'i}\epsilon^{\mathrm{c}}_{jj'} - \delta_{j'j}\epsilon^{\mathrm{v}}_{ii'} - \delta_{i'i}\delta_{j'j}V_{ij} \right) \psi^{x}_{i'j'} = \hbar\omega_x \psi^{x}_{ij}, \tag{5.5}$$

where indices i, i' (j, j') correspond to the position of the hole (electron). The expression for the dipole-moment matrix elements in the exciton basis [Eq. (3.50)], adapted to the situation at hand, reads as

$$M_x = \sum_i \psi^{x*}_{ii} d_i^{\mathrm{cv}}, \tag{5.6}$$

while the carrier–phonon coupling constants in the exciton basis [Eq. (3.51)] are

$$\Gamma^{i\lambda_i}_{\bar{x}x} = g^{\mathrm{c}}_{i\lambda_i} \sum_j \psi^{\bar{x}*}_{ji} \psi^{x}_{ji} - g^{\mathrm{v}}_{i\lambda_i} \sum_j \psi^{\bar{x}*}_{ij} \psi^{x}_{ij}. \tag{5.7}$$

5.2.2 Parametrization of the Model Hamiltonian

The model Hamiltonian was parameterized to yield values of band gaps, bandwidths, band offsets, and exciton binding energies that are representative of typical OPV materials. The values

Table 5.1: Values of model parameters used in computations on the two-band model of a D/A heterojunction.

Parameter	Value
N	11
a (nm)	1.0
U (eV)	0.48
ε_r	3.0
$E_{g,D}$ (eV)	1.5
$E_{g,A}$ (eV)	1.95
$\Delta E_{DA}^{\mathrm{c}}$ (eV)	0.5
$\Delta E_{DA}^{\mathrm{v}}$ (eV)	0.95
J_D^{c} (eV)	0.105
J_D^{v} (eV)	-0.295
J_A^{c} (eV)	0.15
J_A^{v} (eV)	-0.15
J_{DA}^{c} (meV)	75
J_{DA}^{v} (meV)	-75
$\hbar\omega_{\mathrm{p},1}$ (meV)	10
g_1 (meV)	28.5
$\hbar\omega_{\mathrm{p},2}$ (meV)	185
g_2 (meV)	57.0
T (K)	300
t_0 (fs)	50

of model parameters used in numerical computations are summarized in Table 5.1. While these values largely correspond to the PCPDTBT/PCBM interface, we note that our goal is to reach general conclusions valid for a broad class of interfaces. Consequently, in the following sections, we also vary most of the model parameters and study the effects of these variations.

The electronic parameters of the heterojunction are the electron (ϵ_i^{c}) and hole (ϵ_i^{v}) on-site energies, and the electron (J_D^{c}, J_A^{c}, J_{DA}^{c}) and hole (J_D^{v}, J_A^{v}, J_{DA}^{v}) transfer integrals in the donor part, the acceptor part, and between them. The electron and hole on-site energies may be combined (together with the transfer integrals) into more informative parameters characterizing the heterojunction, namely, the single-particle band gaps of the donor ($E_{g,D}$) and acceptor ($E_{g,A}$) parts, and the LUMO–LUMO ($\Delta E_{DA}^{\mathrm{c}}$) and HOMO–HOMO ($\Delta E_{DA}^{\mathrm{v}}$) offsets. The band alignment produced by our model, together with a pictorial definition of the aforementioned quantities, is displayed in Fig. 5.4(b). The single-particle band gap of the donor part $E_{g,D}$, as well as the LUMO–LUMO offset $\Delta E_{DA}^{\mathrm{c}}$, assume values that are representative of the low-band-gap

PCPDTBT polymer used in the most efficient OSCs [27, 145]. The single-particle band gap of the acceptor $E_{g,A}$ and electron and hole transfer integrals J_A^{c} and J_A^{v} are tuned to values typical of fullerene and its derivatives [26, 146]. Electron (J_D^{c}) and hole (J_D^{v}) transfer integrals in the donor are extracted from the conduction and valence bandwidths in the intrachain direction of the PCPDTBT polymer. To obtain the bandwidths, an electronic structure calculation is performed on a straight infinite polymer chain. The calculation is based on the density functional theory (DFT) in the local density approximation (LDA), as implemented in the QUANTUM-ESPRESSO [147] package. Since our model is one-dimensional, transfer integrals are then obtained as 1/4 of the respective bandwidths. The values of the transfer integral between the two materials are chosen to be similar to the values obtained in the *ab initio* study of P3HT/PCBM heterojunctions [148].

The dielectric constant ε_r assumes a value typical for organic materials, while the value of the on-site Coulomb interaction U is selected so that the binding energies of both the donor and acceptor exciton are around 300 meV. The value of the lattice spacing a is of the same order of magnitude as the typical distance between constitutive elements of organic semiconductors. We set the number of sites in a single material to $N = 11$, which is reasonable having in mind that the typical dimensions of phase segregated domains in BHJ morphology are considered to be 10–20 nm [33].

Following common practice when studying all-organic heterojunctions [141, 149], we take one low-energy and one high-energy phonon mode per site. For simplicity, we assume that energies of both phonon modes, as well as their couplings to carriers, have the same values in both materials. The high-frequency phonon mode of energy 185 meV ($\approx$ 1500 cm^{-1}), which is present in both materials, was suggested to be crucial for ultrafast electron transfer in the P3HT/PCBM blend [139]. Recent theoretical calculations of the phonon spectrum and electron–phonon coupling constants in P3HT indicate the presence of low-energy phonon modes ($\lesssim$ 10 meV) that strongly couple to carriers [150]. The chosen values of phonon-mode energies fall in the ranges in which the phonon density of states in conjugated polymers is high [151] and the local electron–vibration couplings in PCBM are pronounced [20]. We select the values of the carrier–phonon coupling constants on the basis of the value of polaron binding energy, which can be estimated from an expression similar to Eq. (4.14) that reads as [129]:

$$\epsilon_{\mathrm{b}}^{\mathrm{pol}}=\sum_{i=1}^{2}\epsilon_{\mathrm{b},i}^{\mathrm{pol}}=\sum_{i=1}^{2}\frac{g_i^2}{2|J|}\frac{1}{\sqrt{\left(1+\frac{\hbar\omega_{\mathrm{p},i}}{2|J|}\right)^2-1}}, \tag{5.8}$$

where $\epsilon_{\mathrm{b},i}^{\mathrm{pol}}$ are the contributions of low- and high-frequency phonon modes to the polaron binding energy. We take $g_2/g_1=2$ and estimate their numerical values assuming that $\epsilon_{\mathrm{b}}^{\mathrm{pol}}=20$ meV and $|J|=125$ meV.

The exciting pulse is centered around $t=0$ and assumes the form

$$E(t)=E_0\cos(\omega_c t)\theta(t+t_0)\theta(t_0-t), \tag{5.9}$$

where ω_c is its central frequency, while the duration of the pulse is $2t_0$. As has been already discussed in Ch. 4, the pulse duration should be large enough so that the pulse is spectrally narrow enough (the energy of the initially generated excitons is around the central frequency of the pulse). On the other hand, since our focus is on processes happening on subpicosecond time scale, the pulse should be as short as possible in order to disentangle the carrier generation during the pulse from free-system evolution after the pulse. As a compromise between these two requirements, we choose $t_0=50$ fs. We note that the principal results and conclusions to be presented do not crucially depend on the particular value of t_0 nor on the wave form of the excitation. For more details on the last point, see the Supplementary Material associated to Ref. [134], where we have performed computations for the wave forms given in Eqs. (5.9) and (5.37). Having in mind that a typical photoexcitation of a realistic heterojunction predominantly affects its donor part, we set the interband dipole matrix elements d_i^{cv} in the acceptor ($i=N,\dots,2N-1$) to zero, while in the donor they all assume the same value d^{cv} so that $d^{\mathrm{cv}}E_0=0.2$ meV (weak excitation).

5.2.3 Classification of Exciton States

Let us now introduce the classification of exciton states at the model heterojunction. Figure 5.4(c) displays part of the exciton spectrum produced by our model. Exciton states can be classified according to the relative position of the electron and the hole. The classification is unambiguous only for $J^{\mathrm{c}}_{DA} = J^{\mathrm{v}}_{DA} = 0$ (noninteracting heterojunction), when each exciton state $x^{(0)}$ [the subscript (0) is used for the noninteracting heterojunction] can be classified into one of the following four groups:

(a) if both the electron and the hole are in the donor, it is a donor exciton (XD) state,

(b) if both the electron and the hole are in the acceptor, it is an acceptor exciton (XA) state,

(c) if the electron is in the acceptor, while the hole is in the donor, it is a space-separated exciton state,

(d) if the electron is in the donor, while the hole is in the acceptor, it is an eDhA state.

Since eDhA states are energetically very well separated from other groups of exciton states, they will not be of interest in further discussion. In the group of space-separated states, CT and CS states can be further discriminated by the mean electron–hole distance, which is defined as

$$\langle r_{\mathrm{e-h}} \rangle_{x^{(0)}} = \sum_{ij} |i-j| \left| \psi_{ij}^{x^{(0)}} \right|^2 . \tag{5.10}$$

When the electron–hole interaction is set to zero, the mean electron–hole distance for all the space-separated states is equal to N. For the nonzero Coulomb interaction, we consider a space-separated state as a CS state if its mean electron–hole distance is larger than (or equal to) N, otherwise we consider it as a CT state.

In general case, when at least one of J^{c}_{DA}, J^{v}_{DA} is different from zero (interacting heterojunction), it is advantageous to explicitly separate the D/A interaction from the interacting-carrier part of the Hamiltonian [Eq. (5.1)],

$$H_{\mathrm{c}} = H_{\mathrm{c}}^{(0)} + H_{DA}, \tag{5.11}$$

where

$$H_{DA} = -J_{DA}^{\mathrm{c}} \left(c_{N-1}^{\dagger} c_N + c_N^{\dagger} c_{N-1} \right) + J_{DA}^{\mathrm{v}} \left(d_{N-1}^{\dagger} d_N + d_N^{\dagger} d_{N-1} \right) \tag{5.12}$$

is the D/A interaction, and $H_{\mathrm{c}}^{(0)}$ describes interacting carriers at the noninteracting heterojunction. Exciton states of the noninteracting heterojunction $\psi_{ij}^{x^{(0)}}$ and the corresponding exciton energies $\hbar\omega_{x^{(0)}}$ are obtained by solving the electron–hole pair eigenproblem of $H_{\mathrm{c}}^{(0)}$. Exciton states of the interacting heterojunction ψ_{ij}^{x} are linear combinations of exciton states of the noninteracting heterojunction

$$\psi_{ij}^{x} = \sum_{x^{(0)}} C_{xx^{(0)}} \psi_{ij}^{x^{(0)}}, \tag{5.13}$$

and their character is obtained using this expansion. Namely, for each group $X^{(0)}$ of the exciton states of the noninteracting heterojunction, we compute the overlap of state x (of the interacting heterojunction) with states belonging to this group

$$C_{X^{(0)}}^{x} = \sum_{x^{(0)} \in X^{(0)}} \left| C_{xx^{(0)}} \right|^2 . \tag{5.14}$$

The character of state x is then the character of the group $X^{(0)}$ for which the overlap $C_{X^{(0)}}^{x}$ is maximum.

The exciton dissociation and charge separation on subpicosecond time scales are studied by following time evolution of the (incoherent) populations of donor, acceptor, CT, and CS exciton states. The incoherent exciton population of exciton state x, $\bar{n}_{xx}$, is defined in Eq. (3.46), while the incoherent populations of various groups X of exciton states are gives as

$$N_X^{\mathrm{incoh}} = \sum_{x \in X} \bar{n}_{xx}. \tag{5.15}$$

Similarly to Ch. 4, here, we also frequently normalize quantities N_X^{incoh} to the total exciton population N_{tot} defined in Eq. (3.54). Another way to study ultrafast exciton dissociation and charge separation is by computing the probabilities $f_{\mathrm{e}}(t,r)$ [$f_{\mathrm{h}}(t,r)$] that an electron (a hole) is located at site r at instant t. Using the contraction identities embodied in Eqs. (3.37) and (3.38), we obtain

$$f_\mathrm{e}(t,r)=\frac{\sum_{\bar{x}x}\left(\sum_{r_\mathrm{h}}\psi^{\bar{x}*}_{r_\mathrm{h}r}\psi^{x}_{r_\mathrm{h}r}\right)n_{\bar{x}x}(t)}{\sum_x n_{xx}(t)}, \tag{5.16}$$

$$f_\mathrm{h}(t,r)=\frac{\sum_{\bar{x}x}\left(\sum_{r_\mathrm{e}}\psi^{\bar{x}*}_{rr_\mathrm{e}}\psi^{x}_{rr_\mathrm{e}}\right)n_{\bar{x}x}(t)}{\sum_x n_{xx}(t)}. \tag{5.17}$$

Consequently, the probability that an electron is in the acceptor at time t is

$$P^\mathrm{e}_A(t)=\sum_{r=N}^{2N-1}f_\mathrm{e}(t,r). \tag{5.18}$$

5.3 Numerical Results

The presentation of the results of our numerical calculations on the model system defined in Sec. 5.2 is divided in two parts. First, we observe that the populations of CT and CS states predominantly build up during the action of the excitation, and that the changes in these populations occurring on $\sim$100-fs time scales after the excitation are rather small. This conclusion, i.e., the direct optical generation as the principal source of space-separated charges on ultrafast time scales following the excitation, is then shown to be robust against reasonable variations of model parameters. Since the focus of our study is on the ultrafast exciton dynamics at photoexcited heterojunctions, all the computations are carried out for 1 ps in total (including the duration of the pulse).

A few comments regarding the numerics are in order. The model system described in Sec. 5.2 does not possess translational symmetry, meaning that the reduction in the number of active density matrices due to the symmetry cannot be achieved here. Similarly to Sec. 4.3, the central frequency of the excitation ω_c and the thermal energy k_BT determine the number of exciton states that are actually involved in the ultrafast dynamics. Here, our model features $(2N)^2=484$ exciton states in total, while actual computations are performed using up to 150–200 lowest-lying states. Since the total number of phonon modes is $4N=44$, the number of active single-phonon-assisted density matrices $n_{\bar{x}x(i\lambda_i)^+}$ is of the order of 10^6. The parallelization scheme adopted here is the same as that described in Sec. 4.3. Again, having separated out the rapid free rotation of coherent quantities y_x and $y_{x(i\lambda_i)^+}$ [see Eq. (3.93)], the equations of motion for quantities $\tilde{y}_x$,

$\tilde{y}_{x(i\lambda_i)^+}$, $n_{\bar{x}x}$, and $n_{\bar{x}x(i\lambda_i)^+}$ can be integrated with the time step of $\Delta t = 0.8$ fs. Computing 1 ps of the dynamics requires 1,250 integration steps. The parallel programs are typically executed on 64 processors, and the execution time is of the order of one hour.

5.3.1 Interfacial Dynamics on Ultrafast Time Scales

Figure 5.5(a) shows the time dependence of the numbers of donor, CT, and CS excitons for the 100-fs-long excitation with central frequency $\hbar\omega_c = 1.5$ eV, which excites the system well above the lowest donor or space-separated exciton state, see Fig. 5.4(c). The number of all three types of excitons grows during the action of the exciting field, whereas after the electric field has vanished, the number of donor excitons decreases and the numbers of CT and CS excitons increase. However, the changes in the exciton numbers brought about by the free-system evolution alone are much less pronounced than the corresponding changes during the action of the electric field, as is shown in Fig. 5.5(a). The population of CS excitons builds up during the action of the electric field, so that after the first 100 fs of the calculation, CS excitons comprise 7.6% of the total exciton population, see the inset of Fig. 5.5(a). In the remaining 900 fs, when the dynamics is governed by the free Hamiltonian, the population of CS excitons further increases to 9.6%. A similar, but less extreme, situation is also observed in the relative number of CT excitons, which at the end of the pulse form 14% of the total population and in the remaining 900 fs of the computation their number further grows to 24%. Therefore, if only the free-system evolution were responsible for the conversion from donor to CT and CS excitons, the population of CT and CS states at the end of the pulsed excitation would assume much smaller values than we observe. We are led to conclude that the population of CT and CS excitons on ultrafast ($\lesssim$ 100-fs) time scales is mainly established by direct optical generation. Transitions from donor to CT and CS excitons are present, but on this time scale are not as important as is currently thought.

Figure 5.5(b) displays quantity f_e as a function of site index r at different times t. The probability of an electron being in the acceptor is a monotonically increasing function of time t, see the inset of Fig. 5.5(b). It increases, however, more rapidly during the action of the electric field than after the electric field has vanished: in the first 100 fs of the calculation, it increases

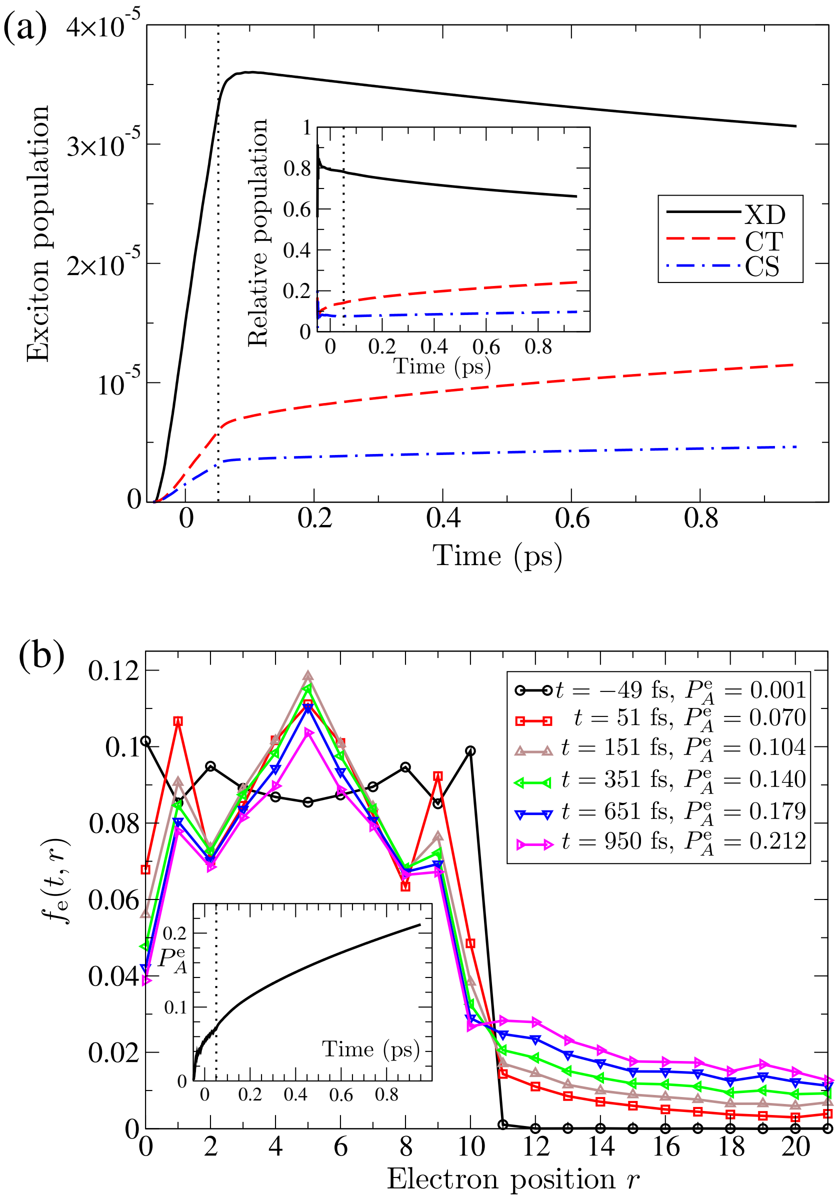

FIGURE 5.5: (a) Time dependence of the numbers of donor (XD), CT, and CS excitons. The inset shows the time dependence of these quantities normalized to the total exciton population in the system. (b) Probability that at time t an electron is located at site r as a function of r for various values of t. In the legend, the probability that at instant t an electron is located in the acceptor is given, while the inset shows its full time dependence. Dotted vertical lines indicate the end of the excitation.

from virtually 0 to 0.070, while in the next 100 fs it only rises from 0.070 to 0.104, and at the end of the computation it assumes the value 0.210. The observed time dependence of the probability that an electron is located in the acceptor further corroborates our hypothesis of direct optical generation as the main source of separated carriers on ultrafast time scales. If only transitions from donor to CT and CS excitons led to ultrafast charge separation starting from a donor exciton, the values of the considered probability would be smaller than we observe.

The rationale behind the direct optical generation of space-separated charges is the resonant coupling between donor excitons and (higher-lying) space-separated states, which stems from the resonant mixing between single-electron states in the donor and acceptor modulated by the electronic coupling between materials. This can be seen in more detail from the level alignment in Fig. 5.4(b), which shows that, since the electronic bandwidth in the acceptor is comparable to the LUMO–LUMO offset, there are single-electron states in the two materials that are nearly resonant and thus prone to a resonant “hybridization”. The mixing leads to higher-lying CT and CS states having a non-negligible amount of donor character and acquiring nonzero dipole moment from donor excitons; these states can thus be directly generated from the ground state. It should be stressed that the mixing, in turn, influences donor states, which have certain amount of space-separated character. A more comprehensive discussion on the resonant mixing mechanism is deferred for Sec. 6.2.3.

5.3.2 Impact of Model Parameters on Ultrafast Exciton Dynamics

Our central conclusion was so far obtained using only one set of model parameters and it is therefore important to check its sensitivity on system parameters. To this end, we vary one model parameter at a time, while all the other parameters retain the values listed in Table 5.1.

We start by investigating the influence of the transfer integral between the donor and acceptor $J_{DA}^{\mathrm{c/v}}$. Higher values of $J_{DA}^{\mathrm{c/v}}$ favor charge separation, since the relative numbers of CT and CS excitons, together with the probability that an electron is in the acceptor, increase, whereas the relative number of donor excitons decreases with increasing $J_{DA}^{\mathrm{c/v}}$, see Figs. 5.6(a)–(c). In light of the proposed mechanism of ultrafast direct optical generation of space-separated charges, the

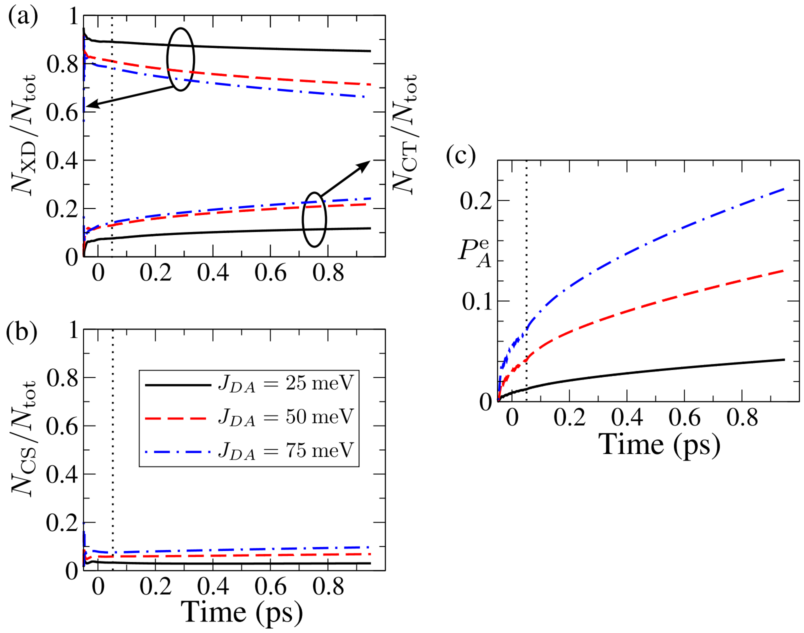

FIGURE 5.6: Time dependence of the relative number of (a) donor and CT, (b) CS excitons, and (c) the probability P_A^{e} that an electron is in the acceptor, for different values of the transfer integrals $|J_{DA}^{\mathrm{c}}| = |J_{DA}^{\mathrm{v}}| = J_{DA}$ between the donor and the acceptor. Dotted vertical lines indicate the end of the excitation.

observed trends can be easily rationalized. Stronger electronic coupling between materials leads to stronger mixing between donor and space-separated states, i.e., a more pronounced donor character of CT and CS states and consequently a larger dipole moment for direct creation of CT and CS excitons from the ground state.

The results concerning the effects of the energy offset $\Delta E_{DA}^{\mathrm{c}}$ between LUMO levels in the donor and acceptor are summarized in Figs. 5.7(a)–(c). The parameter $\Delta E_{DA}^{\mathrm{c}}$ determines the energy width of the overlap region between single-electron states in the donor and acceptor, see Fig. 5.4(b). The smaller is $\Delta E_{DA}^{\mathrm{c}}$, the greater is the number of virtually resonant single-electron states in the donor and in the acceptor and therefore the greater is the number of (higher-lying) CT and CS states that inherit nonzero dipole moments from donor states and may thus be directly excited from the ground state. This manifests as a larger number of CT and CS excitons, as well as a larger probability that an electron is in the acceptor, with decreasing $\Delta E_{DA}^{\mathrm{c}}$.

Figures 5.8(a)–(c) show the effects of electron delocalization in the acceptor on the ultrafast dynamics at the model heterojunction. Delocalization effects are mimicked by varying the electronic coupling in the acceptor. While increasing J_A^{c} has virtually no effect on the relative

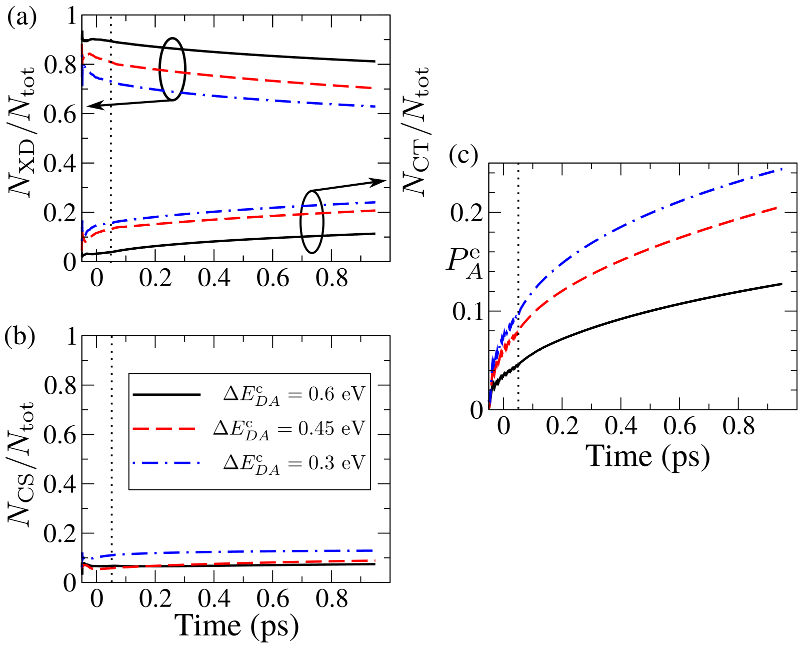

FIGURE 5.7: Time dependence of the relative number of (a) donor and CT, (b) CS excitons, and (c) the probability P^{e}_{A} that an electron is in the acceptor, for different values of the LUMO–LUMO energy offset $\Delta E^{\mathrm{c}}_{DA}$. Dotted vertical lines indicate the end of the excitation.

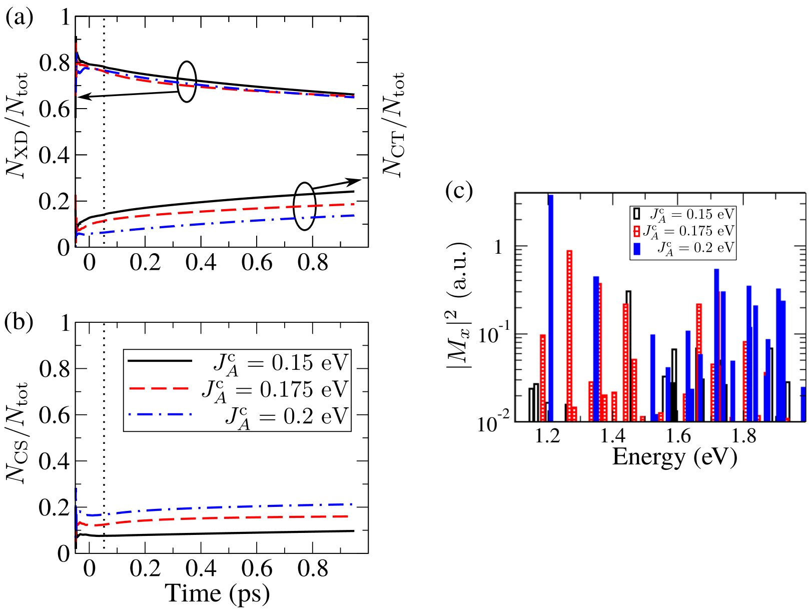

FIGURE 5.8: Time dependence of the relative number of (a) donor and CT, and (b) CS excitons, for different values of electronic coupling in the acceptor J^{c}_{A}. (c) Squared moduli of dipole matrix elements (in arbitrary units) for direct generation of CS excitons from the ground state for different values of electronic coupling in the acceptor J^{c}_{A}. Dotted vertical lines indicate the end of the excitation. Note that, globally, squared moduli of dipole matrix elements are largest for $J^{\mathrm{c}}_{A} = 0.2$ eV (completely filled bars).

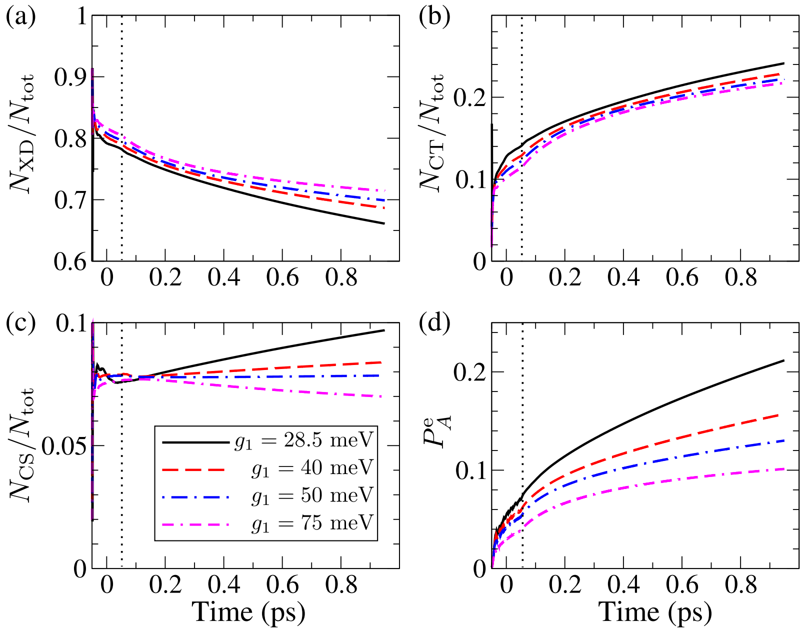

FIGURE 5.9: Time dependence of the relative number of (a) donor, (b) CT , (c) CS excitons, and (d) the probability P_A^{e} that an electron is in the acceptor, for different strengths of the carrier–phonon interaction. Dotted vertical lines indicate the end of the excitation.

number of donor excitons, it leads to an increased participation of CS and a decreased participation of CT excitons in the total exciton population. CT states, in which the electron–hole interaction is rather strong, are mainly formed from lower-energy single-electron states in the acceptor and higher-energy single-hole states in the donor. These single-particle states are not subject to strong resonant mixing with single-particle states of the other material. However, CS states are predominantly composed of lower-energy single-hole donor states and higher-energy single-electron acceptor states; the mixing of the latter group of states with single-electron donor states is stronger for larger J_A^{c}, just as in case of smaller $\Delta E_{DA}^{\mathrm{c}}$, see Fig. 5.4(b). Therefore the dipole moments for direct generation of CS excitons generally increase when increasing J_A^{c}, see Fig. 5.8(c), whereas the dipole moments for direct generation of CT excitons at the same time change only slightly, which can account for the trends of the participation of CS and CT excitons in Figs. 5.8(a) and 5.8(b).

We now turn our attention to the effects that the strength of the carrier–phonon interaction has on the ultrafast exciton dynamics at heterointerfaces. In Figs. 5.9(a)–(d), we present the results with the fixed ratio $g_2/g_1 = 2.0$ and the polaron binding energies defined in Eq. (5.8) assuming the values of approximately 20, 40, 60, and 140 meV, in ascending order of g_1. We note that it is not straightforward to predict the effect of the variations of carrier–phonon interaction strength on the population of space-separated states. Single-phonon-assisted processes preferentially couple exciton states of the same character, i.e., a donor exciton state is more strongly coupled to another donor state than to a space-separated state. This is apparent from Eq. (5.7) that expresses the carrier–phonon matrix elements in the exciton basis. On the one hand, stronger carrier–phonon interaction implies more pronounced exciton dissociation and charge separation because of stronger coupling between donor and space-separated states. On the other hand, stronger carrier–phonon interaction leads to faster relaxation of initially generated donor excitons within the donor exciton manifold to low-lying donor states. Low-lying donor states are essentially uncoupled from space-separated states, i.e., they exhibit low probabilities of exciton dissociation and charge separation. Our results, shown in Figs. 5.9(a)–(d), indicate that stronger carrier–phonon interaction leads to smaller number of CT and CS excitons, as well as the probability that an electron is in the acceptor, and to greater number of donor excitons. We also note that stronger carrier–phonon interaction changes the trend displayed by the population of CS states. While for the weakest interaction studied CS population grows after the excitation, for the strongest interaction studied CS population decays after the excitation. This is a consequence of more pronounced phonon-assisted processes leading to population of low-energy CT states once a donor exciton performs a transition to a space-separated state. This discussion can rationalize the changes in relevant quantities summarized in Figs. 5.9(a)–(d); the magnitudes of the changes observed are, however, rather small. In previous studies [141, 142], which did not deal with the initial exciton generation step, stronger carrier–phonon interaction is found to suppress quite strongly the charge separation process. The weak influence of the carrier–phonon interaction strength on ultrafast heterojunction dynamics that we observe supports the mechanism of ultrafast direct optical generation of space-separated charges. If the charge separation process at heterointerfaces were mainly driven by the free-system evolution, greater changes in the quantities describing charge separation efficiency would be expected with varying carrier–phonon interaction strength.

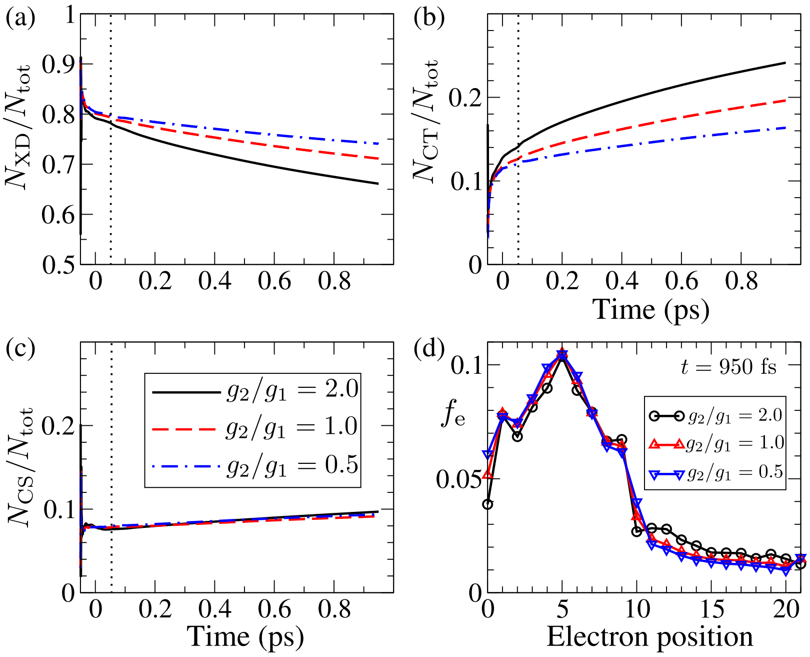

FIGURE 5.10: Time dependence of the relative number of: (a) donor, (b) CT, and (c) CS excitons for different ratios g_2/g_1 of high-frequency to low-frequency phonon mode coupling constants. (d) The distribution of an electron throughout the system $f_{\mathrm{e}}(t,r)$ 900 fs after the end of the pulsed excitation for different ratios g_2/g_1.

Additionally, we perform computations for a fixed value of $\epsilon_{\mathrm{b}}^{\mathrm{pol}} = 20$ meV and different values of the ratio g_2/g_1 among coupling constants of high- and low-frequency phonon modes. The result presented in Fig. 5.10(a)–(d) shows that the increase of the ratio g_2/g_1 increases the number of CT excitons and decreases the number of donor excitons, while the population of CS states exhibits only a weak increase. Stronger coupling to the high-frequency phonon mode (with respect to the low-frequency one) enhances charge separation by decreasing the number of donor excitons, but at the same time promotes phonon-assisted processes towards more strongly bound CT states, which is seen in Fig. 5.10(d) as larger probability f_{e} on acceptor sites close to the interface (sites 11–14). Consequently, the population of CS states remains nearly constant.

In the end, let us comment on the influence of temperature on the ultrafast exciton dynamics at a heterojunction. Results presented in Figs. 5.11(a)–(d) suggest that the ultrafast dynamics exhibits weak temperature dependence, which is consistent with existing theoretical [152] and experimental [153] insights, and also with the mechanism of direct optical generation of space-separated carriers. However, we observe that at lower temperature the normalized number of

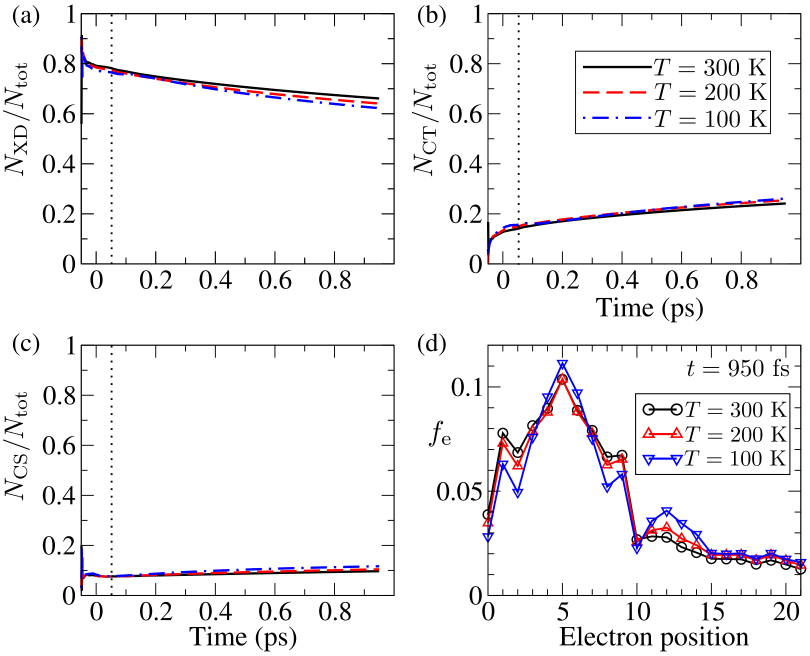

Figure 5.11: Time dependence of the relative number of: (a) donor, (b) CT, and (c) CS excitons for different temperatures. (d) The distribution of an electron throughout the system $f_{\mathrm{e}}(t, r)$ 900 fs after the end of the pulsed excitation for different temperatures.

donor excitons slightly decreases, while normalized numbers of CT and CS excitons weakly increase. Additionally, we observe an increase in the probability that an electron is located in the acceptor next to the interface (sites 11–14) as the temperature is decreased, which is a manifestation of larger population of bound (low-energy) CT states as the temperature is decreased.

In summary, we find that regardless of the particular values of varied model parameters ($J^{\mathrm{c/v}}_{DA}$, $\Delta E^{\mathrm{c}}_{DA}$, J^{c}_{A}, carrier–phonon coupling constants), the majority of CT and CS states that are present at $\sim$ 100 fs after photoexcitation have been directly generated during the excitation. Trends in quantities describing ultrafast heterojunction dynamics that we observe varying model parameters can be explained by taking into consideration the proposed mechanism of ultrafast direct optical generation of space-separated charges.

5.4 Ultrafast Spectroscopy Signatures

As discussed in Sec. 5.1.1, exciton dynamics on ultrafast time scales is typically probed experimentally using the ultrafast pump–probe spectroscopy. In such experiments, the presence of space-separated charges on ultrafast time scales after photoexcitation has been established and the energy resonance between donor exciton and space-separated states was identified as responsible for efficient charge generation [36], in agreement with our numerical results. However, while our results indicate that the majority of space-separated charges that are present at ~ 100 fs after photoexcitation have been directly optically generated, interpretation of experiments [36] suggests that these states become populated by the transition from donor exciton states. To understand the origin of this apparent difference, we numerically compute ultrafast pump–probe signals in the framework of our heterojunction model. For completeness, Sec. 5.4.1 briefly summarizes the conventional interpretation of experimental DTSs, which focuses on the dynamics of populations and completely disregards coherences. In Sec. 5.4.2, we present the theoretical treatment of ultrafast TA experiments adapted for the system at hand. Assuming that the probe pulse is deltalike, we obtain an analytic expression relating the differential transmission ΔT to the nonequilibrium state of the system "seen" by the probe pulse. The expression provides a very clear and direct interpretation of the results of ultrafast TA experiments and allows to distinguish between contributions stemming from exciton populations and coherences, challenging the existing interpretations. It is used in Sec. 5.4.3 to numerically compute DTSs.

5.4.1 Basics of Ultrafast Transient Absorption Spectroscopy and Conventional Interpretation of Experimental Signals

Figure 5.12(a) depicts the principle scheme of a femtosecond time-resolved TA spectroscopy experiment [154–156]. The sample is first irradiated by an intense pump pulse that excites the sample and initiates the nonequilibrium dynamics of the excited species. Temporal evolution of the state of the sample is subsequently examined using a second, weaker, probe pulse, whose time delay with respect to the pump pulse (the so-called pump–probe delay τ) can be tuned. Pulse duration limits the temporal resolution of the experiment, so that pulses should be as short as possible to resolve the fastest photophysical processes. On the other hand, the pump pulse should be as spectrally narrow as possible, so that it can selectively excite the optical transition of interest. Therefore, there is a trade-off between the temporal and spectral resolution in a

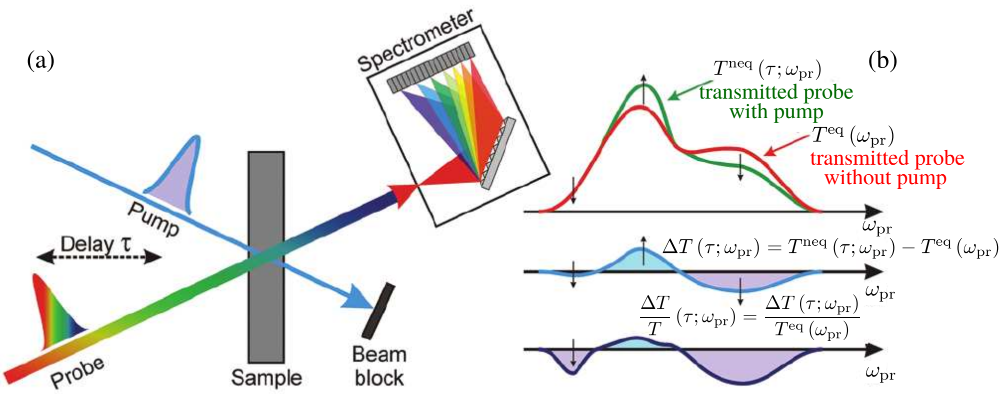
(a)
Spectrometer
Pump
Delay τ
Probe
Sample
Beam block
(b)
$T^{\rm neq}(\tau;\omega_{\rm pr})$
transmitted probe with pump
$T^{\rm eq}(\omega_{\rm pr})$
transmitted probe without pump
$\omega_{\rm pr}$
$\Delta T(\tau;\omega_{\rm pr}) = T^{\rm neq}(\tau;\omega_{\rm pr}) - T^{\rm eq}(\omega_{\rm pr})$
$\omega_{\rm pr}$
$\frac{\Delta T}{T}(\tau;\omega_{\rm pr}) = \frac{\Delta T(\tau;\omega_{\rm pr})}{T^{\rm eq}(\omega_{\rm pr})}$
$\omega_{\rm pr}$

FIGURE 5.12: (a) Schematic view of a femtosecond time-resolved TA experiment. The pump is essentially monochromatic, whereas the probe is a broadband pulse. (b) Calculation of the DTS. Adapted from Ref. [156] with permission of The Royal Society of Chemistry (RSC) on behalf of the Centre National de la Recherche Scientifique (CNRS) and the RSC.

pump–probe experiment. The probe pulse should be as short as possible, because a spectrally wide (broadband) probe pulse enables simultaneous measurements at many different frequencies. Having passed through the sample, the broadband probe pulse is spectrally resolved in a spectrometer. The experimental quantity of interest is the DTS that is a function of both the probe frequency $\omega_{\rm pr}$ and the pump–probe delay τ

$$\frac{\Delta T}{T}(\tau;\omega_{\rm pr}) = \frac{T^{\rm neq}(\tau;\omega_{\rm pr}) - T^{\rm eq}(\omega_{\rm pr})}{T^{\rm eq}(\omega_{\rm pr})}. \tag{5.19}$$

The transmission of the sample that is initially (before the action of the probe) unexcited is denoted by $T^{\rm eq}(\omega_{\rm pr})$ and it is an equilibrium property of the sample. On the other hand, the transmission of the pump-driven system $T^{\rm neq}(\tau;\omega_{\rm pr})$ is a nonequilibrium quantity and it depends on both the probe frequency and the time delay between the pump and probe.

The conventional interpretation of the DTS is performed by disregarding coherent effects and concentrating on the dynamics of populations of excited states [155, 156]. The action of the pump pulse populates excited states by reducing the occupation of the ground state. Let us distinguish between different types of the DTS.

(a) If the probe frequency is greater than or equal to the ground state absorption edge, the absorption of the pumped sample is weaker than the equilibrium absorption, because the ground state population is depleted by pumping. In other words, the transmission of the pumped sample is greater than the equilibrium transmission, and the DTS is positive. Such a signal is commonly denoted as the ground state bleaching (GSB).

(b) If the probe frequency is less than or equal to the ground state absorption edge, a probe photon may trigger the stimulated emission from the excited state back to the ground state. The stimulated emission (SE) is characterized by a positive DTS.

(c) The probe frequency may be resonant with a transition from an excited state to some other higher-lying excited state. The hallmark of the photoinduced absorption (PIA) is a negative DTS. In principle, PIA signal can be observed at any probe frequency, depending on the energy levels of the system under study.

Let us now emphasize that an analysis of an experimental DTS and its deconvolution into the above-mentioned three types of signals is a highly nontrivial task. For example, since PIA may occur at any probe frequency, it may spectrally overlap with GSB and SE signals, and even prevail over them. The interpretation of experimental signals, therefore, is usually done in combination with the results of quantum chemical calculations, from which one can gain insight into the excitation energies of the system, as well as possible transitions between excited states.

5.4.2 Theoretical Treatment of Ultrafast Transient Absorption Spectroscopy

Our theoretical approach to a TA experiment considers the interaction with the pump pulse as described in Ch. 3, i.e., within the density matrix formalism employing the DCT scheme up to the second order in the pump field. Furthermore, we assume that the interaction with the probe pulse does not change significantly the nonequilibrium state created by the pump pulse, and it is treated in the linear response regime. The corresponding nonequilibrium dipole–dipole retarded correlation function is then used to calculate DTSs [157, 158].

To study time-resolved TA experiments, we extend our two-band lattice model of a bilayer by including more single-electron (single-hole) energy levels per site. More details on this multi-band model can be found in Sec. 6.2, where its Hamiltonian is precisely formulated. Here, we investigate in more details only those aspects of the multiband model that are necessary to formulate a theoretical framework in which ultrafast TA experiments can be studied. Multiple single-electron (single-hole) levels on each site should be dipole-coupled among themselves in order to enable probe-induced transitions between various exciton states. We denote by $c_{i\beta_i}^\dagger$ ($c_{i\beta_i}$) creation (annihilation) operators for electrons on site i and in conduction-band orbital β_i; similarly, $d_{i\alpha_i}^\dagger$ ($d_{i\alpha_i}$) create (annihilate) a hole on site i and in valence-band orbital α_i. The dipole-moment operator in terms of electron and hole operators assumes the form

$$P = \sum_{\substack{i \\ \beta_i\alpha_i}} d_i^{\mathrm{cv}} \left(c_{i\beta_i}^\dagger d_{i\alpha_i}^\dagger + d_{i\alpha_i} c_{i\beta_i} \right) + \sum_{\substack{i \\ \beta_i \neq \beta_i'}} d_i^{\mathrm{cc}} c_{i\beta_i}^\dagger c_{i\beta_i'} - \sum_{\substack{i \\ \alpha_i \neq \alpha_i'}} d_i^{\mathrm{vv}} d_{i\alpha_i'}^\dagger d_{i\alpha_i}. \tag{5.20}$$

Intraband dipole matrix elements d_i^{cc} (d_i^{vv}) describe electron (hole) transitions between different single-electron (single-hole) states on site i, as opposed to the interband matrix elements d_i^{cv}, which are responsible for the exciton generation. Performing transition to the exciton basis, which is defined analogously to Eq. (5.5) [see also Eq. (6.4)], dipole matrix elements for transitions from the ground state to exciton state x are [see also Eq. (6.5)]

$$M_x = \sum_{\substack{i \\ \beta_i\alpha_i}} d_i^{\mathrm{cv}} \psi_{(i\alpha_i)(i\beta_i)}^{x*}, \tag{5.21}$$

while those for transitions from exciton state x to exciton state $\bar{x}$ are

$$M_{\bar{x}}^x = \sum_{\substack{i \\ \alpha_i \neq \alpha_i'}} \sum_{\substack{j \\ \beta_j}} \psi_{(i\alpha_i)(j\beta_j)}^{\bar{x}*} d_i^{\mathrm{vv}} \psi_{(i\alpha_i')(j\beta_j)}^x - \sum_{\substack{i \\ \beta_i \neq \beta_i'}} \sum_{\substack{j \\ \alpha_j}} \psi_{(j\alpha_j)(i\beta_i')}^{\bar{x}*} d_i^{\mathrm{cc}} \psi_{(j\alpha_j)(i\beta_i)}^x. \tag{5.22}$$

Further developments are facilitated by working with the Hamiltonian that is explicitly expressed in terms of exciton creation and annihilation operators, see Eq. (3.89), and that is relevant for the second-order (low-density) dynamics. The operator P [Eq. (5.20)] expressed in terms of operators $X_x, X_x^\dagger$, which are defined as

$$X_x^\dagger = \sum_{\substack{i\alpha_i \\ j\beta_j}} \psi_{(i\alpha_i)(j\beta_j)}^x c_{j\beta_j}^\dagger d_{i\alpha_i}^\dagger, \tag{5.23}$$

assumes the form

$$P = \sum_x \left(M_x X_x^\dagger + M_x^* X_x \right) - \sum_{\bar{x}x} M_{\bar{x}}^x X_{\bar{x}}^\dagger X_x. \tag{5.24}$$

In the last equation, we retain only contributions whose expectation values are at most of the second order in the pump field.

We concentrate on the so-called nonoverlapping regime [157], in which the probe pulse, described by its electric field $e(t)$, acts after the pump pulse. We take that our system meets the condition of optical thinness, i.e., the electromagnetic field originating from probe-induced dipole moment can be neglected compared to the electromagnetic field of the probe. In the following considerations, the origin of time axis $t = 0$ is taken to be the instant at which the probe pulse starts. The pump pulse finishes at $t = -\tau$, where τ is the time delay between (the end of) the pump and (the start of) the probe. The pump creates a nonequilibrium state of the system which is, at the moment when the probe pulse starts, described by the density matrix $\rho(0)$, which implicitly depends on the pump–probe delay τ.

In the linear-response regime, the probe-induced dipole moment $d_p(t)$ for $t > 0$ is expressed as [157]

$$d_p(t) = \int \mathrm{d}t' \, \chi(t, t') \, e(t'), \tag{5.25}$$

where $\chi(t, t')$ is the nonequilibrium retarded dipole–dipole correlation function

$$\chi(t, t') = -\frac{\mathrm{i}}{\hbar} \theta(t - t') \, \mathrm{Tr} \left(\rho(0) [P(t), P(t')] \right). \tag{5.26}$$

Time dependence in Eq. (5.26) is governed by the Hamiltonian of the system in the absence of external fields [Eq. (3.89)]

$$H_{E(t)=0} = H_0 + H_{\mathrm{x-p}}, \tag{5.27}$$

where H_0 is the noninteracting Hamiltonian of excitons in the phonon field [the first two terms on the right-hand side of Eq. (3.89)], while $H_{\mathrm{x-p}}$ accounts for exciton–phonon interaction [the third term on the right-hand side of Eq. (3.89)]. For an ultrashort probe pulse, $e(t) = e_0 \delta(t)$, probe-induced dipole moment assumes the form

$$d_p(t) = e_0\chi(t,0) = e_0\left(-\frac{\mathrm{i}}{\hbar}\right)\mathrm{Tr}\left(\rho(0)[P(t),P(0)]\right). \tag{5.28}$$

The probe pulse tests the possibility of transitions between various exciton states, i.e., it primarily affects carriers. Therefore, as a reasonable approximation to the full time-dependent operator $P(t)$ appearing in Eq. (5.28), operator $P^{(0)}(t)$, evolving according to the noninteracting Hamiltonian H_0 in Eq. (5.27), may be used. This leads us to the central result for the probe-induced dipole moment:

$$d_p(t) = e_0\left(-\frac{\mathrm{i}}{\hbar}\right)\mathrm{Tr}\left(\rho(0)[P^{(0)}(t),P(0)]\right). \tag{5.29}$$

The commutator on the right-hand side of Eq. (5.29) can be derived using the commutation relations embodied in Eq. (3.87), in which four-index coefficients $C_{\bar{x}x}^{\bar{x}'x'}$ defined in Eq. (3.88) assume the form

$$\begin{aligned}
C_{\bar{x}x}^{\bar{x}'x'} =& \sum_{\substack{\bar{j}\bar{\beta}_j\\ j\beta_j}}\left(\sum_{i\alpha_i}\psi^{\bar{x}'*}_{(i\alpha_i)(\bar{j}\bar{\beta}_j)}\psi^{x'}_{(i\alpha_i)(j\beta_j)}\right)\left(\sum_{i\alpha_i}\psi^{\bar{x}}_{(i\alpha_i)(\bar{j}\bar{\beta}_j)}\psi^{x*}_{(i\alpha_i)(j\beta_j)}\right)\\
&+\sum_{\substack{\bar{i}\bar{\alpha}_i\\ i\alpha_i}}\left(\sum_{j\beta_j}\psi^{\bar{x}'*}_{(\bar{i}\bar{\alpha}_i)(j\beta_j)}\psi^{x'}_{(i\alpha_i)(j\beta_j)}\right)\left(\sum_{j\beta_j}\psi^{\bar{x}}_{(\bar{i}\bar{\alpha}_i)(j\beta_j)}\psi^{x*}_{(i\alpha_i)(j\beta_j)}\right).
\end{aligned} \tag{5.30}$$

The final result for the commutator $[P^{(0)}(t),P(0)]$ is

$$\begin{aligned}
[P^{(0)}(t),P(0)] =& \sum_x |M_x|^2\left(\mathrm{e}^{-\mathrm{i}\omega_x t}-\mathrm{e}^{\mathrm{i}\omega_x t}\right)\\
&-\sum_{\bar{x}_1x_1}\sum_{xx'}\left(M_x^*M_{x'}C_{x'x}^{\bar{x}_1x_1}\mathrm{e}^{-\mathrm{i}\omega_x t}-M_xM_{x'}^*C_{xx'}^{\bar{x}_1x_1}\mathrm{e}^{\mathrm{i}\omega_x t}\right)X_{\bar{x}_1}^\dagger X_{x_1}\\
&-\sum_{xx'}\left(M_xM_{x'}^x\right)^*\mathrm{e}^{-\mathrm{i}\omega_x t}X_{x'}+\sum_{xx'}M_xM_{x'}^x\mathrm{e}^{\mathrm{i}\omega_x t}X_{x'}^\dagger\\
&+\sum_{xx'}\left(M_xM_{x'}^x\right)^*\mathrm{e}^{-\mathrm{i}(\omega_{x'}-\omega_x)t}X_{x'}-\sum_{xx'}M_xM_{x'}^x\mathrm{e}^{\mathrm{i}(\omega_{x'}-\omega_x)t}X_{x'}^\dagger\\
&+\sum_{\bar{x}xx'}M_{x'}^xM_x^{\bar{x}}\mathrm{e}^{\mathrm{i}(\omega_{x'}-\omega_x)t}X_{x'}^\dagger X_{\bar{x}}-\sum_{\bar{x}xx'}M_x^{x'}M_{\bar{x}}^x\mathrm{e}^{-\mathrm{i}(\omega_{x'}-\omega_x)t}X_{\bar{x}}^\dagger X_{x'}.
\end{aligned} \tag{5.31}$$

The expectation values [with respect to $\rho(0)$] of the operators appearing in the last equation are simply the active purely electronic density matrices of our formalism computed when the probe pulse starts, i.e., $\mathrm{Tr}\left(\rho(0)X_x\right) = y_x(0)$ and $\mathrm{Tr}\left(\rho(0)X_{\bar{x}}^\dagger X_x\right) = n_{\bar{x}x}(0)$.

Inserting Eq. (5.31) into Eq. (5.29), we observe two different types of contributions to the probe-induced dipole moment $d_p(t)$. Contributions of the first type oscillate at frequencies ω_x corresponding to probe-induced transitions between the ground state and exciton state x, while those of the second type oscillate at frequencies $\omega_{\bar{x}} - \omega_x$ corresponding to probe-induced transitions between exciton states $\bar{x}$ and x. Here, we focus our attention on the process of PIA, in which an exciton in state x performs a transition to another state $\bar{x}$ under the influence of the probe field. Therefore, we will further consider only the second type of contributions, i.e., in the expression for the commutator $[P^{(0)}(t), P(0)]$, we retain only the last four summands on the right-hand side of Eq. (5.31).

The frequency-dependent transmission coefficient $T(\omega)$ is defined as [157] (we use SI units)

$$T(\omega) = 1 + \frac{c\mu_0}{\mathcal{S}\hbar}\,\mathrm{Im}\left\{\hbar\omega\,\frac{d_p(\omega)}{e(\omega)}\right\}, \tag{5.32}$$

where $d_p(\omega)$ and $e(\omega)$ are Fourier transformations of $d_p(t)$ and $e(t)$, respectively, $\mathcal{S}$ is the irradiated area of the sample, while μ_0 is the magnetic permeability of the vacuum. Here, we concentrate on obtaining an expression for part of the differential transmission that stems from processes of PIA. In Eq. (5.19), the equilibrium transmission of the sample $T^{\mathrm{eq}}(\omega)$ appears. However, $T^{\mathrm{eq}}(\omega)$ is expected to reflect only transitions involving the ground state, because it is a property of the unexcited sample. Since our aim is to make only qualitative, but not quantitative, comparisons to experimental PIA signals, we will not further consider $T^{\mathrm{eq}}(\omega)$. We compute

$$\Delta T_{\mathrm{PIA}}\left(\tau;\omega\right) = T_{\mathrm{PIA}}^{\mathrm{neq}}\left(\tau;\omega\right), \tag{5.33}$$

where $T_{\mathrm{PIA}}^{\mathrm{neq}}\left(\tau;\omega\right)$ is computed by the Fourier transformation of the aforementioned second type of contributions to the probe-induced dipole moment $d_p(t)$. Computing the Fourier transformation $d_p(\omega)$, we obtain integrals of the type

$$\int_0^{+\infty} \mathrm{d}t\, \mathrm{e}^{\mathrm{i}(\omega-\Omega+\mathrm{i}\eta)t} = \frac{\mathrm{i}}{\omega-\Omega+\mathrm{i}\eta}, \tag{5.34}$$

where we have introduced a positive infinitesimal parameter η to ensure the integral convergence. Physically, introducing η effectively accounts for the line broadening [158]. For simplicity, we assume that only one value of η is used in all the integrals of the type (5.34). Finally, inserting the result for $d_p(\omega)$ into Eqs. (5.32) and (5.33), the following expression is obtained

$$\begin{aligned}
\Delta T_{\mathrm{PIA}}(\tau;\omega) \propto \operatorname{Im}\Bigg\{ & \sum_{xx'} (M_x M^x_{x'})^* \frac{\hbar\omega}{\hbar\omega - (\hbar\omega_{x'} - \hbar\omega_x) + \mathrm{i}\eta} y_{x'}(0) - \\
& - \sum_{xx'} M_x M^x_{x'} \frac{\hbar\omega}{\hbar\omega + (\hbar\omega_{x'} - \hbar\omega_x) + \mathrm{i}\eta} y^*_{x'}(0) + \\
& + \sum_{\bar{x}xx'} M^x_{x'} M^{\bar{x}}_x \frac{\hbar\omega}{\hbar\omega + (\hbar\omega_{x'} - \hbar\omega_x) + \mathrm{i}\eta} y^*_{x'}(0) y_{\bar{x}}(0) - \\
& - \sum_{\bar{x}xx'} M^{x'}_x M^x_{\bar{x}} \frac{\hbar\omega}{\hbar\omega - (\hbar\omega_{x'} - \hbar\omega_x) + \mathrm{i}\eta} y^*_{\bar{x}}(0) y_{x'}(0) + \\
& + \sum_{\bar{x}xx'} M^x_{x'} M^{\bar{x}}_x \frac{\hbar\omega}{\hbar\omega + (\hbar\omega_{x'} - \hbar\omega_x) + \mathrm{i}\eta} \bar{n}_{x'\bar{x}}(0) - \\
& - \sum_{\bar{x}xx'} M^{x'}_x M^x_{\bar{x}} \frac{\hbar\omega}{\hbar\omega - (\hbar\omega_{x'} - \hbar\omega_x) + \mathrm{i}\eta} \bar{n}_{\bar{x}x'}(0) \Bigg\}.
\end{aligned} \tag{5.35}$$

In the last equation, we have explicitly separated coherent from incoherent contributions by introducing the correlated parts of exciton populations and exciton–exciton coherences $\bar{n}_{\bar{x}x}$, whose definition is given in Eq. (3.47). The coherences between exciton states and the ground state $y_x(0)$, as well as correlated parts of exciton–exciton coherences $\bar{n}_{\bar{x}x}(0)$ ($\bar{x} \neq x$), are expected to approach zero for sufficiently long time delays between the pump and the probe. In this limit, Eq. (5.35) contains only incoherent exciton populations $\bar{n}_{xx}$:

$$\begin{aligned}
\Delta T_{\mathrm{PIA}}(\tau;\omega) \propto & - \sum_{xx'} |M^x_{x'}|^2 \frac{\eta \cdot \hbar\omega}{(\hbar\omega + (\hbar\omega_{x'} - \hbar\omega_x))^2 + \eta^2} \bar{n}_{x'x'}(0) \\
& + \sum_{xx'} |M^x_{x'}|^2 \frac{\eta \cdot \hbar\omega}{(\hbar\omega - (\hbar\omega_{x'} - \hbar\omega_x))^2 + \eta^2} \bar{n}_{x'x'}(0).
\end{aligned} \tag{5.36}$$

This expression is manifestly negative when it describes probe-induced transitions from exciton state x' to some higher-energy exciton state x. The last conclusion is in agreement with the usual experimental interpretation of pump–probe spectra, where negative DTS corresponds to PIA [155]. It is expected that Eq. (5.36) correctly describes the PIA signal on picosecond or longer time scales, because the coherences between exciton states and the ground state y_x typically decay on $\lesssim$ 100-fs time scale after the pump field has vanished, while exciton–exciton coherences typically decay on picosecond time scales or longer. Our full expression for the PIA signal [Eq. (5.35)] demonstrates that, in the ultrafast regime, it is expected that both coherences between exciton states and the ground state $y_x(0)$ and exciton–exciton coherences $\bar{n}_{\bar{x}x}(0)$ ($\bar{x} \neq x$), along with incoherent exciton populations $\bar{n}_{xx}(0)$, play significant role. The signal embodied Eq. (5.35) describes PIA, but it is not manifestly negative. Therefore, our theoretical developments suggest that the correspondence between the sign of the differential transmission signal and its type (GSB, SE, or PIA) does not necessarily hold on ultrafast time scales.

5.4.3 Numerical Results: Ultrafast Differential Transmission Signals

In order to compute PIA signals and at the same time keep the numerics manageable, we extend our model by introducing only one additional single-electron level both in the donor and in the acceptor and one additional single-hole level in the donor. Such an extension is motivated by the fact that the dipole-induced coupling between two exciton states is strongest when these two states are of the same character, see Eqs. (5.22) and (5.24). Therefore, probing the PIA from donor (space-separated) states is expected to involve higher-lying donor (space-separated) states, the existence of which requires additional higher-lying single-electron states in both materials and higher-lying single-hole states in the donor. Additional energy levels in the donor and the corresponding bandwidths are extracted from the aforementioned electronic structure calculation on an infinitely long PCPDTBT polymer chain. The additional single-electron level is located ca. 1.16 eV above the single-electron level used in all the calculations and the bandwidth of the corresponding zone is estimated to be ca. 0.48 eV. The additional single-hole level is located ca. 1.13 eV below the single-hole level used in all the calculations and the bandwidth of the corresponding zone is estimated to be ca. 0.57 eV. The additional energy level in the acceptor is extracted from an electronic structure calculation on the C_{60} molecule. The calculation is based on DFT using either LDA or B3LYP exchange–correlation functional (both choices give similar results) and 6-31G basis set and was performed using the NWChem package [159]. We found that the additional single-electron level lies around 1 eV above the single-electron level used in all the calculations. The bandwidth of the corresponding zone is set to 0.6 eV, see Table 5.1.

Here, we assume that the waveform of the pump pulse is

$$E(t) = E_0 \cos(\omega_c t) \exp\left(-\frac{t^2}{\tau_G^2}\right) \theta(t + t_0)\theta(t_0 - t), \tag{5.37}$$

where we take $\tau_G = 20$ fs and $t_0 = 50$ fs, while the probe is

$$e(t) = e_0 \delta(t - (t_0 + \tau)), \tag{5.38}$$

with variable pump–probe delay τ. The intraband dipole matrix elements d_i^{cc}, d_i^{vv} in Eq. (5.20) are assumed to be equal in the whole system

$$d_i^{\mathrm{cc}} = d_i^{\mathrm{vv}} = d^{\mathrm{intra}} = \frac{1}{2} d^{\mathrm{cv}}. \tag{5.39}$$

The positive parameter η, which effectively accounts for the line broadening, is set to $\eta = 50$ meV. Variations in η do not change qualitative features of the presented PIA spectra, which was checked in the Supplementary Material associated to Ref. [134]. In actual computations of the signal given in Eq. (5.35), we should remember that the pump pulse finishes at instant t_0, while in Eq. (5.35) all the quantities are taken at the moment when the probe starts, which is now $t_0 + \tau$; in other words, $y_x(0) \to y_x(t_0 + \tau)$, $\bar{n}_{\bar{x}x}(0) \to \bar{n}_{\bar{x}x}(t_0 + \tau)$ when we compute pump–probe signals using Eq. (5.35) and the pump and probe are given by Eqs. (5.37) and (5.38), respectively.

In the following, we separately show the total signal [full Eq. (5.35)], the y-part of the signal [the first two sums in Eq. (5.35)], and the $\bar{n}$-part of the signal [the third sum in Eq. (5.35)]. We note that it would be possible to further separate the $\bar{n}$-part of the signal into the contribution stemming from incoherent exciton populations $\bar{n}_{xx}$ [Eq. (5.36)] and exciton–exciton coherences

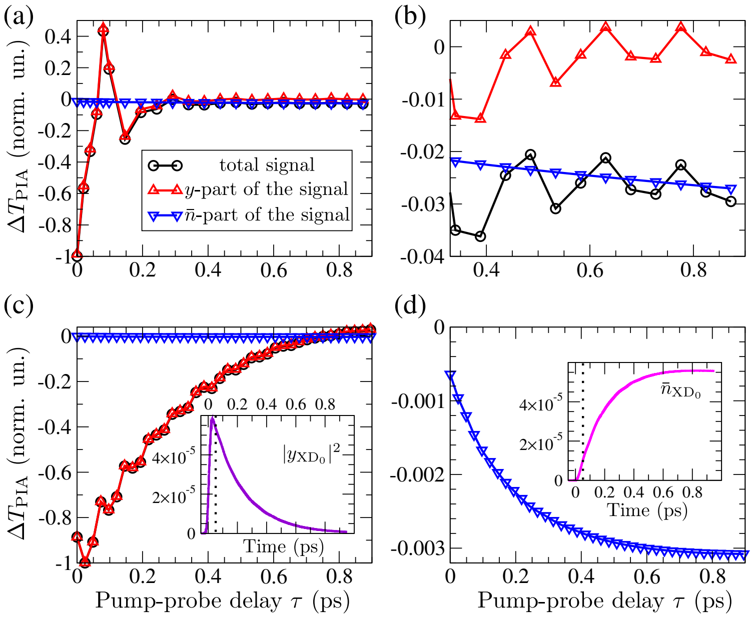

FIGURE 5.13: DTS ΔT_{PIA} [Eq. (5.35)] as a function of the pump–probe delay for: (a) pump at 1.5 eV (826 nm) and probe at 1 eV (1240 nm) testing PIA dynamics from space-separated states, and (c) pump resonant with the lowest donor exciton (1.21 eV, 1025 nm) and probe at 1.13 eV (1096 nm) testing PIA dynamics from donor states. The inset of (c) shows the coherent exciton population $|y_{\text{XD}_0}|^2$ of the lowest donor state XD_0. (b) The same signal as in (a) at longer pump–probe delays ($>$ 300 fs). (d) $\bar{n}$-part of the signal shown in (c); the inset displays the incoherent exciton population $\bar{n}_{\text{XD}_0}$ of the lowest donor state.

$\bar{n}_{\bar{x}x}$ ($\bar{x} \neq x$). However, their explicit separation shows that, on time scales of our interest, the overall $\bar{n}$-part of the signal is qualitatively very similar to its contribution stemming from incoherent exciton populations only, which is shown in the Supplementary Material associated to Ref. [134]. Therefore, for the simplicity of further discussion, we may consider the $\bar{n}$-part of the signal as completely originating from incoherent exciton populations.

In Figs. 5.13(a) and (b) we show PIA signal from space-separated states after pumping at 1.5 eV, which initially generates donor excitons that are well above the lowest donor state, see Fig. 5.4(c). The frequency ω in Eq. (5.35) satisfies $\hbar\omega = 1$ eV, which is (for the adopted values of model parameters) appropriate for observing PIA from space-separated states. At small pump–probe delays ($\tau \lesssim$ 300 fs), we see that the oscillatory features stemming from coherences between exciton states and the ground state (y-part of the signal) dominate the dynamics. At larger delays, the part originating from established (incoherent) exciton populations ($\bar{n}$-part of the signal) prevails, see Fig. 5.13(b), and the shape of the signal resembles the shapes of signals from space-separated states in Fig. 4(c) of Ref. [36]. The signal decreases at larger delays, which correlates very well with the fact that the numbers of CT and CS excitons increase, see Fig. 5.5(a). In other words, at larger pump–probe delays, at which the influence of coherences between exciton states and the ground state is small, the signal can be unambiguously interpreted in terms of charge transfer from the donor to the acceptor.

Figures 5.13(c) and (d) display PIA signal from donor excitons following the pump excitation at the lowest donor state (1.21 eV). The frequency ω in Eq. (5.35) satisfies $\hbar\omega = 1.13$ eV, which is appropriate for studying the PIA from donor states. The overall signal shape is qualitatively similar to the shape of donor exciton PIA signal in Fig. 4(a) of Ref. [36], but the interpretation of its origin is rather different. While the authors of Ref. [36] suggest that the monotonically increasing PIA signal from donor excitons reflects their transfer to space-separated states, our signal predominantly originates from coherences between donor states and the ground state [y-part of the signal in Fig. 5.13(c)]. Furthermore, the shape of the total signal matches very well the decay of the coherent population of the lowest donor exciton, see the inset of Fig. 5.13(c), while the shape of the $\bar{n}$-part of the signal corresponds well to the changes in the incoherent population of the lowest donor state, see the inset of Fig. 5.13(d). This incoherent population does not decay during our computation: immediately after the pump pulse it rises and at longer times it reaches a plateau, which signals that the donor exciton population is "blocked" in the lowest donor state. The lowest donor exciton is very strongly dipole-coupled to the ground state, its population comprising around 75% of the total generated population. Therefore, according to our numerical results, the observed PIA signal from donor excitons in this case mimics the conversion from coherent to incoherent exciton population of the lowest donor state. This, however, does not necessarily mean that the concomitant charge transfer is completely absent in this case. Instead, the presence of coherences between exciton states and the ground state, which dominate the signal for all pump–probe delays we studied, prevents us from attributing the signal to the population transfer from donor excitons to space-separated states. The aforementioned conversion from coherent to incoherent exciton population of the lowest donor state is rather slow because of the relatively weak coupling between low-lying donor excitons on the one hand and space-separated states on the other hand (this weak coupling was also appreciated in Ref. [36]). On the other hand, pumping well above the lowest donor and space-separated states, the couplings between these species are stronger and more diverse than for the pump resonant with the lowest donor exciton; this situation resembles the one encountered for the excitation condition in Fig. 4(c) of Ref. [36].

5.5 Discussion and Significance of Our Results

In this chapter, we have presented a study of the subpicosecond exciton dynamics in a one-dimensional model of a D/A heterointerface. The principal advantage of our method over other methods used in literature [52, 58, 141, 142, 160] is the fact that it treats both the generation of excitons and their further separation on equal footing and that it deals with all the relevant interactions on a fully quantum level. Since we explicitly consider the exciton generation from an initially unexcited heterojunction, we are able to assess the importance of the direct optical generation of spatially separated charges with respect to other proposed mechanisms of their generation on subpicosecond time scales. We find that the resonant electronic coupling between donor and space-separated states does not only enhance the transfer from the former to the latter group of states [36, 49], but also opens up a new and important pathway to obtain space-separated charges: their direct optical generation [143, 144]. While this mechanism has been proposed on the basis of electronic structure and model Hamiltonian calculations, which did not include any dynamics, our study is, to the best of our knowledge, the first to investigate the possibility of direct optical generation of separated charges by performing a fully quantum and statistical investigation of ultrafast exciton dynamics at a heterointerface. We conclude that the largest part of space-separated charges that are present on ~ 100-fs time scales after the initial photoexcitation are directly optically generated, contrary to the general belief that they originate from ultrafast transitions from donor states. Our results, therefore, do not only confirm the theoretical hypotheses about the possibility of the direct optical generation of space-separated charges [143, 144], but position them into a wider framework by performing a study of subpicosecond dynamics of electronic excitations in a photoexcited D/A blend.

The resonant coupling between states of donor excitons and space-separated charges is at the heart of the direct optical generation of the latter group of states. This coupling is mediated by the D/A transfer integrals (J^{c}_{DA}, J^{v}_{DA}) and it ultimately originates from the resonant mixing between single-electron states in the donor and acceptor parts of the heterojunction. It makes space-separated states acquire nonzero dipole moment from states of donor excitons. In other words, it is a redistribution of oscillator strengths between donor and space-separated states that makes the latter group of states accessible directly from the ground state. The last point was previously highlighted in studies conducted on two- [143] and three-dimensional [144] heterojunction models. Differently from our one-dimensional model, in which the D/A coupling is restricted to only two sites ($N-1$ and N) adjacent to the interface, in higher-dimensional models the dominant part of the D/A coupling involves more than a single pair of sites. Since we convincingly demonstrate that, in our one-dimensional model, the redistribution of oscillator strengths promotes the direct optical generation into the main source of space-separated carriers on ultrafast time scales, we speculate that this conclusion would remain valid in a more realistic higher-dimensional model of a heterointerface. While there is absorption intensity transfer from donor to space-separated states brought about by their resonant mixing, the absorption still primarily occurs in the donor part of a heterojunction, see Fig. 5.5(a). Our results show that on ultrafast time scales the direct optical generation as a source of space-separated carriers is more important than transitions from donor to space-separated states. This, however, does not mean that initially generated donor excitons are not transformed into space-separated states. They indeed are, see Figs. 5.5(a) and (b), but the characteristic time scale on which populations of space-separated states change due to the free-system evolution is longer than 100 fs.

We find that regardless of the particular values of varied model parameters ($J^{\mathrm{c/v}}_{DA}$, $\Delta E^{\mathrm{c}}_{DA}$, J^{c}_{A}, carrier–phonon coupling constants), the majority of CT and CS states that are present at ~ 100 fs after photoexcitation have been directly generated during the excitation. The ultrafast generation of separated charges at heterointerfaces is more pronounced when the D/A electronic coupling (J^{c}_{DA}, J^{v}_{DA}) is larger or when the energy overlap region between single-electron states in the donor and acceptor is wider, either by increasing the electronic coupling J^{c}_{A} in the acceptor or decreasing the LUMO–LUMO offset $\Delta E^{\mathrm{c}}_{DA}$ between the two materials, see Fig. 5.4(b). Our results are, therefore, in agreement with studies emphasizing the beneficial effects of larger electronic couplings among materials [160], better charge delocalization [52, 138, 141, 160], and smaller LUMO–LUMO offset [161] on charge separation. We find that strong carrier–phonon interaction suppresses charge separation, in agreement with previous theoretical studies [141, 142] in which the effects of variations of carrier–phonon coupling constants have been systematically investigated. However, changes in the quantities we use to monitor charge separation with variations of carrier–phonon coupling strength are rather small, which we interpret to be consistent with the ultrafast direct optical generation of space-separated charges. Our theoretical treatment of ultrafast exciton dynamics is fully quantum, but it is expected to be valid for not too strong coupling of excitons to lattice vibrations, since the phonon branch of the hierarchy is truncated at a finite order, see Ch. 3 and Sec. 4.1. If the influence of phonons on excitons were too strong, the hierarchy of equations would have to be truncated at a higher level, which would make it computationally intractable. When the effects of lattice motion on excitons are strong, one has, in turn, to consider the feedback of excitons on phonons, which is not captured by the current approach. The feedback of excitons on the lattice motion can be relatively easily included in a mixed quantum/classical approach, where excitons are treated quantum mechanically, while the lattice motion is treated classically. To estimate the importance of the feedback of excitons on the lattice motion, we have performed the computation using the surface hopping approach [162, 163]. Results of this computation, which can be found in the Supplementary Material associated to Ref. [134], show that the feedback effect of excitons on the lattice motion, which is expected to be important for stronger exciton–phonon interaction, is rather small. We therefore expect that more accurate treatment of exciton–phonon interaction is not crucial to describe heterojunction dynamics on ultrafast time scales. If one wants to treat more accurately strong exciton–phonon interaction and yet remain in the quantum framework, other theoretical approaches based on state-of-the-art multiconfigurational techniques [56, 59], infinite resummations within the Green's function formalism [164, 165], or variational ansätze for the wave function of electron–phonon system [142] have to be employed. We have also checked that the introduction of the diagonal static disorder in our model does not significantly alter qualitative features of the proposed picture of ultrafast exciton dynamics at heterointerfaces, see a more detailed discussion in Ref. [134]. The last conclusion is in agreement with the results of a systematic investigation of the effects of disorder on charge separation at model D/A interfaces [50], which suggest that, regardless of the degree of disorder, the essential physics of free hole and electron generation remains the same.

Despite a simplified model of organic semiconductors, our theoretical treatment takes into account all relevant effects. Consequently, our approach to ultrafast pump–probe experiments produces results that are in qualitative agreement with experiments and confirms the previously observed dependence of the exciton dynamics on the excess photon energy [36]. Our results indicate that the interpretation of ultrafast pump–probe signals is involved, as it is hindered by coherences (dominantly by those between exciton states and the ground state) that cannot be neglected on the time scales studied. Time scales on which coherent features are prominent depend on the excess photon energy. We find that higher values of the excess photon energy enable faster disappearance of the coherent part of the signal since they offer a wealth of phonon-assisted transitions between exciton states, which makes the conversion from coherent to incoherent exciton populations faster. Pumping at the lowest donor exciton, our signal is (at subpicosecond pump–probe delays) dominated by its coherent part, the conversion from coherent to incoherent exciton populations is slow, and therefore it cannot be interpreted in terms of exciton population transfer between various states.

Chapter 6

Identification of Ultrafast Photophysical Pathways in Photoexcited Organic Heterojunctions

In previous chapter, we have provided evidence that the primary source of separated charges observed in photoexcited OSCs on ultrafast time scales is their direct optical generation. The aim of this chapter is to further supplement this picture by isolating the actual photophysical pathways along which the subpicosecond heterojunction dynamics proceeds. The motivation for the investigation to be presented is described in Sec. 6.1. The model that we adopt, its parameterization, and its features relevant for the interpretation of our results are introduced in Sec. 6.2. Section 6.3 is devoted to a detailed discussion of our numerical results that permit us to individuate the photophysical pathways followed by photoinduced electronic excitations on ultrafast time scales. These results are presented in our recent publication [166], while their position within the broader picture of light-to-charge conversion in D/A OSCs is thoroughly discussed in Sec. 6.4.

6.1 Motivation

As we have already emphasized, the coupling of photogenerated carriers to lattice vibrations has been repeatedly recognized as an essential factor in ultrafast charge separation occurring at D/A heterojunctions. Recent theoretical investigation by Huix-Rotllant et al. [59] has revealed that the subpicosecond exciton dynamics is governed by the interplay between charge delocalization and phonon-induced relaxation. In greater detail, the exciton states of mixed donor and space-separated character, in which charges are delocalized throughout the heterojunction, are found to open up a multitude of photophysical pathways for ultrafast dissociation of initial donor excitons, which are concurrent with phonon-assisted relaxation within the donor and space-separated manifolds.

The fact that, in most efficient OSCs, the electron-accepting material is based on the fullerene and its soluble derivatives, is intimately connected to the electronic structure of the fullerene molecule [137]. Due to the high symmetry of the C_{60} molecule, its LUMO, LUMO+1, and LUMO+2 orbitals are degenerate in energy. Their degeneracy is broken in the fullerene derivative PCBM [148, 167, 168], giving rise to three energetically close bands of electronic states in PCBM aggregates. While each of these bands is $\sim$ 0.1 eV wide, the width of the combined electronic band they form is $\sim$ 0.4–0.5 eV. In other words, there is a broad range of electronic states that can accept the electron that is transferred from the initial donor exciton, which has been recognized as highly important for efficient and ultrafast charge separation in D/A blends containing PCBM as the acceptor [51, 58]. The results presented in Ref. [58] suggest that the electronic band of a PCBM aggregate that originates from the LUMO+2 orbital of PCBM molecules is responsible for the formation of the so-called bridge CT state, which is resonant with CT states featuring electrons that are delocalized away from the interface. The presence of the bridge CT state combined with the phonon-induced transitions between nearly degenerate states promotes an ultrafast charge separation pathway that completely circumvents the strongly bound and localized CT state. Let us also mention that, upon the functionalization of C_{60}, together with the degeneracy of its LUMO, LUMO+1, and LUMO+2 orbitals, the degeneracy of its LUMO+3, LUMO+4, and LUMO+5 orbitals is also broken. The last three orbitals are situated at around 1 eV above the LUMO, LUMO+1, and LUMO+2 orbitals.

The influence of higher-than-LUMO acceptor orbitals on exciton dissociation has been investigated by Ma and Troisi [169]. They conclude that the precise energy position of higher-than-LUMO acceptor orbitals can modulate the exciton dissociation rate by orders of magnitude by opening up new exciton dissociation channels. The enhancement of the dissociation rate is observed as a consequence of the resonance between the initial donor state and higher-lying CT states whose electrons belong to the band stemming from a higher-than-LUMO acceptor orbital. The appearance of this dissociation pathway suggests that the initial donor exciton may be converted into a pair of free charges without involving the lowest-energy CT state. The central quantities that determine whether such a conversion of donor excitons to free charges is possible or not are the LUMO–LUMO offset and energy differences between higher-than-LUMO orbitals and the LUMO orbital. The LUMO–LUMO offset in the P3HT/PCBM blend can be quite large (around 1 eV) and thus comparable to the energy separation between LUMO and LUMO+3 orbitals of the PCBM molecule. It can therefore be expected that the electronic states of a PCBM aggregate that arise from LUMO+3, LUMO+4, and LUMO+5 orbitals of the PCBM molecule may play a nontrivial role in the ultrafast interfacial dynamics of the P3HT/PCBM blend. Surprisingly, it seems that the effect of these orbitals has not received enough attention in previous model studies of the P3HT/PCBM heterojunction. The ultrafast electron transfer observed in Ref. [170] has been ascribed to the energy overlap between the state of the photoexcited electron and the electronic states of the fullerene aggregate. The result presented in Fig. 3(e) of Ref. [170] suggests that this overlap involves the electronic states of the fullerene aggregate stemming from the LUMO+3, LUMO+4, and LUMO+5 orbitals of the PCBM molecule. The same study also reports on the existence of the so-called charge bridging state in which the electron is delocalized across the P3HT/PCBM interface. The *ab initio* calculations by Kanai and Grossman [148] have also evidenced the presence of a charge bridging state that is formed by the resonant overlap between electronic single-particle states in P3HT and C_{60}. The charge bridging state is readily accessible from the initially photogenerated P3HT exciton state and it also exhibits a significant overlap with exciton states in which the electron is located on the fullerene, but away from its interface with the polymer. Liu et al. [171] recognize that the presence of charge bridging state is extremely susceptible to the exact geometry of the P3HT/PCBM interface. Since the aforementioned *ab initio* studies of a polymer/fullerene interface [148, 170, 171] investigated the interface comprising a single oligomer and a single fullerene molecule, they were not able to conclusively assess the role of the charge bridging state in ultrafast charge separation. Two possibilities for how a charge bridging state may enhance ultrafast charge separation have been put forward [172].

On the one hand, charge bridging states may act as intermediate states for conversion of initial donor excitons to free charges because they exhibit quite good overlap with both of them. On the other hand, charge bridging states may facilitate ultrafast free-carrier generation by acting as additional absorbing states at the heterointerface. Due to the aforementioned resonant overlap, a redistribution of oscillator strengths occurs, and charge bridging states acquire oscillator strength from donor states.

Our model of a D/A heterojunction that is introduced in Ch. 5 can be straightforwardly extended to include more than only one single-electron (single-hole) state per site. By analyzing its ultrafast dynamics that is triggered by a photoexcitation, we may be able to provide a more detailed picture of the relevance of higher-than-LUMO orbitals for ultrafast charge separation at D/A heterointerfaces. Moreover, such a model enables a more detailed basic understanding of the role of the resonant mixing mechanism in ultrafast interfacial dynamics.

6.2 Model Description

6.2.1 Multiband Model Hamiltonian of a Heterojunction

The model we use here is a one-dimensional multiband semiconductor model on a lattice that consists of N donor and N acceptor sites. The sites $0, \dots, N-1$ belong to the donor part, whereas the sites $N, \dots, 2N-1$ belong to the acceptor part of the heterojunction. Multiple single-electron levels on site i are counted by index β_i, so that Fermi operators $c^\dagger_{i\beta_i}$ ($c_{i\beta_i}$) create (destroy) electrons on site i and in single-electron state β_i. Analogously, single-hole levels on site i are counted by index α_i, so that Fermi operators $d^\dagger_{i\alpha_i}$ ($d_{i\alpha_i}$) create (destroy) holes on site i and in single-hole state α_i. The phonon modes on site i are counted by index λ_i. The total Hamiltonian is given by Eq. (2.34) in which the interacting-carrier Hamiltonian is

$$\begin{aligned} H_\mathrm{c} = {} & \sum_{\substack{i\beta_i \\ j\beta'_j}} \epsilon^{\mathrm{c}}_{(i\beta_i)(j\beta'_j)} c^\dagger_{i\beta_i} c_{j\beta'_j} - \sum_{\substack{i\alpha_i \\ j\alpha'_j}} \epsilon^{\mathrm{v}}_{(i\alpha_i)(j\alpha'_j)} d^\dagger_{i\alpha_i} d_{j\alpha'_j} \\ & + \frac{1}{2} \sum_{\substack{i\beta_i \\ j\beta'_j}} V_{ij}\, c^\dagger_{i\beta_i} c^\dagger_{j\beta'_j} c_{j\beta'_j} c_{i\beta_i} + \frac{1}{2} \sum_{\substack{i\alpha_i \\ j\alpha'_j}} V_{ij}\, d^\dagger_{i\alpha_i} d^\dagger_{j\alpha'_j} d_{j\alpha'_j} d_{i\alpha_i} - \sum_{\substack{i\beta_i \\ j\alpha_j}} V_{ij}\, c^\dagger_{i\beta_i} d^\dagger_{j\alpha_j} d_{j\alpha_j} c_{i\beta_i}, \end{aligned} \tag{6.1}$$

the free-phonon Hamiltonian is the same as in Eq. (5.2), the carrier–phonon interaction is described by

$$H_{\mathrm{c-p}} = \sum_{i\beta_i} \sum_{\lambda_i} g^{\mathrm{c}}_{i\beta_i\lambda_i} c^{\dagger}_{i\beta_i} c_{i\beta_i} (b^{\dagger}_{i\lambda_i} + b_{i\lambda_i}) - \sum_{i\alpha_i} \sum_{\lambda_i} g^{\mathrm{v}}_{i\alpha_i\lambda_i} d^{\dagger}_{i\alpha_i} d_{i\alpha_i} (b^{\dagger}_{i\lambda_i} + b_{i\lambda_i}), \tag{6.2}$$

while the generation of carriers by means of an optical field is governed by

$$H_{\mathrm{c-f}} = -E(t) \sum_{i\alpha_i\beta_i} d^{\mathrm{cv}}_{i\alpha_i\beta_i} (c^{\dagger}_{i\beta_i} d^{\dagger}_{i\alpha_i} + d_{i\alpha_i} c_{i\beta_i}). \tag{6.3}$$

Similarly to our discussion in Sec. 5.2, we assume that quantities $\epsilon^{\mathrm{c}}_{(i\beta_i)(j\beta'_j)}$ $\left(\epsilon^{\mathrm{v}}_{(i\alpha_i)(j\alpha'_j)}\right)$, which represent electron (hole) on-site energies and transfer integrals, are nonzero only for certain combinations of their indices. In more detail, we take that $\epsilon^{\mathrm{c}}_{(i\beta_i)(j\beta'_j)}$ is non-zero when it represents

(a) on-site energy $\epsilon^{\mathrm{c}}_{i\beta_i}$ of electron level β_i on site i for $i = j$ and $\beta_i = \beta'_i$;

(b) negative electron transfer integral between nearest neighbors of band β_i, $-J^{\mathrm{c,int}}_{i\beta_i}$, for i and j both belonging to the same part of the heterojunction, $|i - j| = 1$, and $\beta_i = \beta'_j$;

(c) negative electron transfer integral between nearest neighbors of different bands, $-J^{\mathrm{c,ext}}_{i\beta_i\beta'_j}$, for i and j both belonging to the same part of the heterojunction, $|i - j| = 1$, and $\beta_i \neq \beta'_j$;

(d) negative electron transfer integral between different parts of the heterojunctions, $-J^{\mathrm{c}}_{DA}$, for $i = N - 1$ and $j = N$ or *vice versa*.

The Coulomb interaction potential is again modeled by using the Ohno potential, see Eq. (4.2). The frequency of the electric field is such that it creates electron–hole excitations. The interband dipole matrix elements are $d^{\mathrm{cv}}_{i\alpha_i\beta_i}$, while we neglect intraband dipole matrix elements.

The exciton basis eigenstates $\psi^{x}_{(i\alpha_i)(j\beta_j)}$ are obtained by solving the eigenvalue problem that is similar to Eq. (5.5) and reads as

$$\sum_{\substack{i'\alpha'_i \\ j'\beta'_j}} \left(\delta_{ii'}\delta_{\alpha_i\alpha'_i}\epsilon^{\mathrm{c}}_{(j\beta_j)(j'\beta'_j)} - \delta_{jj'}\delta_{\beta_j\beta'_j}\epsilon^{\mathrm{v}}_{(i\alpha_i)(i'\alpha'_i)} - \delta_{ii'}\delta_{\alpha_i\alpha'_i}\delta_{jj'}\delta_{\beta_j\beta'_j}V_{ij} \right) \psi^{x}_{(i'\alpha'_i)(j'\beta'_j)} = \hbar\omega_x\, \psi^{x}_{(i\alpha_i)(j\beta_j)}. \tag{6.4}$$

The dipole-moment matrix element for the direct generation (from the ground state) of excitons in state x is given as

$$M_x = \sum_i \sum_{\alpha_i\beta_i} \psi^{x*}_{(i\alpha_i)(i\beta_i)} d^{\mathrm{cv}}_{i\alpha_i\beta_i}, \tag{6.5}$$

while exciton–phonon matrix elements describing transitions from exciton state x to exciton state $\bar{x}$ assisted by phonon $(i\lambda_i)$ are

$$\Gamma^{i\lambda_i}_{\bar{x}x} = \sum_{\beta_i}\sum_{j\alpha_j} g^{\mathrm{c}}_{i\beta_i\lambda_i} \psi^{\bar{x}*}_{(j\alpha_j)(i\beta_i)} \psi^{x}_{(j\alpha_j)(i\beta_i)} - \sum_{\alpha_i}\sum_{j\beta_j} g^{\mathrm{v}}_{i\alpha_i\lambda_i} \psi^{\bar{x}*}_{(i\alpha_i)(j\beta_j)} \psi^{x}_{(i\alpha_i)(j\beta_j)}. \tag{6.6}$$

6.2.2 Parameterization of the Model Hamiltonian

The model Hamiltonian parameterization employed in Ch. 5 assumes that the sites in the donor region of the heterojunction belong to one polymer chain, which extends in the direction perpendicular to the D/A interface. The hole delocalization occurs along a polymer chain and it is quite good, as evidenced by the value of the transfer integral J_D^{v} in Table 5.1. However, in the most efficient polymer/fullerene blends, polymer chains form the ordered structure described in Ch. 1, they are mutually parallel and parallel to the D/A interface, see also Fig. 1.10. Recent studies of ultrafast exciton dissociation [173] and charge separation [52] in two-dimensional models of a D/A interface featuring mutually parallel polymer chains have suggested that these processes crucially depend on the electronic properties and geometry in the direction perpendicular to the D/A interface (and polymer chains, too). Motivated by these findings, we assume that each site in the donor part of the heterojunction effectively substitutes a polymer chain and, consequently, charge delocalization in the donor part of the heterojunction is assumed to occur between different polymer chains. In actual computations, we take one single-electron level per site in the donor and one single-hole level per site in both the donor and acceptor. In order to mimic the presence of higher-than-LUMO orbitals energetically close to the LUMO level (which is a situation typical of fullerenes), as well as to investigate the effects of single-electron levels situated at around 1 eV above the LUMO level on the exciton dissociation, we take four single-electron levels per site in the acceptor. Different types of electronic couplings are schematically indicated in Figure 6.1, while the values of model parameters used in computations are summarized

TABLE 6.1: Values of model parameters used in computations on the multiband model of a D/A heterojunction.

Parameter	Value
N	11
a (nm)	1.0
U (eV)	0.65
ε_r	3.0
$\epsilon_{D,0}^{\mathrm{c}}$ (eV)	2.63
$J_{D,0}^{\mathrm{c,int}}$ (eV)	0.1
$\epsilon_{D,0}^{\mathrm{v}}$ (eV)	-0.3
$J_{D,0}^{\mathrm{v,int}}$ (eV)	-0.15
$\epsilon_{A,0}^{\mathrm{c}}$ (eV)	1.565
$\epsilon_{A,1}^{\mathrm{c}}$ (eV)	1.865
$\epsilon_{A,2}^{\mathrm{c}}$ (eV)	2.565
$\epsilon_{A,3}^{\mathrm{c}}$ (eV)	2.865
$J_{A,0}^{\mathrm{c,int}}$ (eV)	0.05
$J_{A,1}^{\mathrm{c,int}}$ (eV)	0.025
$J_{A,2}^{\mathrm{c,int}}$ (eV)	0.05
$J_{A,3}^{\mathrm{c,int}}$ (eV)	0.025
$J_{A,01}^{\mathrm{c,ext}}$ (eV)	0.02
$J_{A,12}^{\mathrm{c,ext}}$ (eV)	0.02
$J_{A,23}^{\mathrm{c,ext}}$ (eV)	0.02
$\epsilon_{A,0}^{\mathrm{v}}$ (eV)	-1.03
$J_{A,0}^{\mathrm{v,int}}$ (eV)	-0.15
J_{DA}^{c} (eV)	0.1
J_{DA}^{v} (eV)	-0.1
$\hbar\omega_{\mathrm{p},1}$ (meV)	10.0
g_1 (meV)	42.0
$\hbar\omega_{\mathrm{p},2}$ (meV)	185.0
g_2 (meV)	94.0
T (K)	300.0

in Table 6.1. These values are selected so that the main characteristics of the single-particle and exciton spectrum (bandwidths, band alignments, exciton and charge transfer state binding energies) within the model correspond to the ones observed in P3HT/PCBM material system. We take the HOMO level of the donor material to be the zero of the energy scale.

The value of the transfer integral $J_{D,0}^{\mathrm{v,int}}$ was chosen so as to agree with the HOMO bandwidth along the π-stacking direction of the regioregular P3HT [24, 25] and the values of the hole transfer integral along the π-stacking direction of the same material [174, 175]. The electron

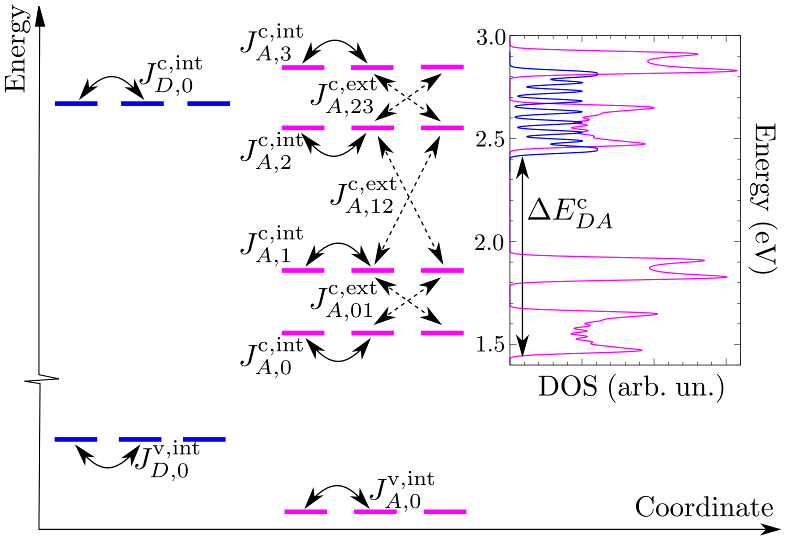

FIGURE 6.1: Illustration of the model system indicating different transfer integrals present in Table 6.1. The plot on the right shows the single-particle DOS for electrons in the neat donor (blue curve) and acceptor (magenta curve) materials obtained using the values of relevant parameters listed in Table 6.1. The electronic states of the isolated materials are computed by diagonalizing the free-electron Hamiltonian [the first term on the right-hand side of Eq. (6.1)] in which the D/A coupling is set to 0. The DOS was then calculated by broadening each of the states obtained by a Gaussian with the standard deviation of 10 meV.

transfer integral $J^{c,int}_{D,0}$ should be of similar magnitude as the hole transfer integral along the π-stacking direction [174]. Energies of the single-electron and single-hole levels in the donor, as well as the on-site Coulomb interaction U, were chosen so that the lowest donor exciton state is located at around 2.0 eV, while the HOMO–LUMO gap (single-particle gap) is around 2.4 eV, i.e., the binding energy of the donor exciton is around 0.4 eV [26, 176].

Electron transfer integrals in the acceptor $J^{c,int}_{A,0}$, $J^{c,int}_{A,1}$ and $J^{c,ext}_{A,01}$, together with the energy difference $\epsilon^{c}_{A,1} - \epsilon^{c}_{A,0}$ between single-electron states, are chosen to reproduce the most important features of the low-energy part of the electronic density of states (DOS) of fullerene aggregates [51, 58], such as the combined (total) bandwidth of $\sim$ 0.4–0.5 eV and the presence of two separated groups of allowed states. Let us note that, because of the reduced dimensionality of our model, we cannot expect to reproduce details of the actual DOS, but only its gross features. We therefore believe that taking two instead of three orbitals energetically close to the LUMO orbital is reasonable within our model. The electronic DOS in the acceptor produced by our model is shown in the inset of Fig. 6.1. Magnitudes of transfer integrals in the acceptor are also in agreement with the values reported in the literature [20, 146]. We have also included the single-electron fullerene states which are located at around 1 eV above the lowest single-electron state. It is well known that these states in C_{60} are also triply degenerate and that this degeneracy is lifted in $PC_{60}BM$. Since we use a model system, we take, for simplicity, that the degeneracy is lifted in the same manner as in the case of lowest single-electron levels, i.e., we take $J^{\mathrm{c,int}}_{A,0} = J^{\mathrm{c,int}}_{A,2}$, $J^{\mathrm{c,int}}_{A,1} = J^{\mathrm{c,int}}_{A,3}$, $J^{\mathrm{c,int}}_{A,01} = J^{\mathrm{c,int}}_{A,23}$, and $\epsilon^{\mathrm{c}}_{A,3} - \epsilon^{\mathrm{c}}_{A,2} = \epsilon^{\mathrm{c}}_{A,1} - \epsilon^{\mathrm{c}}_{A,0}$, while $\epsilon^{\mathrm{c}}_{A,2} - \epsilon^{\mathrm{c}}_{A,0} = 1$ eV. For the magnitudes of the energy difference $\epsilon^{\mathrm{c}}_{A,0} - \epsilon^{\mathrm{v}}_{A,0}$ and the transfer integral $J^{\mathrm{v,int}}_{A,0}$ listed in Table 6.1, the single-particle gap in the acceptor part of the heterojunction assumes the value of 2.2 eV, which is similar to the literature values for PCBM [26].

The energy differences $\Delta_{\mathrm{XD-CT}}$ and $\Delta_{\mathrm{XA-CT}}$ between the lowest excited state of the heterojunction (the lowest CT state) and the lowest exciton states in the donor and acceptor respectively, are directly related to LUMO–LUMO and HOMO–HOMO energy offsets between the materials. Literature values of $\Delta_{\mathrm{XD-CT}}$ representative of P3HT/PCBM blends are usually calculated for the system consisting of one PCBM molecule and one oligomer and range from 0.7 eV [177] to 1.3 eV [178]. Liu and Troisi [179] obtained $\Delta_{\mathrm{XD-CT}} = 0.97$ eV and pointed out that taking into account partial electron delocalization over fullerene molecules can significantly lower the XD–CT energy difference. For parameters listed in Table 6.1, $\Delta_{\mathrm{XD-CT}} = 0.68$ eV, which is a reasonable value, since we do account for carrier delocalization effects. The LUMO–LUMO offset $\Delta E^{\mathrm{c}}_{DA}$ (see Figure 6.1) produced by the model parameters is around 0.96 eV and the lowest CT state is located at 1.32 eV. The energy difference $\Delta_{\mathrm{XA-CT}} = 0.42$ eV, so that the HOMO–HOMO offset is around 0.73 eV and the lowest XA state is approximately at 1.74 eV, both of which compare well with the available data [26]. The magnitudes of the transfer integrals J^{c}_{DA} and J^{v}_{DA} between the two materials are taken to be similar to the values obtained in Ref. [148].

Interband matrix elements of the dipole moment $d^{\mathrm{cv}}_{i\alpha_i\beta_i}$ are assumed not to depend on band indices α_i, β_i and to be equal on all sites belonging to the single material, $d^{\mathrm{cv}}_{i\alpha_i\beta_i} = d^{\mathrm{cv}}_{D}$ for $i = 0, \ldots, N-1$ and $d^{\mathrm{cv}}_{i\alpha_i\beta_i} = d^{\mathrm{cv}}_{A}$ for $i = N, \ldots, 2N-1$. Since the focus of our study is on the dissociation of donor excitons, in all the computations we set $d^{\mathrm{cv}}_{A} = 0$.

Similarly to the parameterization employed in Ch. 5, we assume that each site contributes one low-frequency and one high-frequency phonon mode. Their energies ($\hbar\omega_{\mathrm{p},1}$ and $\hbar\omega_{\mathrm{p},2}$) are the same as in Ch. 5. The values of g_1 and g_2 listed in Table 6.1 are obtained by assuming that the polaron binding defined in Eq. (5.8) is equal to $\epsilon_{\mathrm{b}}^{\mathrm{pol}} = 50$ meV, that both modes contribute equally to it ($\epsilon_{\mathrm{b},1}^{\mathrm{pol}} = \epsilon_{\mathrm{b},2}^{\mathrm{pol}}$), and that $|J| = 125$ meV.

6.2.3 Role of the D/A Coupling and the Resonant Mixing Mechanism

The classification of exciton states in general case of the interacting heterojunction, when at least one of J_{DA}^{c}, J_{DA}^{v} is different from zero, is performed in the manner described in Sec. 5.2.3. Therefore, here, we will not present the detailed procedure, but only reformulate certain expressions so that they can be used to investigate the multiband model in this chapter. The expression for the electron–hole separation in exciton state x is similar to Eq. (5.10) and reads as

$$\langle r_{\mathrm{e-h}} \rangle_x = \sum_{\substack{i\alpha_i \\ j\beta_j}} \left| \psi^x_{(i\alpha_i)(j\beta_j)} \right|^2 |i - j|, \tag{6.7}$$

while the D/A interaction is [see also Eq. (5.12)]

$$\begin{aligned} H_{DA} = &- J_{DA}^{\mathrm{c}} \sum_{\substack{\beta_{N-1} \\ \beta_N}} \left(c^\dagger_{(N-1)\beta_{N-1}} c_{N\beta_N} + c^\dagger_{N\beta_N} c_{(N-1)\beta_{N-1}} \right) \\ &+ J_{DA}^{\mathrm{v}} \sum_{\substack{\alpha_{N-1} \\ \alpha_N}} \left(d^\dagger_{(N-1)\alpha_{N-1}} d_{N\alpha_N} + d^\dagger_{N\alpha_N} d_{(N-1)\alpha_{N-1}} \right) . \end{aligned} \tag{6.8}$$

The electron in a space-separated state is predominantly located in the acceptor part of the heterojunction, while the hole is located in the donor part. Since there is a number of single-electron levels per acceptor site, the electron in a space-separated state can be in different electronic bands originating from these single-electron levels. A useful quantity for further classification of space-separated states is

$$p_x(\beta) = \sum_{j=N}^{2N-1} \sum_{i\alpha_i} \left| \psi^x_{(i\alpha_i)(j\beta)} \right|^2 , \tag{6.9}$$

which represents the conditional probability that, given that the electron in state x is in the acceptor, it belongs to the electronic band stemming from the single-electron level β. The index of the electronic band β_x to which the electron in space-separated state x predominantly belongs is then the value of β for which the conditional probability p_x is maximal. In other words, space-separated state x belongs to the CT_{β_x} band. Due to the large energy separation between the lower two (0 and 1) and the higher two (2 and 3) single-electron levels in the acceptor, the electronic coupling $J_{A,12}^{\mathrm{c,ext}}$, which couples space-separated states belonging to CT_0 and CT_1 bands to the ones belonging to CT_2 and CT_3 bands, is not effective. Therefore, the space-separated states from CT_0 and CT_1 bands are very weakly mixed with (and essentially isolated from) space-separated states of CT_2 and CT_3 bands, which permits us to separately analyze these two subgroups of space-separated states.

In Ch. 5, we have remarked that it is the resonant mixing between single-electron states in the donor and the acceptor that is at the heart of the absorption intensity redistribution among donor and space-separated states, which renders the latter states directly accessible from the ground state. The resonant mixing is possible because the LUMO–LUMO offset is comparable to the width of the electronic band in the acceptor. Let us now examine in more detail the role of the D/A coupling in the resonant mixing.

To start, it is convenient to schematically represent exciton wave functions $\psi_{(i\alpha_i)(j\beta_j)}^{x(0)}$ and $\psi_{(i\alpha_i)(j\beta_j)}^{x}$ in the coordinate space. For the clarity of the discussion, we assume that we have only one single-electron and single-hole state per site throughout the system (as is the case in our investigations in Ch. 5). This assumption does not compromise the validity of the conclusions to be presented in the case of more single-particle states per site. On the abscissa of our coordinate space is the hole coordinate, while on the ordinate is the electron coordinate.

The wave functions of exciton states $x^{(0)}$ of the noninteracting heterojunction are confined to a single quadrant of our coordinate space, see Fig. 6.2(a). For example, the wave function of a donor exciton state is nonzero only when both electron and hole coordinates are between 0 and $N-1$, and similarly for other groups of exciton states. Because of the D/A interaction H_{DA} [Eq. (6.8)], exciton states x of the interacting heterojunction are mixtures of different exciton states $x^{(0)}$ of the noninteracting heterojunction, see Eq. (5.13). Therefore, the wave function of a general exciton state at the interacting heterojunction is not confined to the quadrant which is in Fig. 6.2(a) labeled by its prevalent character, but is nonzero also in other quadrants. The D/A

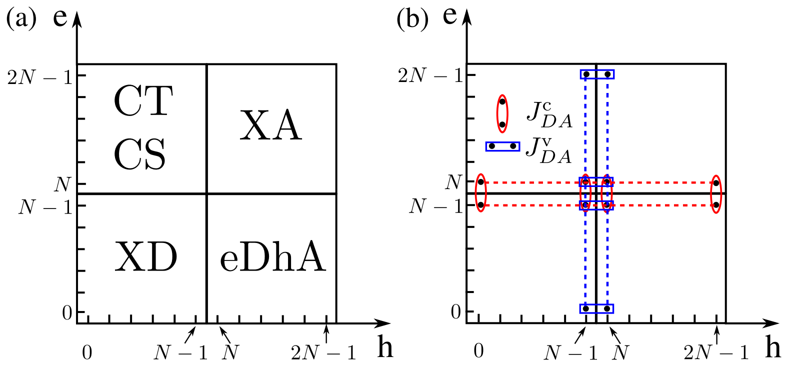

FIGURE 6.2: (a) At the noninteracting heterojunction, the wave function of each exciton state is confined to a single quadrant in the position space of the electron and hole. (b) The points at which the sums on the right-hand side of Eq. (6.11) are evaluated: the points relevant to the computation of the first and the second sum are grouped by red ellipses, the points relevant to the computation of the third and the fourth sum are grouped by blue rectangles.

interaction H_{DA} is written in the noninteracting-heterojunction exciton basis as

$$H_{DA} = \sum_{\bar{x}^{(0)} x^{(0)}} h_{\bar{x}^{(0)} x^{(0)}} \left|\bar{x}^{(0)}\right\rangle \left\langle x^{(0)}\right| , \tag{6.10}$$

with

$$\begin{aligned} h_{\bar{x}^{(0)} x^{(0)}} = & -J_{DA}^{\mathrm{c}} \sum_{\substack{k\alpha_k \\ \beta_{N-1}\beta_N}} \left(\psi^{\bar{x}^{(0)}*}_{(k\alpha_k)(N-1,\beta_{N-1})} \psi^{x^{(0)}}_{(k\alpha_k)(N\beta_N)} + \psi^{\bar{x}^{(0)}*}_{(k\alpha_k)(N\beta_N)} \psi^{x^{(0)}}_{(k\alpha_k)(N-1,\beta_{N-1})} \right) \\ & + J_{DA}^{\mathrm{v}} \sum_{\substack{k\beta_k \\ \alpha_{N-1}\alpha_N}} \left(\psi^{\bar{x}^{(0)}*}_{(N-1,\alpha_{N-1})(k\beta_k)} \psi^{x^{(0)}}_{(N\alpha_N)(k\beta_k)} + \psi^{\bar{x}^{(0)}*}_{(N\alpha_N)(k\beta_k)} \psi^{x^{(0)}}_{(N-1,\alpha_{N-1})(k\beta_k)} \right) . \end{aligned} \tag{6.11}$$

The points at which the sums in the last equation (disregarding band indices) are to be evaluated are presented in Fig. 6.2(b). The first two sums in Eq. (6.11) are nonzero only when one state is of XD, and the other is of space-separated character. Similarly, the other two sums in Eq. (6.11) are nonzero only when one state is of XA, and the other is of space-separated character. Therefore, if $J_{DA}^{\mathrm{c}} \neq 0$ and $J_{DA}^{\mathrm{v}} = 0$, XA states of the interacting heterojunction are identical to XA states of the noninteracting heterojunction, while XD (space-separated) states of the interacting heterojunction are generally combinations of XD and space-separated states of the noninteracting heterojunction. Similarly, if $J^{\mathrm{c}}_{DA} = 0$ and $J^{\mathrm{v}}_{DA} \neq 0$, XD states of the interacting heterojunction are identical to XD states of the noninteracting heterojunction, while XA (space-separated) states of the interacting heterojunction are generally combinations of XA and space-separated states of the noninteracting heterojunction.

The exact mechanism of this mixing is different in different parts of the exciton spectrum. Let us start with the lower-energy part of the spectrum, which contains space-separated states belonging to CT_0 and CT_1 bands. Single-electron states in the acceptor that originate from levels 0 and 1 do not exhibit strong resonant mixing with single-electron states in the donor, thanks to the large energy separation between these two groups of states. Therefore, the relevant partitioning of the interacting-carrier Hamiltonian H_{c} is the one embodied in Eq. (5.11), where the D/A interaction H_{DA} [Eq. (6.8)] is explicitly separated from the Hamiltonian $H^{(0)}_{\mathrm{c}}$ of interacting carriers at the noninteracting heterojunction. Coefficients $C_{xx^{(0)}}$ in the expansion [Eq. (5.13)] of exciton state x (of the interacting heterojunction) in terms of exciton states $x^{(0)}$ (of the noninteracting heterojunction) are obtained as solutions to the eigenvalue problem

$$\sum_{x^{(0)}} \left(\delta_{x^{(0)}\bar{x}^{(0)}} \hbar\omega_{x^{(0)}} + h_{\bar{x}^{(0)}x^{(0)}}\right) C_{xx^{(0)}} = \hbar\omega_x C_{x\bar{x}^{(0)}}. \tag{6.12}$$

Since $h_{\bar{x}^{(0)}x^{(0)}}$ contains products of two exciton wave functions, $|h_{\bar{x}^{(0)}x^{(0)}}|$ is generally much smaller than $\left|J^{\mathrm{c/v}}_{DA}\right|$. Therefore, most of the states in the lower-energy part of the interacting-heterojunction spectrum are almost identical to the respective states of the noninteracting-heterojunction spectrum. However, whenever $|h_{\bar{x}^{(0)}x^{(0)}}| \sim |\hbar\omega_{\bar{x}^{(0)}} - \hbar\omega_{x^{(0)}}|$, there exists at least one state of the interacting heterojunction that is a mixture of states $\bar{x}^{(0)}$ and $x^{(0)}$ (which have different characters!) of the noninteracting heterojunction. In other words, states $\bar{x}^{(0)}$ and $x^{(0)}$, which are virtually resonant in energy, exhibit resonant mixing to form the so-called bridge states of the interacting heterojunction. Apart from their dominant character, which is obtained as previously explained, bridge states also have nontrivial overlaps with noninteracting-heterojunction states of other characters. For example, if $J^{\mathrm{v}}_{DA} = 0$, all the bridge states of the interacting heterojunction are of mixed XD and space-separated character; if $J^{\mathrm{c}}_{DA} = 0$, all the bridge states of the interacting heterojunction are of mixed XA and space-separated character; if both couplings are nonzero, bridge states of the interacting heterojunction are of mixed XD, XA, and space-separated character. The emergence of bridge states in the low-energy part of the exciton spectrum requires subtle energy alignment of exciton, i.e., two-particle, states. Bridge states formed by resonances between two-particle states are thus rather scarce. Having a certain amount of the donor character, bridge states acquire oscillator strengths from donor states and can thus be directly generated from the ground state. In the rest of our paper, it is convenient to consider as a bridge state any state (in the lower-energy part of the exciton spectrum) of dominant CS, CT or XA character whose amount of donor character [as defined in Eq. (5.14)] is at least 0.01.

On the other hand, in the high-energy region of the exciton spectrum, which contains space-separated states belonging to CT_2 and CT_3 bands, there is significant mixing between single-electron states in the acceptor stemming from levels 2 and 3 and single-electron states in the donor. In this case, instead of the decomposition of the interacting-carrier part of the Hamiltonian given in Eq. (5.11), it is more convenient to separate the carrier–carrier interaction [last three terms in Eq. (6.1)] from the part describing noninteracting carriers [first two terms in Eq. (6.1)]. The latter part of the interacting-carrier Hamiltonian then gives rise to single-electron states of the whole heterojunction that are in general delocalized on both the donor and acceptor as a consequence of the resonant mixing between single-electron states in the two materials. Since one single-electron state of the entire system generally participates in many two-particle states, exciton states having at least one carrier delocalized throughout the heterojunction are ubiquitous in the high-energy region of the spectrum. They also generally have greater amount of donor character than the bridge states in the low-energy part of the spectrum, *vide infra*, making them easily accessible from the ground state by a (suitable) photoexcitation. The dominant character of these states can be different and to our further discussion are relevant space-separated (CT and CS) states of CT_2 and CT_3 bands with partial donor character, which will be further termed photon-absorbing charge-bridging (PACB) states. This term has been repeatedly used in the literature to denote space-separated states in which charges are delocalized throughout the system [148, 171, 172]. We note that the PACB states within our model do not have any other immediate relationship with PACB states reported in *ab initio* studies of D/A interfaces apart from the charge-bridging property and relatively large oscillator strengths permitting their

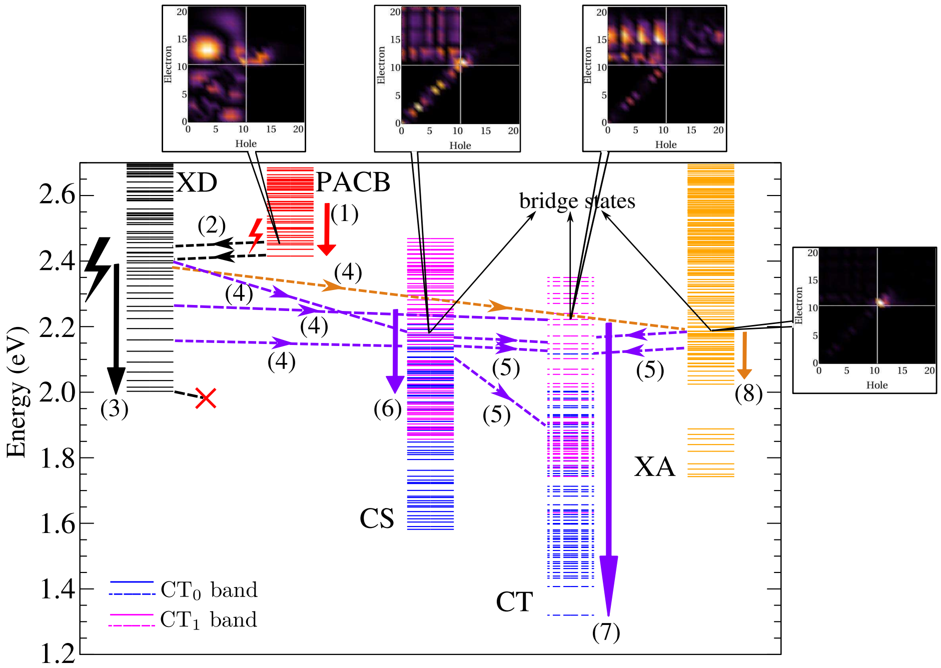

FIGURE 6.3: Exciton states relevant for our study divided in different groups. In the third (the fourth) column (from the left), blue and magenta lines denote CS (CT) states belonging to CT_0 and CT_1 band, respectively. Ultrafast exciton dynamics proceeds along the photophysical pathways denoted by (1)–(8), which are further specified in Sec. 6.3. The solid arrows [pathways (1), (3), (6), (7), and (8)] indicate the deexcitation processes occurring within one group of exciton states, whereas the dashed arrows [pathways (2), (4), and (5)] denote transitions among different groups of exciton states. The black (red) bolt denotes the direct photoexcitation of excitons in donor (PACB) states. Representative PACB and bridge states are accompanied by plots of the exciton wave function square modulus in the coordinate space.

direct optical generation.

The bridge states owe their name to the fact that they indirectly connect, via phonon-assisted processes, a state of pure XD character to a state of pure space-separated character. In our model, these two states cannot be involved in a single-phonon-assisted process because of the form of exciton-phonon matrix elements $\Gamma^{i\lambda_i}_{\bar{x}x}$, see Eq. (6.6), which contain products of exciton wave functions taken at the same point. Therefore, single-phonon-assisted transitions among exciton states of the same character are most intense and probable. A state of pure XD character can, however, also be coupled (via processes mediated by a donor phonon) to a bridge state, which can then be coupled to a state of pure space-separated character (via single-phonon processes mediated by acceptor phonons).

In the remaining part of our study, we will for ease of presentation adopt the following classification of the exciton states. Since space-separated states belonging to CT$_2$ and CT$_3$ bands which are relevant to our study are PACB states, we will not discriminate between CT and CS states in CT$_2$ and CT$_3$ bands, but rather refer to all of them as PACB states. We will, however, distinguish between CS and CT states in CT$_0$ and CT$_1$ bands and, for brevity of discussion, we will denote them simply as CS and CT states. This classification facilitates the understanding of the role that PACB states play in ultrafast interfacial dynamics by enabling direct comparison between results obtained with all four and only two lower orbitals per acceptor site, *vide infra*. The comparison is plausible since there is a well defined correspondence between XA, CT, and CS states in the lower-energy part of the exciton spectrum (four orbitals per acceptor site) and the corresponding states when only two orbitals per acceptor site are taken into account. The part of the exciton spectrum that is relevant for our study is shown in Fig. 6.3.

6.3 Numerical Results

In this section, we present results for the exciton dynamics at the model heterojunction during and after its pulsed excitation. The form of the excitation is

$$E(t) = E_0 \cos(\omega_c t) \exp\left(-\frac{t^2}{\tau_G^2}\right) \theta(t+t_0)\theta(t_0-t), \tag{6.13}$$

where ω_c is its central frequency, $2t_0$ is its duration, τ_G is the characteristic time of the Gaussian envelope, and $\theta(t)$ is the Heaviside step function. In all the computations, we set $t_0 = 50$ fs and $\tau_G = 20$ fs. As has been discussed in Sec. 5.2.2, the results of the numerical investigations in Ch. 5 are not particularly susceptible to the exact wave form of the exciting electric field. The reason for such a behavior lies in the relatively low value of the LUMO–LUMO offset and relatively good charge delocalization, which promote quite fast conversion of the initially created coherent exciton populations towards the incoherent ones by means of phonon-assisted processes. Even though the wave form given in Eq. (5.9) generally makes coherent quantities decay more slowly than the wave form embodied in Eq. (6.13), our numerical computations in the two cases witness almost the same dynamics due to the very efficient phonon-assisted processes. Here, however, the LUMO–LUMO offset is almost two times larger than in Ch. 5, while the carrier delocalization is weaker. Therefore, here, the conversion of coherent into incoherent populations is expected to be slower and more dependent on the particular form of the exciting field. In order to avoid artificially long conversion times that arise when combining the wave form given in Eq. (5.9) with the values of model parameters listed in Table 6.1, we opt here for the excitation form given in Eq. (6.13).

Apart from computing the (normalized) incoherent exciton populations of various groups of exciton states [Eq. (5.15)], ultrafast exciton dynamics is studied here in more detail by defining energy- and time-resolved exciton populations $\varphi_X(E,t)$ of states belonging to group X as

$$\varphi_X(E,t) = \frac{1}{N_{\text{tot}}} \sum_{x\in X} n_{xx}(t)\,\delta(E-\hbar\omega_x). \tag{6.14}$$

$\varphi_X(E,t)\Delta E$ represents the number (normalized to the total exciton population N_{tot}) of excitons from group X residing in the states whose energies are between E and $E+\Delta E$. Having in mind Eq. (3.46), which relates coherent, incoherent, and total exciton population of exciton state x, quantity $\varphi_X(E,t)\Delta E$ can be decomposed into its coherent

$$\varphi_X^{\text{coh}}(E,t) = \frac{1}{N_{\text{tot}}} \sum_{x\in X} |y_x(t)|^2\,\delta(E-\hbar\omega_x), \tag{6.15}$$

and incoherent part

$$\varphi_X^{\text{incoh}}(E,t) = \frac{1}{N_{\text{tot}}} \sum_{x\in X} \bar{n}_{xx}(t)\,\delta(E-\hbar\omega_x). \tag{6.16}$$

The plots of φ_X^{coh} as a function of E and t provide information about states in which excitons are initially generated (the initial exciton distribution) and the time scale on which the conversion from coherent to incoherent exciton populations takes place. The plots of φ_X^{incoh} as a function of E and t reveal actual pathways along which (incoherent) excitons are redistributed, starting from the initial exciton distribution. Computing the energy- and time-resolved exciton populations $\varphi_X(E,t)$ or the exciton DOS, we represent δ functions by a Gaussian with the standard deviation of 10 meV.

Let us briefly comment on the numerical effort that has to be employed to study ultrafast exciton dynamics in the model introduced in Sec. 6.2. The model supports $5N \times 2N = 10N^2 = 1210$ exciton states in total. In actual computations, we usually take around 500 lowest-energy exciton states. As in Ch. 5, the total number of phonon modes is $2N = 44$, so that the number of active single-phonon-assisted density matrices $n_{\bar{x}x(i\lambda_i)^+}$ is typically of the order of 10^7, while the numbers of active density matrices of other types are much smaller. In other words, computations of ultrafast exciton dynamics require an integration of $\sim 10^7$ mutually coupled differential equations. The integrations are performed on a number of processors in parallel as described in the opening of Sec. 4.3. Due to the specific features of the parameter set employed here, see the discussion following Eq. (6.13), the time step of the integration is $\Delta t = 0.4$ fs. The computations are typically performed on 64 processors, and propagating the active density matrices for 1 ps requires 2500 time steps and takes of the order of 10–20 hours. We also note that the computation of quantities $\varphi_X^{\mathrm{coh}}(E,t)$ and $\varphi_X^{\mathrm{incoh}}(E,t)$ significantly contributes to the total execution time.

6.3.1 General Analysis of Ultrafast Interfacial Dynamics

We start with the analysis of the ultrafast exciton dynamics when model parameters assume the values listed in Table 6.1 and the system is excited at the bright donor state located around $\hbar\omega_c = 2.35$ eV, which is significantly above the lowest donor state, see Fig. 6.3. We also present the results obtained taking into account only two lower single-electron levels (of energies $\epsilon^{\mathrm{c}}_{A,0}$ and $\epsilon^{\mathrm{c}}_{A,1}$) in the acceptor per site, while the values of all other model parameters are as listed in Table 6.1. The comparison of these results helps us understand the effects that the presence of two higher single-electron levels in the acceptor has on ultrafast exciton dynamics in our model.

In Fig. 6.4(a) we show the time dependence of the total coherent exciton population $N_{\mathrm{coh}} = \sum_x |y_x|^2$, total incoherent exciton population $N_{\mathrm{incoh}} = \sum_x \bar{n}_{xx}$, and total exciton population N_{tot}. Exciting well above the lowest donor state, the conversion from coherent to incoherent exciton populations is rapid and is completed in a couple of tens of femtoseconds after the end of the pulsed excitation. Figures 6.5(a)–(e) present density plots of energy- and time-resolved

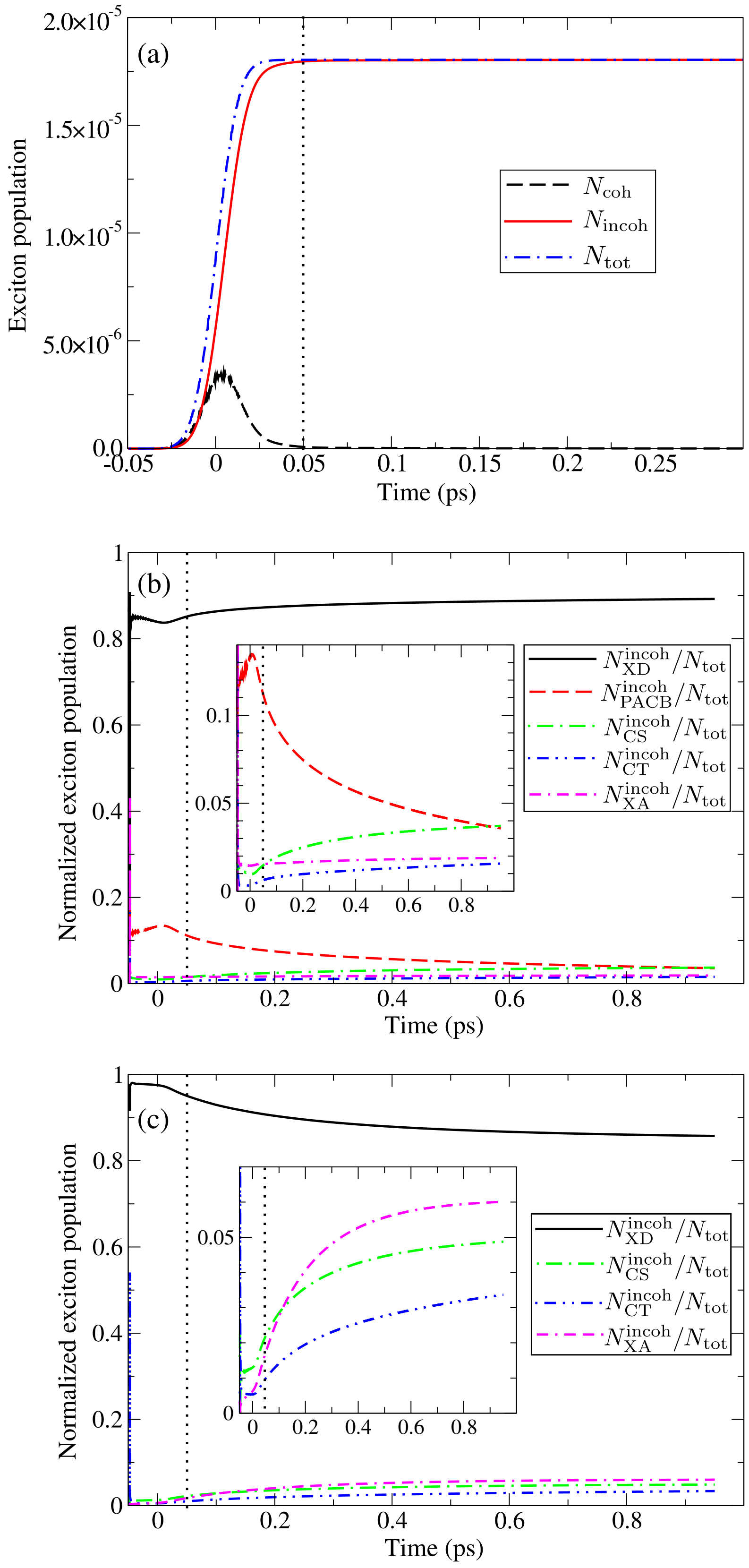

FIGURE 6.4: Time dependence of (a) the total exciton population and its coherent and incoherent parts, (b) and (c) normalized incoherent populations of different groups of exciton states. In (a) and (b), we take four single-electron levels per acceptor site, while in (c) we take only two lower single-electron levels ($\epsilon^{c}_{A,0}$ and $\epsilon^{c}_{A,1}$) per acceptor site. The dotted vertical lines denote the end of the excitation.

distributions $\varphi_X^{\mathrm{coh}}(E,t)$ of coherent exciton populations for different groups of exciton states X. Comparing the ranges of color bars in Figs. 6.5(a)–(e), we conclude that the excitation predominantly generates donor excitons. We observe in Fig. 6.5(a) that the initially populated donor states are the states located around 2.35 and 2.42 eV, together with the lowest donor state at around 2 eV. Even though we pump well above the lowest donor state, this state is prone to the direct optical generation because of its very large dipole moment M_x [Eq. (6.5)] for direct generation from the ground state and the spectral width of the pulse. Apart from donor states, PACB states are also initially populated, see Fig. 6.5(b). In Figs. 6.5(c)–(e) we see that energy positions of the bright spots in the density plots on the left correspond very well to the energy positions of red bars, which indicate bridge states of dominant CS, CT, and XA character, on the right. In other words, these states can be directly optically generated from the ground state, as already discussed.

The time dependence of normalized incoherent populations of different groups of exciton states is presented in Fig. 6.4(b). Figure 6.4(c) shows normalized incoherent populations in the model with only two accessible electronic states (of energies $\epsilon_{A,0}^{\mathrm{c}}$ and $\epsilon_{A,1}^{\mathrm{c}}$) at each acceptor site. Comparing Figs. 6.4(b) and (c), we conclude that the presence of PACB states significantly affects exciton dynamics on ultrafast time scales. In the presence of only two lower electronic levels in the acceptor, the number of donor excitons decreases, while the numbers of CS, CT, and XA excitons increase after the excitation, see Fig. 6.4(c). On the other hand, taking into account the presence of higher-lying electronic orbitals in the acceptor and pumping well above the lowest donor exciton, the populations of XD, XA, CT and CS states increase, while the population of PACB states decreases after the excitation, see Fig. 6.4(b). The fact that donor states acquire population after the end of the pulse may at first seem counter-intuitive, since initially generated donor excitons are expected to dissociate, performing transitions to the space-separated manifold. Having significant amount of donor character, PACB states are well coupled (via single-phonon-assisted processes) to the manifold of donor excitons, while their coupling to space-separated states belonging to CT_0 and CT_1 bands is essentially negligible, as discussed in the paragraph following Eq. (6.9). Therefore, instead of performing single-phonon-assisted transitions to lower-energy space-separated states, initially generated PACB excitons perform

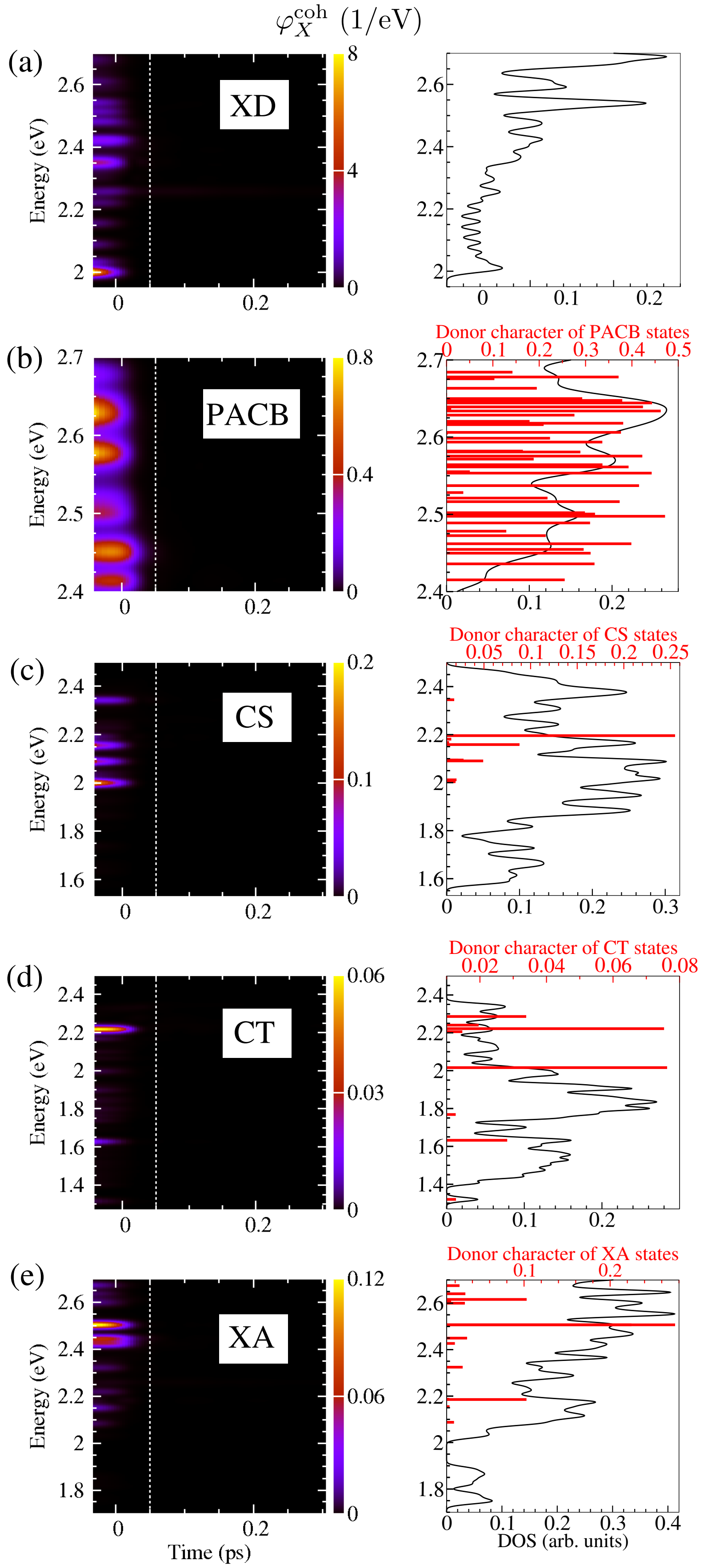

FIGURE 6.5: Density plots of $\varphi_X^{\mathrm{coh}}(E,t)$ for (a) XD, (b) PACB, (c) CS, (d) CT, and (e) XA states. Each density plot is complemented with the plot of the corresponding exciton DOS. In panels (b)–(e), exciton DOS plots contain amounts of the donor character of exciton states, see Eq. (5.14) [in panels (c)–(e), as long as it is greater than 0.01].

transitions towards donor states, i.e., the number of donor excitons increases at the expense of excitons initially generated in PACB states. While at the end of the pulse excitons in PACB states comprise around 11% of the total exciton population, 900 fs after the pulse their participation in the total population reduces to 4%. At the same time, the normalized number of donor excitons increases from around 85% to around 89% of the total exciton population, meaning that some of the donor excitons are converted into XA, CT, and CS states, which is seen in Fig. 6.4(b) as the increase in the populations of these states.

In the model with four accessible electronic orbitals per acceptor site, the major part of space-separated states that are populated on 100-fs time scales following the excitation are directly generated PACB states. This conclusion is in line with our results presented in Ch. 5, where the LUMO–LUMO offset is comparable to the effective bandwidth of the LUMO band of the acceptor. PACB states acquire nonzero oscillator strengths due to the energy alignment between single-electron states stemming from the donor LUMO orbital and higher-than-LUMO acceptor orbitals, meaning that they can be directly optically generated when exciting donor states. If only electronic orbitals close to the LUMO orbital are taken into account, populations of space-separated states present on 100-fs time scales after the excitation mainly reside in bridge states, which are formed by resonant mixing between two-particle states. The populations of bridge states are dominantly built by phonon-assisted transitions from initially generated donor excitons (since the direct generation of excitons in bridge states is not very pronounced for the excitation studied). Therefore, in our model, the PACB states can enhance the generation of space-separated charges on ultrafast time scales by allowing for their direct optical generation and not by acting as intermediate states of charge separation starting from intial donor excitons.

6.3.2 Individuation of Ultrafast Photophysical Pathways

In order to unravel the photophysical pathways along which the ultrafast exciton dynamics proceeds, in Figs. 6.6(a)–(e) we depict the density plots of $\varphi_X^{\mathrm{incoh}}(E,t)$ for various groups X of exciton states. As already explained, the excitons initially generated in PACB states (red bolt in Fig. 6.3) undergo deexcitation within the PACB manifold [pathway (1) in Fig. 6.3] followed by

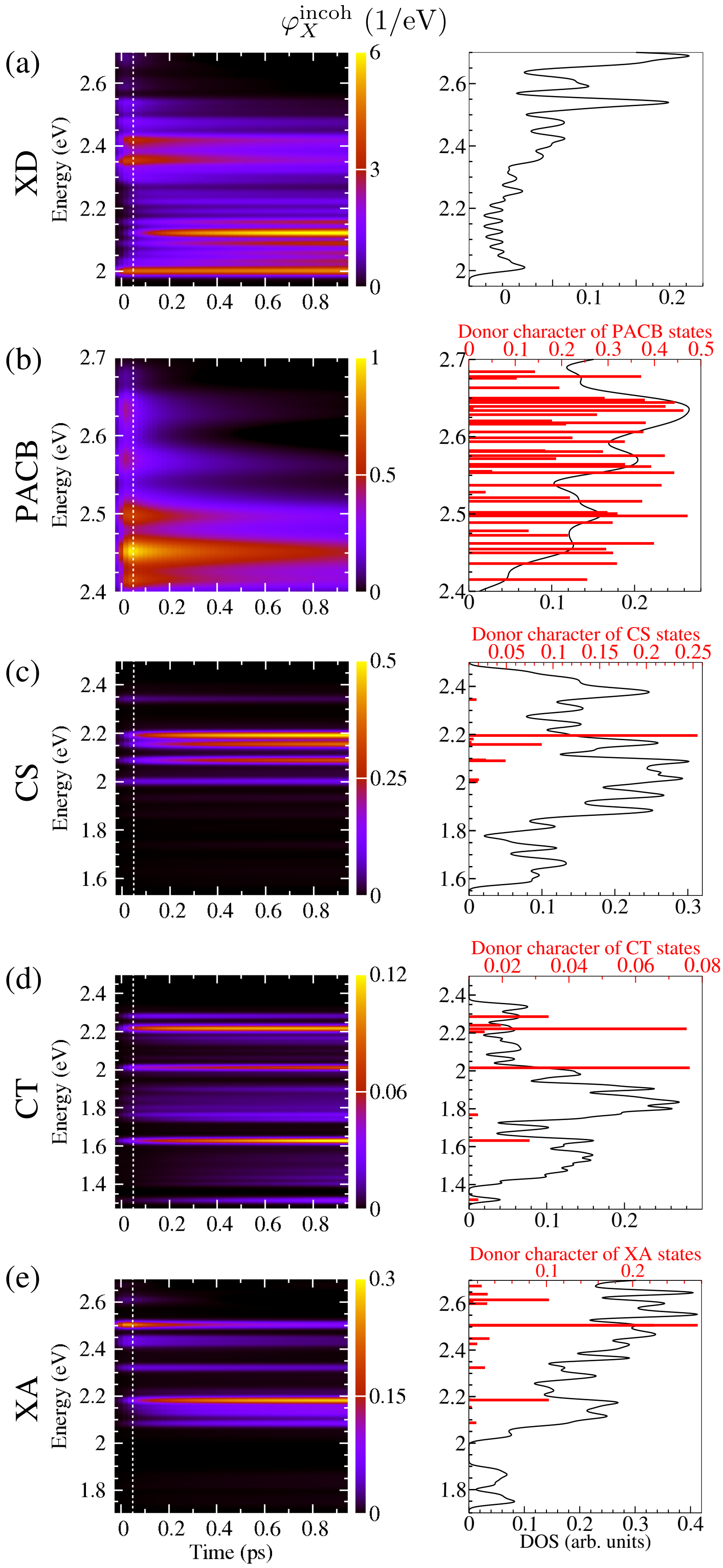

FIGURE 6.6: Density plots of $\varphi_X^{\mathrm{incoh}}(E,t)$ for (a) XD, (b) PACB, (c) CS, (d) CT, and (e) XA states. Each density plot is accompanied by the plot of the corresponding exciton DOS. In panels (b)–(e), the exciton DOS plots contain the amount of the donor character of exciton states, see eq 5.14 [in panels (c)–(e), as long as it is greater than 0.01].

phonon-mediated transitions towards the manifold of donor states [pathway (2) in Fig. 6.3], see Figure 6.6(b). Donor excitons (either the ones initially generated in higher-lying bright states, see the black bolt in Fig. 6.3, or the ones originating from PACB excitons) are involved in a series of ultrafast phonon-assisted transitions towards lower-energy states. Most of these transitions happen within the XD manifold [pathway (3) in Fig. 6.3], see the series of more or less bright bands in the density plot of Fig. 6.6(a), which is consistent with the fact that donor excitons comprise the largest part of the total exciton population at every instant. The deexcitation within the XD manifold proceeds until the lowest XD state is reached. In fact, we see that already for $t \gtrsim 250$ fs, XD population resides mainly in the lowest donor state at around 2 eV and the donor state at around 2.13 eV. The lowest donor state is almost uncoupled from the space-separated manifold, acting as a trap state for exciton dissociation, which is in line with other studies [59]. The other donor state (at around 2.13 eV) acting as a trap state for exciton dissociation is specific to our computation.

In the course of the deexcitation from the higher-lying donor states and before reaching a trap state for exciton dissociation, a donor exciton can perform a transition to a bridge state [pathway (4) in Fig. 6.3]. As seen in Figs. 6.6(c)–(e), the energy positions of the bright bands in the density plots on the left match exactly the energy positions of red bars displaying the amount of donor character of dominantly space-separated or XA states on the right. Figures 6.7(b)–(d) depict probability distributions of the electron and hole in representative bridge states of different dominant characters, while Fig. 6.7(a) shows the same quantities for particular PACB states. All the bridge states exhibit carrier delocalization throughout the system; this property makes them accessible from the initial states of donor excitons. The same holds for PACB states: since the carriers in these states are delocalized throughout the heterojunction, these states inherit oscillator strengths from donor excitons and may thus be directly accessed by an optical excitation. Moreover, this property enables efficient phonon-assisted coupling between PACB states and donor states. The bridge states gain significant populations during the first 100 fs following the excitation [pathway (4) in Fig. 6.3] and concomitantly the excitons initially generated in PACB states perform phonon-mediated transitions towards donor states [pathway (2) in Fig. 6.3].

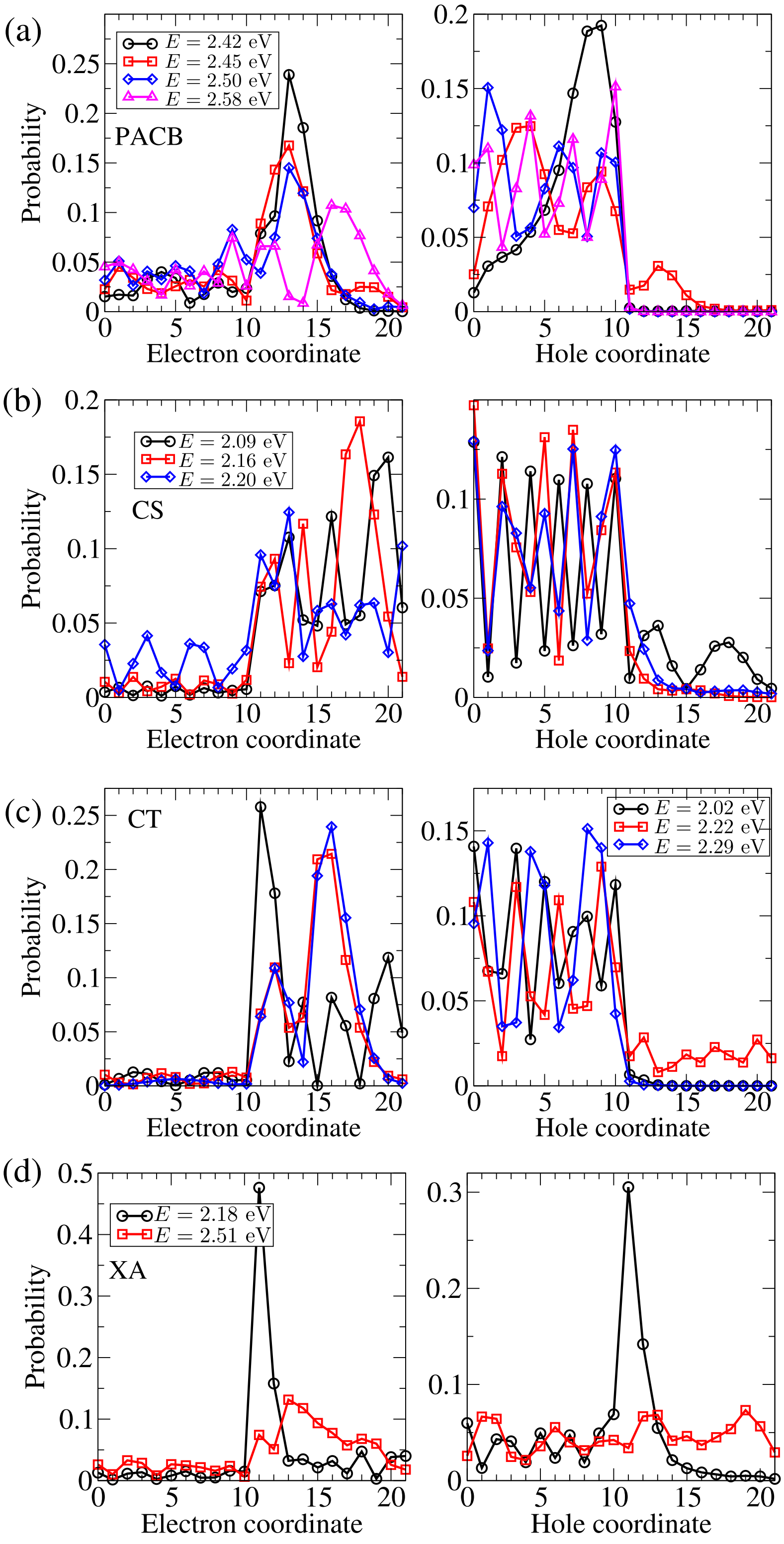

FIGURE 6.7: The probability distributions of the electron (left) and hole (right) in representative (a) PACB states and bridge states of dominant (b) CS, (c) CT, and (d) XA character.

Once the exciton has reached a bridge state, it can deexcite within the manifold of its dominant character [pathways (6)–(8) in Fig. 6.3] or it can perform a transition to the CT manifold [pathway (5) in Fig. 6.3] followed by a number of downward transitions within this manifold [pathway (7) in Fig. 6.3], see the series of more or less bright bands between 1.3 and 2.2 eV in the density plot of Fig. 6.6(d). The gradual deexcitation within the CT manifold leads to the delayed build-up of populations of low-energy CT states [pathway (7) in Fig. 6.3], see bright bands at around 1.62 and 1.32 eV in the density plot in Fig. 6.6(d), which happens on a picosecond time scale. Apart from mediating the charge separation, bridge states can also act as competing final states. In our computation, at every instant, virtually all CS excitons reside in bridge states of dominant CS character, and the progressive deexcitation within the CS manifold [pathway (6) in Fig. 6.3] is not pronounced, see Fig. 6.6(c). Analogous situation is observed analyzing the energy- and time-resolved populations of XA states [pathway (8) in Fig. 6.3] in Fig. 6.6(e). This twofold role of bridge states observed in our computations is in agreement with conclusions of previous studies [140].

6.3.3 Influence of Model Parameters on Ultrafast Exciton Dynamics

Here, we discuss on how changes in values of some of the model parameters affect the picture of ultrafast interfacial dynamics obtained so far.

The exact photophysical pathways along which the exciton dynamics proceeds on ultrafast time scales strongly depend on the frequency of the excitation, the exciton dissociation being more pronounced for larger excess energy [36, 180]. We examine ultrafast exciton dynamics for three different excitations of central frequencies $\hbar\omega_c = 2.35$, 2.25, and 2 eV (excitation at the lowest donor state). As the central frequency of the excitation is decreased, i.e., as the initially generated donor excitons are closer in energy to the lowest donor state, the conversion from coherent to incoherent exciton population is slower and the time scale on which exciton coherences with the ground state dominate the interfacial dynamics is longer, see Fig. 6.8(b). At the same time, the participation of excitons in PACB states in the total exciton population is decreased, whereas donor excitons comprise larger part of the total population, see Fig. 6.8(a). Namely, as

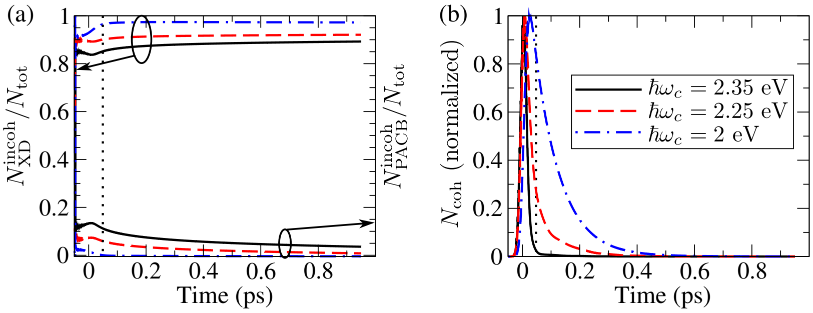

FIGURE 6.8: Time dependence of (a) the normalized number of excitons in donor and PACB states, and (b) the total coherent exciton population, for different central frequencies of the excitation. For convenience, the total coherent population shown in (b) is normalized so that its maximal value is equal to 1.

the central frequency is lowered towards the lowest donor state, the initial optical generation of excitons in PACB states is less pronounced and the pathways (1) and (2) in Fig. 6.3 become less important, while the possible photophysical pathways of the initially generated donor excitons become less diverse. Therefore, the phonon-assisted processes responsible for the conversion from coherent to incoherent exciton populations and for the ultrafast phonon-mediated transitions from donor states towards space-separated states are less effective. As a consequence, the conversion from coherent to incoherent exciton populations is slower, and initially generated donor excitons tend to remain within the manifold of donor states [pathway (3) in Fig. 6.3, down to the lowest donor state, is preferred to pathways (4)–(7), which may lead to space-separated states]. The latter fact is especially pronounced exciting at the lowest donor state, which is very weakly coupled to the space-separated manifold, when around 80% of the total exciton population lies in the lowest donor state, meaning that the ultrafast charge transfer upon excitation at this state is not significant.

For the values of model parameters listed in Table 6.1, the LUMO–LUMO offset is rather large, and the bridge states emerge as a consequence of the energy resonance between two-particle (exciton) states. The energies of these states, as well as their number and amount of the donor character, are therefore very sensitive to the particular exciton energy level alignment at the heterojunction. On the other hand, the properties of PACB states are not expected to be particularly sensitive to the details of the energy level alignment, since they originate from resonances between single-electron states in the donor and acceptor. In order to demonstrate this difference between bridge states and PACB states, we perform computations with different, but very close, values of the LUMO–LUMO offset. The LUMO–LUMO offset is varied by changing all the parameters $\epsilon^{\text{c}}_{A,0}$, $\epsilon^{\text{c}}_{A,1}$, $\epsilon^{\text{c}}_{A,2}$, $\epsilon^{\text{c}}_{A,3}$, $\epsilon^{\text{v}}_{A,0}$ in Table 6.1 by the same amount, keeping all the other model parameters fixed. The effects of small variations of LUMO–LUMO offset are studied for $J^{\text{v}}_{DA} = 0$, when all the bridge states are of mixed XD and space-separated character and, since $d^{\text{cv}}_{A} = 0$, XA states do not participate in the ultrafast exciton dynamics. The exclusion of XA states from the dynamics decreases significantly the numerical effort and at the same time allows us to concentrate on the dynamics of ultrafast electron transfer, instead of considering both electron transfer and exciton transfer. The main qualitative features of the ultrafast exciton dynamics described earlier remain the same, which has been explicitly checked in the Supporting Information associated to Ref. [166]. Figure 6.9(a) presents the time dependence of the normalized number of excitons in PACB states, while Fig. 6.9(b) shows the normalized number of excitons in space-separated states 900 fs after the excitation for different LUMO–LUMO offsets ranging from 950 to 980 meV in steps of 5 meV. Small variations in the LUMO–LUMO offset between 955 and 975 meV weakly affect the portion of PACB excitons in the total exciton population. However, for the LUMO–LUMO offset of 980 meV, the normalized number of excitons in PACB states is somewhat higher than for the other considered values, while this number is somewhat smaller for the LUMO–LUMO offset of 950 meV. Namely, for larger LUMO–LUMO offsets, the lowest state of CT_2 band is closer to the central frequency of the excitation, and the direct optical generation of excitons in PACB states is more pronounced. For smaller LUMO–LUMO offsets, the initial generation of excitons in PACB states is to a certain extent suppressed because the energy difference between the lowest state of CT_2 band and the central frequency of the excitation is larger. On the other hand, the relative number of space-separated excitons can change up to three times as a result of small changes in the LUMO–LUMO offset. The different behavior displayed by the relative numbers of PACB excitons and space-separated excitons is a consequence of different mechanism by which PACB states and bridge states emerge. The peak in the normalized number of space-separated excitons observed for the LUMO–LUMO offset of 965 meV signalizes that the exciton-level alignment at this point favors either (i) formation of more bridge states of dominant space-separated character than at other points or (ii) formation

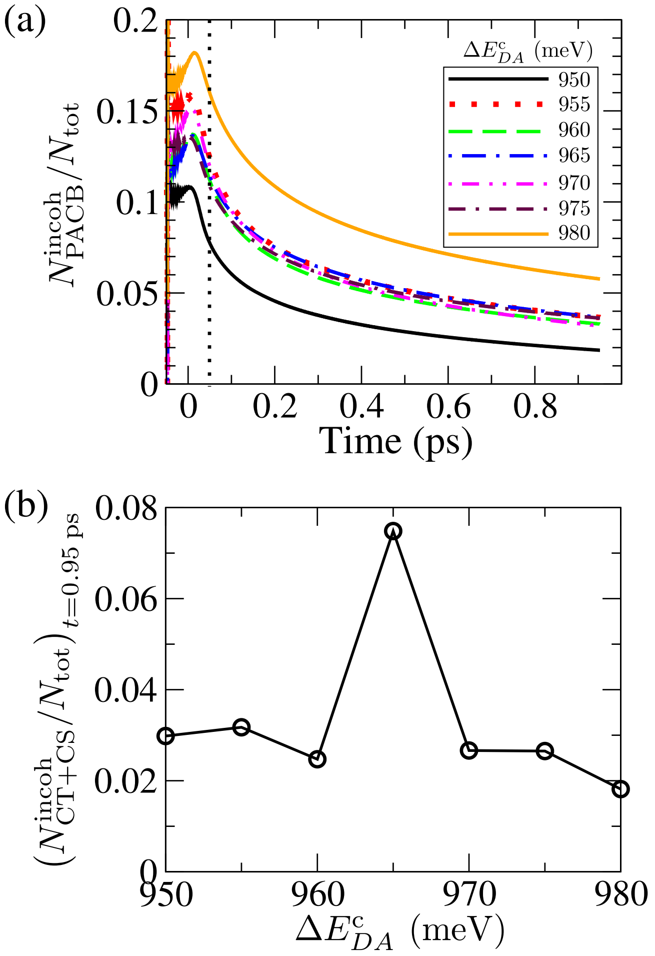

FIGURE 6.9: (a) Time dependence of the normalized number of PACB excitons for different values of the LUMO–LUMO offset $\Delta E^{\mathrm{c}}_{DA}$. (b) The relative number of excitons in space-separated (CT and CS) states 900 fs after the excitation for different values of $\Delta E^{\mathrm{c}}_{DA}$. The system is excited at $\hbar\omega_c = 2.35$ eV.

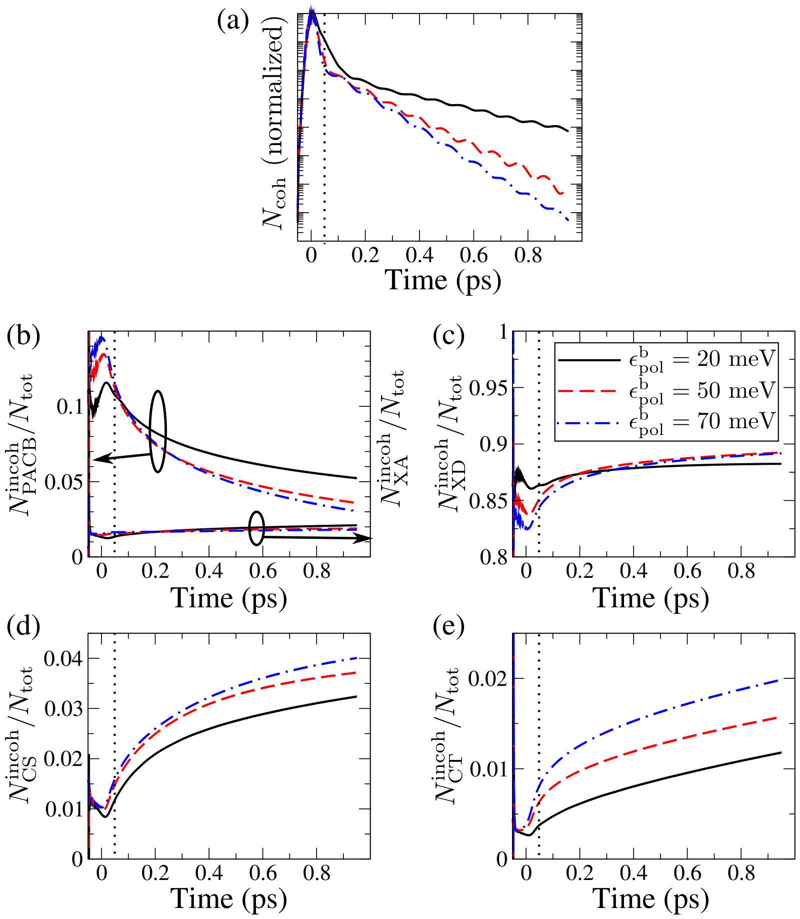

FIGURE 6.10: (a) Time dependence of the total coherent exciton population N_{coh} for different carrier–phonon interaction strengths. For convenience, N_{coh} is normalized so that its maximum assumes the same value for all studied interaction strengths. Dynamics of normalized incoherent excition populations of (b) PACB and XA, (c) XD, (d) CS, and (e) CT states, for different interaction strengths.

of bridge states that couple more strongly to initial donor states than bridge states at other points.

We now analyze the ultrafast exciton dynamics for different strengths of the carrier–phonon coupling, exciting the system at $\hbar\omega_c = 2.35$ eV. The polaron binding energy $\epsilon^{\mathrm{b}}_{\mathrm{pol}}$ [Eq. (5.8)], which is a measure of the carrier–phonon interaction strength, assumes values of 20, 50, and 70 meV. Since the carrier–phonon interaction mediates the conversion from coherent to incoherent exciton populations, weaker carrier–phonon coupling makes this conversion somewhat slower, see Fig. 6.10(a). We note that, for all the interaction strengths considered, the total coherent population decays 100 times (compared to its maximal value) in $\lesssim 100$ fs following the excitation, meaning that the conversion is in all three cases relatively fast.

The normalized number of excitons in PACB states is smaller for stronger carrier–phonon interaction, see Fig. 6.10(b). The characteristic time scale for the decay of the population of PACB states is shorter for stronger carrier–phonon interaction, which is a consequence of stronger phonon-mediated coupling among PACB states and donor states [pathway (2) in Fig. 6.3]. For larger interaction strength, the populations of CS and CT states comprise larger part of the total exciton population, see Figs. 6.10(d) and (e). Namely, the stronger is the carrier–phonon interaction, the more probable are the transitions from donor states to bridge states [pathway (4) in Fig. 6.3] and the larger are the populations of CS and CT states [pathways (5)–(7) in Fig. 6.3]. The relative number of acceptor excitons does not change very much with the carrier–phonon interaction strength, see Fig. 6.10(b). The variation in the relative number of donor excitons brought about by the changes in the interaction strength is governed by a number of competing factors. First, stronger carrier–phonon interaction favors larger number of donor excitons, since phonon-assisted transitions from PACB to XD states [pathway (2) in Fig. 6.3] are more pronounced. Second, for stronger interaction, the transitions from XD to bridge states are more probable [pathway (4) in Fig. 6.3]. Third, since phonon-mediated transitions are most pronounced between exciton states of the same character, stronger interaction may also favor deexcitation of donor populations within the XD manifold [down to the lowest XD state, pathway (3) in Fig. 6.3] to possible transitions (via bridge states) to the space-separated manifold [pathways (4)–(7) in Fig. 6.3]. From Fig. 6.10(c) we see that, as a result of all these factors, the relative number of donor excitons does not change monotonously with the interaction strength.

To understand how the changes in carrier–phonon interaction strength affect the photophysical pathways along which the ultrafast exciton dynamics proceeds, in Figs. 6.11(a)–(l) we present energy- and time-resolved incoherent populations of various groups of exciton states (in different rows) and for different interaction strengths (in different columns). While for the strongest studied interaction initially generated higher-lying donor excitons and excitons in PACB states leave the initial states rapidly, see Figs. 6.11(i) and (j), for the weakest studied interaction strength significant exciton population remains in these states during the first picosecond of the exciton dynamics, see Figs. 6.11(a) and (b). The deexcitation of donor excitons takes place predominantly within the XD manifold (pathway (3) in Fig. 6.3) for all three interaction strengths, compare the

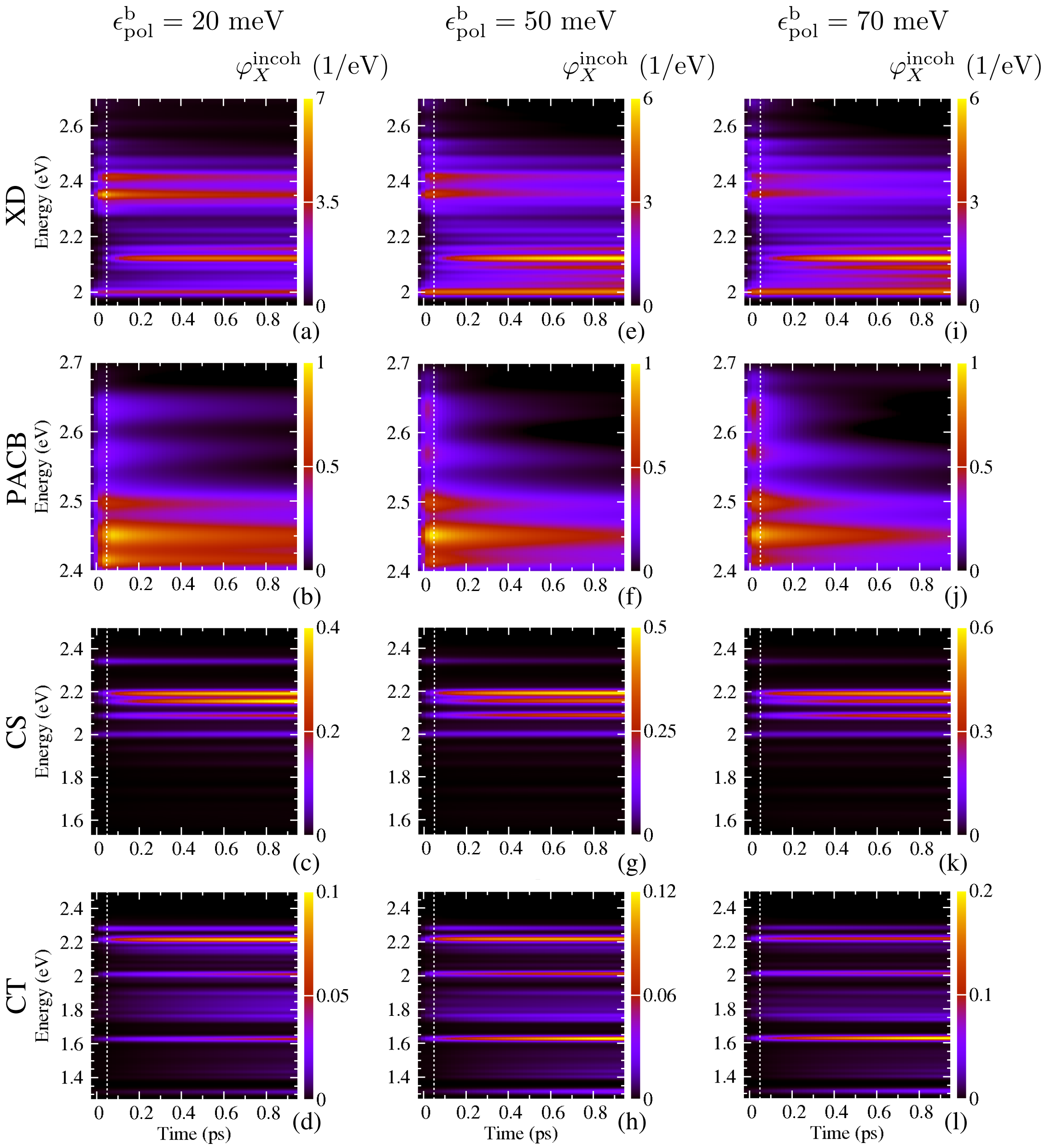

FIGURE 6.11: Energy- and time-resolved incoherent exciton populations $\varphi_X^{\mathrm{incoh}}(E, t)$ for different carrier–phonon interaction strengths: (a), (b), (c), and (d): $g_1 = 26.7$ meV, $g_2 = 59.7$ meV; (e), (f), (g), and (h): $g_1 = 42.2$ meV, $g_2 = 94.3$ meV; (i), (j), (k), and (l): $g_1 = 54.0$ meV, $g_2 = 111.6$ meV. Groups of exciton states: (a), (e), and (i): XD states; (b), (f), and (j): PACB states; (c), (g), and (k): CS states; (d), (h), and (l): CT states.

ranges of color bars in Figs. 6.11(a), (e), and (i). For the weakest studied interaction, the lowest donor state, which is a trap for the exciton dissociation, is largely bypassed in the course of the deexcitation, whereas for stronger carrier–phonon interactions this state acquires significant population already from the beginning of the excitation. Energy- and time-resolved populations of CS states are very nearly the same for all three interaction strengths studied, see Figs. 6.11(c), (g), and (k). The major part of the CS population resides in bridge states, and the deexcitation within the subset of CS states [pathway (6) in Fig. 6.3] is not very pronounced. On the other hand, the deexcitation within the subset of CT states [pathway (7) in Fig. 6.3], down to the lowest CT state, is observed for all the interaction strengths considered, see the series of more or less bright bands in Figs. 6.11(d), (h) and (l). While for the weakest interaction the largest portion of the CT population resides in the bridge state of CT character located at around 2.2 eV, for the strongest interaction the major part of the CT population is located in the lowest state of CT_1 band at around 1.63 eV.

The carrier–phonon coupling thus acts in two different ways. On the one hand, stronger carrier–phonon interaction enhances exciton dissociation and subsequent charge separation by (i) enabling phonon-assisted transitons from a donor state to space-separated states via bridge states [pathways (4) and (5) in Fig. 6.3] and (ii) enabling phonon-assisted transitions within the space-separated manifold once a space-separated state is reached [pathways (6) and (7) in Fig. 6.3]. On the other hand, stronger carrier–phonon coupling is detrimental to exciton dissociation and further charge separation because (i) it makes donor states more easily accessible from initially generated PACB excitons [pathway (2) in Fig. 6.3] and similarly it may favor backward transitions from a bridge state to a donor state with respect to transitions to the space-separated manifold and (ii) downward phonon-assisted transitions make low-energy CT states, which are usually considered as traps for charge separation, populated on a picosecond time scale following the excitation [pathway (7) in Fig. 6.3].

6.4 Discussion and Significance of Our Results

The results presented in this chapter complement our results in Ch. 5 by providing a more detailed account of the subpicosecond exciton dynamics at D/A heterojunctions. The model we employ here is constructed as an effective one-dimensional model intended to describe ultrafast dynamics of charge separation in the direction perpendicular to the interface, in which the hole separates from its sibiling electron in the interchain direction. The model is parameterized using the literature data for the archetypal P3HT/PCBM blend. We effectively take into account the most important features of the band structure of PCBM aggregates that have been indicated as highly important for ultrafast free-charge generation in conjugated polymer/PCBM blends [51, 58]. Moreover, we also investigate the role played by the electronic states stemming from PCBM orbitals situated at ca. 1 eV above its LUMO orbital, which has remained rather unexplored.

We reveal that these higher-than-LUMO molecular orbitals contribute to ultrafast free-charge generation by giving rise to an additional group of photon-absorbing states, the so-called PACB states. PACB states form as a consequence of the resonant mixing between single-electron states in the donor and acceptor and carriers in them are highly delocalized throughout the heterojunction. We observe that excitons in PACB states relax towards the donor manifold on a picosecond time scale, and thus speculate that, if they were to be converted into free carriers, this conversion would have to occur before their relaxation towards donor states, i.e., on a subpicosecond time scale.

On the other hand, we find that the resonant mixing between exciton (two-particle) states brings about the formation of the so-called bridge states, which also exhibit charge delocalization, but do not primarily act as additional photon-absorbing states at the interface. Instead, they serve as gateways for the donor excitons into the space-separated manifold, so that the populations of low-lying space-separated states are built by progressive deexcitation within the space-separated manifold on a picosecond time scale following the excitation. The transitions of donor excitons towards bridge states are concurrent and compete with their pronounced relaxation towards the lowest-lying donor states, which we identify as a trap state for subpicosecond exciton dissociation and charge separation.

Our results demonstrate the strong dependence of the ultrafast exciton dynamics on the central frequency of the excitation. Exciting well above the lowest-lying donor state, there is a multitude of photophysical pathways by which the initial donor excitons can reach the space-separated manifold before reaching the lowest-lying donor state, such as the pathway black bolt [$\rightarrow$ (3)] $\rightarrow$ (4) $\rightarrow$ (5) $\rightarrow$ (6) in Fig. 6.3. Exciting at the lowest-energy donor state, population transfer towards space-separated states is not pronounced. The last two statements are in agreement with the conclusions of Ref. [59]. The role of the carrier–phonon interaction in subpicosecond exciton dynamics is quite complex because it may, at the same time, enhance and suppress the build-up of the populations of space-separated states. As a result of these counterbalancing effects, we conclude that stronger carrier–phonon coupling is to some extent beneficial to ultrafast charge separation, see Figs. 6.10(a)–(e), but its influence is not particularly strong.

In the end, all of the above-presented results indicate that the number of space-separated charges that are present at $\sim$ 1 ps after photoexcitation is rather small, being typically less than 10% of the number of excited electron–hole pairs. On the other hand, in most efficient OSC devices, IQEs close to 100% have been reported [7, 61]. In light of an ongoing debate on the origin of high IQE and the time scale necessary for the full charge separation to occur, our results suggest that time scales longer than the picosecond one are in fact needed to separate charges. Let us also emphasize that many of the ultrafast photophysical pathways that we individuate eventually produce electron–hole pairs that are in some sense strongly bound. For example, the pathway black bolt $\rightarrow$ (3) in Fig. 6.3 leads to the build-up of the population in the lowest-energy donor state, which features a poor connectivity with space-separated states. Actually, the largest portion of the excitons in donor states (and of all photogenerated excitons, too) is blocked in the lowest-lying donor state. Furthermore, the pathways black bolt [$\rightarrow$ (3)] $\rightarrow$ (4) $\rightarrow$ (5) $\rightarrow$ (7) and red bolt [$\rightarrow$ (1)] $\rightarrow$ (2) [$\rightarrow$ (3)] $\rightarrow$ (4) $\rightarrow$ (5) $\rightarrow$ (7) in Fig. 6.3 take the excitons initially generated in donor and PACB states towards the low-lying CT states. Therefore, if we are to achieve an efficient light-to-charge conversion in a D/A blend, a mechanism that leads to escape of charges from the low-energy donor and CT states on longer time scales needs to exist. While the precise mechanism of this long-time charge separation out of bound pair states will be discussed in the following chapter, let us mention here that our results fit well into the picture of free-charge generation that emerges from the experimental study conducted by Grupp et al. [181] Namely, using the transient absorption spectroscopy, the authors of Ref. [181] investigate the photoinduced electronic dynamics in the P3HT/PCBM blend after the excitation of the P3HT moiety and compare it to the dynamics of neat P3HT excited in the same manner. They observe that, on subpicosecond time scales, the spectrally resolved differential transmission signal of the P3HT/PCBM blend is essentially the same as that of pristine P3HT. The differences in the signals of the blend and neat polymer material arise only on ~ 10 ps time scales after the pump, when the signal of neat P3HT suggests that excited-state populations start to deplet due to recombination processes. However, the signal of the P3HT/PCBM blend does not display such a feature which, in combination with the observed build-up of the population of the strongly bound CT state, implies that free-carrier generation predominantly occurs from that state on a time scale that is at least an order of magnitude longer than the one involving “hot” and delocalized CT states.

Chapter 7

Incoherent Charge Separation at Photoexcited Organic Bilayers

While our focus in previous chapters was on understanding the fundamentals of subpicosecond dynamics of photoinduced electronic excitations in D/A OSCs, in this chapter we concentrate on unraveling the physical mechanisms that are crucial to charge separation occurring on much longer time scales. Since long-time charge separation is commonly believed to be assisted by the internal electric field in the solar cell, Sec. 7.1 introduces (on a very simple level) solar cells as electric devices and defines the internal electric field more precisely. In Sec. 7.2, we discuss our motivation for investigating the so-called incoherent charge separation in light of relevant experimental and theoretical results existing in the literature. The model and appropriate theoretical method are introduced in Sec. 7.3. Our findings are thoroughly presented in Sec. 7.4, whose content is based upon our recent publication [182]. The aim of Sec. 7.5 is to emphasize our principal findings and their significance in a broader picture of light-to-charge conversion in D/A OSCs.

7.1 Solar Cells as Electric Devices

Before reviewing the experimental and theoretical results that are relevant for the long-time charge separation at a D/A interface, let us introduce in a simplified way the notion of the internal (or interfacial) electric field at the interface [183]. A good starting point for our discussion here is Fig. 1.9, which summarizes the band alignment at a D/A interface. Since full charge separation

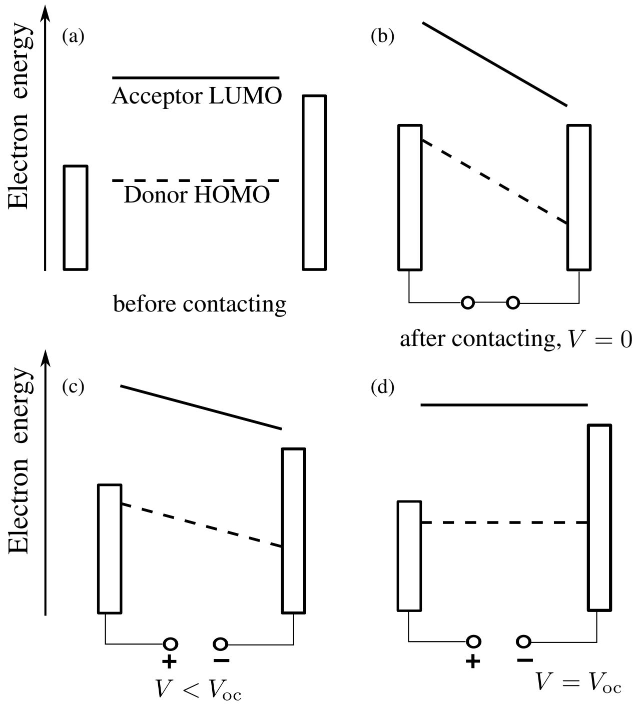

FIGURE 7.1: Positions of the electron energy levels in metal contacts (rectangles), acceptor (solid line), and donor (dashed) that are relevant for the operation of an OSC. (a) Relevant energy levels of metal contacts and the active layer in isolation. (b) Having short-circuited the contacts, the built-in electric field appears in the cell and the relevant energy levels of the active layer are tilted. (c) Making the left contact positive with respect to the right contact, the magnitude of the internal electric field is reduced with respect to the built-in field. (d) Under open-circuit (also flat-band) conditions, the externally applied electric field corresponding to the open-circuit voltage precisely compensates the built-in electric field.

is possibly achieved once the electron is in the acceptor, while the hole is in the donor region of the interface, the LUMO level of the acceptor material and the HOMO level of the donor material are of particular relevance, together with the Fermi levels of metal contacts. Only these levels are shown in Fig. 7.1(a), which describes metal contacts and the active layer in isolation. Due to the difference in the Fermi levels of metal contacts in Fig. 7.1(a), their short-circuiting gives rise to the so called built-in electric field in the region between them, whose magnitude is such that the Fermi levels of the short-circuited contacts equalize, see Fig. 7.1(b). The built-in electric field is directed from the contact of higher Fermi level [right contact in Fig. 7.1(a)] towards the contact of lower Fermi level [left contact in Fig. 7.1(a)], i.e., it is directed from the acceptor towards the donor region of the interface. In the dark, there is no electric current. Under illumination, the built-in electric field drives photogenerated spatially separated electrons and holes in opposite directions, i.e., it promotes the separation of space-separated electron–hole pairs. In more formal terms, the built-in electric field induces the tilt of the bands, which makes photogenerated electrons move energetically downwards, towards the contact of higher Fermi level, while holes move energetically upwards, towards the contact of lower Fermi level, see Fig. 7.1(b).

The tilt of the bands can be regulated by applying an additional external voltage between the contacts. The internal electric field in the device is then a superposition of the built-in electric field and the external electric field. If the left contact is made positive with respect to the right contact, see Fig. 7.1(c), we say that the so-called forward bias is applied, and the magnitude of the internal electric field, which determines the slope of the bands, is decreased with respect to the built-in electric field. At open-circuit conditions, when the potential of the right contact is by V_{oc} (the so-called open-circuit voltage) higher than the potential of the left contact, the externally applied electric field exactly compensates the built-in electric field, the bands become flat, while the current is equal to zero, see Fig. 7.1(d). In this simplistic model, V_{oc} is exactly equal to the the difference between Fermi levels of the contacts divided by the elementary charge. Further elevation of the potential difference between the contacts makes us leave the solar-cell operation regime and enter the operation regime of light-emitting diodes, in which carriers are injected from the contacts into the active layer. On the other hand, the so-called reverse bias corresponds to the left contact being negative with respect to the right contact. The reverse bias increases the internal electric field with respect to the built-in electric field. The carriers generated under illumination in the reverse-bias regime drift in the strong electric field towards the respective electrode, and the device works as a photodetector.

The current-voltage characteristic of a solar cell in the dark and under illumination is schematically presented in Fig. 7.2. In the dark, the current is essentially absent until the contacts start to inject carriers at voltages that are larger than the open-circuit voltage. Under illumination, the current flows in the direction opposite to that of the dark current. Maximum photocurrent flows under short-circuit conditions (the so-called short-circuit current j_{sc}), the current is equal to zero at the open circuit, while between these two limits the solar cell generates useful power. By modulating the voltage between the contacts, the internal electric field in the cell

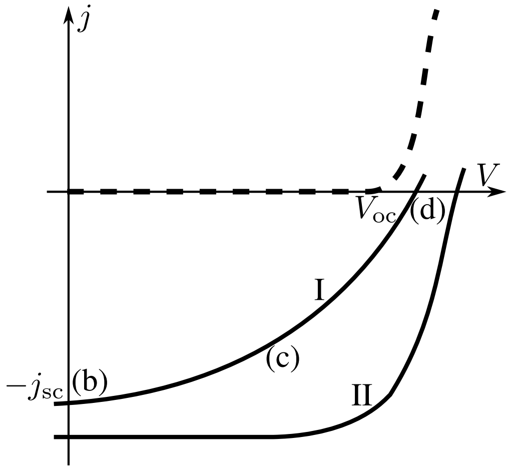

Figure 7.2: Current-voltage characteristic (j-current density, V-voltage) of a solar cell in the dark (dashed line) and under illumination (solid line, curve I). The letters (b), (c), and (d) correspond to Figs. 7.1(b), (c), and (d), respectively. The $j-V$ characteristic II is flatter and shows less pronounced electric field-dependence of the free-charge generation than the characteristic I.

drops from its maximum value, i.e., the built-in electric field, at short-circuit conditions, to zero at open-circuit conditions. Typical values of the built-in electric field in OSCs are of the order of 5×10^6–10^7 V/m.

7.2 Experimental and Theoretical Background

7.2.1 Overview of Recent Experimental Results

The standpoint of "hot" charge separation mechanisms, which assume that the conversion of absorbed photons to free charges is completed within the first $\sim$ 100 fs after the excitation by exploiting some form of quantum mechanical coherence, has recently been questioned in a number of experimental studies. In particular, Vandewal et al. [61] measure the spectral profile of the IQE, i.e., the IQE as a function of the energy of exciting photons, of a wide range of material combinations used in OSCs (polymer/fullerene, small-molecule/fullerene, and polymer/polymer blends). While the IQE spectral profile had been obtained eariler, see, e.g., Ref. [60], Vandewal et al. succeeded in extending the usually investigated spectral range down to the selective excitation of the lowest-lying "cold" CT state. Measurements in the spectral region that is situated below the absoprtion regions of individual donor and acceptor materials are extremely challenging. In simple terms, the oscillator strengths characterizing direct transitions from the ground state to the low-lying CT states are much smaller than those associated to the direct optical generation of donor excitons, mainly due to a much smaller overlap between electron and hole wave functions in CT states. Vandewal et al. overcome the challenge by measuring the inverse process, i.e., the radiative emission from the CT states to the ground state. Using the emission spectrum thus obtained, they reconstruct the absorption spectrum of the emissive species by employing additional theoretical analyses. Here, let us only mention that the theoretical developments make use of the Boltzmann populations of the ground- and excited-state energy levels during the emission experiment together with the optical reciprocity theorem. Eventually, the fraction of photons of energy E that are absorbed is uniquely related to the flux of photons of energy E that are emitted. The experimental results indicate that, in all the material combinations examined, the efficiency with which the absorbed photons are converted into free charges does not depend on whether the carriers are generated directly in the "cold" CT state or in some other higher-energy exciton state. In the most efficient D/A blends, the IQE is around 90% even when the "cold" CT state is selectively excited.

The experimental findings reported by Vandewal et al. imply that, even though there are ultrafast ("hot", coherent) pathways towards the current-producing pair states, the majority of free charges that are eventually extracted at the electrodes are obtained on a much longer time scale in a process that involves the strongly bound and interface-pinned CT state. The relaxation of the initially generated "hot" CT states is so fast and efficient that the separation predominantly happens upon reaching the "cold" CT state and is, as such, exclusively determined by the properties of the "cold" state. This, however, does not necessarily mean that coherent and incoherent charge separation mechanisms contradict each other. As argued in Ref. [184], both mechanisms may be at play in most efficient OSCs: free charges are generated on both the ultrashort and much longer time scales. The study of Vandewal et al. (and to some extent Ref. [184]) simply suggest that the majority of free carriers are obtained on a long time scale, starting from the "cold" CT state. However, the driving force that enables the oppositely charged electron and hole in the "cold" CT state to overcome their mutual Coulomb barrier remains elusive. By measuring the current-voltage ($j - V$) characteristics of a number of D/A blends, Vandewal and coworkers find that, in blends featuring higher IQEs, the $j - V$ characteristics are flatter in the relevant fourth quadrant (compare curves I and II in Fig. 7.2), while the "cold" states are less bound and more delocalized compared to blends displaying smaller IQEs [61]. Flat $j - V$ characteristics suggest that the role of the internal electric field in the free-charge generation is only marginal. Enhancing charge delocalization is proposed to be a promising route towards more efficient light-to-charge conversion in OSCs.

Further experimental evidence for long-time charge separation out of the "cold" CT state come from Vithanage et al. [62], who performed measurements on the archetypal P3HT/PCBM blend by using time-resolved electric field-induced second harmonic method to probe the dynamics of the internal electric field with subpicosecond time resolution. The experiment is set up in the pump–probe configuration, where the pump pulse photogenerates excitons, while the probe pulse, which acts after a variable time delay, is used to follow the time evolution of the internal electric field in the blend by measuring the second harmonic generation efficiency. From the temporal evolution of the experimental signal, the time-dependent electron–hole distance in the separating charge pair can be extracted. Experimental results demonstrate that the time scale on which the electron–hole separation exhibits a significant increase in of the order of tens of picoseconds. On subpicosecond time scales, the electron–hole distance is actually very small ($\lesssim 1$ nm), which is consistent with the aforementioned ultrafast relaxation of initial "hot" CT excitons towards the bottom of the CT manifold. On a picosecond time scale following photoexcitation, as a results of the quite fast three-dimensional diffusion, the electron–hole pairs evolve into still bound pairs whose intrapair separations reach several nanometers. On still longer (~ 100 ps) time scales, the electrons and holes become free primarily due to the diffusion-controlled separation by incoherent hops throughout the respective materials, while the role of the drift in the internal electric field is only marginal. The authors emphasize the importance of the dimensionality to achieve a fully separated pair state. Namely, in the presence of the disorder, which induces localization effects, full charge separation is achieved only by circumventing ubiquitous localized states. This is possible only if one takes into consideration all possible separation paths an electron and a hole can follow, which can be done correctly only within a three-dimensional model of a D/A blend. The effect of the dimensionality is also denoted as the entropic effect, *vide infra*.

Similar conclusions emerged from the investigation by Devižis et al. [63]. They studied charge separation at a small-molecule/fullerene bilayer and suggested that, at electric fields typically encountered within working OSCs, full charge separation is achieved on a $\sim$ 100 ps time scale starting from the "cold" CT state. Finally, as has been described in Sec. 6.4, the report by Grupp et al. [181] also implies that the overwhelming part of separation events takes place out of the strongly bound and localized CT state.

7.2.2 Overview of Recent Theoretical Results

According to our back-of-the-envelope calculation of the binding energy $\epsilon_\mathrm{b}^\mathrm{CT}$ of the "cold" CT exciton [see Eq. (1.3)], the depth of the Coulomb barrier that holds together the electron and hole in this state is of the order of 0.5 eV. Lately, there has appeared a number of theoretical proposals challenging the common view that the separation from the "cold" CT state requires surmounting an immense energy barrier [31, 185–187]. All of these studies use thermodynamic arguments applied to a D/A interface in thermal equilibrium at temperature T and emphasize the importance of the entropic effect for charge separation. Since the temperature is fixed, the barrier opposing charge separation is not determined by the difference in (internal) energies E of the free-charge and "cold" CT state, but rather by the difference in free energies $F = E - TS$, where S is the entropy. In this context, the entropy is related to the number of configurations in which an electron–hole pair, whose electron is in the acceptor, while the hole is in the donor, may be arranged at a D/A interface. The entropy is, therefore, closely related to the dimensionality; higher-dimensional interfaces feature more pronounced entropic effects [31, 185]. It is suggested that the combined effect of entropy and disorder [186] or entropy and carrier delocalization [187] can substantially reduce (or even eliminate) the Coulomb barrier, so that the electron and hole in the "cold" CT state are not thermodynamically bound and thus might separate if there are no kinetic obstacles.

The charge separation from the strongly bound CT state has been extensively studied within the framework of the Onsager–Braun model [64, 65] and its modifications [188]. Basically, the separation probability is determined by the competition between the electric field- and temperature-dependent dissociation of the localized electron–hole pair, which occurs at rate $k_{\mathrm{diss}}(F,T)$, and its recombination to the ground state, the lifetime of the pair being τ. The electric field- and temperature-dependent separation yield $\varphi(F,T)$ is then equal to

$$\varphi(F,T)=\frac{1}{1+\left(k_{\mathrm{diss}}(F,T)\tau\right)^{-1}}, \tag{7.1}$$

where, within the Onsager–Braun model,

$$k_{\mathrm{diss}}(F,T)=\frac{3\left(\mu_{\mathrm{e}}+\mu_{\mathrm{h}}\right)e}{4\pi\varepsilon_0\varepsilon_r r_{\mathrm{CT}}^3}\exp\left(-\frac{\epsilon_{\mathrm{b}}^{\mathrm{CT}}}{k_BT}\right)\frac{J_1\left(2\sqrt{-2b}\right)}{\sqrt{-2b}}, \tag{7.2}$$

$$b=\frac{e^3F}{8\pi\varepsilon_0\varepsilon_r k_BT}. \tag{7.3}$$

In the last three equations, T is the temperature, while F is the magnitude of the interfacial electric field. The electron–hole separation in the "cold" CT state is denoted as r_{CT}, μ_{e} and μ_{h} are electron and hole mobilities, respectively, while J_1 is the Bessel function of order one. Free parameters in the model are the intrapair separation r_{CT} and the so-called mobility–lifetime product $\left(\mu_{\mathrm{e}}+\mu_{\mathrm{h}}\right)\tau$. The mobility–lifetime product basically describes the competition between the pair recombination to the ground state and its escape towards free-charge state, which is assumed to be more probable if the carriers are more mobile. The most important features of the Onsager–Braun model can be readily appreciated from Eqs. (7.1), (7.2), and (7.3). The model predicts strong dependence of the separation yield on both the electric field and the temperature. While the temperature dependence is essentially exponential, see Eq. (7.2), the dependence on the electric field is more complex.[1] The Onsager–Braun model has been revealed successful in reproducing experimental photodissociation yields in bulk molecular D/A crystals [189], but it has been recognized as unsuitable for conjugated polymer/fullerene blends [66]. In the following paragraphs, we briefly summarize the main reasons for this inadequacy and discuss how the challenges thus arising have been tackled in the literature.

---

[1] At weak fields, it is customary to use the expansion $\frac{J_1\left(2\sqrt{-2b}\right)}{\sqrt{-2b}}=1+b+\frac{b^2}{3}+\frac{b^3}{18}+\ldots$. However, investigations performed in a broader range of electric field strengths usually prefer to use tabulated values of J_1.

To start with, the Onsager–Braun model employs the approximation of localized point charge carriers that does not hold in a conjugated polymer/fullerene blend. In this regard, it has been proposed that the hole delocalization along conjugated segments of polymer chains can enhance charge separation [190–192] since the kinetic energy of hole oscillations along chains lowers the Coulomb barrier between the electron and hole. Another effect that has been recognized as highly beneficial for charge separation at D/A interfaces is the formation of a dipolar layer at an interface of two materials with different electron affinities (different LUMO levels). Namely, experimental studies evidence partial electron transfer from the donor to the acceptor even in the dark, i.e., in the absence of a photoexcitation [193]. The layers of the partial negative charge in the acceptor and the partial positive charge in the donor are adjacent to one another, separated by a distance of the order of a nanometer, and thus form a dipolar layer. Let us assume that polymer chains are parallel to the D/A interface and that the electron in the "cold" CT state is localized on an acceptor molecule. The potential energy of the hole residing on the polymer chain adjacent to the electron localization site is the sum of interaction energies with the electron and with the partial charges of the dark dipoles. The motion of the hole is then restricted by the presence of partial positive dipole charges along the chain, which effectively form a potential well. In the harmonic approximation and on the quantum level, the zero-point energy of the hole in the potential well can then promote the escape of the hole to the next polymer chain (measured from the interface) [67, 194]. The combination of the effects due to the hole delocalization and the presence of dark interfacial dipoles has been demonstrated to reproduce the essential features of experimental photocurrent data [195]. Furthermore, the combination of the on-chain hole delocalization and the dimensional (entropic) effects has been suggested as the main reason for weakly field-dependent and very efficient charge separation at polymer/fullerene bilayers [68]. However, we note that all of the aforementioned studies account for delocalization effects in an effective way, for example, by introducing the hole effective mass for the on-chain motion [66, 68, 191, 194, 195] or by evenly smearing the charge throughout the delocalization region [190].

Second, in order for the Onsager–Braun model to reproduce experimental data, the mobility–lifetime product should assume unrealistically high values, meaning that either carrier mobility or pair lifetime should be unrealistically large. Kinetic Monte Carlo (kMC) studies have demonstrated that efficient and weakly field- and temperature-dependent charge separation can be achieved when relevant parameters are carefully chosen on the basis of experimental data [69, 70]. The analysis performed by the authors of Ref. [69] emphasizes that the bulk carrier mobility and the experimentally measured photoluminescence decay lifetime are not the appropriate values that should be used in Eq. (7.2). They obtain that the decisive event in the splitting of the "cold" CT exciton is its escape to the state in which the carriers are not adjacent to the interface, but their separation is somewhat larger, while their recombination becomes improbable. The escape from the "cold" CT state to this state means that the carriers move on a short length scale. The mobility value that is appropriate to describe this motion is not the bulk mobility, which characterizes the motion over long length scales, but rather the terahertz mobility. The terahertz mobility is typically much larger than the bulk mobility, so that using the bulk mobility dramatically underestimates the mobility–lifetime product. The correlation between the lifetime of the photoluminescence signal from the CT state and its lifetime should also be critically assessed. The CT photoluminescence is sensitive to the CT population, which can decrease both due to the radiative recombination and due to escape of the CT exciton to a free-charge state. Therefore, in blends in which the CT separation is efficient, the CT photoluminescence decay lifetime seriously underestimates the actual lifetime of the CT state, because its population is predominantly depleted by charge separation.

Third, the Onsager–Braun model does not capture the effects of the (energetic and/or spatial) disorder on charge separation. In Ref. [196], Rubel et al. present an analytical treatment of charge separation in a one-dimensional disordered chain and conclude that, at least at low interfacial electric fields, the disorder may enhance the separation of geminate electron–hole pairs. Recent kMC results also point towards the beneficial role of not too strong energetic disorder on charge separation [197].

Here, a study on the separation of geminate electron–hole pairs within a one-dimensional model of a bilayer is presented. Our model takes into account the physical effects that have been recognized as highly relevant to the process of charge separation, namely the carrier delocalization, energetic disorder, electron–hole interaction, carrier recombination, and the interaction of carriers with the phonon bath and the interfacial electric field. Instead of working in the commonly used position space, we transfer the description of charge separation to the space spanned by the exciton basis states. This transfer permits us to properly account for carrier delocalization effects. The charge separation is then conceived as a sequence of phonon bath-assisted transitions among different exciton states that starts from a particular state and ends once a free-charge state is reached.

7.3 Model and Method

7.3.1 Model Hamiltonian

The theoretical model that we employ to describe incoherent charge separation at an organic bilayer is essentially the same as the model we have used to study ultrafast exciton dynamics in Ch. 6. A bilayer is modeled by using the one-dimensional multiband semiconductor model that has been introduced in greater detail in Sec. 6.2. The model Hamiltonian is

$$H = H_{\mathrm{c}} + H_{\mathrm{p}} + H_{\mathrm{c-p}} + H_{\mathrm{c-\mathbf{F}}}, \tag{7.4}$$

where H_{c} is the interacting-carrier part of the Hamiltonian that assumes the same form as in Eq. (6.1), H_{p} is the free-phonon Hamiltonian given in Eq. (5.2), the carrier–phonon interaction $H_{\mathrm{c-p}}$ is precisely the same as in Eq. (6.2), while $H_{\mathrm{c-\mathbf{F}}}$ describes the interaction of carriers with the interfacial electric field **F** that is assumed to be uniform throughout the system

$$H_{\mathrm{c-\mathbf{F}}} = \sum_{i\beta_i} e\mathbf{F}\cdot\mathbf{r}_i\, c_{i\beta_i}^\dagger c_{i\beta_i} - \sum_{i\alpha_i} e\mathbf{F}\cdot\mathbf{r}_i\, d_{i\alpha_i}^\dagger d_{i\alpha_i}. \tag{7.5}$$

In the last equation, $\mathbf{r}_i$ is the position vector of site i, while vector **F** is assumed to be perpendicular to the D/A interface and directed opposite the internal electric field of a space-separated electron–hole pair (in which the electron is in the acceptor, while the hole is in the donor).

There are, however, some important differences between the model used here and the one in Ch. 6. For example, here, we do take into account the diagonal static disorder, i.e., the on-site energies of electrons $\left(\epsilon^{\mathrm{c}}_{i\beta_i}\right)$ and holes $\left(\epsilon^{\mathrm{v}}_{i\alpha_i}\right)$ depend on site index i. The disorder is the essential element of our model, since disorder-induced localization effects enable us to isolate exciton states that are similar to states of free charges, as will be detailed in the following.

Similarly to other numerical studies, which obtain charge separation efficiency by tracking the faith of a single electron–hole pair, we confine ourselves to the single-exciton subspace, see Sec. 3.5.3. We describe charge separation in the exciton basis, whose basis vectors are stationary states of an electron–hole pair that are supported by the model interface. Here, the exciton basis includes the interaction with the internal electric field $\mathbf{F}$, i.e., it is obtained by solving the two-particle eigenvalue problem $\left(H_{\mathrm{c}} + H_{\mathrm{c}-\mathbf{F}}\right)|x\rangle = \hbar\omega_x|x\rangle$, which in the basis of single-particle states localized at lattice sites reads as

$$\begin{aligned}\sum_{\substack{i'\alpha_i'\\ j'\beta_j'}} \Big(&\delta_{ii'}\delta_{\alpha_i\alpha_i'}\epsilon^{\mathrm{c}}_{(j\beta_j)(j'\beta_j')} - \delta_{jj'}\delta_{\beta_j\beta_j'}\epsilon^{\mathrm{v}}_{(i\alpha_i)(i'\alpha_i')}\\ &- \delta_{ii'}\delta_{\alpha_i\alpha_i'}\delta_{jj'}\delta_{\beta_j\beta_j'}\left(V_{ij} - q\mathbf{F}\cdot\left(\mathbf{r}_j - \mathbf{r}_i\right)\right)\Big)\,\psi^x_{(i'\alpha_i')(j'\beta_j')}\\ &= \hbar\omega_x\,\psi^x_{(i\alpha_i)(j\beta_j)}.\end{aligned} \tag{7.6}$$

Therefore, the exciton basis states contain complete information on the effects of carrier delocalization, disorder, and the internal electric field. It is convenient to classify the exciton basis states in a manner similar to the one we employed in Chapters 5 and 6, where we differentiated between donor exciton states, acceptor exciton states, and space-separated exciton states. Here, we are interested in full charge separation, which results in almost free carriers capable of producing electric current. Therefore, we have to individuate exciton states of our model that resemble these free-carrier states. To this end, we introduce the notion of the contact region of the bilayer which consists of sites $0,\dots,l_c-1$ in the donor part and $2N-l_c,\dots,2N-1$ in the acceptor part of the bilayer. If both electron and hole are primarily located in the contact region (the electron in its acceptor part and the hole in its donor part), we consider them as fully separated carriers. More quantitatively, we say that space-separated exciton state x is a contact state (state of fully separated carriers) if

$$\sum_{i=0}^{l_c-1}\sum_{j}\sum_{\alpha_i\beta_j}|\psi^x_{(i\alpha_i)(j\beta_j)}|^2 \geq 0.7, \tag{7.7}$$

and

$$\sum_{i}\sum_{j=2N-l_c}^{2N-1}\sum_{\alpha_i\beta_j}|\psi^x_{(i\alpha_i)(j\beta_j)}|^2 \geq 0.7. \tag{7.8}$$

The space-separated states that are not contact states will be further referred to as CT states. We point out that the localization induced by disorder is crucial to identify contact states. In the perfectly ordered system, there are no space-separated states that meet the criteria of spatial localization given in Eqs. (7.7) and (7.8).

7.3.2 Theoretical Approach to Incoherent Charge Separation

This chapter aims at analyzing the incoherent charge separation, i.e., charge separation that occurs on long time scales so that coherent features are not pronounced and consequently carrier dynamics can be well described in terms of populations only. Here, we work in the basis of electron–hole pair states x and study charge separation by finding a stationary solution to an appropriate equation for populations f_x of exciton states. Similarly to Ref. [196], we assume that contact states act as absorbing states in the course of charge separation, i.e., once an exciton reaches a contact state, it is removed from the system. This removal may be interpreted as the extraction of the fully separated electron and hole at the electrodes. Instead of studying charge separation in the commonly used position space, we picture it in the space spanned by the exciton basis states as a process that starts from an initial state, proceeds through a series of phonon bath-assisted transitions between exciton states, and finishes once a contact state is reached. Therefore, we find the stationary solution to equations for populations f_x of exciton states x which do not belong to the group of contact states (further denoted as C). These equations are Pauli master equations in which the interaction with the phonon bath leads to transitions between exciton states. The time evolution of the population of exciton state $x \notin C$ is described by

$$\frac{\mathrm{d}f_x}{\mathrm{d}t} = g_x - \tau_x^{-1} f_x - \sum_{x'} w_{x'x} f_x + \sum_{x' \notin C} w_{xx'} f_{x'}, \tag{7.9}$$

where g_x is the generation rate of state x (the number of excitons generated per unit time in state x), τ_x is the lifetime of exciton state x, $w_{x'x}$ is the rate of phonon bath-induced transition from state x to state x', while the condition $x' \notin C$ on the summation in the fourth term is due to the assumption of absorbing contact states.

We are searching for the stationary solution f_x^0 to Eq. (7.9), which satisfies

$$0 = g_x - \tau_x^{-1} f_x^0 - \sum_{x'} w_{x'x} f_x^0 + \sum_{x' \notin C} w_{xx'} f_{x'}^0. \tag{7.10}$$

With the stationary populations of exciton states at hand, we can compute the separation probability

$$\varphi = \frac{\sum_{x' \in C} \sum_{x \notin C} w_{x'x} f_x^0}{\sum_{x \notin C} g_x}, \tag{7.11}$$

and the recombination probability

$$\rho = \frac{\sum_{x \notin C} \tau_x^{-1} f_x^0}{\sum_{x \notin C} g_x}. \tag{7.12}$$

Using Eq. (7.9), it can be shown that $\varphi + \rho = 1$. Different choices of g_x allow us to investigate incoherent charge separation starting from different initial states.

The phonon bath-assisted transition rates from exciton state x to exciton state x', $w_{x'x}$, can be obtained using the Fermi golden rule. Let us assume that the sets of oscillators localized on each lattice site are identical, i.e., in Eqs. (5.2) and (6.2), we assume that index λ_i, which counts local oscillators on site i, does not depend on i and can be replaced by λ.[2] In the relevant subspace of single electron–hole excitations, the carrier–phonon interaction can be rewritten as [see also Eq. (3.85)]

$$H_{\mathrm{c-p}} = \sum_{\substack{x'x \\ i\lambda}} \Gamma_{x'x}^{i\lambda} \, |x'\rangle\langle x| \left(b_{i\lambda}^\dagger + b_{i\lambda} \right), \tag{7.13}$$

---

[2] Actually, our choices of phonon modes and carrier–phonon coupling constants in Chapters 5 and 6 implicitly contain the same assumption.

where the interaction constants in the exciton basis read as [see also Eq. (6.6)]

$$\Gamma^{i\lambda}_{x'x} = \sum_{\beta_i}\sum_{j\alpha_j} g^{\mathrm{c}}_{i\beta_i\lambda}\psi^{x'*}_{(j\alpha_j)(i\beta_i)}\psi^{x}_{(j\alpha_j)(i\beta_i)} - \sum_{\alpha_i}\sum_{j\beta_j} g^{\mathrm{v}}_{i\alpha_i\lambda}\psi^{x'*}_{(i\alpha_i)(j\beta_j)}\psi^{x}_{(i\alpha_i)(j\beta_j)}. \tag{7.14}$$

Therefore, the phonon bath-assisted transition rate from state x to state x' is

$$\begin{aligned} w_{x'x} &= \frac{2\pi}{\hbar}\sum_{i\lambda}|\Gamma^{i\lambda}_{x'x}|^2\delta(\hbar\omega_{x'}-\hbar\omega_x-\hbar\omega_\lambda)\, n^{\mathrm{ph}}(\hbar\omega_\lambda) \\ &+ \frac{2\pi}{\hbar}\sum_{i\lambda}|\Gamma^{i\lambda}_{x'x}|^2\delta(\hbar\omega_{x'}-\hbar\omega_x+\hbar\omega_\lambda)\left(1+n^{\mathrm{ph}}(\hbar\omega_\lambda)\right) \end{aligned} \tag{7.15}$$

where $n^{\mathrm{ph}}(E) = (\mathrm{e}^{\beta E}-1)^{-1}$ is the Bose–Einstein occupation number at temperature $T = (k_B\beta)^{-1}$. The right-hand side of Eq. (7.15) can be simplified by further assuming that all the interaction constants $g^{\mathrm{c}}_{i\beta_i\lambda}$ and $g^{\mathrm{v}}_{i\alpha_i\lambda}$ are independent of site and band indices and are equal to g_λ. Introducing the so-called spectral density $J(E)$ by

$$J(E) = \sum_\lambda |g_\lambda|^2\delta(E-\hbar\omega_\lambda), \tag{7.16}$$

we obtain

$$w_{x'x} = \frac{2\pi}{\hbar}P_{x'x}\, J(|\hbar\omega_{x'}-\hbar\omega_x|)n(\hbar\omega_{x'}-\hbar\omega_x), \tag{7.17}$$

where

$$P_{x'x} = \sum_i \left| \sum_{\substack{j\alpha_j\\ \beta_i}} \psi^{x'*}_{(j\alpha_j)(i\beta_i)}\psi^{x}_{(j\alpha_j)(i\beta_i)} - \sum_{\substack{j\beta_j\\ \alpha_i}} \psi^{x'*}_{(i\alpha_i)(j\beta_j)}\psi^{x}_{(i\alpha_i)(j\beta_j)} \right|^2, \tag{7.18}$$

whereas

$$n(E) = \begin{cases} n^{\mathrm{ph}}(E), E > 0 \\ 1 + n^{\mathrm{ph}}(-E), E < 0 \end{cases} \tag{7.19}$$

The transition rates $w_{x'x}$ do not depend solely on the energy difference $\hbar\omega_{x'} - \hbar\omega_x$ between exciton states x' and x, but also on spatial properties (e.g., spatial localization and mutual overlap) of these states, which is described by quantity $P_{x'x}$ (the so-called spatial proximity factor). The spatial proximity factor between exciton states of the same character is in general much larger than the one between states of different characters. In other words, for the same energy difference $\hbar\omega_{x'} - \hbar\omega_x$, the transition probability $w_{x'x}$ [Eq. (7.17)] is much larger when states x' and x are of the same character than when their characters are different. The last point will be repeatedly used in further discussion.

7.3.3 Parameterization of the Model Hamiltonian

The parameterization of the model Hamiltonian is almost the same as in Ch. 6, where the values of model parameters are chosen to be appropriate to describe charge separation at the archetypal regioregular P3HT/PCBM interface in the direction perpendicular to the interface (and polymer chains). Even though the values of model parameters are selected by using the literature data for one particular D/A blend, we emphasize that our aim is to unveil fundamental physical effects responsible for very efficient charge separation at an all-organic bilayer. Therefore, many of the parameters will be varied (within reasonable limits), and the effects of these variations on charge separation yield will be rationalized. This is also of practical relevance, since the trends observed in such variations may suggest which material properties should be tuned in order to maximize the separation efficiency.

Actual computations are performed on the model system having one single-electron level per site in the donor and one single-hole level per site in both the donor and acceptor. In order to mimic the presence of higher-than-LUMO orbitals energetically close to the LUMO level, which is a situation typical of fullerenes [51, 137], we take two single-electron levels per acceptor site. While in Ch. 6 we have accounted for the higher-than-LUMO acceptor orbitals that are situated at ca. 1 eV above the LUMO level, here, motivated by the quite large energy separation between the lowest-energy PACB state and the lowest-energy donor (or CT) state, we do not consider these orbitals. The HOMO level of the ordered donor material is taken as the zero of the energy scale. The model is schematically depicted in Fig. 7.3.

Within each region of the bilayer, the on-site energies of electrons and holes are drawn from a Gaussian distribution function. For example, the probability density that the energy of the

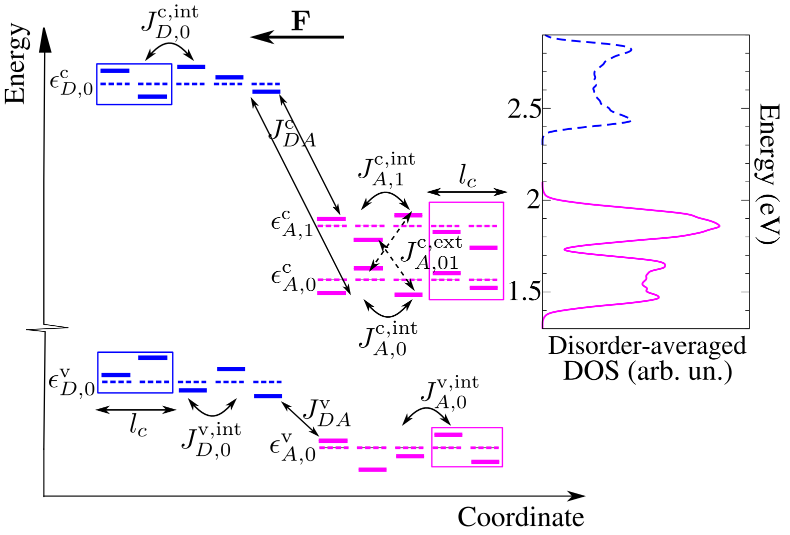
Energy
$J^{\mathrm{c,int}}_{D,0}$
F
$\epsilon^{\mathrm{c}}_{D,0}$
J^{c}_{DA}
$J^{\mathrm{c,int}}_{A,1}$
l_c
$\epsilon^{\mathrm{c}}_{A,1}$
$J^{\mathrm{c,ext}}_{A,01}$
$\epsilon^{\mathrm{c}}_{A,0}$
$J^{\mathrm{c,int}}_{A,0}$
$\epsilon^{\mathrm{v}}_{D,0}$
l_c
$J^{\mathrm{v,int}}_{D,0}$
J^{v}_{DA}
$\epsilon^{\mathrm{v}}_{A,0}$
$J^{\mathrm{v,int}}_{A,0}$
Coordinate
2.5
2
1.5
Energy (eV)
Disorder-averaged
DOS (arb. un.)

FIGURE 7.3: Schematic view of the model system indicating different transfer integrals and average on-site energies listed in Table 7.1. The dashed lines represent average on-site energies, while solid lines represent actual on-site energies, which vary from site to site due to the diagonal static disorder. The contact region of the bilayer is denoted by rectangles. **F** is the vector of the interfacial electric field. The plot on the right presents the single-particle DOS for electrons in the isolated acceptor (full line) and donor (dashed line) regions of the bilayer averaged over different disorder realizations, compare to the similar plot in Fig. 6.1. For each disorder realization, the electronic states of the isolated regions are obtained by diagonalizing the free-electron Hamiltonian [the first term on the right-hand side of Eq. (6.1)] in which the D/A coupling J^{c}_{DA} is set to 0. The DOS for that disorder realization is computed by broadening each of the single-electron states obtained by a Gaussian whose standard deviation is equal to 10 meV.

electron on donor site i ($0 \leq i \leq N-1$) is in the vicinity of $\epsilon^{\mathrm{c}}_{i,0}$ can be expressed as

$$f(\epsilon^{\mathrm{c}}_{i,0}) = \frac{1}{\sigma\sqrt{2\pi}} \exp\left(-\frac{(\epsilon^{\mathrm{c}}_{i,0} - \epsilon^{\mathrm{c}}_{D,0})^2}{2\sigma^2}\right) \tag{7.20}$$

where $\epsilon^{\mathrm{c}}_{D,0}$ is the average electron on-site energy in the donor, and σ is the standard deviation of the Gaussian distribution. We assume that the deviations of on-site energies from their average values are uncorrelated; this assumption regards both on-site energies of electrons (holes) on different sites and on-site energies of electrons and holes on the same site. The disorder strength is determined by parameter σ, which typically assumes values of the order of 100 meV [198]. In order to obtain analytical insights into charge separation efficiency, we opt for a lower value of $\sigma = 50$ meV, which does lead to localization effects, but does not completely destroy charge delocalization. Moreover, the disorder-averaged values of relevant quantities, such as exciton binding energies, LUMO–LUMO, and HOMO–HOMO offsets, assume values that are quite close (within few tens of meV) to the respective values in the ordered system, which will thus often be used in the discussion.

While the choice of the values of model parameters has been elaborated in Ch. 6, here, for completeness, we summarize these values in Table 7.1, and we only discuss in greater detail the values that are different from those used in the previous chapter or do not appear therein.

The number N of lattice sites in the donor and acceptor is selected so that the length of the model bilayer, $2Na$, is similar to the linear dimensions of the polymer/fullerene bilayers used in experiments [66, 192, 195]. According to our discussion in Sec. 7.3.1, our definition of contact states as analogues of free-charge states within our model contains two main ingredients: the linear dimension of the contact region l_c (in units of lattice spacing), and the threshold probability of the localization of the electron and hole in the contact region that permits us to identify contact states. The linear dimension of the contact region l_c is chosen so that the reasonable variations in l_c, as well as in the aforementioned threshold probability, do not affect qualitatively the numerical results to be presented, which has been explicitly checked in the Supporting Information associated to Ref. [182].

TABLE 7.1: Values of Model Parameters Used in Computations.

Parameter	Value
N	30
l_c	11
a (nm)	1.0
U (eV)	0.65
ε_r	3.0
$\epsilon^{\mathrm{c}}_{D,0}$ (eV)	2.63
$J^{\mathrm{c,int}}_{D,0}$ (eV)	0.1
$\epsilon^{\mathrm{v}}_{D,0}$ (eV)	-0.3
$J^{\mathrm{v,int}}_{D,0}$ (eV)	-0.15
$\epsilon^{\mathrm{c}}_{A,0}$ (eV)	1.565
$\epsilon^{\mathrm{c}}_{A,1}$ (eV)	1.865
$J^{\mathrm{c,int}}_{A,0}$ (eV)	0.05
$J^{\mathrm{c,int}}_{A,1}$ (eV)	0.025
$J^{\mathrm{c,ext}}_{A,01}$ (eV)	0.02
$\epsilon^{\mathrm{v}}_{A,0}$ (eV)	-1.03
$J^{\mathrm{v,int}}_{A,0}$ (eV)	-0.15
J^{c}_{DA} (eV)	0.1
J^{v}_{DA} (eV)	-0.1
σ (meV)	50
η	1.5
E_c (meV)	10
τ_0 (ps)	250
$A_{\mathrm{A/D}}$	0.5
T (K)	300

For the spectral density of the phonon bath, we take the Ohmic spectral density [199]

$$J(E) = \eta E \mathrm{e}^{-E/E_c}, \tag{7.21}$$

which is characterized by two parameters: the dimensionless parameter η describes the strength of the system–bath coupling, while E_c is the energy cutoff determining the energy range of phonon modes that are strongly coupled to the system. For the Holstein-like system–bath coupling and in the limiting case of a charge carrier localized on a single lattice site, the polaron binding energy is given by $\epsilon_{\mathrm{b}}^{\mathrm{pol}} = \sum_\lambda |g_\lambda|^2/(\hbar\omega_\lambda)$ [18]. In terms of spectral density $J(E)$, and specifically for the Ohmic spectral density, the polaron binding energy can be expressed as

$$\epsilon_{\mathrm{b}}^{\mathrm{pol}} = \int_0^{+\infty} \mathrm{d}E \, \frac{J(E)}{E} = \eta E_c. \tag{7.22}$$

It is equal to the geometry relaxation energy Λ_{rel} upon charging a molecule and to one half of the reorganization energy Λ_{reorg} [18]. In Ref. [51], the relaxation energy of the $\mathrm{PC_{60}BM}$ anion was estimated to be $\Lambda_{\mathrm{rel}} = 15$ meV. The authors of Ref. [200] found that the polaron binding energy in a long straight polythiophene chain is of the order of 10 meV. We use these estimates and take the polaron binding energy $\epsilon_{\mathrm{b}}^{\mathrm{pol}} = 15$ meV (the reorganization energy is then $\Lambda_{\mathrm{reorg}} = 30$ meV). We assume that the system–bath coupling is strongest for the low-frequency phonon modes and therefore take that $E_c = 10$ meV and $\eta = 1.5$.

There are different kinds of recombination processes that limit the efficiency of OSCs [201]. The recombination of an electron–hole pair that originates from the absorption of a single photon is geminate recombination. On the other hand, an electron and a hole undergoing a nongeminate recombination event do not originate from the same photon. Here, we consider only geminate recombination, which at a D/A interface may occur as (a) the recombination of excitons photogenerated in a neat donor or acceptor material, or (b) the recombination of excitons in CT states. The recombination can be further classified as radiative or nonradiative. In neat polymers, recombination predominantly occurs via nonradiative processes [127]. In D/A blends, the major part of charges recombine nonradiatively either at the interface or in the donor material [202].

However, there is no simple model that describes the rate of nonradiative recombination in terms of microscopic material properties. It is intuitively clear that the smaller is the overlap between the electron and hole probability densities, the smaller is the rate of their recombination and the longer is the lifetime of the pair. In previous model studies of charge separation at D/A interfaces, the last point has been recognized as the steep dependence of the exciton lifetime on the electron–hole separation [203], so that the recombination is assumed to occur exclusively from the strongly bound CT state [195, 196, 203], or a formula describing the aforementioned distance dependence is proposed [68]. Here, to each exciton state x, be it a state in the neat material or a CT state, we assign the lifetime τ_x that is inversely proportional to the weighted overlap of the electron and hole wave function moduli

$$\tau_x = \tau_0 \left(\sum_{i=0}^{N-1} |\phi_i^{x,\mathrm{e}}| \left|\phi_i^{x,\mathrm{h}}\right| + A_{\mathrm{A/D}} \sum_{i=N}^{2N-1} |\phi_i^{x,\mathrm{e}}| \left|\phi_i^{x,\mathrm{h}}\right| \right)^{-1} . \tag{7.23}$$

In the last expression, the moduli of the wave function of the electron and hole in exciton state x are defined as

$$|\phi_i^{x,\mathrm{e}}| = \sqrt{\sum_{\beta_i} \sum_{j\alpha_j} \left| \psi^x_{(j\alpha_j)(i\beta_i)} \right|^2}, \tag{7.24}$$

$$\left|\phi_i^{x,\mathrm{h}}\right| = \sqrt{\sum_{\alpha_i} \sum_{j\beta_j} \left| \psi^x_{(i\alpha_i)(j\beta_j)} \right|^2}, \tag{7.25}$$

while τ_0 and $A_{\mathrm{A/D}}$ are constants which are determined so that the lifetimes of the lowest CT, XD, and XA states in the ordered system agree with the values reported in the literature. The expression for the lifetime given in Eq. (7.23) captures the fact that larger electron–hole overlap favors faster recombination of the pair. Singlet exciton lifetimes in a variety of conjugated polymers used in organic solar cells are of the order of hundreds of picoseconds [127]. Time-resolved photoluminescence measurements yield the singlet exciton lifetime in neat P3HT around 470 ps and in neat PCBM around 740 ps [204]. From the transient absorption measurements performed in blends of P3HT and different fullerenes, the lifetime of the CT state was determined to be around 3 ns [205]. For the values of model parameters listed in Table 7.1, the lifetime of the lowest CT state in the ordered system is $\tau_{\mathrm{CT}}^{\mathrm{ord}} \sim 2.5$ ns, the lifetime of the lowest XD state

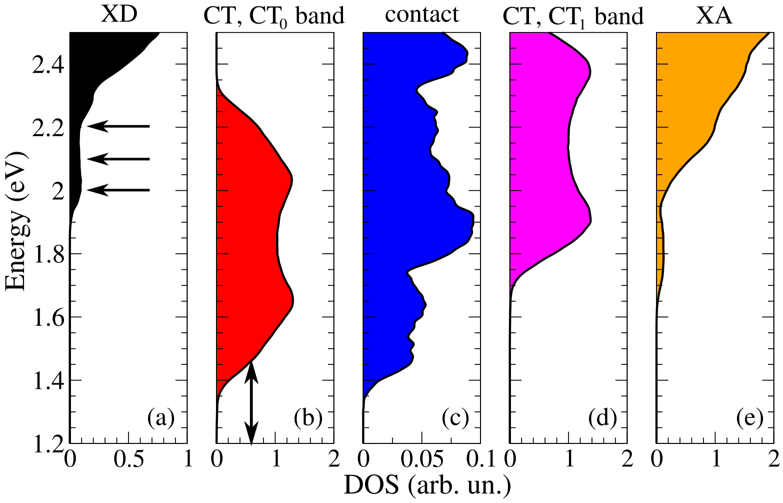

FIGURE 7.4: Disorder-averaged exciton DOS (in arbitrary units and at $F = 0$) for (a) donor exciton states, (b) CT states belonging to CT_0 band, (c) contact states, (d) CT states belonging to CT_1 band, and (e) acceptor exciton states. The horizontal arrows in (a) indicate approximate energies of XD states serving as initial states of charge separation. The vertical double-sided arrow in (b) indicates the energy range of the CT states acting as initial states of charge separation. The DOS in a single disorder realization is obtained by broadening each exciton level by a Gaussian whose standard deviation is equal to 10 meV.

in the ordered system is $\tau_{\mathrm{XD}}^{\mathrm{ord}} \sim 400$ ps, and the lifetime of the lowest XA state in the ordered system is $\tau_{\mathrm{XA}}^{\mathrm{ord}} \sim 800$ ps.

7.4 Numerical Results

In this section, we present the results concerning the yield of charge separation starting from CT and donor states. In all the computations, we average over different disorder realizations and all the results to be presented are averaged over 256 disorder realizations. In the Supporting Information associated to Ref. [182], we have checked that averaging over 200–300 disorder realizations is enough to provide us with convergent results for the separation efficiency. In order to facilitate the discussion, in Figs. 7.4(a)–(e) we present disorder-averaged DOS for different groups of exciton states. Similarly as in Ch. 6, we discriminate between CT states belonging to CT_0 and CT_1 bands. We say that a CT state belongs to the CT_0 (CT_1) band if its electron primarily belongs to the electronic band in the acceptor part of the bilayer arising from the single-electron level of average energy $\epsilon_{A,0}^{\mathrm{c}}$ ($\epsilon_{A,1}^{\mathrm{c}}$), see also the discussion following Eq. (6.9).

The numerical effort in the computations in previous chapters was concentrated on the propagation of the active density matrices in time, while obtaining exciton basis states and their energies was not numerically demanding. Here, however, solving the exciton eigenvalue problem embodied in Eq. (7.6) is much more time-consuming than finding the stationary solution to the system of rate equations given in Eq. (7.9). The system schematically depicted in Fig. 7.3 supports $3N \times 2N = 6N^2$ exciton states in total, which for $N = 30$ gives 5400 exciton states. In other words, the matrix whose eigenvalue problem has to be solved contains $5400 \times 5400 \approx 3 \times 10^7$ entries. Bearing in mind the tight-binding nature of the Hamiltonian employed, most of these entries are equal to zero. However, we *a priori* need all the eigenvalues and all the corresponding eigenvectors. Once we know the exciton spectrum and the generation rate g_x, which determines the initial condition of charge separation, we can find the stationary solution to the system of rate equations using only a portion of the exciton states obtained. Similarly to Sec. 4.3, the size of this portion is determined by the energies of exciton states from which the separation initiates and the thermal energy $k_B T$. Typically, when studying the separation of the strongly bound CT exciton, we formulate rate equations for approximately 1,000 lowest-energy exciton states. On the other hand, when studying the separation of donor excitons, the number of exciton states ultimately considered, depending on the energy of the initial state, varies between 2,000 and 4,000. Computing the stationary solution to the system of rate equations, therefore, requires inversion of a matrix that typically comprises of the order of 10^6 entries for the separation of the strongly bound CT state and of the order of 10^7 entries for the separation of donor excitons, which is not particularly numerically demanding. The HPC resource is not used to facilitate diagonalization or inversion of a matrix. Both of these operations are done on single processors using the appropriate LAPACK routines, while the HPC resource is used to simultaneously perform computations for a number of disorder realizations. For one disorder realization and one value of the internal electric field, the computation of the separation yield lasts for approximately 30 minutes.

7.4.1 Charge Separation from the Strongly Bound CT State

As starting states for the charge separation process, here we consider CT states belonging to the CT_0 band. One particular CT state out of all the states in the CT_0 band is chosen by requiring that the mean electron–hole separation defined in Eq. (6.7) be minimal. We will further refer to such a state as the strongly bound CT state. The strongly bound CT state is located on the lower edge of the disorder-averaged DOS of CT excitons belonging to the CT_0 band, see the vertical double-sided arrow in Fig. 7.4(b). We set the generation rate g_x appearing in Eq. (7.9) to be different from zero only for the strongly bound CT state.

The field-dependent separation yield from this state is presented by circles in Fig. 7.5(a). The separation yield is above 0.6 for all the examined values of the electric field down to $F = 0$. Figure 7.5(b) presents the low-energy tail of the DOS of contact states [see Fig. 7.4(c)] along with the distribution of energies of the lowest-energy contact state. Figure 7.5(c) shows the low-energy tail of the DOS of CT states [see Fig. 7.4(c)] together with the distribution of energies of the initial strongly bound CT state. The disorder-averaged energy difference between the lowest-energy contact state and the initial CT state may serve as an estimate of the average energy barrier that an electron–hole pair in the initial CT state has to surmount in order to reach the nearest free-charge state. We obtain the average barrier of approximately 0.13 eV ($\approx 5\ k_BT$ at room temperature), which is lower (at least by a factor of 2) than usually assumed when considering separation of the strongly bound CT exciton [34]. Further discussion reveals that the actual barrier to be overcome is smaller than the energy difference between the lowest-energy contact state and the initial CT state. Namely, the intermediate CT states, lying between the initial CT state and the lowest-energy contact state and exhibiting larger electron–hole distances compared to the initial CT state, are crucial to the successful separation of the initial strongly bound pairs. Stronger electric field is beneficial to exciton separation which, combined with the fact that the separation yield is above 0.5 even at $F = 0$, implies that it exhibits relatively weak dependence on the magnitude of the electric field.

It is instructive to analyze the results presented in Fig. 7.5(a) from the viewpoint of single disorder realizations. In Figs. 7.6(a)–(d) we present distributions of the separation yield in single

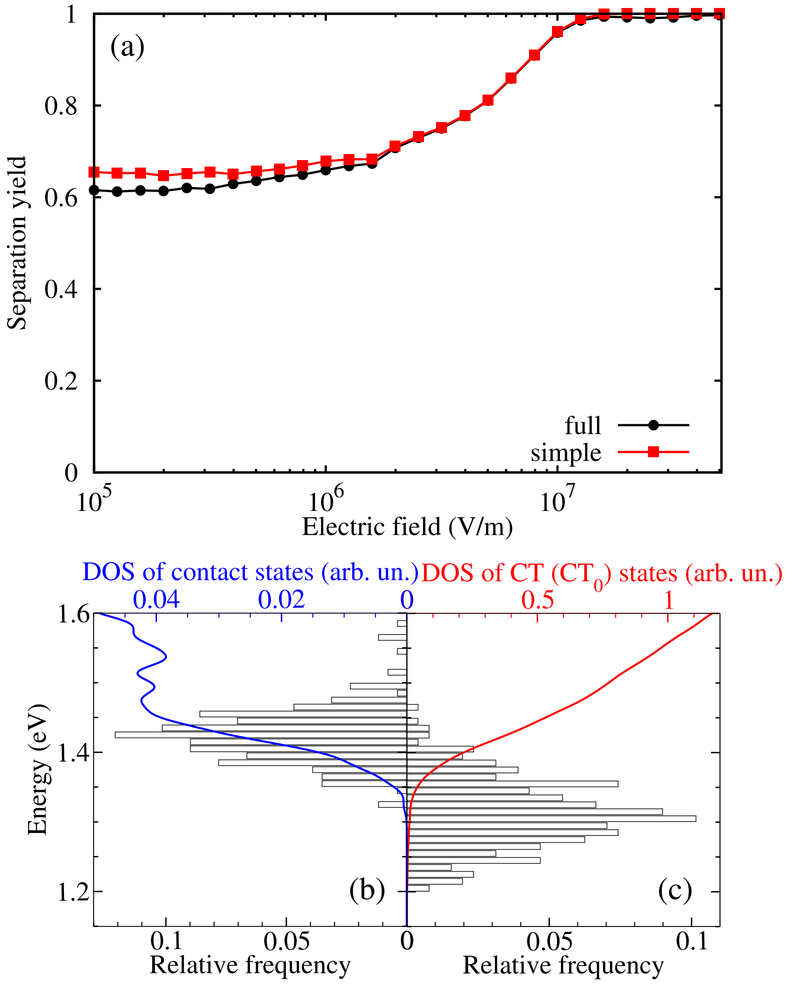

FIGURE 7.5: (a) Field-dependent yield of charge separation from the strongly bound CT state. The data labeled by "full" are obtained by numerically solving Eq. (7.9), while the data labeled by "simple" are computed using Eq. (7.32). The low-energy edges of the disorder-averaged DOS (full lines) for (b) contact states and (c) CT states belonging to the CT_0 band. The bars depict histograms of the distribution of the energy of (b) the lowest-energy contact state and (c) the initial strongly bound CT state. The width of the bins on the energy axis is 10 meV, while $F = 0$.

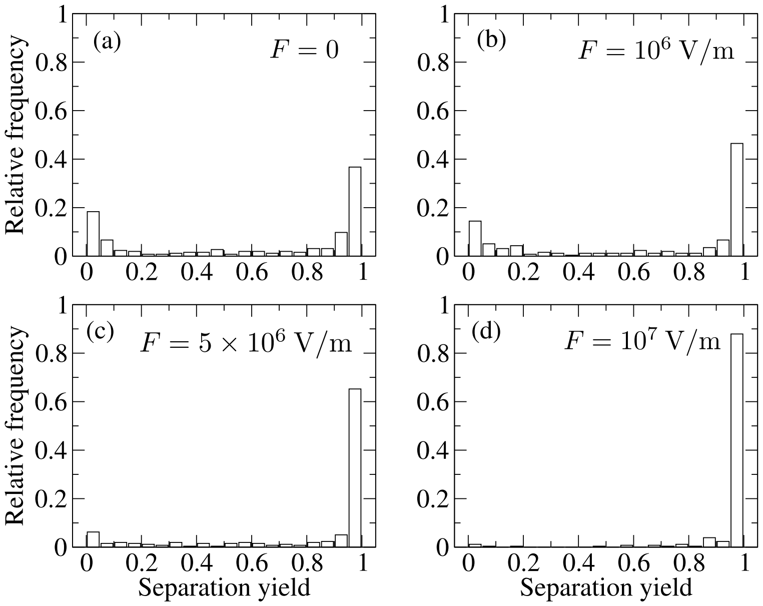

FIGURE 7.6: Histograms showing the distribution of the yield of charge separation from the strongly bound CT state for different strengths of the electric field: (a) $F = 0$, (b) $F = 10^6$ V/m, (c) $F = 5 \times 10^6$ V/m, and (d) $F = 10^7$ V/m. The width of the bins for the separation yield is 0.05.

disorder realizations at different strengths of the electric field. A distinctive feature of all the histograms is quite small number of disorder realizations for which the separation yield assumes values in an intermediate range (say between 0.2 and 0.8). Even at zero electric field, the number of disorder realizations in which the separation yield is high (above 0.8) is greater than the number of those in which the separation yield is low (below 0.2), which can account for the mean separation yield above 0.5 even at zero field. As the electric field is increased, the number of disorder realizations in which the separation yield is low or intermediate decreases, while the number of disorder realizations in which the separation yield is high increases, see Figs. 7.6(b)–(d). At $F = 10^7$ V/m, the separation yield is between 0.95 and 1 for somewhat less than 90% of disorder realizations, see Fig. 7.6(d), meaning that the mean yield is close to 1. Relevant to this discussion are also the relative positions of the lower-energy tails of the DOS of CT states belonging to the CT_0 band and the DOS of contact states, which are presented in the Supporting Information associated to Ref. [182]. There, we observe that the effect of increasing F on the DOS tails consists of decreasing the energy difference between the edges of CT and contact DOS. For sufficiently strong field, the lowest contact state is situated energetically below the strongly bound CT state.

We now establish which factors primarily determine the separation yield and propose an analytical formula that is capable of reproducing the separation yield in single disorder realizations (and consequently the mean separation yield) quite well. Let us begin by noticing that the initial CT state is usually strongly coupled (by means of phonon bath-assisted transitions) to only a couple of exciton states which are of CT character and whose electron–hole separation (and consequently the lifetime) is larger than in the initial CT state. We further refer to these states as intermediate states. Moreover, intermediate states are in general very well coupled to other space-separated states, meaning that, in principle, there is no kinetic obstacle for an exciton in the intermediate state to undergo a series of phonon bath-assisted transitions in which the electron–hole separation gradually increases, and finally reach a contact state. However, since the coupling among the initial state and intermediate states is appreciable, the "implosion" of the pair, i.e., the back-transfer from intermediate states to the initial CT state followed by the recombination event, should not be omitted from the analysis. The recombination from intermediate states, as well as from all the subsequent states paving the way toward contact states, is not probable, since the lifetimes of all these states are quite long compared to the inverse transition rates among them. In other words, the recombination occurs almost exclusively from the initial CT state. We may therefore assume that the only rate-limiting step during charge separation is the escape from the initial strongly bound CT state x_{init}. The separation yield is then determined by the competition between the recombination rate in the initial CT state, the escape rate from the initial CT state toward intermediate states, and the back-transfer rate from intermediate states to the initial CT state. This competition may be described using a simple kinetic model whose variables are populations of the initial CT state and intermediate states (which are considered as a single state). Recombination is possible only from the initial CT state, while contact states may be reached from intermediate states. The stationarity of the initial CT state population f^0_{init} demands that

$$g_{\text{init}} = \left(\tau^{-1}_{\text{init}} + w_{\text{inter,init}}\right) f^0_{\text{init}} - w_{\text{init,inter}}\, f^0_{\text{inter}}, \tag{7.26}$$

while a similar condition for the stationary population f^0_{inter} of intermediate states reads as

$$\left(w_{\mathrm{init,inter}} + w_{\mathrm{contact,inter}}\right) f^0_{\mathrm{inter}} = w_{\mathrm{inter,init}}\, f^0_{\mathrm{init}}. \tag{7.27}$$

In Eqs. (7.26) and (7.27), g_{init} is the generation rate of the initial CT state, τ_{init} is its lifetime, $w_{\mathrm{inter,init}}$ is the total escape rate from the initial CT state x_{init} toward intermediate states x_{inter}

$$w_{\mathrm{inter,init}} = \sum_{x_{\mathrm{inter}}} w_{x_{\mathrm{inter}} x_{\mathrm{init}}}, \tag{7.28}$$

and $w_{\mathrm{init,inter}}$ is the total back-transfer rate to the initial CT state from intermediate states

$$w_{\mathrm{init,inter}} = \sum_{x_{\mathrm{inter}}} w_{x_{\mathrm{init}} x_{\mathrm{inter}}}. \tag{7.29}$$

The total escape rate from all the intermediate states toward contact states is

$$w_{\mathrm{contact,inter}} = \sum_{x_{\mathrm{inter}}} \sum_{x_{\mathrm{f}}}{}' w_{x_{\mathrm{f}} x_{\mathrm{inter}}} \tag{7.30}$$

where, for each intermediate state x_{inter}, the summation over final states x_{f} is carried out only over the states from which further transitions toward contact states are possible (it should not include the transitions back to the initial CT state). An adaptation of Eq. (7.11) to the problem at hand gives the following expression for the separation yield

$$\varphi = \frac{w_{\mathrm{contact,inter}}\, f^0_{\mathrm{inter}}}{g_{\mathrm{init}}}. \tag{7.31}$$

Combining Eqs. (7.26), (7.27), and (7.31), we obtain the following expression for the separation yield

$$\varphi = \frac{1}{1 + \left(\tau_{\mathrm{init}} w_{\mathrm{inter,init}}\right)^{-1} \left(1 + \frac{w_{\mathrm{init,inter}}}{w_{\mathrm{contact,inter}}}\right)}. \tag{7.32}$$

We point out that all four quantities (τ_{init} ,$w_{\mathrm{inter,init}}$, $w_{\mathrm{init,inter}}$, and $w_{\mathrm{contact,inter}}$) entering Eq. (7.32) are characteristic of each disorder realization, i.e., Eq. (7.32) contains no free parameters. It is

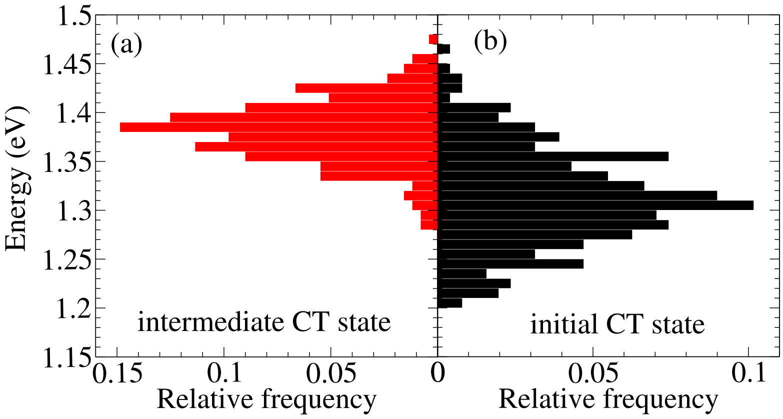

FIGURE 7.7: Histograms showing distributions of energies of (a) the intermediate CT state (which is most strongly coupled to the initial CT state), and (b) the initial CT state. The histograms are computed for $F = 0$.

then remarkable that it reproduces quite well the field-dependent separation yield for each disorder realization, and consequently the disorder-averaged separation yield, which is presented by squares in Fig. 7.5(a).

The preceding discussion suggests that the barrier the initial CT exciton has to surmount in order to reach a contact state is determined by the energy difference $\hbar\omega_{\mathrm{inter}} - \hbar\omega_{\mathrm{init}}$ between the initial CT state and the intermediate CT state exhibiting strongest coupling to the initial state. In Figs. 7.7(a) and (b) we present distributions of energies of the intermediate [Fig. 7.7(a)] and the initial [Fig. 7.7(b)] CT state at $F = 0$. We estimate that the average energy difference $\langle\hbar\omega_{\mathrm{inter}} - \hbar\omega_{\mathrm{init}}\rangle$ is around 0.07 eV, which is smaller than the average energy difference between the lowest contact state and the initial CT state. Therefore, already at $F = 0$, the average energy barrier opposing the separation from the initial CT state is $\approx 3\ k_BT$ at room temperature. For stronger F, the height of the barrier decreases, and the barrier is almost eliminated at $F \gtrsim 10^7$ V/m, when $\langle\hbar\omega_{\mathrm{inter}} - \hbar\omega_{\mathrm{init}}\rangle \lesssim 10$ meV.

Equation (7.32) gives the separation yield which is always an upper bound to the true separation yield obtained by numerically solving rate equations embodied in Eq. (7.9). Deriving Eq. (7.32), we assume that there is only one rate-limiting step in the process of charge separation from the initial CT state (namely, the escape from the initial CT state to intermediate states), while further transitions from intermediate states toward contact states occur with certainty. However, in reality, some of these further transitions may present another obstacle to full charge separation and, in order to fully reproduce the numerical data, Eq. (7.32) should be corrected so as to take other rate-limiting steps into account (it turns out that such corrections are really important only for strong enough disorder, *vide infra*). We can elaborate more on the last point by noticing that Eq. (7.32) is actually a version of the Rubel's formula [196] that describes the separation of an exciton initially in state 1 through a series of incoherent hops $1 \rightleftharpoons 2 \rightleftharpoons \cdots \rightleftharpoons n \rightharpoonup n+1$ among localized states which terminates when free-charge state $n+1$ is reached

$$\varphi_{\mathrm{Rubel}} = \frac{1}{1 + (\tau_1 w_{21})^{-1}\left(1 + \sum_{i=2}^{n} \prod_{j=2}^{i} \frac{w_{j-1,j}}{w_{j+1,j}}\right)}. \tag{7.33}$$

One of the main assumptions behind the Rubel's formula is that the recombination event is possible only from the initial CT state 1, its rate being τ_1^{-1}. This assumption is satisfied in our computations, as we obtain that the major part of recombination events occurs from the initial CT state, so that we may identify τ_{init} in Eq. (7.32) with τ_1 in Eq. (7.33). The first rate-limiting step is the escape from the initial CT state to more separated (and thus longer-lived) intermediate states, which justifies the identification of $w_{\mathrm{inter,init}}$ in Eq. (7.32) with w_{21} in Eq. (7.33). Further rate-limiting steps are taken into account in Eq. (7.33) by the term $\sum_{i=2}^{n} \prod_{j=2}^{i} \frac{w_{j-1,j}}{w_{j+1,j}}$ that takes care of the fact that, at each step j that has to be completed in order to reach state i, there is a competition between the escape rate $w_{j+1,j}$ toward the free-charge state $n+1$ and the back-transfer rate $w_{j-1,j}$ toward the initial state 1. Rubel et al. have assumed that the pathway from the initial to the final state is such that hops are possible only between neighboring states in the sequence $1 \rightleftharpoons 2 \rightleftharpoons \cdots \rightleftharpoons n \rightharpoonup n+1$, while in our model hops are in principle possible among any two exciton states. Thus, in our model it is difficult to isolate particular separation paths and ensure that they do not interfere among themselves. Nevertheless, as evidenced by quite good agreement between the results presented by circles and squares in Fig. 7.5(a), taking into account only the first rate-limiting step is a reasonable approximation to the full numerical data. This approximation is, however, plausible only for not too strong disorder. For stronger disorder, disorder-induced localization effects become more pronounced and, on its way toward contact states, an exciton may reach a state exhibiting strong localization. Owing to its strong localization, this state is poorly coupled to other states, meaning that it may act as another recombination center, or it may "reflect" excitons toward the initial state, i.e., it acts a trap state for charge separation. Neither of these two possibilities is captured by Eq. (7.32); therefore, it cannot accurately reproduce the separation yield for stronger disorder, as we discuss more thoroughly in the next paragraph.

We continue our discussion on the effects of disorder by investigating the separation yield for different disorder strengths σ at zero electric field. Along with the data emerging from numerically solving Eq. (7.9), in Fig. 7.8(a) we present the data obtained by means of Eq. (7.32). We observe that the dependence of φ on σ is not monotonic. Namely, for very low values of σ (typically $\sigma < 20$ meV in our one-dimensional model), contact states are generally absent from the spectrum (the disorder is so weak that disorder-induced localization effects are not pronounced), and consequently the separation yield within our model is exactly equal to zero in the majority of disorder realizations. This is different from predictions of other models describing incoherent charge separation [196, 197], according to which the separation yield is different from zero for all the values of disorder strength down to $\sigma = 0$. Therefore, the predictions of our model are not reliable for too low disorder. Bearing in mind that typical disorder strength in organic semiconductors is considered to be of the order of 100 meV [198], the aforementioned feature of our model does not compromise its relevance. For stronger disorder (typically $\sigma > 20$ meV), contact states start to appear in the spectrum and their number grows with increasing σ. At the same time, the average energy difference $\langle \hbar\omega_{\text{inter}} - \hbar\omega_{\text{init}} \rangle$ between the intermediate state and the initial CT state decreases, see Fig. 7.8(b), and the escape rate $w_{\text{inter,init}}$ from the initial CT state to intermediate states increases [see Eq. (7.17)]. Since the disorder is still not too strong, further separation from intermediate states is much more probable than the “implosion” of the pair, meaning that typically $w_{\text{init,inter}}/w_{\text{contact,inter}} \ll 1$. The last statement, combined with the fact that τ_{init} essentially does not depend on σ, gives that the separation yield determined by Eq. (7.32) increases with increasing σ. However, there exists an optimal disorder strength σ_{opt} for which the separation yield attains a maximum value, so that for $\sigma > \sigma_{\text{opt}}$ an increase in the disorder strength leads to a decreased separation yield. In our numerical computations, σ_{opt} is around 60 meV, in good agreement with results of Ref. [197], which also point towards the existence of the optimal disorder strength. Although for strong disorder the number of contact states is large, the pronounced disorder-induced localization starts to impede phonon-assisted

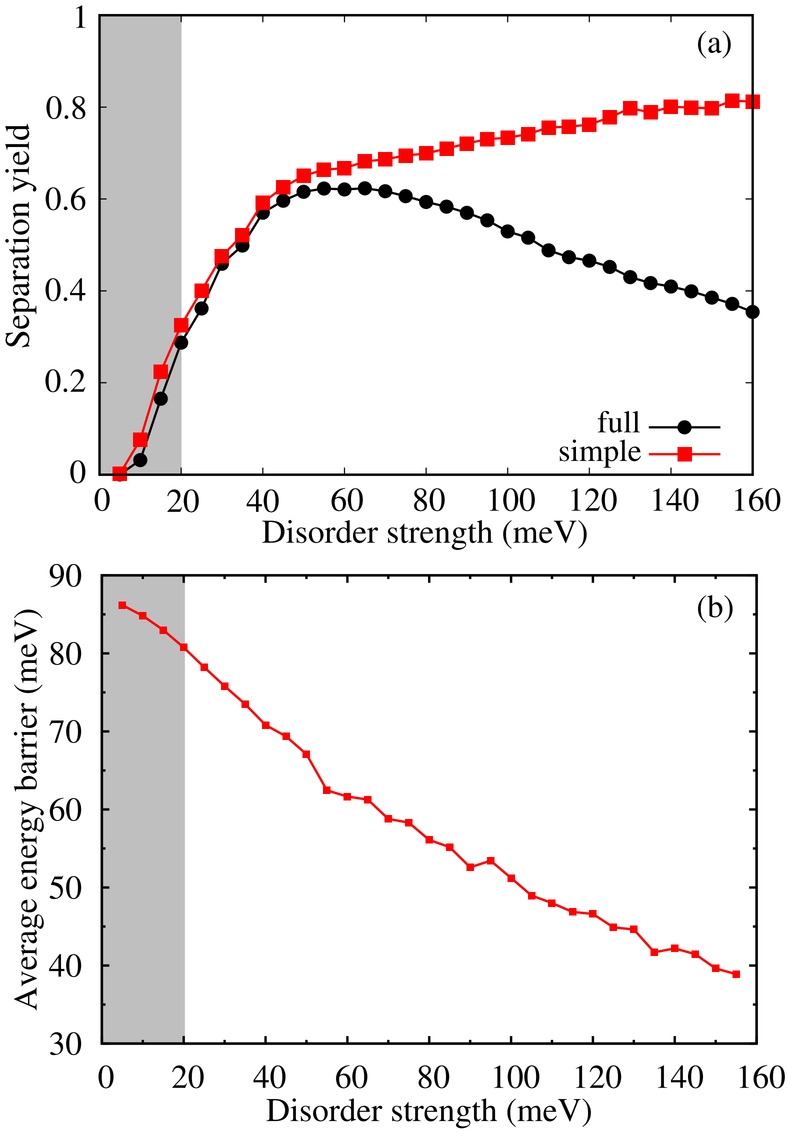

FIGURE 7.8: (a) Yield of charge separation from the strongly bound CT state at $F = 0$ for different strengths σ of the diagonal static disorder. The gray area indicates the range of disorder strength in which the predictions of our model are not reliable. The data labeled by ”full“ are obtained by numerically solving rate equations [Eq. (7.9)], while the data labeled by ”simple“ are computed using Eq. (7.32). (b) Average energy barrier $\langle \hbar\omega_{\text{inter}} - \hbar\omega_{\text{init}} \rangle$ between the initial and intermediate CT state as a function of the disorder strength.

transitions among exciton states. The number of trap states for charge separation (cf. previous paragraph) increases, meaning that there is more than just a single rate-limiting step during the separation of the initial electron–hole pair. This leads to an increased probability of the "implosion" of the pair into the initial CT state or the pair recombination directly from trap states. Therefore, the separation yield is decreased. As can be inferred from Fig. 7.8(a), the yield computed using Eq. (7.32) (circles) is again an upper bound to the separation yield obtained by numerically solving rate equations [Eq. (7.9), squares] and approximates it quite well only for $\sigma \lesssim \sigma_{\mathrm{opt}}$, while for $\sigma > \sigma_{\mathrm{opt}}$ the two separation yields exhibit opposite trends with increasing disorder strength. While the true separation yield decreases for $\sigma > \sigma_{\mathrm{opt}}$, the yield given by Eq. (7.32) monotonically increases in the entire examined range of disorder strength, consistent with the fact that $\langle \hbar\omega_{\mathrm{inter}} - \hbar\omega_{\mathrm{init}} \rangle$ monotonically decreases with increasing σ. Namely, Eq. (7.32) does not capture further rate limiting steps in the course of charge separation, and the highly successful escape from the initial CT state to intermediate states does not guarantee full charge separation.

The apparent simplicity of our model enables us to systematically study the effects of variations of different model parameters on the efficiency of charge separation starting from the strongly bound CT state. Let us first examine how the variations in the electron delocalization in the acceptor (mimicked by variations in the transfer integral $J_{A,0}^{\mathrm{c,int}}$) and in the hole delocalization in the donor (mimicked by variations in the transfer integral $J_{D,0}^{\mathrm{v,int}}$) affect the separation yield. We obtain that better delocalization of carriers promotes higher separation yields, see Figs. 7.9(a) and (b). This can be rationalized using Eq. (7.32), which determines the separation yield as a function of only a couple of parameters, and following the variation of these parameters with varying carrier delocalization. When the separation yield is high [greater than 0.8 already at zero field and for the lowest investigated values of $J_{A,0}^{\mathrm{c,int}}$ and $J_{D,0}^{\mathrm{v,int}}$, cf. the discussion of Figs. 7.6(a)–(d)], reasonable variations in $J_{A,0}^{\mathrm{c,int}}$ and $J_{D,0}^{\mathrm{v,int}}$ do not dramatically influence the separation yield, which remains high. When the separation yield is low or intermediate (less than 0.8 at zero field and for the lowest investigated values of $J_{A,0}^{\mathrm{c,int}}$ and $J_{D,0}^{\mathrm{v,int}}$), it exhibits a pronounced increase with increasing transfer integrals $J_{A,0}^{\mathrm{c,init}}$ and $J_{D,0}^{\mathrm{v,init}}$. Namely, better carrier delocalization leads to an increase in the escape rate $w_{\mathrm{inter,init}}$ from the initial CT state which,

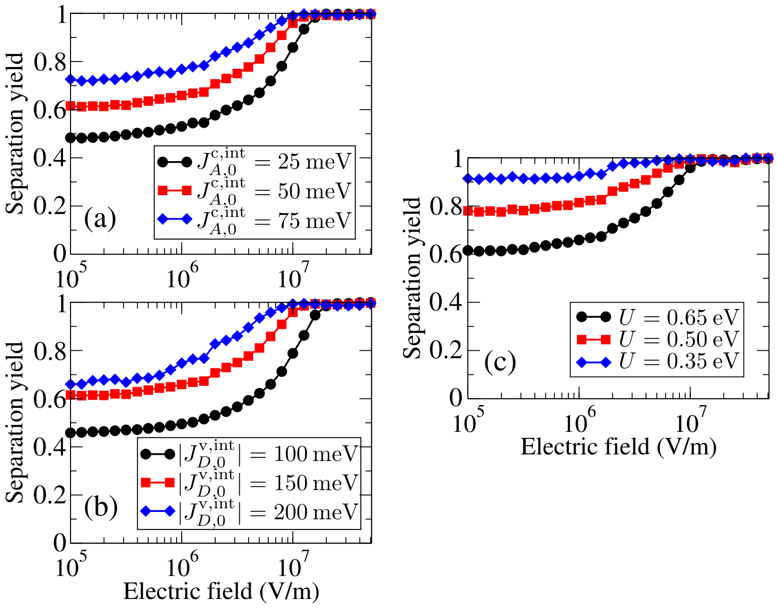

FIGURE 7.9: Field-dependent separation yield from the strongly bound CT state for different values of (a) the electron transfer integral $J_{A,0}^{\mathrm{c,int}}$ in the acceptor, (b) the hole transfer integral $J_{D,0}^{\mathrm{v,int}}$ in the donor, and (c) the on-site Coulomb interaction U.

along with the fact that τ_{init} remains largely unaffected by variations in $J_{A,0}^{\mathrm{c,init}}$ and $J_{D,0}^{\mathrm{v,init}}$, means that the separation yield determined by Eq. (7.32) is higher.

Next, we comment on the variations that the separation yield undergoes when the magnitude of the on-site Coulomb interaction U is changed. In Fig. 7.9(c) we observe that weaker electron–hole interaction leads to more efficient charge separation from the strongly bound CT state. Again, this beneficial effect of weaker Coulomb interaction may be attributed to the product $\tau_{\mathrm{init}} w_{\mathrm{inter,init}}$ being (on average) larger for weaker Coulomb interaction. On a more intuitive level, the trends in the separation yield presented in Figs. 7.9(a)–(c) may be rationalized by following the changes in the disorder-averaged energy difference $\langle \hbar\omega_{\mathrm{inter}} - \hbar\omega_{\mathrm{init}} \rangle$ with changing the degree of carrier delocalization and the strength of the electron–hole interaction. We find that better carrier delocalization and weaker electron–hole interaction favor lower values of $\langle \hbar\omega_{\mathrm{inter}} - \hbar\omega_{\mathrm{init}} \rangle$, or, in other words, lower the separation barrier from the CT state. For example, for $J_{A,0}^{\mathrm{c,int}} = 25$, 50, and 75 meV, the average energy barrier assumes values of 76, 67, and 55 meV, respectively. Similarly, for $U = 0.65$, 0.5, and 0.35 eV, $\langle \hbar\omega_{\mathrm{inter}} - \hbar\omega_{\mathrm{init}} \rangle$ is equal to 67, 52, and 33 meV, respectively. Let us also note that each of the effects studied

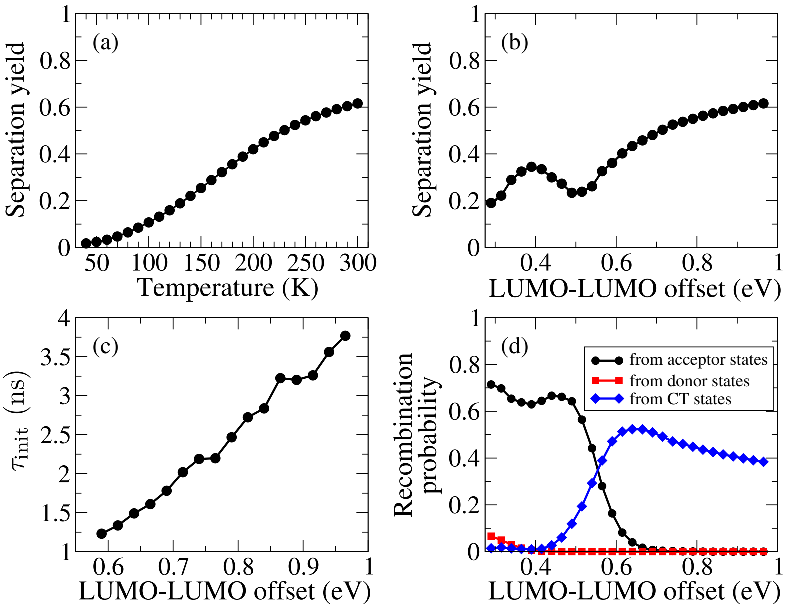

FIGURE 7.10: Yield of charge separation from the strongly bound CT state at zero electric field as a function of (a) the temperature, and (b) the LUMO–LUMO offset. (c) The lifetime τ_{init} of the strongly bound CT state as a function of the LUMO–LUMO offset. (d) The probability of recombination from acceptor (circles), donor (squares), and CT (diamonds) states for different values of the LUMO–LUMO offset. The reported values of the LUMO–LUMO offset refer to the ordered system. Note that the range of LUMO–LUMO offset displayed in panel (c) is narrower than that displayed in panels (b) and (d).

can on its own improve the separation from the strongly bound CT state, since its binding energy strongly depends both on the degree of carrier delocalization and the Coulomb interaction, compare to the discussion of the results [Figs. 7.13(a)–(c)] concerning charge separation from the closely separated donor state.

We have also studied the temperature dependence of the process of charge separation from the strongly bound CT state. We observe an approximately sixfold decrease in the separation yield when the temperature is decreased from 300 to 100 K, see Fig. 7.10(a). On temperature reduction from 300 to below 50 K, the separation yield reduces for more than an order of magnitude. These observations are in agreement with other numerical studies of charge separation from the strongly bound CT state [70], and with experimentally obtained temperature dependence of the photocurrent under an excitation at the low-energy edge of the CT manifold [60].

The effect of the variations in the LUMO–LUMO offset on the separation yield is studied by changing average on-site energies $\epsilon^{c}_{A,0}$, $\epsilon^{c}_{A,1}$, and $\epsilon^{v}_{A,0}$ in the acceptor part of the bilayer by the same amount, keeping all the other model parameters listed in Table 7.1 unchanged. In first approximation, these variations manifest themselves in Figs. 7.4(a)–(e) as rigid translations of the DOS of space-separated exciton states [Figs. 7.4(b)–(d)] with respect to the DOS of donor and acceptor exciton states [Figs. 7.4(a) and (e)]. Figure 7.10(b) presents the dependence of the separation yield at zero electric field on the LUMO–LUMO offset. For the LUMO–LUMO offset greater than approximately 0.5 eV, we observe that the separation yield monotonically decreases with decreasing the LUMO–LUMO offset, see Fig. 7.10(b). A decrease in the LUMO–LUMO offset leads to a decreased energy difference between the lowest acceptor (and also donor) state and the initial CT state, see also Figs. 7.4(a)–(e). We may thus expect that a sufficient decrease in the LUMO–LUMO offset results in the involvement of acceptor and donor states in the separation from the strongly bound CT state. The transitions from the space-separated manifold toward the acceptor (donor) manifold are in general much less probable than the ones inside the space-separated manifold. However, once an exciton enters the acceptor (donor) manifold, it can easily recombine, since the typical lifetime of acceptor (donor) states is shorter than the lifetime of the initial CT state. In other words, the fact that acceptor (donor) states participate in the separation of the strongly bound CT exciton is seen as a decrease in the separation yield which is due to the enhanced recombination from acceptor (donor) states. This is clearly seen in Fig. 7.10(d), which provides data on recombination probability from different groups of exciton states. While the recombination from acceptor states can partially account for the decrease in the separation yield observed for LUMO–LUMO offsets below 0.65 eV, see the data represented by circles in Fig. 7.10(d), the recombination from donor states is reflected in the decrease seen for LUMO–LUMO offsets below 0.4 eV, see the data represented by squares in Fig. 7.10(d). Another way to estimate the aforementioned values uses Figs. 7.4(a)–(e) and bears in mind that the LUMO–LUMO offset for that arrangement of exciton energies is ca. 0.97 eV. Namely, a rigid translation of Figs. 7.4(b)–(d) by approximately 0.3 eV (upward in energy) makes the initial CT state energetically close to the acceptor states in the low-energy tail of the acceptor DOS, meaning that they can participate in the separation of the initial CT state. Similarly, a rigid translation of Figs. 7.4(b)–(d) by approximately 0.55 eV makes the initial CT state energetically close to the donor states in the low-energy tail of the donor DOS. However, in order to understand the behavior of the separation yield in the whole range of LUMO–LUMO offsets displayed in

Fig. 7.10(b), we have to remember that lower LUMO–LUMO offset promotes better coupling between the two parts of the bilayer, which is mediated by the D/A couplings J_{DA}^{c} and J_{DA}^{v}. As a consequence, when the LUMO–LUMO offset is in the range of 0.6–1 eV, its reduction enhances the electron–hole overlap in CT states, thus decreasing their lifetime [see Eq. (7.23) and Fig. 7.10(c)] and increasing the recombination from CT states [see the data represented by diamonds in Fig. 7.10(d)]. Therefore, enhanced recombination from CT states can explain the decrease in the separation yield with decreasing LUMO–LUMO offset observed for LUMO–LUMO offsets above approximately 0.65 eV.

7.4.2 Charge Separation from a Donor Exciton State

Here, we aim at understanding which factors control charge separation starting from a donor exciton state. In numerical computations, the generation rate g_x appearing in Eq. (7.9) is set to a non-zero value only for donor states. In Chapters 5 and 6, we have noted that the low-energy (closely separated and strongly bound) donor states are essentially isolated from the manifold of space-separated states and thus act as trap states for the separation of the initial donor excitons on subpicosecond time scales. On the contrary, higher-energy (more separated and loosely bound) donor states exhibit appreciable coupling to the space-separated manifold and we may thus expect that charge separation starting from these states should be more probable than the one starting from closely separated donor states.

We perform computations of the yield of the separation of donor excitons of different energies. We focus on the energy windows centered around $E_{\mathrm{init}} = 2.0$ eV (the optical gap of the ordered donor material), $E_{\mathrm{init}} = 2.1$ eV, and $E_{\mathrm{init}} = 2.2$ eV (significantly above the optical gap of the ordered donor material), which is indicated by horizontal arrows in Fig. 7.4(a). Since the precise energies of donor states are determined by the disorder, we choose the initial donor state among the states that lie in the 50 meV-wide energy windows centered around the aforementioned energies. One particular donor state out of the chosen states is selected by the requirement that the squared modulus of the dipole moment for the direct generation of donor exciton state x, which is proportional to $\left|\sum_{i\in\mathrm{D};\alpha_i\beta_i}\psi^{x}_{(i\alpha_i)(i\beta_i)}\right|^2$ [see Eq. (6.5)], be maximum. In

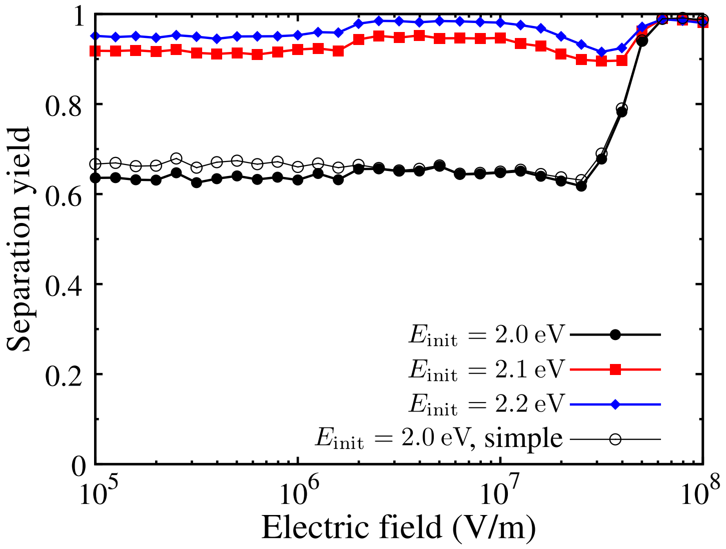

FIGURE 7.11: Field-dependent yield of charge separation starting from donor exciton states of different energies. The data represented by filled symbols are obtained by solving the full set of rate equations [Eq. (7.9)]. The data represented by empty circles are obtained by solving the reduced set of rate equations [Eq. (7.34)] in case $E_{\text{init}} = 2.0$ eV.

other words, among donor states in a given energy window, we select the state whose direct generation from the ground state is most probable. Such a choice of the initial donor state is motivated by the results presented in Ch. 6, where we have observed that quite high fraction of photogenerated excitons remain in the initially photoexcited donor state on a picosecond time scale following the excitation, see, e.g., Figs. 6.11(a)–(l).

In Fig. 7.11, we compare the yields of charge separation starting from donor states of different energies. As we have expected, charge separation starting from a higher-energy donor state is more efficient than the one starting from a closely separated donor state. The yield of the separation from a donor state situated around $E_{\text{init}} = 2.2$ eV is practically field-independent and greater than 0.9 for all the examined values of the electric field down to $F = 0$. The yield is somewhat higher for $E_{\text{init}} = 2.2$ eV than for $E_{\text{init}} = 2.1$ eV. On the other hand, the yield of the separation from the closely separated donor state ($E_{\text{init}} = 2.0$ eV) is lower: it is almost constant for electric fields $F \lesssim 5 \times 10^7$ V/m, its value being around 0.6, after which it rises and reaches values close to 1 at $F \sim 10^8$ V/m. The value of the electric field at which the separation from a closely separated donor state occurs with certainty is almost an order of magnitude larger than in the case of charge separation from the strongly bound CT state, see Fig. 7.5(a), which is consistent with the fact that the binding energy of the donor exciton is larger than the binding energy of the CT exciton.

Let us now analyze in more detail the separation of the closely separated donor exciton ($E_{\text{init}} = 2.0$ eV). Our data suggest that the major part of recombination events occur from donor exciton states. This is consistent with the fact that phonon bath-assisted transitions starting from the closely separated donor exciton state couple it most strongly to other donor states, while coupling to the space-separated manifold is in principle much weaker (we note that its coupling to an acceptor state is practically negligible). The states of the space-separated manifold to which the closely separated donor state can couple are typically well spatially separated, long-lived, and exhibit good coupling to other space-separated states. In other words, despite the weak coupling, once an exciton in the closely separated donor state performs a transition to the space-separated manifold, it is highly probable that it will eventually reach a fully separated state. Instead of finding the stationary solution to the full set of rate equations [Eq. (7.9)] for all exciton states (excluding contact states), we may compute the separation yield by solving the rate equations in which we explicitly consider only donor states $x \in \text{XD}$ and treat exciton states x' that are not of donor character as absorbing states

$$0 = g_x - \tau_x^{-1} f_x^0 - \sum_{x'} w_{x'x} f_x^0 + \sum_{x' \in \text{XD}} w_{xx'} f_{x'}^0. \tag{7.34}$$

The separation yield, computed by inserting the solution to Eq. (7.34) into the following expression for the separation yield [compare to Eq. (7.11)]

$$\varphi = \frac{\sum_{x' \notin \text{XD}} \sum_{x \in \text{XD}} w_{x'x} f_x^0}{\sum_{x \in \text{XD}} g_x} \tag{7.35}$$

is presented in case $E_{\text{init}} = 2.0$ eV by empty circles in Fig. 7.11. We note that the agreement between the two results (full and empty circles in Fig. 7.11) is quite good, thus validating our simple picture of charge separation from a low-energy donor state. The same procedure can be repeated when considering the separation starting from higher-energy donor states, but the agreement between the results obtained by solving Eq. (7.34) and full system of rate equations

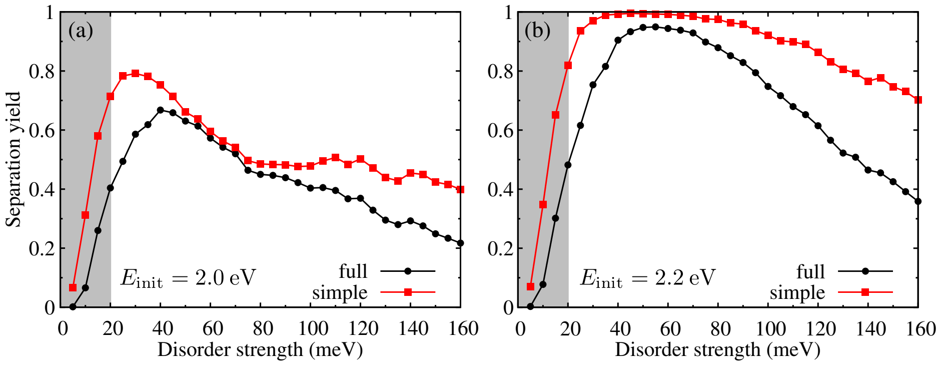

FIGURE 7.12: Separation yield at zero electric field for different strengths σ of the diagonal static disorder. The initial state of charge separation is a donor exciton state of energy around (a) $E_{\rm init} = 2.0$ eV, and (b) $E_{\rm init} = 2.2$ eV. The data labeled by "full" are obtained by numerically solving the full set of rate equations [Eq. (7.9)], whereas the data labeled by "simple" emerge from the numerical solution to the reduced set of rate equations [Eq. (7.34)]. Similarly to Fig. 7.8(a), the gray area indicates the range of disorder strength in which the predictions of our model are not reliable.

[Eq. (7.9)] is worse. An analysis of recombination events suggests that, in these cases, the acceptor exciton states are an equally important recombination channel as the donor exciton states. Namely, when the initial donor state is loosely bound, its direct coupling to acceptor states cannot be neglected. Further discussion on the limits of validity of the simple picture of charge separation from donor states embodied in Eq. (7.34) is presented in the next paragraph.

We now turn to the influence of the diagonal static disorder on the yield of charge separation starting from donor exciton states of different energies at zero electric field. We focus our attention on the initial donor states whose energies are around $E_{\rm init} = 2.0$ eV and $E_{\rm init} = 2.2$ eV. Together with the separation yield emerging from numerically solving the full set of rate equations given in Eq. (7.9) (the true separation yield), in Figs. 7.12(a) and (b) we also present the data obtained by solving the reduced set of rate equations [Eq. (7.34)]. We observe that the separation yield exhibits similar trends with varying disorder strength as when the separation starts from the strongly bound CT state [cf. Fig. 7.8(a)]. In particular, for not too strong disorder, the yield increases with increasing disorder strength, it attains the maximum value when the disorder assumes its optimal value, after which it decreases. For all the examined values of disorder strength, the yield of the separation starting from the donor state of energy $E_{\rm init} = 2.2$ eV is higher than in the case $E_{\rm init} = 2.0$ eV, compare data represented by circles in Figs. 7.12(a) and (b), which again suggests that excitons initially in higher-energy donor states separate more efficiently than the ones initially in lower-energy donor states. While the maximum yield of separation starting from the donor state of energy $E_{\mathrm{init}} = 2.0$ eV is around 0.7, the maximum yield in the case $E_{\mathrm{init}} = 2.2$ eV is above 0.9. For both initial states of charge separation, the yield computed by numerically solving the reduced set of rate equations [squares in Figs. 7.12(a) and (b)] is an upper bound to the true separation yield [circles in Figs. 7.12(a) and (b)] for all the examined values of σ. For $E_{\mathrm{init}} = 2.0$ eV, the separation yield computed by solving the reduced set of rate equations reproduces the true separation yield very well when the disorder strength is from around 40 meV to around 90 meV, while for stronger disorder the agreement between the yields computed in two manners deteriorates. This suggests that, for moderate disorder strength, our simple picture of charge separation from the closely separated donor state, embodied in Eq. (7.34), is plausible. At stronger disorder, the localization effects become more important and recombination may occur from states that do not belong to the donor manifold as well. On the other hand, the agreement between the two separation yields in case $E_{\mathrm{init}} = 2.2$ eV is less satisfactory than in case $E_{\mathrm{init}} = 2.0$ eV, see Fig. 7.12(b).

We also examine the dependence of the separation yield starting from the closely separated donor state on the magnitude of electron ($J_{D,0}^{\mathrm{c,int}}$) and hole ($J_{D,0}^{\mathrm{v,int}}$) transfer integrals in the donor part of the bilayer. We find that reasonable variations in these quantities do not induce major changes in the separation yield, see Figs. 7.13(a) and (b), which stands in contrast to the beneficial effect that better charge delocalization has on the separation of the strongly bound CT exciton, see Figs. 7.9)(a) and (b). The reason for this behavior is the fact that the donor exciton binding energy, which is a rough measure of the energy barrier which has to be overcome in order for free charges to form, is not strongly dependent on the carrier delocalization in the donor. The factor that primarily determines the binding energy of the donor exciton is the strength of the Coulomb interaction. Figure 7.13(c) presents the field-dependent separation yield for different values of the on-site Coulomb interaction U. As anticipated, we find that lowering U leads to a higher separation yield.

The temperature-dependent separation yield at zero electric field is shown in Fig. 7.14(a). We see that lower temperature leads to lower separation yield since the phonon bath-assisted pro-

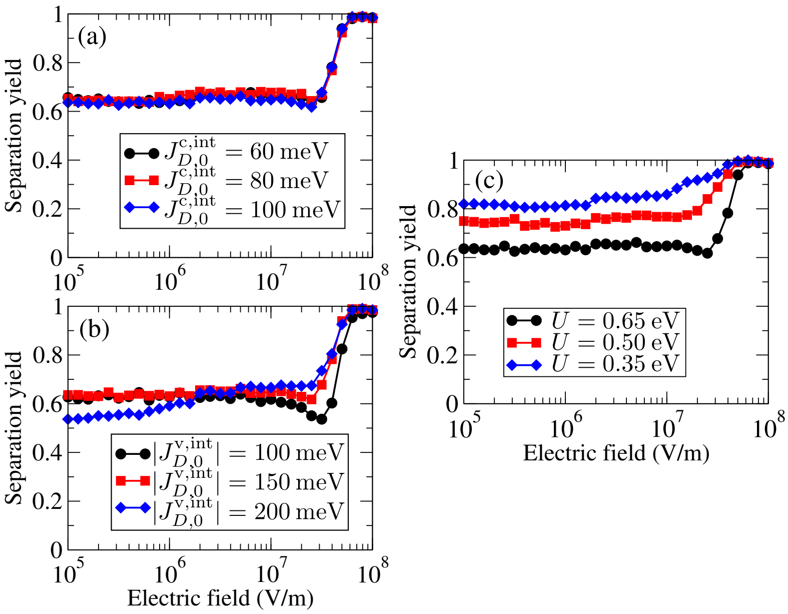

FIGURE 7.13: Field-dependent yield of charge separation starting from the closely separated donor exciton state ($E_{\mathrm{init}} = 2.0$ eV) for different values of (a) the electron transfer integral $J_{D,0}^{\mathrm{c,int}}$ in the donor, (b) the hole transfer integral $J_{D,0}^{\mathrm{v,int}}$ in the donor, and (c) the on-site Coulomb interaction U.

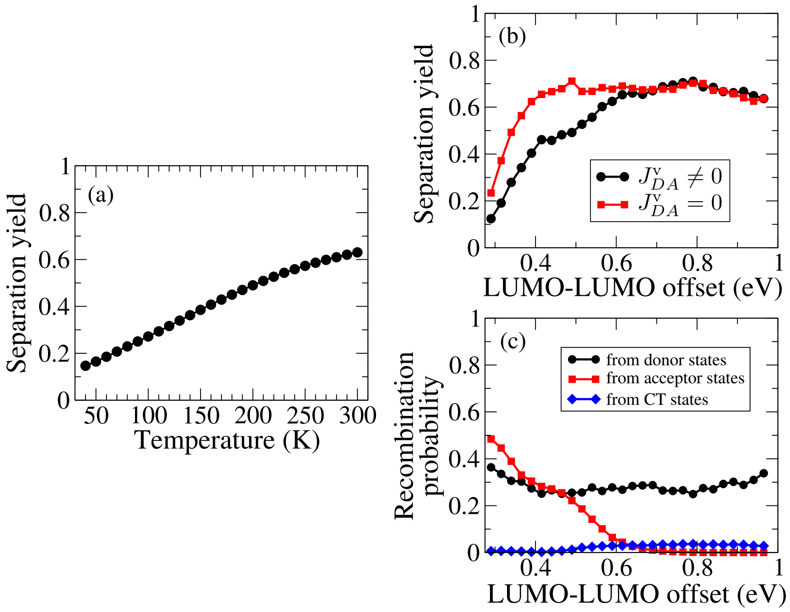

FIGURE 7.14: Yield of charge separation starting from the closely separated donor state ($E_{\mathrm{init}} = 2.0$ eV) at zero electric field as a function of (a) the temperature, and (b) the LUMO–LUMO offset. (c) The recombination probability from donor (circles), acceptor (squares), and CT (diamonds) states as a function of the LUMO–LUMO offset. The reported values of the LUMO–LUMO offset refer to the ordered system. In panel (b), we present results in which acceptor states are included ($J_{DA}^{\mathrm{v}} \neq 0$) and excluded ($J_{DA}^{\mathrm{v}} = 0$) from the computation.

cesses transferring an exciton in a donor state to the space-separated manifold (and, eventually, to a state of fully separated charges) are weaker. The separation yield exhibits a sixfold decrease when the temperature is lowered from the room temperature to around 50 K. The intensity of the temperature variation-induced effect on the separation yield is somewhat smaller than in case of the separation starting from the strongly bound CT state, compare to Fig. 7.10(a).

In the end, we examine how the value of the LUMO–LUMO offset affects charge separation from the closely separated donor state. Figure 7.14(b) presents the separation yield as a function of the LUMO–LUMO offset for the values of model parameters listed in Table 7.1 ($J_{DA}^{\mathrm{v}} \neq 0$, circles), as well as for $J_{DA}^{\mathrm{v}} = 0$ (squares), i.e., when states of acceptor excitons are excluded from the computation. For the LUMO–LUMO offset above approximately 0.6 eV, we observe that the separation yield in both cases is essentially the same and weakly dependent on the particular value of the LUMO–LUMO offset. This indicates that, in this range of LUMO–LUMO offsets, charge separation starting from the closely separated donor state does not involve acceptor exciton states, which once again validates our simple picture of charge separation from that state [formally embodied in Eq. (7.34)]. However, when the LUMO–LUMO offset is below 0.6 eV, the separation yield in case $J_{DA}^{\mathrm{v}} \neq 0$ starts to decrease with decreasing the LUMO–LUMO offset. On the other hand, in case $J_{DA}^{\mathrm{v}} = 0$, similar decrease in the separation yield is observed only when the LUMO–LUMO offset is lower than approximately 0.4 eV. The different behavior of the separation yield in the two cases signalizes that, when the LUMO–LUMO offset assumes values lower than ca. 0.6 eV, states of acceptor excitons are involved in charge separation and the observed decrease is due to the recombination from acceptor states. As we have already noted in the analysis of Fig. 7.10(b), when the LUMO–LUMO offset is around 0.6 eV, the low-energy tails of the CT and acceptor exciton DOS become energetically close. Further analysis of recombination events from different groups of exciton states, whose results are reported in Fig. 7.14(c), shows that the contribution of the recombination from acceptor states to the total recombination probability becomes appreciable when the LUMO–LUMO offset is around 0.6 eV. When acceptor states are excluded from the computation, the independence of the separation yield on the LUMO–LUMO offset can be inferred from the flat recombination probability from the donor states [circles in Fig. 7.14(c)], which is disturbed when the energy of the strongly bound CT state is approximately equal to the energy of the initial donor state, which occurs for the LUMO–LUMO offset below around 0.4 eV. For even smaller values of the LUMO–LUMO offset, all the space-separated states are energetically above the initial donor state, meaning that full charge separation can be achieved only by means of energetically-upward processes. The decrease in the separation yield with decreasing the LUMO–LUMO offset can then be attributed to an increased probability of recombination from donor states, which is clearly seen in Fig. 7.14(c).

7.5 Discussion and Significance of Our Results

Using a one-dimensional model of an all-organic bilayer, we have modeled and investigated the process of incoherent charge separation out of CT and donor exciton states. The main advantage of our model over existing approaches is that it properly takes into account carrier delocalization, whose importance for efficient charge separation in OPV systems has been repeatedly recognized [66, 68, 190, 191, 194, 195]. The carrier delocalization is fully and naturally taken into account by working in the exciton basis, rather than in the commonly used position basis. The charge separation is then conceived as a sequence of environment-assisted transitions among exciton basis states that terminates once a free-charge state is reached. Another important ingredient of our model is the diagonal static disorder, which is crucial to identify the counterparts of free-charge states within our description.

Many of the studies mentioned in Sec. 7.2 underline the beneficial role played by the system's dimensionality in the conversion of strongly bound excitons to free charges. Therefore, comments on our results in view of the reduced dimensionality of our model are in order. Although formally one-dimensional, the proposed model of a bilayer can be regarded as a two- (or three-) dimensional model consisting of periodically repeated linear systems identical to the one shown in Fig. 7.3 that are isolated from each other, i.e., the transfer integrals between (neighboring) linear systems are equal to zero. We have established that, within our one-dimensional model, the degree of charge delocalization, quantified by the values of the electron and hole transfer integrals, is one of the factors influencing the (CT exciton) separation efficiency, see Figs. 7.9(a) and (b). On simple grounds, better delocalization is beneficial to charge separation because it increases the mean distance (in the direction of a single linear system, which is perpendicular to the D/A interface) between the electron and hole located in the acceptor and donor, respectively. If we assigned nonzero values to transfer integrals coupling different linear systems, the charges could also delocalize along the direction perpendicular to the linear systems (parallel to the D/A interface) and further increase their separation. Therefore, it may be expected that the separation yield would be enhanced in such genuinely two- (or three-) dimensional model. This line of reasoning is supported by studies highlighting the beneficial role of hole delocalization along polymer chains in charge separation [68, 191], particularly if we keep in mind that the values of the intrachain transfer integrals are typically larger than the ones employed in this study. We may also say that the separation yields we obtain using an effectively one-dimensional model are the lower limit to the ones that would be obtained in a higher-dimensional system. Another possible interpretation of our results is that they suggest that, in order to describe fundamental reasons for efficient charge separation at all-organic bilayers, it is more important to properly account for charge delocalization than for dimensionality effects.

Next, we discuss our assumptions concerning the strength of the carrier–bath interaction. We take that the polaron binding energy is $\epsilon_\mathrm{b}^\mathrm{pol} = 15$ meV, which is significantly lower than values commonly reported in electronic-structure studies of single PCBM molecules [20, 168]. The selection of the values of model parameters implicitly suggests that each lattice site may be imagined to substitute a polymer chain or a group of fullerene molecules. In this regard, carrier transfer from one site to another should not be interpreted as transfer between single molecules supporting localized carrier states, but rather as transfer between two aggregates of molecules supporting delocalized carrier states. It has been demonstrated recently that, in such a case, the definition of $\epsilon_\mathrm{b}^\mathrm{pol}$ [given in the text between Eqs. (7.21) and (7.22)] should be corrected so as to take into account delocalization effects, which can substantially reduce $\epsilon_\mathrm{b}^\mathrm{pol}$ [206]. Having all these things considered, we believe that our choice of the magnitude of $\epsilon_\mathrm{b}^\mathrm{pol}$ is reasonable. Larger $\epsilon_\mathrm{b}^\mathrm{pol}$ (while keeping all other model parameters fixed) would result in a higher separation yield, because the phonon bath-induced transition rates [Eq. (7.17)] would be larger. In this sense, our results may also be regarded as the lower limit to the separation yield computed for larger $\epsilon_\mathrm{b}^\mathrm{pol}$.

Another common choice for the spectral density $J(E)$ [Eq. (7.16)] when studying charge separation in photosynthetic [199] and OPV systems [58, 207] is the so-called Drude–Lorentz spectral density

$$J_{\mathrm{DL}}(E)=\frac{2}{\pi}\,\Delta\,\frac{E\cdot\hbar\gamma}{E^2+(\hbar\gamma)^2}, \tag{7.36}$$

which is characterized by two parameters, Δ and $\hbar\gamma$. According to the relation between the spectral density and the polaron binding energy embodied in Eq. (7.22), parameter Δ represents the polaron binding energy, whereas $\hbar\gamma$ determines the energy range of bath modes whose coupling to the system is appreciable. While the behavior of the Ohmic spectral density [Eq. (7.21)] at large energies ($E \gg E_c$) is essentially exponential, the Drude–Lorentz spectral density decreases only algebraically for $E \gg \hbar\gamma$. Therefore, the Drude–Lorentz spectral density generally favors coupling to a wider range of phonon modes than does the Ohmic spectral density employed in our numerical computations. It is then not surprising that the Drude–Lorentz spectral density promotes even higher separation yields than the Ohmic spectral density, which has been demonstrated in the Supporting Information associated to Ref. [182].

Our principal conclusion is that the synergy between moderate energetic disorder and carrier delocalization can explain quite high and relatively weakly field-dependent separation efficiencies observed in solar cells photoexcited at the low-energy edge of the CT manifold [61], see Fig. 7.5(a). At electric fields typically encountered in a working organic solar cell ($F \sim$ 5–10 V/μm), the efficiency of the separation of the strongly bound CT exciton is above 0.8. Our analytical treatment, which is sensible for not too strong disorder, reveals that the separation of the strongly bound CT exciton is actually governed by the competition between the recombination from the initial CT state and the escape towards more separated and long-lived intermediate CT states, from which further separation proceeds without kinetic obstacles, see Eq. 7.32. Strong disorder destroys this simple picture, and the appearance of well-separated and strongly localized states following the intermediate states prevents electron–hole pairs from eventually reaching contact states. Our finding that better charge delocalization promotes more efficient separation of the strongly bound CT exciton further corroborates the conclusions of Ref. [61], which emphasize that, in the most efficient OSCs, the strongly bound CT state is only weakly bound and quite delocalized. Moreover, we observe a much milder temperature dependence of the separation yield [see Fig. 7.10(a)] than the (predominantly) exponential one predicted by the Onsager–Braun model, see Eqs. (7.1), (7.2), and (7.3), in agreement with experimental [60] and theoretical studies [70]. The fact that larger LUMO–LUMO offsets favor more efficient free-charge generation out of the strongly bound CT state is attributed to an increased recombination probability from acceptor and donor states observed for smaller LUMO–LUMO offsets, see Figs. 7.10(b) and (d).

The separation of donor excitons is also quite efficient, and its yield depends on the exciton energy, see Fig. 7.11. The electric field required to separate the closely separated donor exciton with certainty is almost an order of magnitude higher than the one needed to separate the strongly bound CT exciton. Our results suggest that the separation of the closely separated donor exciton exhibits only one rate-limiting step, i.e., the escape to the space-separated manifold. Carrier delocalization does not strongly influence this escape, see Figs. 7.13(a) and (b). The donor exciton separation shows weak temperature dependence, see Fig. 7.14(a), while its decrease with decreasing the LUMO–LUMO offset is attributed to the recombination from acceptor states, see Figs. 7.14(b) and (c). Relatively weak disorder is beneficial to donor exciton separation, while strong disorder suppresses it, see Figs. 7.12(a) and (b).

In summary, our results provide unambiguous evidence that efficient charge separation can be achieved even out of strongly bound pair states and are supported by experiments [61, 181] suggesting that free-charge generation predominantly occurs on long time scales, from localized initial conditions.

Chapter 8

Conclusion

This thesis presents a detailed account of the fundamental physical mechanisms that govern the dynamics of photoinduced electronic excitations in D/A OSCs. Even though an ever-growing power of computational facilities has enabled us to depict microscopic processes occurring in a variety of materials with an unprecedented temporal and spatial resolution, their fundamental physical understanding still lacks. Therefore, in this thesis, we concentrate on apparently simple, but physically grounded, model Hamiltonians, while comprehensive investigations of their dynamics provide us with important insights that will be once again briefly summarized in the following text.

Organic semiconductors are physical systems whose theoretical description is quite challenging because their basic properties are very different from those of inorganic semiconductors, the theoretical study of which was one of the milestones of the 20th-century physics. The electronic energy bands in typical organic semiconductors are narrow, the dielectric screening is weak, the coupling of carriers to lattice vibrations in strong, while the disorder is omnipresent. Instead of creating free carriers, an optical excitation of an organic semiconductors creates Coulomb-correlated strongly bound electron–hole pairs, i.e., excitons. A sensible description of the light-to-charge conversion by means of organic semiconductors requires that a number of physical effects be treated simultaneously and on equal footing. Moreover, experimental findings indicating an ever-faster time scale of the light-to-charge conversion in the most efficient OSCs [36–38] demand that the theoretical treatment be fully quantum.

The starting point for our study is the rather general standard semiconductor Hamiltonian that explicitly takes into account carrier delocalization, electron–hole interaction, carrier–phonon interaction, and the interaction with an external optical field, see Ch. 2. The model Hamiltonian can, under certain approximations, be reduced to the well-known Wannier and Frenkel exciton models, but is actually more general than them. The fully quantum and statistical treatment of the dynamics triggered by a pulsed optical excitation of the model system relies upon the density matrix formalism, see Ch. 3. The carrier branch of the infinite hierarchy of mutually coupled equations describing the temporal evolution of density matrices is truncated by employing the DCT scheme up to the second order in the exciting field. The second order is the lowest order in the exciting field in which excitonic effects can be conclusively studied, and, as we have described, the respective truncation is intimately related to the low-density limit, i.e., to confining the dynamics to the single-exciton subspace. From the methodological point of view, our main contribution regards the truncation of the phonon branch of the hierarchy. Guided by the energy and particle-number conservation laws, which have to be met once the pulsed excitation has vanished, we perform a specific truncation of the phonon branch on the level of single-phonon-assisted density matrices. Although such a treatment of the carrier–phonon coupling precludes us from treating polaronic effects, which are sometimes considered as highly important in organic semiconductors, recent theoretical results suggesting that charge carriers in these systems are of nonpolaronic nature make our approach sensible.

Theoretical investigations of the exciton formation and initial stages of exciton relaxation in the model of a neat organic semiconductor reveal that these processes happen on a multitude of time scales, see Ch. 4, which has also been observed experimentally [46, 47]. In greater detail, our numerical computations, which capture processes occurring on picosecond or shorter time scales, suggest that the initially generated coherent exciton populations are transformed into incoherent ones on a $\sim$ 50-fs time scale, which is followed by the build-up of the Coulomb correlation and the formation of bound electron–hole pairs on a $\sim$ 500-fs time scale. The ultrafast stages of exciton relaxation dynamics are observed on a picosecond time scale. Despite the fact that our model contains some oversimplifications, the time scales emerging from our computations are consistent with the experimental ones.

Our study of ultrafast exciton dynamics in photoexcited D/A interfaces has provided relevant insights into the origin of spatially separated charge carriers that have been experimentally observed on such short time scales, see Ch. 5. Our approach to the problem considers exciton generation by means of an optical excitation, exciton dissociation, and further charge separation on equal footing and on a fully quantum level. The common interpretation of the results of ultrafast time-resolved spectroscopic studies indicates that states of spatially separated charges become populated on a $\sim$ 100-fs time scale by means of the ultrafast population transfer from the initially excited donor exciton states [36–38]. Our results, however, demonstrate that the main source of space-separated charges on $\sim$ 100-fs time scales is their direct optical generation from the ground state. Such a route towards space-separated charges is possible due to the redistribution of oscillator strengths among donor and space-separated states, which is mediated by their resonant "hybridization". Previous proposals that the long-range charge separation in D/A OSCs may be achieved through the direct optical generation of space-separated pairs [143, 144] were motivated by the studies of the absorption spectrum of D/A interfaces, which identified the aforementioned absorption intensity redistribution, but were unable to fully appreciate its actual relevance. Our work, therefore, complements these studies by examining the ultrafast exciton dynamics triggered by the excitation of a D/A interface and is capable of demonstrating that the direct optical generation of space-separated charges is their main source on ultrafast time scales.

We also embark on the theoretical treatment of ultrafast time-resolved transient absorption spectroscopy. By combining our approach to the ultrafast exciton dynamics with recent theoretical developments concerning the computation of the differential transmission signal [157], we derive an analytical expression for the signal that explicitly demonstrates that both populations and coherences, rather than only populations, are expected to govern experimental signals on subpicosecond time scales. Our numerical computations of differential transmission signals reveal that, in some cases, the signal is expected to predominantly originate from coherences between exciton states and the ground state, which seriously challenges its usual interpretations in terms of population transfer.

The conclusions underlined in the last two paragraphs do not necessarily imply that there is no population transfer from initially generated donor towards space-separated states. Indeed, although we observe the direct creation of space-separated pairs, the optical excitation still primarily generates donor excitons, which have to be separated in order to generate photocurrent. Therefore, the identification of photophysical pathways along which the subpicosecond exciton dynamics proceeds is an important task, which is undertaken in Ch. 6. We individuate two prominent categories of space-separated states that appear along these pathways. The PACB states contribute to the ultrafast generation of separated charges as additional photon absorbers at the interface, but exhibit rapid transitions towards the donor manifold. On the other hand, bridge states act as gateways for the donor excitons into the space-separated manifold. Once a donor exciton enters the space-separated manifold, a progressive deexcitation within this manifold leads to its relaxation towards bound CT states on a picosecond time scale. The numerically obtained participation of space-separated charge pairs in the total exciton population at ~ 1 ps following the excitation suggests that the production of separated charges predominantly occurs on a longer time scale. On a picosecond time scale, the major part of exciton population resides in donor states, and there is also a number of strongly bound CT excitons, both of which should still be separated to produce photocurrent.

Motivated by these findings, and also by experimental suggestions that even strongly bound CT pairs are efficiently separated [61], in Ch. 7 we address the problem of long-time (incoherent) charge separation. The model Hamiltonian is essentially the same as in our studies of ultrafast exciton dynamics: instead of accounting for the interaction with the time-dependent optical field, we now take into account the influence of the internal electric field in a solar cell, and additionally consider exciton recombination and disorder. We find that the combination of carrier delocalization and moderate energetic disorder makes the separation of strongly bound CT pairs possible. Contrarily to the widespread view that the strongly bound CT exciton separation requires surmounting an immense energy barrier, we conclude that the actual barrier opposing the separation is determined by the energy position of the so-called intermediate CT state. Compared to the initial strongly bound CT state, the intermediate state is more separated and long-lived. For not too strong disorder, carriers in the intermediate state are bound to exhibit the full separation. The probability with which the strongly bound CT state separates in then primarily determined by the competition between its transition towards intermediate states and its recombination to the ground state, which is formally embodied in the analytical expression we propose. The separation yield exhibits relatively weak dependence on both the electric field and the temperature, which is consistent with existing experimental and theoretical results. Very strong disorder is detrimental to full charge separation, because the disorder-induced localization prevents excitons in intermediate states from certainly reaching the free-charge states. Better carrier delocalization is found to enhance the separation of the strongly bound CT state. The separation of donor excitons is also weakly field- and temperature-dependent and quite efficient. It also depends on the exciton energy, higher-energy donor states separating more efficiently.

In the end, our results are consistent with the recent experimental findings concerning light-to-charge conversion in D/A OSCs. While free-charge generation on subpicosecond time scales following an optical excitation is possible, the results emerging from our treatment of ultrafast exciton dynamics suggest that the overwhelming part of free carriers are produced on a time scale longer than the picosecond one, from pair states that are (strongly) bound [61, 181]. We provide unambiguous evidence that such a separation is indeed possible despite apparently unfavorable conditions (poor charge delocalization, presence of the disorder, etc.). In light of recent attempts of the scientific community to build a comprehensive description of light-to-charge conversion in OSCs on multiple time (and length) scales, our model could potentially be part of such multiscale models of OPV devices. The very initial stages of exciton dynamics can be described by employing our fully quantum and statistical description, which provides us with the populations of different exciton states at a picosecond time scale after photoexcitation. This output could then be used as input for our semiclassical model that treats charge separation on longer time scales.

Appendix A

Proofs of the Expansion and Truncation Theorems in the Phonon-Free Case

A.1 Proof of the Expansion Theorem

The proof of the expansion theorem is conducted by using complete induction in n. It is convenient to decompose the interaction with the optical field [Eq. (2.38)] in the following manner

$$H_{\mathrm{c-f}} = H_{\mathrm{c-f}}^{(-)} + H_{\mathrm{c-f}}^{(+)}, \tag{A.1}$$

where $H_{\mathrm{c-f}}^{(-)}$ [the first term on the right-hand side of Eq. (2.38)] annihilates one electron–hole pair, while $H_{\mathrm{c-f}}^{(+)}$ [the second term on the right-hand side of Eq. (2.38)] creates one electron–hole pair.

If $\hat{N}_e$ and $\hat{N}_h$ are respectively electron and hole number operators defined in Eqs. (3.15a) and (3.15b), the following equalities hold

$$\left[\hat{N}_{e/h}, H_{\mathrm{c}}\right] = 0, \quad \left[\hat{N}_{e/h}, H_{\mathrm{c-f}}^{(\pm)}\right] = \pm H_{\mathrm{c-f}}^{(\pm)}. \tag{A.2}$$

The expansion theorem is valid for $n = 0$ since

$$\hat{N}_{e/h}|\psi(t)\rangle^{(0)} = \mathrm{e}^{-\mathrm{i}H_{\mathrm{c}}t/\hbar}\hat{N}_{e/h}|0\rangle = 0. \tag{A.3}$$

Let us suppose that the expansion theorem holds for some $n \geq 1$,

$$|\psi(t)\rangle^{(n)} = \sum_{n_p=n,n-2,\ldots,\geq 0} |n_p, n_p, n, t\rangle, \tag{A.4}$$

so that the inequality $n_p \leq n$ is satisfied and the difference $n - n_p$ is even. The contribution of order $n+1$ in the optical field may be written as

$$|\psi(t)\rangle^{(n+1)} = \sum_{n_p=n,n-2,\ldots,\geq 0} \left(|n_p, n_p, n, t\rangle^{(-)} + |n_p, n_p, n, t\rangle^{(+)} \right), \tag{A.5}$$

where, according to Eq. (3.13),

$$|n_p, n_p, n, t\rangle^{(\pm)} = \frac{1}{\mathrm{i}\hbar} \int_0^t \mathrm{d}t' \, \mathrm{e}^{-\mathrm{i}H_\mathrm{c}(t-t')/\hbar} H_{\mathrm{c-f}}^{(\pm)}(t') |n_p, n_p, n, t'\rangle. \tag{A.6}$$

Using Eq. (A.2), we conclude that

$$\hat{N}_{e/h} |n_p, n_p, n, t\rangle^{(\pm)} = (n_p \pm 1) \, |n_p, n_p, n, t\rangle^{(\pm)}, \tag{A.7}$$

i.e., state $|n_p, n_p, n, t\rangle^{(\pm)}$ contains $n_p \pm 1$ electrons and $n_p \pm 1$ holes. Moreover, since state $|n_p, n_p, n, t\rangle$ is proportional to E^n, Eq. (A.6) gives that state $|n_p, n_p, n, t\rangle^{(\pm)}$ is proportional to E^{n+1}. We may, therefore, identify

$$|n_p, n_p, n, t\rangle^{(+)} = |n_p + 1, n_p + 1, n + 1, t\rangle, \tag{A.8a}$$

$$|n_p, n_p, n, t\rangle^{(-)} = |n_p - 1, n_p - 1, n + 1, t\rangle. \tag{A.8b}$$

Because of the inequality $n_p \leq n$, the inequality $n_p \pm 1 \leq n + 1$ is also satisfied. As the difference $n - n_p$ is even, we have that the difference $n + 1 - (n_p \pm 1)$ is also even. Therefore, the expansion of state $|\psi(t)\rangle^{(n+1)}$ in states with definite numbers of electrons and holes reads as

$$|\psi(t)\rangle^{(n+1)} = \sum_{n_p=n+1,n-1,\ldots,\geq 0} |n_p, n_p, n+1, t\rangle, \tag{A.9}$$

which completes the proof of the expansion theorem.

A.2 Proof of the Truncation Theorem

Let A denote the density matrix given in Eq. (3.17), i.e.,

$$A = \langle \underbrace{c^\dagger \dots c^\dagger}_{n_u} \underbrace{c^\dagger d^\dagger \dots c^\dagger d^\dagger}_{n_p^+ \text{ pairs}} \underbrace{dc \dots dc}_{n_p^- \text{ pairs}} \underbrace{c \dots c}_{n_u} \rangle. \tag{A.10}$$

The proof of the truncation theorem for the density matrix embodied in Eq. (3.18) is analogous to the one that will be presented.

According to the expansion theorem, A can be expanded in powers of the exciting field as follows

$$A(t) = \sum_{n=0}^{+\infty} A^{(n)}(t), \text{ where } A^{(n)} \propto E^n, \tag{A.11}$$

$$\begin{aligned} A^{(n)}(t) = \sum_{k=0}^{n} \sum_{p,p' \geq 0} \langle n-k-2p, n-k-2p, n-k, t| \underbrace{c^\dagger \dots c^\dagger}_{n_u} \underbrace{c^\dagger d^\dagger \dots c^\dagger d^\dagger}_{n_p^+ \text{ pairs}} \times \\ \times \underbrace{dc \dots dc}_{n_p^- \text{ pairs}} \underbrace{c \dots c}_{n_u} |k-2p', k-2p', k, t\rangle. \end{aligned} \tag{A.12}$$

The operator $\underbrace{dc \dots dc}_{n_p^- \text{ pairs}} \underbrace{c \dots c}_{n_u}$ attempts to annihilate $n_p^- + n_u$ electrons from state $|k-2p', k-2p', n, t\rangle$, which gives a nontrivial results when $k - 2p' \geq n_p^- + n_u$ and results in a state containing $k - 2p' - (n_p^- + n_u)$ electrons and $k - 2p' - n_p^-$ holes. On the other hand, the product of creation operators $\underbrace{c^\dagger \dots c^\dagger}_{n_u} \underbrace{c^\dagger d^\dagger \dots c^\dagger d^\dagger}_{n_p^+ \text{ pairs}}$ acting to the left on state $\langle n-k-2p, n-k-2p, n-k, t|$ leads to a nontrivial state containing $n - k - 2p - (n_p^+ + n_u)$ electrons and $n - k - 2p - n_p^+$ holes under condition $n - k - 2p \geq n_p^+ + n_u$. The scalar product of bra and ket thus obtained is nonzero for $n - k - 2p - (n_p^+ + n_u) = k - 2p' - (n_p^- + n_u) = n_s \geq 0$, where we introduce a nonnegative integer n_s. Summing these two equalities, we conclude that the contribution $A^{(n)}(t)$ is nonzero when

$$n = 2n_s + 2(p + p') + n_p^+ + n_p^- + 2n_u. \tag{A.13}$$

Having in mind that the total number of electron operators in A is $m = n_p^+ + n_p^- + 2n_u$, we finally obtain that the following equality

$$n = m + 2(p + p' + n_s) \text{ with } p + p' + n_s \geq 0 \tag{A.14}$$

is satisfied for all nonvanishing contributions $A^{(n)}$, which is the content of the truncation theorem.

Appendix B

Contraction Relations Relevant for the Second-Order Dynamics

This appendix is devoted to the formal proof of contraction relations [Eqs. (3.37) and (3.38)] that are used to eliminate (phonon-assisted) electron and hole populations and intraband polarizations $C_{ab}^{\alpha\beta}$ and $D_{ab}^{\alpha\beta}$ in terms of exciton populations $N_{abcd}^{\alpha\beta}$. The proof to be presented closely follows the derivation of contraction relations presented in Ref. [71]. This derivation leans on the fact that the standard semiconductor Hamiltonian given in Eqs. (2.34)–(2.38) commutes with the operator of the total number of particles which in the electron–hole picture reads as

$$\hat{N}_{\text{total}} = \sum_{k\in\text{VB}} d_k d_k^\dagger + \sum_{k\in\text{CB}} c_k^\dagger c_k = N_{\text{VB}} + \sum_{k\in\text{CB}} c_k^\dagger c_k - \sum_{k\in\text{VB}} d_k^\dagger d_k. \tag{B.1}$$

N_{VB} is the total number of occupied states, which is equal to the total number of particles in the system. According to the central theorem of the DCT scheme, the purely electronic density matrices relevant for the second-order dynamics are single- and two-particle quantities, i.e., contain at most four Fermi operators. We will not, therefore, formulate contraction relations in a general form, but will rather limit ourselves to the relation that exists between single-particle and two-particle density matrices in a system with fixed number of particles.

The density matrix of a system with fixed number of particles N_{VB} can always be expressed as a linear combination of density matrices for pure states, in which each state is an eigenvector of the total particle-number operator $\hat{N}_{\text{total}}$ with eigenvalue N_{VB}. Let us exploit the last feature to compute

$$\begin{aligned} N_{\mathrm{VB}} C_{ab}^{\alpha\beta} &= \mathrm{Tr}\left(\hat{N}_{\mathrm{total}} \rho \, c_a^\dagger c_b \hat{F}^{\alpha\beta}\right) \\ &= N_{\mathrm{VB}} C_{ab}^{\alpha\beta} + \sum_{k\in\mathrm{CB}} \langle c_k^\dagger c_k c_a^\dagger c_b \hat{F}^{\alpha\beta}\rangle - \sum_{k\in\mathrm{VB}} \langle d_k^\dagger d_k c_a^\dagger c_b \hat{F}^{\alpha\beta}\rangle. \end{aligned} \tag{B.2}$$

Rearranging the last expression by using the anticommutation relations given in Eqs. (2.19) and (2.21), we obtain

$$C_{ab}^{\alpha\beta} = \sum_{k\in\mathrm{VB}} N_{akkb}^{\alpha\beta} - \sum_{k\in\mathrm{CB}} \langle c_a^\dagger c_k^\dagger c_k c_b \hat{F}^{\alpha\beta}\rangle = \sum_{k\in\mathrm{VB}} N_{akkb}^{\alpha\beta} + \mathcal{O}(E^4), \tag{B.3}$$

where in the last step we used the central theorem of the DCT scheme. Therefore, within the dynamics up to the second order in the applied field, the electron populations and intraband coherences are redundant because they may be expressed entirely in terms of exciton populations. In a similar fashion, we express hole populations and intraband coherences as

$$D_{ab}^{\alpha\beta} = \sum_{k\in\mathrm{CB}} N_{kabk}^{\alpha\beta} - \sum_{k\in\mathrm{VB}} \langle d_a^\dagger d_k^\dagger d_k d_b \hat{F}^{\alpha\beta}\rangle = \sum_{k\in\mathrm{CB}} N_{kabk}^{\alpha\beta} + \mathcal{O}(E^4). \tag{B.4}$$

Let us note, in passing, that Eqs. (B.3) and (B.4) are special cases of the following equation that relates the single-particle and two-particle density matrices in a system with fixed number N_{VB} of particles

$$(N_{\mathrm{VB}} - 1) \langle a_p^\dagger a_q \hat{F}^{\alpha\beta}\rangle = \sum_{k\in\mathrm{VB,CB}} \langle a_p^\dagger a_k^\dagger a_k a_q \hat{F}^{\alpha\beta}\rangle. \tag{B.5}$$

In Eq. (B.5), indices p, q may represent valence-band or conduction-band states (there are four different possibilities) and the corresponding operators are defined in Eq. (2.9). We have checked that Eq. (B.5) is satisfied for $p, q \in$ CB and $p, q \in$ VB. When $p \in$ VB and $q \in$ CB, Eq. (B.5) reduces to

$$(N_{\mathrm{VB}} - 1) \, Y_{pq}^{\alpha\beta} = (N_{\mathrm{VB}} - 1) \, Y_{pq}^{\alpha\beta} + \sum_{k\in\mathrm{CB}} \langle c_k^\dagger c_k^\dagger d_p c_q \hat{F}^{\alpha\beta}\rangle - \sum_{k\in\mathrm{VB}} \langle d_k^\dagger d_k d_p c_q \hat{F}^{\alpha\beta}\rangle, \tag{B.6}$$

which is an identity within the second order treatment, since contributions $\langle c_k^\dagger c_k^\dagger d_p c_q \hat{F}^{\alpha\beta}\rangle$ and

$\langle d_k^\dagger d_k d_p c_q \hat{F}^{\alpha\beta} \rangle$ are of the third order in the optical field. Similar reasoning applies for $p \in \mathrm{CB}$ and $q \in \mathrm{VB}$. In conclusion, the DCT scheme up to the second order in the optical field is compatible with the general relation expressed in Eq. (B.5).

Appendix C

Markov and Adiabatic Approximations

Let us suppose that we want to find time evolution of quantity $z(t)$ whose dynamics is governed by

$$\dot{z}(t) + \mathrm{i}\Omega z(t) = \sum_i y_i(t). \tag{C.1}$$

The variable z performs free oscillations with frequency Ω, while quantities $y_i(t)$ acting as source terms in Eq. (C.1) can be factorized into slowly varying parts $y_i^0(t)$ and rapid free oscillations with frequencies ω_i,

$$y_i(t) = \tilde{y}_i(t)\,\mathrm{e}^{-\mathrm{i}\omega_i t}. \tag{C.2}$$

Equations resembling Eq. (C.1) are typically encountered in the density matrix formalism. Namely, Heisenberg equations of motion are first-order differential equations, while source terms are typically higher-order density matrices to which the density matrix under consideration couples. Let us suppose that at the initial instant, which is taken to be $-\infty$, $\lim\limits_{t\to-\infty} z(t) = 0$. Equation (C.1) can then be formally integrated to give

$$z(t) = \sum_i \mathrm{e}^{-\mathrm{i}\omega_i t} \int_0^{+\infty} \mathrm{d}\tau\, \tilde{y}_i(t-\tau)\,\mathrm{e}^{-\mathrm{i}(\Omega-\omega_i)\tau}. \tag{C.3}$$

Within Markov approximation [72, 90, 119], one assumes that the dominant time dependence of the integrand in Eq. (C.3) is given by the exponential term, while functions $\tilde{y}_i(t-\tau)$ are slowly varying (with respect to the exponential term). Therefore, $\tilde{y}_i(t-\tau)$ can be approximated by their values at instant t, $\tilde{y}_i(t-\tau) \approx \tilde{y}_i(t)$, and taken out of the integral. Next, in order to have a well defined initial condition at $t \to -\infty$, we assume that the source terms are switched on adiabatically, which amounts to adding a small positive imaginary part to all frequencies ω_i appearing in Eq. (C.2), i.e., $\omega_i \to \omega_i + \mathrm{i}\eta$ where $\eta \to +0$. This is the so-called adiabatic approximation. Solving the integral in Eq. (C.3), we obtain

$$z(t) = \sum_i y_i(t) \, \frac{\mathrm{i}}{\omega_i - \Omega + \mathrm{i}\eta}. \tag{C.4}$$

We can now use that, for $\eta \to +0$,

$$\frac{1}{\omega_i - \Omega + \mathrm{i}\eta} \to -\mathrm{i}\pi\delta\left(\omega_i - \Omega\right) + \mathcal{P}\left(\frac{1}{\omega_i - \Omega}\right), \tag{C.5}$$

where $\mathcal{P}$ denotes the principal value. The solution to Eq. (C.1) within Markov and adiabatic approximations may therefore be expressed as

$$z(t) = \sum_i \left[\pi\delta\left(\omega_i - \Omega\right) + \mathrm{i}\mathcal{P}\left(\frac{1}{\omega_i - \Omega}\right)\right] y_i(t). \tag{C.6}$$

This is also known as the semiclassical solution to Eq. (C.1). The imaginary part of the first factor on the right-hand side of Eq. (C.6), which involves the principal value, leads to polaron shifts in energies. When the result embodied in Eq. (C.6) is further used within the density matrix theory, it is a common practice to neglect the principal value in Eq. (C.6) and retain only the part involving the delta function.

Appendix D

Further Details about Closing the Hierarchy of Equations

D.1 Closing the Phonon Branch of the Hierarchy

Similarly to the main text, here, we concentrate on closing the phonon branch of the hierarchy that emerges from density matrices $n_{\bar{x}x}$. Essentially the same procedure should be applied to close the phonon branch that stems from density matrices y_x.

As we have already emphasized, the expressions for two-phonon-assisted density matrices cited in the main text [Eq. (3.74) and a similar expression for $\delta n_{\bar{x}x\rho^+\sigma^+}$] should be inserted in Eq. (3.69). This insertion is accompanied by the random phase approximation, that is introduced and justified in this appendix. To this end, let us note that, whenever we deal with a translationally symmetric system, the eigenstates of a single electron–hole pair, which are introduced in Sec. 2.2, can always be described similarly to Wannier excitons. As demonstrated in greater detail in Ch. 2 of Ref. [86], the eigenstates of an electron–hole pair are then characterized by the center-of-mass wave vector $\mathbf{K}$ and the integer quantum number ν that describes the internal motion of the pair. The fact that $\mathbf{K}$ and ν unambiguously classify exciton states can be derived without resorting to approximations (e.g., the effective mass approximation and the approximations on Coulomb integrals) we introduced in Sec. 2.3.1, i.e., just by using the translational symmetry of the system. In general, there is no simple analytic expression for the exciton binding energy as a function of ν that is similar to Eq. (2.76). Nevertheless, the fact that, in a translationally symmetric system, a general exciton index x may be replaced by combination $(\mathbf{K},\nu)$ is sufficient to achieve certain simplifications in the theory.

When the system possesses translational symmetry, only the density matrices for which the total created wave vector is equal to the total annihilated wave vector can acquire nontrivial values in the course of the system's evolution, see, e.g., Ref. [102]. In this sense, single-phonon-assisted density matrices $n_{(\overline{\mathbf{Q}}\overline{\nu})(\mathbf{Q}\nu)\mathbf{q}_\mu^+}$ exhibit nontrivial time evolution provided that the condition $\overline{\mathbf{Q}}+\mathbf{q}_\mu=\mathbf{Q}$ is satisfied. The carrier–phonon matrix elements in exciton representation $\Gamma^{\mathbf{q}_\mu}_{(\overline{\mathbf{Q}}\overline{\nu})(\mathbf{Q}\nu)}$ are nonzero only when $\mathbf{Q}=\overline{\mathbf{Q}}+\mathbf{q}_\mu$. Having these remarks in mind, the insertion of Eq. (3.74) into the first term describing the coupling of single-phonon-assisted density matrix $n_{(\overline{\mathbf{Q}}\overline{\nu})(\mathbf{Q}\nu)\mathbf{q}_\mu^+}$ to higher-order phonon-assisted density matrices [Eq. (3.69)] gives

$$
\begin{aligned}
&-\frac{1}{\mathrm{i}\hbar}\sum_{\rho\bar{x}'}\Gamma^{\rho*}_{\bar{x}\bar{x}'}\delta n_{\bar{x}'x\mu^+\rho^-}\\
&=\frac{\pi}{\hbar}\sum_{\mathbf{q}_\rho,\nu',\overline{\nu}'}\Gamma^{\mathbf{q}_\rho*}_{(\mathbf{Q}-\mathbf{q}_\mu,\overline{\nu})(\mathbf{Q}-\mathbf{q}_\mu+\mathbf{q}_\rho,\overline{\nu}')}\Gamma^{\mathbf{q}_\rho}_{(\mathbf{Q},\nu)(\mathbf{Q}+\mathbf{q}_\rho,\nu')}(1+n^{\mathrm{ph}}_{\mathbf{q}_\rho})\times\\
&\qquad\qquad\times\delta(\hbar\omega_{(\mathbf{Q}+\mathbf{q}_\rho,\nu')}-\hbar\omega_{(\mathbf{Q},\nu)}-\hbar\omega_{\mathbf{q}_\rho})n_{(\mathbf{Q}-\mathbf{q}_\mu+\mathbf{q}_\rho,\overline{\nu}')(\mathbf{Q}+\mathbf{q}_\rho,\nu')\mathbf{q}_\mu^+}\\
&-\frac{\pi}{\hbar}\sum_{\mathbf{q}_\rho,\overline{\nu}',\overline{\nu}''}\Gamma^{\mathbf{q}_\rho*}_{(\mathbf{Q}-\mathbf{q}_\mu,\overline{\nu})(\mathbf{Q}-\mathbf{q}_\mu+\mathbf{q}_\rho,\overline{\nu}')}\Gamma^{\mathbf{q}_\rho}_{(\mathbf{Q}-\mathbf{q}_\mu,\overline{\nu}'')(\mathbf{Q}-\mathbf{q}_\mu+\mathbf{q}_\rho,\overline{\nu}')}n^{\mathrm{ph}}_{\mathbf{q}_\rho}\times\\
&\qquad\qquad\times\delta(\hbar\omega_{(\mathbf{Q}-\mathbf{q}_\mu+\mathbf{q}_\rho,\overline{\nu}')}-\hbar\omega_{(\mathbf{Q}-\mathbf{q}_\mu,\overline{\nu}'')}-\hbar\omega_{\mathbf{q}_\rho})n_{(\mathbf{Q}-\mathbf{q}_\mu,\overline{\nu}'')(\mathbf{Q}\nu)\mathbf{q}_\mu^+}\\
&-\frac{\pi}{\hbar}\sum_{\mathbf{q}_\rho,\overline{\nu}',\overline{\nu}''}\Gamma^{\mathbf{q}_\rho*}_{(\mathbf{Q}-\mathbf{q}_\mu,\overline{\nu})(\mathbf{Q}-\mathbf{q}_\mu+\mathbf{q}_\rho,\overline{\nu}')}\Gamma^{\mathbf{q}_\mu*}_{(\mathbf{Q}-\mathbf{q}_\mu+\mathbf{q}_\rho,\overline{\nu}')(\mathbf{Q}+\mathbf{q}_\rho,\overline{\nu}'')}(1+n^{\mathrm{ph}}_{\mathbf{q}_\mu})\times\\
&\qquad\qquad\times\delta(\hbar\omega_{(\mathbf{Q}+\mathbf{q}_\rho,\overline{\nu}'')}-\hbar\omega_{(\mathbf{Q}-\mathbf{q}_\mu+\mathbf{q}_\rho,\overline{\nu}')}-\hbar\omega_{\mathbf{q}_\mu})n^{*}_{(\mathbf{Q},\nu)(\mathbf{Q}+\mathbf{q}_\rho,\overline{\nu}'')\mathbf{q}_\rho^+}\\
&+\frac{\pi}{\hbar}\sum_{\mathbf{q}_\rho,\nu',\overline{\nu}'}\Gamma^{\mathbf{q}_\rho*}_{(\mathbf{Q}-\mathbf{q}_\mu,\overline{\nu})(\mathbf{Q}-\mathbf{q}_\mu+\mathbf{q}_\rho,\overline{\nu}')}\Gamma^{\mathbf{q}_\mu*}_{(\mathbf{Q}-\mathbf{q}_\mu,\nu')(\mathbf{Q},\nu)}n^{\mathrm{ph}}_{\mathbf{q}_\mu}\times\\
&\qquad\qquad\times\delta(\hbar\omega_{(\mathbf{Q},\nu)}-\hbar\omega_{(\mathbf{Q}-\mathbf{q}_\mu,\nu')}-\hbar\omega_{\mathbf{q}_\mu})n^{*}_{(\mathbf{Q}-\mathbf{q}_\mu,\overline{\nu}')(\mathbf{Q}-\mathbf{q}_\mu+\mathbf{q}_\rho,\nu')\mathbf{q}_\rho^+}
\end{aligned}
\tag{D.1}
$$

In the first, the third, and the fourth sums in the previous equation we perform summation of terms which involve complex-valued single-phonon-assisted electronic density matrices over the wave vector $\mathbf{q}_\rho$, whereas in the second sum the summation is not carried out over any of the wave vectors describing the density matrix. In the lowest approximation, we can assume that all the sums apart from the second one are negligible due to random phases at different wave vectors. For the sake of simplicity, in the second sum we keep only the contribution for $\bar{\nu}'' = \bar{\nu}$, thus expressing the coupling to higher-phonon-assisted density matrices only in terms of the single-phonon-assisted density matrix for which the equation is formed. Restoring the more general notation, we obtain the result

$$-\frac{1}{\mathrm{i}\hbar}\sum_{\rho\bar{x}'}\Gamma^{\rho*}_{\bar{x}\bar{x}'}\delta n_{\bar{x}'x\mu^+\rho^-} = -\frac{\pi}{\hbar}\left(\sum_{\rho\tilde{x}}|\Gamma^{\rho}_{\bar{x}\tilde{x}}|^2 n^{\mathrm{ph}}_{\rho}\delta(\hbar\omega_{\bar{x}} - \hbar\omega_{\tilde{x}} + \hbar\omega_{\rho})\right) n_{\bar{x}x\mu^+}. \tag{D.2}$$

Repeating similar procedure with the remaining three terms which describe coupling to density matrices with higher-order phonon assistance in Eq. (3.69), we obtain the result embodied in Eqs. (3.76)−(3.78).

Analogously, the following results for two-phonon-assisted electronic density matrices $\delta y_{x\rho^+\sigma^-}$ and $\delta y_{x\rho^+\sigma^+}$ are obtained, solving their respective differential equations in the Markov and adiabatic approximations

$$\begin{aligned}\delta y_{x\rho^+\sigma^-} = {} & (1 + n^{\mathrm{ph}}_{\sigma})\sum_{x'}\Gamma^{\sigma}_{xx'}\mathcal{D}(\hbar\omega_{x'} - \hbar\omega_{x} - \hbar\omega_{\sigma})y_{x'\rho^+} \\ & - n^{\mathrm{ph}}_{\rho}\sum_{x'}\Gamma^{\rho*}_{x'x}\mathcal{D}^*(\hbar\omega_{x} - \hbar\omega_{x'} - \hbar\omega_{\rho})y_{x'\sigma^-},\end{aligned} \tag{D.3}$$

where function $\mathcal{D}(\epsilon)$ is defined in Eq. (3.75). A similar expression is obtained for the variable $\delta y_{x\rho^+\sigma^+}$. Inserting the results obtained in Eqs. (3.67) and (3.68) and performing the random phase approximation as described, the result given in Eqs. (3.81) and (3.82) is obtained.

D.2 Comments on the Energy Conservation

This part of the appendix is devoted to further comments regarding the energy conservation after the pulsed excitation in our model.

Using Eqs. (3.56), (3.57), (3.49), and (3.63), we obtain the rate at which the energy of carriers and phonons changes after the pulse

$$\partial_t\left(\mathcal{E}_{\mathrm{c}} + \mathcal{E}_{\mathrm{p}}\right) = -\frac{2}{\hbar}\sum_{\mu\bar{x}x}(\hbar\omega_{x} - \hbar\omega_{\bar{x}} - \hbar\omega_{\mu})\mathrm{Im}\{\Gamma^{\mu}_{\bar{x}x}n_{\bar{x}x\mu^+}\}, \tag{D.4}$$

which exactly cancels the part from $\partial_t\,\mathcal{E}_{\mathrm{c-p}}$ [see Eq. (3.58)] that originates from the free rotation term $-\mathrm{i}(\omega_x - \omega_{\bar{x}} - \omega_\mu)n_{\bar{x}x\mu^+}$ in Eq. (3.66). The terms in $\partial_t\,\mathcal{E}_{\mathrm{c-ph}}$ that arise from the second and third terms on the right-hand side of Eq. (3.66) are identically equal to zero each since they are purely real, which is easily checked. Therefore, the rate at which the total energy changes after the pulse is equal to the rate at which the carrier-phonon interaction energy changes due to the coupling of single-phonon-assisted to higher-order phonon-assisted density matrices, $(\partial_t\,\mathcal{E}_{\mathrm{c-p}})_{\mathrm{higher}}$, which is equal to [see Eq. (3.69)]

$$\begin{aligned}(\partial_t\,\mathcal{E}) &= (\partial_t\,\mathcal{E}_{\mathrm{c-p}})_{\mathrm{higher}}\\ &= -\frac{2}{\hbar}\mathrm{Im}\left\{\sum_{\substack{\mu\bar{x}x\\ \rho\bar{x}'}}\Gamma^{\mu}_{\bar{x}x}\Gamma^{\rho*}_{\bar{x}\bar{x}'}\delta n_{\bar{x}'x\mu^+\rho^-}\right\} - \frac{2}{\hbar}\mathrm{Im}\left\{\sum_{\substack{\mu\bar{x}x\\ \rho\bar{x}'}}\Gamma^{\mu}_{\bar{x}x}\Gamma^{\rho}_{\bar{x}'\bar{x}}\delta n_{\bar{x}'x\mu^+\rho^+}\right\}\\ &\quad+\frac{2}{\hbar}\mathrm{Im}\left\{\sum_{\substack{\mu\bar{x}x\\ \rho x'}}\Gamma^{\mu}_{\bar{x}x}\Gamma^{\rho*}_{x'x}\delta n_{\bar{x}x'\mu^+\rho^-}\right\} + \frac{2}{\hbar}\mathrm{Im}\left\{\sum_{\substack{\mu\bar{x}x\\ \rho x'}}\Gamma^{\mu}_{\bar{x}x}\Gamma^{\rho}_{xx'}\delta n_{\bar{x}x'\mu^+\rho^+}\right\}.\end{aligned} \tag{D.5}$$

The first and the third terms on the right-hand side of Eq. (D.5) are separately equal to zero (since the quantities under the sign of the imaginary part are purely real), whereas the second and the fourth terms exactly cancel each other, so the total energy is conserved. In particular, this is true for the form of the correlated parts of two-phonon-assisted density matrix $\delta n_{\bar{x}x\rho^+\sigma^-}$ given in Eq. (3.74) and the similar form of the density matrix $\delta n_{\bar{x}x\rho^+\sigma^+}$. In Eq. (D.5), all the sums are performed over all indices that are present in a particular expression, so the crux of the proof that the energy is conserved is the interchange of dummy indices combined with the properties $\delta n^*_{\bar{x}x\rho^+\sigma^-} = \delta n_{x\bar{x}\sigma^+\rho^-}$ and $\delta n_{\bar{x}x\rho^+\sigma^+} = \delta n_{\bar{x}x\sigma^+\rho^+}$. However, when we apply the random phase approximation, the aforementioned properties are lost and the energy is not conserved any more. For example, the first term on the right-hand side in Eq. (D.5) after performing the random phase approximation is not equal to zero, but to

$$-\frac{2\pi}{\hbar}\left(\sum_{\rho\tilde{x}}|\Gamma^{\rho}_{\bar{x}\tilde{x}}|^2 n^{\mathrm{ph}}_{\rho}\delta(\hbar\omega_{\tilde{x}} - \hbar\omega_{\bar{x}} + \hbar\omega_\rho)\right)\mathrm{Re}\left\{\sum_{\mu\bar{x}x}\Gamma^{\mu}_{\bar{x}x}n_{\bar{x}x\mu^+}\right\}$$

[see Eq. (D.2)], which is just one term of the total rate $(\partial_t \mathcal{E}_{\mathrm{c-p}})_{\mathrm{higher}}$ when we use the result from Eq. (3.76).

Bibliography

[1] *Renewable energy...into the mainstream* (International Energy Agency's Renewable Energy Working Party, 2002).

[2] *Key world energy statistics* (International Energy Agency, 2017).

[3] "L'energia nella scuola Numero 4: Fotovoltaico", Giornale di fisica della Società italiana di fisica, serie speciale (2012).

[4] A.-E. Becquerel, "Mémoire sur les effets électriques produits sous l'influence des rayons solaires", Comptes Rendus **9**, 561–567 (1839).

[5] P. Würfel and U. Würfel, *Physics of solar cells: From basic principles to advanced concepts* (Wiley-VCH Verlag GmbH & Co. KGaA, 2016).

[6] A. Köhler and H. Bässler, *Electronic processes in organic semiconductors: An introduction* (Wiley-VCH Verlag GmbH & Co. KGaA, 2015).

[7] S. H. Park, A. Roy, S. Beaupré, S. Cho, N. Coates, J. S. Moon, D. Moses, M. Leclerc, K. Lee, and A. J. Heeger, "Bulk heterojunction solar cells with internal quantum efficiency approaching 100%", Nat. Photonics **3**, 297–303 (2009).

[8] D. M. Chapin, C. S. Fuller, and G. L. Pearson, "A new silicon p–n junction photocell for converting solar radiation into electrical power", J. Appl. Phys. **25**, 676–677 (1954).

[9] N. W. Ashcroft and N. D. Mermin, *Solid state physics* (Saunders College, Philadelphia, 1976).

[10] C. J. Brabec, J. A. Hauch, P. Schilinsky, and C. Waldauf, "Production aspects of organic photovoltaics and their impact on the commercialization of devices", MRS Bulletin **30**, 50–52 (2005).

[11] G. Chamberlain, “Organic solar cells: A review”, Sol. Cells **8**, 47–83 (1983).

[12] C. W. Tang, “Two-layer organic photovoltaic cell”, Appl. Phys. Lett. **48**, 183–185 (1986).

[13] W. Zhao, S. Li, H. Yao, S. Zhang, Y. Zhang, B. Yang, and J. Hou, “Molecular optimization enables over 13% efficiency in organic solar cells”, J. Am. Chem. Soc. **139**, 7148–7151 (2017).

[14] H. Bässler and A. Köhler, “"Hot or cold": How do charge transfer states at the donor–acceptor interface of an organic solar cell dissociate?”, Phys. Chem. Chem. Phys. **17**, 28451–28462 (2015).

[15] H. Bässler and A. Köhler, “Charge transport in organic semiconductors”, in *Unimolecular and supramolecular electronics I. Topics in current chemistry, vol 312.* Edited by R. M. Metzger (Springer Berlin Heidelberg, 2012).

[16] M. Mladenović and N. Vukmirović, “Charge carrier localization and transport in organic semiconductors: Insights from atomistic multiscale simulations”, Adv. Funct. Mater. **25**, 1915–1932.

[17] M. Pope and C. E. Swenberg, *Electronic processes in organic crystals and polymers* (Oxford University Press, Oxford, 1999).

[18] V. Coropceanu, J. Cornil, D. A. da Silva Filho, Y. Olivier, R. Silbey, and J.-L. Brédas, “Charge transport in organic semiconductors”, Chem. Rev. **107**, 926–952 (2007).

[19] Y. C. Cheng, R. J. Silbey, D. A. da Silva Filho, J. P. Calbert, J. Cornil, and J. L. Brédas, “Three-dimensional band structure and bandlike mobility in oligoacene single crystals: A theoretical investigation”, J. Chem. Phys. **118**, 3764–3774 (2003).

[20] D. L. Cheung and A. Troisi, “Theoretical study of the organic photovoltaic electron acceptor PCBM: Morphology, electronic structure, and charge localization”, J. Phys. Chem. C **114**, 20479–20488 (2010).

[21] R. E. Peierls, *Quantum theory of solids* (Oxford University Press Inc., New York, 2001).

[22] A. J. Heeger, S. Kivelson, J. R. Schrieffer, and W. P. Su, “Solitons in conducting polymers”, Rev. Mod. Phys. **60**, 781–850 (1988).

[23] M. Mladenović and N. Vukmirović, “Effects of thermal disorder on the electronic properties of ordered polymers”, Phys. Chem. Chem. Phys. **16**, 25950–25958 (2014).

[24] A. Maillard and A. Rochefort, “Structural and electronic properties of poly(3-hexylthiophene) π-stacked crystals”, Phys. Rev. B **79**, 115207 (2009).

[25] J. E. Northrup, “Atomic and electronic structure of polymer organic semiconductors: P3HT, PQT, and PBTTT”, Phys. Rev. B **76**, 245202 (2007).

[26] R. A. Street, S. A. Hawks, P. P. Khlyabich, G. Li, B. J. Schwartz, B. C. Thompson, and Y. Yang, “Electronic structure and transition energies in polymer–fullerene bulk heterojunctions”, J. Phys. Chem. C **118**, 21873–21883 (2014).

[27] I.-W. Hwang, C. Soci, D. Moses, Z. Zhu, D. Waller, R. Gaudiana, C. Brabec, and A. Heeger, “Ultrafast electron transfer and decay dynamics in a small band gap bulk heterojunction material”, Adv. Mater. **19**, 2307–2312 (2007).

[28] J.-L. Brédas, J. E. Norton, J. Cornil, and V. Coropceanu, “Molecular understanding of organic solar cells: The challenges”, Acc. Chem. Res. **42**, 1691–1699 (2009).

[29] G. Yu, J. Gao, J. C. Hummelen, F. Wudl, and A. J. Heeger, “Polymer photovoltaic cells: Enhanced efficiencies via a network of internal donor–acceptor heterojunctions”, Science **270**, 1789–1791 (1995).

[30] N. S. Sariciftci, L. Smilowitz, A. J. Heeger, and F. Wudl, “Photoinduced electron transfer from a conducting polymer to buckminsterfullerene”, Science **258**, 1474–1476 (1992).

[31] T. M. Clarke and J. R. Durrant, “Charge photogeneration in organic solar cells”, Chem. Rev. **110**, 6736–6767 (2010).

[32] Y. Tamai, H. Ohkita, H. Benten, and S. Ito, “Exciton diffusion in conjugated polymers: From fundamental understanding to improvement in photovoltaic conversion efficiency”, J. Phys. Chem. Lett. **6**, 3417–3428 (2015).

[33] S. R. Cowan, N. Banerji, W. L. Leong, and A. J. Heeger, “Charge formation, recombination, and sweep-out dynamics in organic solar cells”, Adv. Funct. Mater. **22**, 1116–1128 (2012).

[34] C. Deibel, T. Strobel, and V. Dyakonov, “Role of the charge transfer state in organic donor–acceptor solar cells”, Adv. Mater. **22**, 4097–4111.

[35] C. J. Brabec, G. Zerza, G. Cerullo, S. D. Silvestri, S. Luzzati, J. C. Hummelen, and S. Sariciftci, “Tracing photoinduced electron transfer process in conjugated polymer/fullerene bulk heterojunctions in real time”, Chem. Phys. Lett. **340**, 232–236 (2001).

[36] G. Grancini, M. Maiuri, D. Fazzi, A. Petrozza, H.-J. Egelhaaf, D. Brida, G. Cerullo, and G. Lanzani, “Hot exciton dissociation in polymer solar cells”, Nat. Mater. **12**, 29–33 (2013).

[37] A. E. Jailaubekov, A. P. Willard, J. R. Tritsch, W.-L. Chan, N. Sai, R. Gearba, L. G. Kaake, K. J. Williams, K. Leung, P. J. Rossky, and X.-Y. Zhu, “Hot charge-transfer excitons set the time limit for charge separation at donor/acceptor interfaces in organic photovoltaics”, Nat. Mater. **12**, 66–73 (2013).

[38] S. Gélinas, A. Rao, A. Kumar, S. L. Smith, A. W. Chin, J. Clark, T. S. van der Poll, G. C. Bazan, and R. H. Friend, “Ultrafast long-range charge separation in organic semiconductor photovoltaic diodes”, Science **343**, 512–516 (2014).

[39] A. A. Paraecattil and N. Banerji, “Charge separation pathways in a highly efficient polymer: fullerene solar cell material”, J. Am. Chem. Soc. **136**, 1472–1482 (2014).

[40] F. Gao and O. Inganäs, “Charge generation in polymer–fullerene bulk-heterojunction solar cells”, Phys. Chem. Chem. Phys. **16**, 20291–20304 (2014).

[41] O. Ostroverkhova, “Organic optoelectronic materials: Mechanisms and applications”, Chem. Rev. **116**, 13279–13412 (2016).

[42] C. S. Ponseca, P. Chábera, J. Uhlig, P. Persson, and V. Sundström, “Ultrafast electron dynamics in solar energy conversion”, Chem. Rev. **117**, 10940–11024 (2017).

[43] S. Few, J. M. Frost, and J. Nelson, “Models of charge pair generation in organic solar cells”, Phys. Chem. Chem. Phys. **17**, 2311–2325 (2015).

[44] A. J. Heeger, “Nature of the primary photo-excitations in poly (arylene-vinylenes): Bound neutral excitons or charged polaron pairs”, in *Primary photoexcitations in conjugated polymers: Molecular exciton versus semiconductor band model*, edited by N. S. Sariciftci (World Scientific, 1998).

[45] H. Bässler, “Excitons in conjugated polymers”, in *Primary photoexcitations in conjugated polymers: Molecular exciton versus semiconductor band model*, edited by N. S. Sariciftci (World Scientific, 1998).

[46] N. Banerji, S. Cowan, M. Leclerc, E. Vauthey, and A. J. Heeger, “Exciton formation, relaxation, and decay in PCDTBT”, J. Am. Chem. Soc. **132**, 17459–17470 (2010).

[47] N. Banerji, S. Cowan, E. Vauthey, and A. J. Heeger, “Ultrafast relaxation of the poly(3-hexylthiophene) emission spectrum”, J. Phys. Chem. C **115**, 9726–9739 (2011).

[48] A. A. Bakulin, A. Rao, V. G. Pavelyev, P. H. M. van Loosdrecht, M. S. Pshenichnikov, D. Niedzialek, J. Cornil, D. Beljonne, and R. H. Friend, “The role of driving energy and delocalized states for charge separation in organic semiconductors”, Science **335**, 1340–1344 (2012).

[49] A. Troisi, “How quasi-free holes and electrons are generated in organic photovoltaic interfaces”, Faraday Discuss. **163**, 377–392 (2013).

[50] H. Vázquez and A. Troisi, “Calculation of rates of exciton dissociation into hot charge-transfer states in model organic photovoltaic interfaces”, Phys. Rev. B **88**, 205304 (2013).

[51] B. M. Savoie, A. Rao, A. A. Bakulin, S. Gelinas, B. Movaghar, R. H. Friend, T. J. Marks, and M. A. Ratner, “Unequal partnership: Asymmetric roles of polymeric donor and fullerene acceptor in generating free charge”, J. Am. Chem. Soc. **136**, 2876–2884 (2014).

[52] Z. Sun and S. Stafström, “Dynamics of charge separation at an organic donor-acceptor interface”, Phys. Rev. B **90**, 115420 (2014).

[53] G. Nan, X. Zhang, and G. Lu, “Do "hot" charge-transfer excitons promote free carrier generation in organic photovoltaics?”, J. Phys. Chem. C **119**, 15028–15035 (2015).

[54] H. Tamura, I. Burghardt, and M. Tsukada, “Exciton dissociation at thiophene/fullerene interfaces: The electronic structures and quantum dynamics”, J. Phys. Chem. C **115**, 10205–10210 (2011).

[55] H. Tamura, R. Martinazzo, M. Ruckenbauer, and I. Burghardt, “Quantum dynamics of ultrafast charge transfer at an oligothiophene-fullerene heterojunction”, J. Chem. Phys. **137**, 22A540 (2012).

[56] H. Tamura and I. Burghardt, “Ultrafast charge separation in organic photovoltaics enhanced by charge delocalization and vibronically hot exciton dissociation”, J. Am. Chem. Soc. **135**, 16364–16367 (2013).

[57] E. R. Bittner and C. Silva, “Noise-induced quantum coherence drives photo-carrier generation dynamics at polymeric semiconductor heterojunctions”, Nat. Commun. **5**, 3119 (2014).

[58] S. L. Smith and A. W. Chin, “Phonon-assisted ultrafast charge separation in the PCBM band structure”, Phys. Rev. B **91**, 201302 (2015).

[59] M. Huix-Rotllant, H. Tamura, and I. Burghardt, “Concurrent effects of delocalization and internal conversion tune charge separation at regioregular polythiophene–fullerene heterojunctions”, J. Phys. Chem. Lett. **6**, 1702–1708 (2015).

[60] J. Lee, K. Vandewal, S. R. Yost, M. E. Bahlke, L. Goris, M. A. Baldo, J. V. Manca, and T. V. Voorhis, “Charge transfer state versus hot exciton dissociation in polymer–fullerene blended solar cells”, J. Am. Chem. Soc. **132**, 11878–11880 (2010).

[61] K. Vandewal, S. Albrecht, E. T. Hoke, K. R. Graham, J. Widmer, J. D. Douglas, M. Schubert, W. R. Mateker, J. T. Bloking, G. F. Burkhard, A. Sellinger, J. M. J. Fréchet, A. Amassian, M. K. Riede, M. D. McGehee, D. Neher, and A. Salleo, “Efficient charge generation by relaxed charge-transfer states at organic interfaces”, Nat. Mater. **13**, 63–68 (2014).

[62] D. A. Vithanage, A. Devižis, V. Abramavičius, Y. Infahsaeng, D. Abramavičius, R. C. I. MacKenzie, P. E. Keivanidis, A. Yartsev, D. Hertel, J. Nelson, V. Sundström, and V.

Gulbinas, "Visualizing charge separation in bulk heterojunction organic solar cells", Nat. Commun. **4**, 2334 (2013).

[63] A. Devižis, J. De Jonghe-Risse, R. Hany, F. Nüesch, S. Jenatsch, V. Gulbinas, and J.-E. Moser, "Dissociation of charge transfer states and carrier separation in bilayer organic solar cells: A time-resolved electroabsorption spectroscopy study", J. Am. Chem. Soc. **137**, 8192–8198 (2015).

[64] L. Onsager, "Initial recombination of ions", Phys. Rev. **54**, 554–557 (1938).

[65] C. L. Braun, "Electric field assisted dissociation of charge transfer states as a mechanism of photocarrier production", J. Chem. Phys. **80**, 4157–4161 (1984).

[66] C. Schwarz, S. Tscheuschner, J. Frisch, S. Winkler, N. Koch, H. Bässler, and A. Köhler, "Role of the effective mass and interfacial dipoles on exciton dissociation in organic donor-acceptor solar cells", Phys. Rev. B **87**, 155205 (2013).

[67] S. D. Baranovskii, M. Wiemer, A. V. Nenashev, F. Jansson, and F. Gebhard, "Calculating the efficiency of exciton dissociation at the interface between a conjugated polymer and an electron acceptor", J. Phys. Chem. Lett. **3**, 1214–1221 (2012).

[68] S. Athanasopoulos, S. Tscheuschner, H. Bässler, and A. Köhler, "Efficient charge separation of cold charge-transfer states in organic solar cells through incoherent hopping", J. Phys. Chem. Lett. **8**, 2093–2098 (2017).

[69] T. M. Burke and M. D. McGehee, "How high local charge carrier mobility and an energy cascade in a three-phase bulk heterojunction enable >90% quantum efficiency", Adv. Mater. **26**, 1923–1928 (2014).

[70] H. van Eersel, R. A. J. Janssen, and M. Kemerink, "Mechanism for efficient photoinduced charge separation at disordered organic heterointerfaces", Adv. Funct. Mater. **22**, 2700–2708 (2012).

[71] V. M. Axt and S. Mukamel, "Nonlinear optics of semiconductor and molecular nanostructures: A common perspective", Rev. Mod. Phys. **70**, 145–174 (1998).

[72] F. Rossi and T. Kuhn, “Theory of ultrafast phenomena in photoexcited semiconductors”, Rev. Mod. Phys. **74**, 895–950 (2002).

[73] V. M. Axt and T. Kuhn, “Femtosecond spectroscopy in semiconductors: A key to coherences, correlations and quantum kinetics”, Rep. Prog. Phys. **67**, 433 (2004).

[74] A. Stahl and I. Balslev, *Electrodynamics of the semiconductor band edge* (Springer-Verlag Berlin Heidelberg, 1987).

[75] T. Meier, P. Thomas, and S. Koch, *Coherent semiconductor optics* (Springer-Verlag Berlin Heidelberg, 2007).

[76] E. Hanamura and H. Haug, “Condensation effects of excitons”, Phys. Rep. **33**, 209–284 (1977).

[77] W. Barford, *Electronic and optical properties of conjugated polymers* (Oxford University Press Inc., New York, 2005).

[78] S. Abe, J. Yu, and W. P. Su, “Singlet and triplet excitons in conjugated polymers”, Phys. Rev. B **45**, 8264–8271 (1992).

[79] D. Beljonne, Z. Shuai, G. Pourtois, and J. L. Brédas, “Spin–orbit coupling and intersystem crossing in conjugated polymers: A configuration interaction description”, J. Phys. Chem. A **105**, 3899–3907 (2001).

[80] A. Köhler and H. Bässler, “Triplet states in organic semiconductors”, Mater. Sci. Eng., R **66**, 71–109 (2009).

[81] G. H. Wannier, “The structure of electronic excitation levels in insulating crystals”, Phys. Rev. **52**, 191–197 (1937).

[82] J. Frenkel, “On the transformation of light into heat in solids. I”, Phys. Rev. **37**, 17–44 (1931).

[83] J. Frenkel, “On the transformation of light into heat in solids. II”, Phys. Rev. **37**, 1276–1294 (1931).

[84] H. Haken, *Quantum field theory of solids: An introduction* (North-Holland Publishing Company, 1976).

[85] M. Combescot and W. Pogosov, "Microscopic derivation of Frenkel excitons in second quantization", Phys. Rev. B **77**, 085206 (2008).

[86] R. S. Knox, *Theory of excitons* (Academic Press, 1963).

[87] W. Huhn and A. Stahl, "Self-consistent field theory applied to the semiconductor band edge", Phys. Status Solidi B **124**, 167–177 (1984).

[88] T. Förster, "Delocalized excitation and excitation transfer", in *Bulletin No. 18, Division of biology and medicine* (U. S. Atomic Energy Commission, 1965).

[89] V. Janković and N. Vukmirović, "Dynamics of exciton formation and relaxation in photoexcited semiconductors", Phys. Rev. B **92**, 235208 (2015).

[90] T. Kuhn, "Density matrix theory of coherent ultrafast dynamics", in *Theory of transport properties of semiconductor nanostructures*, edited by E. Schöll (Chapman and Hall, London, 1998).

[91] F. Rossi, *Theory of semiconductor quantum devices: Microscopic modeling and simulation strategies* (Springer-Verlag Berlin Heidelberg, 2011).

[92] L. P. Kadanoff and G. Baym, *Quantum statistical mechanics* (Benjamin, New York, 1962).

[93] L. V. Keldysh, "Diagram technique for nonequilibrium processes", Sov. Phys. JETP **20**, 1018–1026 (1965).

[94] H. Haug and A.-P. Jauho, *Quantum kinetics in transport and optics of semiconductors* (Springer, Berlin, 1996).

[95] A. V. Kuznetsov, "Interaction of ultrashort light pulses with semiconductors: Effective Bloch equations with relaxation and memory effects", Phys. Rev. B **44**, 8721–8744 (1991).

[96] H. Haug, "Interband quantum kinetics with LO-phonon scattering in a laser-pulse-excited semiconductor I. Theory", Phys. Status Solidi B **173**, 139–148 (1992).

[97] L. Bányai, D. B. T. Thoai, C. Remling, and H. Haug, “Interband quantum kinetics with lo-phonon scattering in a laser-pulse-excited semiconductor II. Numerical studies”, Phys. Status Solidi B **173**, 149–157 (1992).

[98] R. Balescu, *Equilibrium and nonequilibrium statistical mechanics* (John Willey and Sons New York, 1975).

[99] P. E. Selbmann, M. Gulia, F. Rossi, E. Molinari, and P. Lugli, “Coupled free-carrier and exciton relaxation in optically excited semiconductors”, Phys. Rev. B **54**, 4660–4673 (1996).

[100] M. Gulia, F. Rossi, E. Molinari, P. E. Selbmann, and P. Lugli, “Phonon-assisted exciton formation and relaxation in GaAs/$\mathrm{Al}_x\mathrm{Ga}_{1-x}\mathrm{As}$ quantum wells”, Phys. Rev. B **55**, R16049–R16052 (1997).

[101] M. Kira and S. Koch, “Many-body correlations and excitonic effects in semiconductor spectroscopy”, Prog. Quant. Electron. **30**, 155–296 (2006).

[102] M. Kira and S. Koch, *Semiconductor quantum optics* (Cambridge University Press, New York, 2012).

[103] H. Haug and S. W. Koch, *Quantum theory of the optical and electronic properties of semiconductors* (World Scientific Publishing, 2004).

[104] R. J. Elliott, “Intensity of optical absorption by excitons”, Phys. Rev. **108**, 1384–1389 (1957).

[105] M. Kira, W. Hoyer, T. Stroucken, and S. W. Koch, “Exciton formation in semiconductors and the influence of a photonic environment”, Phys. Rev. Lett. **87**, 176401 (2001).

[106] W. Hoyer, M. Kira, and S. Koch, “Pair-correlation functions in incoherent electron–hole plasmas”, Phys. Status Solidi B **234**, 195–206 (2002).

[107] W. Hoyer, M. Kira, and S. W. Koch, “Influence of Coulomb and phonon interaction on the exciton formation dynamics in semiconductor heterostructures”, Phys. Rev. B **67**, 155113 (2003).

[108] V. Axt and A. Stahl, "A dynamics-controlled truncation scheme for the hierarchy of density matrices in semiconductor optics", Z. Phys. B **93**, 195–204 (1994).

[109] V. Axt and A. Stahl, "The role of the biexciton in a dynamic density matrix theory of the semiconductor band edge", Z. Phys. B **93**, 205–211 (1994).

[110] K. Victor, V. M. Axt, and A. Stahl, "Hierarchy of density matrices in coherent semiconductor optics", Phys. Rev. B **51**, 14164–14175 (1995).

[111] V. M. Axt, K. Victor, and A. Stahl, "Influence of a phonon bath on the hierarchy of electronic densities in an optically excited semiconductor", Phys. Rev. B **53**, 7244–7258 (1996).

[112] M. Lindberg, Y. Z. Hu, R. Binder, and S. W. Koch, "$\chi^{(3)}$ formalism in optically excited semiconductors and its applications in four-wave-mixing spectroscopy", Phys. Rev. B **50**, 18060–18072 (1994).

[113] J. Shah, *Ultrafast spectroscopy of semiconductors and semiconductor nanostructures* (Springer-Verlag Berlin Heidelberg, 1999).

[114] J. J. Sakurai and J. Napolitano, *Modern quantum mechanics, second edition* (Addison-Wesley, 2011).

[115] K. Siantidis, V. M. Axt, and T. Kuhn, "Dynamics of exciton formation for near band-gap excitations", Phys. Rev. B **65**, 035303 (2001).

[116] K Siantidis, T Wolterink, V. Axt, and T Kuhn, "Formation of excitons from correlated electron–hole pairs", Physica B **314**, 220–223 (2002).

[117] K Siantidis, V. Axt, J Wühr, and T Kuhn, "Theory of exciton formation and relaxation in quantum wires", Phys. Status Solidi A **190**, 743–747 (2002).

[118] T. Kuhn and F. Rossi, "Monte Carlo simulation of ultrafast processes in photoexcited semiconductors: Coherent and incoherent dynamics", Phys. Rev. B **46**, 7496–7514 (1992).

[119] J. Schilp, T. Kuhn, and G. Mahler, "Electron-phonon quantum kinetics in pulse-excited semiconductors: Memory and renormalization effects", Phys. Rev. B **50**, 5435–5447 (1994).

[120] J. Schilp, T. Kuhn, and G. Mahler, "Quantum kinetics of the coupled carrier-phonon system in photoexcited semiconductors", Phys. Status Solidi B **188**, 417–424 (1995).

[121] V. Chernyak and S. Mukamel, "Third-order optical response of intermediate excitons with fractional nonlinear statistics", J. Opt. Soc. Am. B **13**, 1302–1307 (1996).

[122] W. M. Zhang, T. Meier, V. Chernyak, and S. Mukamel, "Intraband terahertz emission from coupled semiconductor quantum wells: A model study using the exciton representation", Phys. Rev. B **60**, 2599–2609 (1999).

[123] C. Haik, T. Seiji, and T. Fumio, "Ultrafast fluorescence upconversion technique and its applications to proteins", FEBS J. **282**, 3003–3015.

[124] M. N. Kobrak and E. R. Bittner, "Quantum molecular dynamics study of polaron recombination in conjugated polymers", Phys. Rev. B **62**, 11473–11486 (2000).

[125] K. Tandon, S. Ramasesha, and S. Mazumdar, "Electron correlation effects in electron-hole recombination in organic light-emitting diodes", Phys. Rev. B **67**, 045109 (2003).

[126] N. Vukmirović, C. Bruder, and V. M. Stojanović, "Electron-phonon coupling in crystalline organic semiconductors: Microscopic evidence for nonpolaronic charge carriers", Phys. Rev. Lett. **109**, 126407 (2012).

[127] S. D. Dimitrov, B. C. Schroeder, C. B. Nielsen, H. Bronstein, Z. Fei, I. McCulloch, M. Heeney, and J. R. Durrant, "Singlet exciton lifetimes in conjugated polymer films for organic solar cells", Polymers **8**, 14 (2016).

[128] M. Levinshtein, S. Rumyantsev, and M. Shur, *Handbook series on semiconductor parameters, volume 1* (World Scientific, 1996).

[129] Y.-C. Cheng and R. J. Silbey, "A unified theory for charge-carrier transport in organic crystals", J. Chem. Phys. **128**, 114713 (2008).

[130] P. Cudazzo, F. Sottile, A. Rubio, and M. Gatti, "Exciton dispersion in molecular solids", J. Phys.: Condens. Matter **27**, 113204 (2015).

[131] A. Troisi and G. Orlandi, “Charge-transport regime of crystalline organic semiconductors: Diffusion limited by thermal off-diagonal electronic disorder”, Phys. Rev. Lett. **96**, 086601 (2006).

[132] K. Fujii, S. Kera, M. Oiwa, K. K. Okudaira, K. Sakamoto, and N. Ueno, “Influence of intramolecular vibrations in charge redistribution at the pentacene–graphite interface”, Surf. Sci. **601**, 3765–3768 (2007).

[133] W. H. Press, S. A. Teukolsky, W. T. Vetterling, and B. P. Flannery, *Numerical recipes in C: The art of scientific computing, second edition* (Cambridge University Press, 1992).

[134] V. Janković and N. Vukmirović, “Origin of space-separated charges in photoexcited organic heterojunctions on ultrafast time scales”, Phys. Rev. B **95**, 075308 (2017).

[135] C. Silva, “Some like it hot”, Nat. Mater. **12**, 5–6 (2012).

[136] I.-W. Hwang, D. Moses, and A. J. Heeger, “Photoinduced carrier generation in P3HT/PCBM bulk heterojunction materials”, J. Phys. Chem. C **112**, 4350–4354 (2008).

[137] T. Liu and A. Troisi, “What makes fullerene acceptors special as electron acceptors in organic solar cells and how to replace them”, Adv. Mater. **25**, 1038–1041 (2013).

[138] S. L. Smith and A. W. Chin, “Ultrafast charge separation and nongeminate electron–hole recombination in organic photovoltaics”, Phys. Chem. Chem. Phys. **16**, 20305–20309 (2014).

[139] S. M. Falke, C. A. Rozzi, D. Brida, M. Maiuri, M. Amato, E. Sommer, A. De Sio, A. Rubio, G. Cerullo, E. Molinari, and C. Lienau, “Coherent ultrafast charge transfer in an organic photovoltaic blend”, Science **344**, 1001–1005 (2014).

[140] H. Tamura, J. G. S. Ramon, E. R. Bittner, and I. Burghardt, “Phonon-driven ultrafast exciton dissociation at donor-acceptor polymer heterojunctions”, Phys. Rev. Lett. **100**, 107402 (2008).

[141] M. H. Lee, J. Aragó, and A. Troisi, “Charge dynamics in organic photovoltaic materials: Interplay between quantum diffusion and quantum relaxation”, J. Phys. Chem. C **119**, 14989–14998 (2015).

[142] S. Bera, N. Gheeraert, S. Fratini, S. Ciuchi, and S. Florens, "Impact of quantized vibrations on the efficiency of interfacial charge separation in photovoltaic devices", Phys. Rev. B **91**, 041107 (2015).

[143] H. Ma and A. Troisi, "Direct optical generation of long-range charge-transfer states in organic photovoltaics", Adv. Mater. **26**, 6163–6167 (2014).

[144] G. D'Avino, L. Muccioli, Y. Olivier, and D. Beljonne, "Charge separation and recombination at polymer–fullerene heterojunctions: Delocalization and hybridization effects", J. Phys. Chem. Lett. **7**, 536–540 (2016).

[145] D. Mühlbacher, M. Scharber, M. Morana, Z. Zhu, D. Waller, R. Gaudiana, and C. Brabec, "High photovoltaic performance of a low-bandgap polymer", Adv. Mater. **18**, 2884–2889 (2006).

[146] H. Tamura and M. Tsukada, "Role of intermolecular charge delocalization on electron transport in fullerene aggregates", Phys. Rev. B **85**, 054301 (2012).

[147] P. Giannozzi and *et al.*, "QUANTUM ESPRESSO: a modular and open-source software project for quantum simulations of materials", J. Phys.: Condens. Matter **21**, 395502 (2009).

[148] Y. Kanai and J. C. Grossman, "Insights on interfacial charge transfer across P3HT/fullerene photovoltaic heterojunction from ab initio calculations", Nano Lett. **7**, 1967–1972 (2007).

[149] E. R. Bittner and J. G. S. Ramon, "Exciton and charge-transfer dynamics in polymer semiconductors", in *Quantum dynamics of complex molecular systems*, edited by D. A. Micha and I. Burghardt (Springer-Verlag, Berlin Heidelberg, 2007).

[150] A. Lücke, F. Ortmann, M. Panhans, S. Sanna, E. Rauls, U. Gerstmann, and W. G. Schmidt, "Temperature-dependent hole mobility and its limit in crystal-phase P3HT calculated from first principles", J. Phys. Chem. B **120**, 5572–5580 (2016).

[151] N. Vukmirović and L.-W. Wang, "Charge carrier motion in disordered conjugated polymers: A multiscale ab initio study", Nano Lett. **9**, 3996–4000 (2009).

[152] A. Chenel, E. Mangaud, I. Burghardt, C. Meier, and M. Desouter-Lecomte, "Exciton dissociation at donor-acceptor heterojunctions: Dynamics using the collective effective mode representation of the spin-boson model", J. Chem. Phys. **140**, 044104 (2014).

[153] R. D. Pensack and J. B. Asbury, "Beyond the adiabatic limit: Charge photogeneration in organic photovoltaic materials", J. Phys. Chem. Lett. **1**, 2255–2263 (2010).

[154] S. Mukamel, *Principles of nonlinear optical spectroscopy* (Oxford University Press, New York, 1995).

[155] J. Cabanillas-Gonzalez, G. Grancini, and G. Lanzani, "Pump-probe spectroscopy in organic semiconductors: Monitoring fundamental processes of relevance in optoelectronics", Adv. Mater. **23**, 5468–5485 (2011).

[156] D. Polli, I. Rivalta, A. Nenov, O. Weingart, M. Garavelli, and G. Cerullo, "Tracking the primary photoconversion events in rhodopsins by ultrafast optical spectroscopy", Photochem. Photobiol. Sci. **14**, 213–228 (2015).

[157] E. Perfetto and G. Stefanucci, "Some exact properties of the nonequilibrium response function for transient photoabsorption", Phys. Rev. A **91**, 033416 (2015).

[158] J. Walkenhorst, U. De Giovannini, A. Castro, and A. Rubio, "Tailored pump-probe transient spectroscopy with time-dependent density-functional theory: Controlling absorption spectra", Eur. Phys. J. B **89**, 128 (2016).

[159] M. Valiev, E. Bylaska, N. Govind, K. Kowalski, T. Straatsma, H. V. Dam, D. Wang, J. Nieplocha, E. Apra, T. Windus, and W. de Jong, "NWChem: A comprehensive and scalable open-source solution for large scale molecular simulations", Comp. Phys. Comm. **181**, 1477 (2010).

[160] A. A. Kocherzhenko, D. Lee, M. A. Forsuelo, and K. B. Whaley, "Coherent and incoherent contributions to charge separation in multichromophore systems", J. Phys. Chem. C **119**, 7590–7603 (2015).

[161] L. J. A. Koster, V. D. Mihailetchi, and P. W. M. Blom, "Ultimate efficiency of polymer/fullerene bulk heterojunction solar cells", Appl. Phys. Lett. **88**, 093511 (2006).

[162] J. C. Tully, “Molecular dynamics with electronic transitions”, J. Chem. Phys. **93**, 1061–1071 (1990).

[163] L. Wang and O. V. Prezhdo, “A simple solution to the trivial crossing problem in surface hopping”, J. Phys. Chem. Lett. **5**, 713–719 (2014).

[164] K. Král and Z. Khás, “Electron self-energy in quantum dots”, Phys. Rev. B **57**, R2061–R2064 (1998).

[165] M. Menšík, J. Pfleger, and P. Toman, “Dynamics of photogenerated polarons and polaron pairs in P3HT thin films”, Chem. Phys. Lett. **677**, 87–91 (2017).

[166] V. Janković and N. Vukmirović, “Identification of ultrafast photophysical pathways in photoexcited organic heterojunctions”, J. Phys. Chem. C **121**, 19602–19618 (2017).

[167] S. Chun-Qi, W. Peng, S. Ying, L. Yan-Jun, Z. Wen-Hua, X. Fa-Qiang, Z. Jun-Fa, L. Guo-Qiao, and L. Hong-Nian, “Electronic structure of PCBM”, Chin. Phys. B **21**, 017102 (2012).

[168] J. Idé, D. Fazzi, M. Casalegno, S. V. Meille, and G. Raos, “Electron transport in crystalline PCBM-like fullerene derivatives: A comparative computational study”, J. Mater. Chem. C **2**, 7313–7325 (2014).

[169] H. Ma and A. Troisi, “Modulating the exciton dissociation rate by up to more than two orders of magnitude by controlling the alignment of LUMO + 1 in organic photovoltaics”, J. Phys. Chem. C **118**, 27272–27280 (2014).

[170] Z. Li, X. Zhang, and G. Lu, “Electron structure and dynamics at poly(3-hexylthiophene)/fullerene photovoltaic heterojunctions”, Appl. Phys. Lett. **98**, 083303 (2011).

[171] T. Liu, D. L. Cheung, and A. Troisi, “Structural variability and dynamics of the P3HT/PCBM interface and its effects on the electronic structure and the charge-transfer rates in solar cells”, Phys. Chem. Chem. Phys. **13**, 21461–21470 (2011).

[172] M. Fujii, W. Shin, T. Yasuda, and K. Yamashita, “Photon-absorbing charge-bridging states in organic bulk heterojunctions consisting of diketopyrrolopyrrole derivatives and PCBM”, Phys. Chem. Chem. Phys. **18**, 9514–9523 (2016).

[173] Z. Sun and S. Stafström, "Dynamics of exciton dissociation in donor-acceptor polymer heterojunctions", J. Chem. Phys. **138**, 164905 (2013).

[174] Y.-K. Lan and C.-I. Huang, "A theoretical study of the charge transfer behavior of the highly regioregular poly-3-hexylthiophene in the ordered state", J. Phys. Chem. B **112**, 14857–14862 (2008).

[175] D. L. Cheung, D. P. McMahon, and A. Troisi, "Computational study of the structure and charge-transfer parameters in low-molecular-mass P3HT", J. Phys. Chem. B **113**, 9393–9401 (2009).

[176] R. S. Bhatta and M. Tsige, "Chain length and torsional dependence of exciton binding energies in P3HT and PTB7 conjugated polymers: A first-principles study", Polymer **55**, 2667–2672 (2014).

[177] G. Grancini, D. Polli, D. Fazzi, J. Cabanillas-Gonzalez, G. Cerullo, and G. Lanzani, "Transient absorption imaging of P3HT:PCBM photovoltaic blend: Evidence for interfacial charge transfer state", J. Phys. Chem. Lett. **2**, 1099–1105 (2011).

[178] Y. Yi, V. Coropceanu, and J.-L. Bredas, "A comparative theoretical study of exciton-dissociation and charge-recombination processes in oligothiophene/fullerene and oligothiophene/perylenediimide complexes for organic solar cells", J. Mater. Chem. **21**, 1479–1486 (2011).

[179] T. Liu and A. Troisi, "Absolute rate of charge separation and recombination in a molecular model of the P3HT/PCBM interface", J. Phys. Chem. C **115**, 2406–2415 (2011).

[180] M. Schulze, M. Hänsel, and P. Tegeder, "Hot excitons increase the donor/acceptor charge transfer yield", J. Phys. Chem. C **118**, 28527–28534 (2014).

[181] A. Grupp, P. Ehrenreich, J. Kalb, A. Budweg, L. Schmidt-Mende, and D. Brida, "Incoherent pathways of charge separation in organic and hybrid solar cells", J. Phys. Chem. Lett. **8**, 4858–4864 (2017).

[182] V. Janković and N. Vukmirović, “Combination of charge delocalization and disorder enables efficient charge separation at photoexcited organic bilayers”, J. Phys. Chem. C **122**, 10343–10359 (2018).

[183] H. Hoppe and N. S. Sariciftci, “Organic solar cells: an overview”, J. Mater. Res. **19**, 1924–1945 (2004).

[184] M. Gerhard, A. P. Arndt, I. A. Howard, A. Rahimi-Iman, U. Lemmer, and M. Koch, “Temperature- and energy-dependent separation of charge-transfer states in PTB7-based organic solar cells”, J. Phys. Chem. C **119**, 28309–28318 (2015).

[185] B. A. Gregg, “Entropy of charge separation in organic photovoltaic cells: the benefit of higher dimensionality”, J. Phys. Chem. Lett. **2**, 3013–3015 (2011).

[186] S. N. Hood and I. Kassal, “Entropy and disorder enable charge separation in organic solar cells”, J. Phys. Chem. Lett. **7**, 4495–4500 (2016).

[187] S. Ono and K. Ohno, “Combined impact of entropy and carrier delocalization on charge transfer exciton dissociation at the donor-acceptor interface”, Phys. Rev. B **94**, 075305 (2016).

[188] M. Wojcik and M. Tachiya, “Accuracies of the empirical theories of the escape probability based on Eigen model and Braun model compared with the exact extension of Onsager theory”, J. Chem. Phys. **130**, 104107 (2009).

[189] T. E. Goliber and J. H. Perlstein, “Analysis of photogeneration in a doped polymer system in terms of a kinetic model for electric-field-assisted dissociation of charge-transfer states”, J. Chem. Phys. **80**, 4162–4167 (1984).

[190] C. Deibel, T. Strobel, and V. Dyakonov, “Origin of the efficient polaron-pair dissociation in polymer-fullerene blends”, Phys. Rev. Lett. **103**, 036402 (2009).

[191] A. V. Nenashev, S. D. Baranovskii, M. Wiemer, F. Jansson, R. Österbacka, A. V. Dvurechenskii, and F. Gebhard, “Theory of exciton dissociation at the interface between a conjugated polymer and an electron acceptor”, Phys. Rev. B **84**, 035210 (2011).

[192] C. Schwarz, H. Bässler, I. Bauer, J.-M. Koenen, E. Preis, U. Scherf, and A. Köhler, "Does conjugation help exciton dissociation? A study on poly(p-phenylene)s in planar heterojunctions with C_{60} or TNF", Adv. Mater. **24**, 922–925 (2012).

[193] W. Osikowicz, M. de Jong, and W. Salaneck, "Formation of the interfacial dipole at organic–organic interfaces: C_{60}/polymer interfaces", Adv. Mater. **19**, 4213–4217.

[194] V. I. Arkhipov, P. Heremans, and H. Bässler, "Why is exciton dissociation so efficient at the interface between a conjugated polymer and an electron acceptor?", Appl. Phys. Lett. **82**, 4605–4607 (2003).

[195] S. Tscheuschner, H. Bässler, K. Huber, and A. Köhler, "A combined theoretical and experimental study of dissociation of charge transfer states at the donor–acceptor interface of organic solar cells", J. Phys. Chem. B **119**, 10359–10371 (2015).

[196] O. Rubel, S. D. Baranovskii, W. Stolz, and F. Gebhard, "Exact solution for hopping dissociation of geminate electron-hole pairs in a disordered chain", Phys. Rev. Lett. **100**, 196602 (2008).

[197] L. Shi, C. K. Lee, and A. P. Willard, "The enhancement of interfacial exciton dissociation by energetic disorder is a nonequilibrium effect", ACS Cent. Sci. **3**, 1262–1270 (2017).

[198] H. Bässler, "Charge transport in disordered organic photoconductors a Monte Carlo simulation study", Phys. Status Solidi B **175**, 15–56 (1993).

[199] A. Kell, X. Feng, M. Reppert, and R. Jankowiak, "On the shape of the phonon spectral density in photosynthetic complexes", J. Phys. Chem. B **117**, 7317–7323 (2013).

[200] K. D. Meisel, H. Vocks, and P. A. Bobbert, "Polarons in semiconducting polymers: study within an extended Holstein model", Phys. Rev. B **71**, 205206 (2005).

[201] C. M. Proctor, M. Kuik, and T.-Q. Nguyen, "Charge carrier recombination in organic solar cells", Prog. Polym. Sci. **38**, 1941–1960 (2013).

[202] T. Kirchartz, K. Taretto, and U. Rau, "Efficiency limits of organic bulk heterojunction solar cells", J. Phys. Chem. C **113**, 17958–17966 (2009).

[203] T. Offermans, S. C. J. Meskers, and R. A. J. Janssen, “Monte-Carlo simulations of geminate electron-hole pair dissociation in a molecular heterojunction: A two-step dissociation mechanism”, Chem. Phys. **308**, 125–133 (2005).

[204] A. P. Arndt, M. Gerhard, A. Quintilla, I. A. Howard, M. Koch, and U. Lemmer, “Time-resolved charge-transfer state emission in organic solar cells: temperature and blend composition dependences of interfacial traps”, J. Phys. Chem. C **119**, 13516–13523 (2015).

[205] J. H. Choi, K.-I. Son, T. Kim, K. Kim, K. Ohkubo, and S. Fukuzumi, “Thienyl-substituted methanofullerene derivatives for organic photovoltaic cells”, J. Mater. Chem. **20**, 475–482 (2010).

[206] N. B. Taylor and I. Kassal, “Generalised Marcus theory for multi-molecular delocalised charge transfer”, Chem. Sci. **9**, 2942–2951 (2018).

[207] Y. Yan, L. Song, and Q. Shi, “Understanding the free energy barrier and multiple timescale dynamics of charge separation in organic photovoltaic cells”, J. Chem. Phys. **148**, 084109 (2018).

Veljko Janković

Curriculum Vitae

Veljko Janković was born on September 23, 1990 in Belgrade, Republic of Serbia. He acquired elementary and high-school education in Belgrade.

In 2009, Veljko Janković enrolled on bachelor studies of physics at the Faculty of Physics, University of Belgrade, and completed them in 2013 with a GPA of 9.97/10.00. As one of the best third-year students at the Faculty of Physics, in 2012 he was awarded *Prof. Dr Đorđe Živanović* prize. In 2013, he started master studies with specialization in condensed matter physics, and finished them in June 2014 by defending the MSc thesis entitled *Nonequilibrium Optical Conductivity in Systems with Localized Electronic States*. The thesis was done in the Scientific Computing Laboratory of the Institute of Physics Belgrade under supervision of Dr Nenad Vukmirović. In October 2014, the thesis was awarded *Prof. Dr Ljubomir Ćirković* prize for the best MSc thesis defended at the Faculty of Physics during the academic year 2013/14.

In November 2014, Veljko Janković started his doctoral studies at the Faculty of Physics, University of Belgrade, with specialization in condensed matter physics. The research project was entirely conducted in the Scientific Computing Laboratory of the Institute of Physics Belgrade and was supervised by Dr Nenad Vukmirović. The project was focused on fundamental physical understanding of the light-to-charge conversion in organic solar cells. In the course of his doctoral programme, Veljko Janković published four peer-reviewed research papers directly connected to the topic of the thesis (papers 2–5) and one paper that is not connected to the topic of the thesis (paper 1).

5. V. Janković and N. Vukmirović, “Combination of Charge Delocalization and Disorder Enables Efficient Charge Separation at Photoexcited Organic Bilayers”, J. Phys. Chem. C, **122**, 10343–10359 (2018).

4. V. Janković and N. Vukmirović, “Identification of Ultrafast Photophysical Pathways in Photoexcited Organic Heterojunctions”, J. Phys. Chem. C **121**, 19602–19618 (2017).

3. V. Janković and N. Vukmirović, “Origin of Space-separated Charges in Photoexcited Organic Heterojunctions on Ultrafast Time Scales”, Phys. Rev. B **95**, 075308 (2017).

2. V. Janković and N. Vukmirović, “Dynamics of Exciton Formation and Relaxation in Photoexcited Semiconductors”, Phys. Rev. B **92**, 235208 (2015).
1. V. Janković and N. Vukmirović, “Nonequilibrium Optical Conductivity in Materials with Localized Electronic States”, Phys. Rev. B **90**, 224201 (2014).

Since November 2014, Veljko Janković has participated in the National Project ON171017 *Modeling and Numerical Simulations of Complex Many-Particle Systems* funded by the Ministry of Education, Science, and Technological Development of the Republic of Serbia. From October 2013 to August 2015, he participated in the European Community FP7 Marie Curie Integration Grant ELECTROMAT, whose head was Dr Nenad Vukmirović. Since 2015, he has participated in the COST Action MP1406 MultiscaleSolar. Veljko Janković has also been involved in the teaching process at the Faculty of Physics, University of Belgrade, as an external collaborator at the Chair of Theoretical Mechanics, Electrodynamics, and Statistical Physics. During the academic year 2013/14, he was a teaching assistant in Theoretical Mechanics (lecturer Prof. Dr Sunčica Elezović-Hadžić). Since the academic year 2014/15, he has been a teaching assistant in Quantum Statistical Physics (lecturers Doc. Dr Mihajlo Vanević and Prof. Dr Zoran Radović). During the school year 2012/13, as well as from the school year 2015/16 to 2017/18, Veljko Janković actively participated in the National Committee for High-School Physics Competitions as one of the authors of problems proposed to the final-year high-school students. He was one of the team leaders of the Serbian national team at *The 5th Romanian Master of Physics* (Bucharest, Romania, February 2016), *The 48th International Physics Olympiad* (Jogjakarta, Indonesia, July 2017), as well as at *The 49th International Physics Olympiad* (Lisbon, Portugal, July 2018). He is fluent in English and Italian languages.

During his doctoral programme, Veljko Janković had an opportunity to present the results of his research in the following conferences and workshops:

8. (oral) V. Janković and N. Vukmirović, “Importance of Carrier Delocalization and Disorder for Incoherent Charge Separation at Organic Bilayers”, E-MRS Spring Meeting 2018, 18–22 June 2018, Strasbourg Convention Center, Strasbourg, France, oral contribution J12.7 (2018).

7. (poster) V. Janković and N. Vukmirović, “Origin of Space-Separated Charges in Photoexcited Organic Heterojunctions on Subpicosecond Time Scales”, The 6th International School and Conference on Photonics, 28 August–1 September 2017, Belgrade, Serbia, Book of Abstracts, p. 164 (2017).

6. (poster) V. Janković and N. Vukmirović, “Origin of Space-Separated Charges in Photoexcited Organic Heterojunctions on Ultrafast Time Scales”, Workshop on Spectroscopy and Dynamics of Photoinduced Electronic Excitations, International Center for Theoretical Physics, Trieste, Italy, 8–12 May 2017.

5. (poster) V. Janković and N. Vukmirović, “Exciton Formation and Relaxation Dynamics in Photoexcited Organic Semiconductors and Their Heterojunctions: Numerical Study”, Gordon Research Conference Electronic Processes in Organic Materials, Barga (Lucca), Italy, 5−10 June 2016, Poster Presentation 41 (2016).

4. (poster) V. Janković and N. Vukmirović, “Nonequilibrium Electrical Transport in Materials with Localized Electronic States”, The 26th International Conference on Amorphous and Nanocrystalline Semiconductors, Aachen, Germany, 13−18 September 2015, Book of Abstracts, p. 72 (2015).

3. (poster) V. Janković and N. Vukmirović, “Nonequilibrium High-Frequency Conductivity in Materials with Localized Electronic States”, The 19th Symposium on Condensed Matter Physics (SFKM), Belgrade, Serbia, 7−11 September 2015, Book of Abstracts, p. 88 (2015).

2. (poster) V. Janković and N. Vukmirović, “Nonequilibrium Terahertz Conductivity in Systems with Localized Electronic States”, EDISON 19, 29 June−2 July 2015, Salamanca, Spain, Book of Abstracts, p. 125 (2015).

1. (poster) V. Janković and N. Vukmirović, “Nonequilibrium Terahertz Conductivity in Materials with Localized Electronic States”, Nanoscale Quantum Optics-Kick off Workshop, 9−10 April 2015, Belgrade, Serbia, Book of Abstracts, p. 55 (2015).

Изјава о ауторству

Име и презиме аутора **Вељко Јанковић**

Број индекса **8010/2014**

Изјављујем

да је докторска дисертација под насловом

Exciton dynamics at photoexcited organic heterojunctions

(Динамика екситона на органским хетероспојевима побуђеним светлошћу)

- резултат сопственог истраживачког рада;
- да дисертација у целини ни у деловима није била предложена за стицање друге дипломе према студијским програмима других високошколских установа;
- да су резултати коректно наведени и
- да нисам кршио ауторска права и користио интелектуалну својину других лица.

Потпис аутора

У Београду, **5. IX 2018.**

Вељко Јанковић

Изјава о истоветности штампане и електронске верзије докторског рада

Име и презиме аутора **Вељко Јанковић**

Број индекса **8010/2014**

Студијски програм **Физика – Физика кондензоване материје**

Наслов рада ***Exciton dynamics at photoexcited organic heterojunctions (Динамика екситона на органским хетероспојевима побуђеним светлошћу)***

Ментор **др Ненад Вукмировић**

Изјављујем да је штампана верзија мог докторског рада истоветна електронској верзији коју сам предао/ла ради похрањена у **Дигиталном репозиторијуму Универзитета у Београду.**

Дозвољавам да се објаве моји лични подаци везани за добијање академског назива доктора наука, као што су име и презиме, година и место рођења и датум одбране рада.

Ови лични подаци могу се објавити на мрежним страницама дигиталне библиотеке, у електронском каталогу и у публикацијама Универзитета у Београду.

Потпис аутора

У Београду, **5. IX 2018.**

Вељко Јанковић

Изјава о коришћењу

Овлашћујем Универзитетску библиотеку „Светозар Марковић“ да у Дигитални репозиторијум Универзитета у Београду унесе моју докторску дисертацију под насловом:

Exciton dynamics at photoexcited organic heterojunctions (Динамика екситона на органским хетероспојевима побуђеним светлошћу)

која је моје ауторско дело.

Дисертацију са свим прилозима предао сам у електронском формату погодном за трајно архивирање.

Моју докторску дисертацију похрањену у Дигиталном репозиторијуму Универзитета у Београду и доступну у отвореном приступу могу да користе сви који поштују одредбе садржане у одабраном типу лиценце Креативне заједнице (Creative Commons) за коју сам се одлучио/ла.

1. Ауторство (CC BY)

2. Ауторство – некомерцијално (CC BY-NC)

[✓ 3.] Ауторство – некомерцијално – без прерада (CC BY-NC-ND)

4. Ауторство – некомерцијално – делити под истим условима (CC BY-NC-SA)

5. Ауторство – без прерада (CC BY-ND)

6. Ауторство – делити под истим условима (CC BY-SA)

(Молимо да заокружите само једну од шест понуђених лиценци.
Кратак опис лиценци је саставни део ове изјаве).

Потпис аутора

У Београду, **5. IX 2018.**

Вељко Јанковић

1. **Ауторство**. Дозвољавате умножавање, дистрибуцију и јавно саопштавање дела, и прераде, ако се наведе име аутора на начин одређен од стране аутора или даваоца лиценце, чак и у комерцијалне сврхе. Ово је најслободнија од свих лиценци.

2. **Ауторство – некомерцијално**. Дозвољавате умножавање, дистрибуцију и јавно саопштавање дела, и прераде, ако се наведе име аутора на начин одређен од стране аутора или даваоца лиценце. Ова лиценца не дозвољава комерцијалну употребу дела.

3. **Ауторство – некомерцијално – без прерада**. Дозвољавате умножавање, дистрибуцију и јавно саопштавање дела, без промена, преобликовања или употребе дела у свом делу, ако се наведе име аутора на начин одређен од стране аутора или даваоца лиценце. Ова лиценца не дозвољава комерцијалну употребу дела. У односу на све остале лиценце, овом лиценцом се ограничава највећи обим права коришћења дела.

4. **Ауторство – некомерцијално – делити под истим условима**. Дозвољавате умножавање, дистрибуцију и јавно саопштавање дела, и прераде, ако се наведе име аутора на начин одређен од стране аутора или даваоца лиценце и ако се прерада дистрибуира под истом или сличном лиценцом. Ова лиценца не дозвољава комерцијалну употребу дела и прерада.

5. **Ауторство – без прерада**. Дозвољавате умножавање, дистрибуцију и јавно саопштавање дела, без промена, преобликовања или употребе дела у свом делу, ако се наведе име аутора на начин одређен од стране аутора или даваоца лиценце. Ова лиценца дозвољава комерцијалну употребу дела.

6. **Ауторство – делити под истим условима**. Дозвољавате умножавање, дистрибуцију и јавно саопштавање дела, и прераде, ако се наведе име аутора на начин одређен од стране аутора или даваоца лиценце и ако се прерада дистрибуира под истом или сличном лиценцом. Ова лиценца дозвољава комерцијалну употребу дела и прерада. Слична је софтверским лиценцама, односно лиценцама отвореног кода.